STRUCTURE AND FUNCTION OF ATYPICAL BTB DOMAINS IN HEALTH AND DISEASE



Thesis submitted by

David A. Cruz Walma

St. Edmund Hall

For the degree of

Doctor of Philosophy

Supervisors: Professor Alex Bullock and Dr. Kenneth Yamada

ABSTRACT

Proteins containing the BTB domain conventionally homodimerise to perform a variety of critical biological processes and serve diverse roles such as transcriptional regulators, voltage-gated ion channels, and E3 ubiquitin ligase substrate adaptors. The molecular mechanisms for many of these proteins, particularly “atypical” BTB proteins forming higher order structures or containing tandem BTB domains, are poorly characterised. This thesis characterised the intramolecular and intermolecular protein interactions of atypical BTB proteins and how such interactions may determine function and disease, particularly of the craniofacial complex. Three complementary approaches were used to achieve the aims of this thesis and included 1) characterising the morphogenic role of the tandem BTB protein BTBD7 in 3D cell culture, 2) investigating the biophysical properties and molecular mechanisms of the tandem BTB protein class, and 3) characterising the structural, biophysical, and mechanistic alterations caused by mutations in the pentameric BTB protein KCTD15. Novel 3D cell culture models alongside several microscopy and proteomic assays revealed BTBD7 may contribute to *in vitro* cellular phenotypes consistent with tubular morphogenesis that were not observed *in vivo*, perhaps due to incomplete knockout of the gene. Size-exclusion chromatography coupled with multi-angle light scattering (SEC-MALS), X-ray crystallography, and several other biophysical assays showed heterogeneity in tandem BTB domain oligomerisation and binding affinities for CUL3. Similar structural and biophysical approaches alongside analytical ultracentrifugation (AUC), differential scanning fluorimetry (DSF), and biolayer interferometry (BLI) showed that human mutations in the BTB domain of KCTD15 caused aberrant BTB domain oligomerisation and inhibited KCTD15 from binding its interaction partner transcription factor AP2. Collectively, this work enhances our understanding of molecular mechanisms of the atypical BTB proteins in normal development as well as pathobiology and provides clarity on how mutations in these proteins cause human disease.

DECLARATION

I declare that no parts of this thesis or its research have been reproduced or accepted for another award, degree, or diploma at another university or learning institution. This thesis contains no other individual's work except where stated in the text. Parts of chapter 5 have been published in Journal of Medical Genetics.

ACKNOWLEDGEMENTS

Pursuing a PhD results in an exceptionally long list of people to thank, making it impossible to name each individually (and remain within the permitted word limit). To those I have failed to acknowledge by name in this section, you have my utmost thanks and gratitude.

I dedicate this dissertation to all those whose mentorship, support, and love have guided me through the past four challenging, yet immensely enjoyable and rewarding, years.

To my mentors – Alex Bullock and Kenneth Yamada. You are both inspiring individuals and brilliant scientists. You have been exceptionally supportive, kind, patient, and irreplaceable mentors guiding me through this complicated, fast-paced program. I can only hope to emulate your qualities as mentors and scientists as I continue my academic career.

To Rob Gilbert, who helped shape my graduate studies from my initial application to Oxford through my thesis defence and beyond. Outside being a continuous presence offering irreplaceable feedback throughout my studies, Rob has led me through the world of teaching and academic leadership and is a major reason I pursue a career in academia. His passion and devotion to students has been an inspiration.

To my clinical school mentor and close friend – Dr. Yung-Tsung Hsu – who provided unparalleled support as I transitioned from clinical school to PhD training and back again. Dr. Hsu emphasises the importance of “thinking outside the box” to make progress in any given field and has been incredibly supportive throughout my unconventional education. Dr. Hsu is wholeheartedly devoted to his students and is another major reason I pursue a teaching career. It is because of Dr. Hsu that I arrive to clinic with a smile every day.

To Dr. Francesca Gori, who first introduced me to the world of rigorous scientific investigation and is one of the main reasons why I pursued a PhD.

To my lab-mates on both sides of the Atlantic: Dr. Zhuoyao Chen, Dr. Jong Fu Wong, Dr. Shaohe Wang, and Dr. Andrew Doyle, who helped create supportive, creative, and friendly learning environments.

教練王春榮和朋友周漢聶，你們在我跑步及生命成長中不可或缺。感謝你們的支持、勉勵，使我在跑步中得到力量，完成艱難的學業。感激有你們以身作則，使我學會堅毅。

Finally, to my parents, Rafael Cruz and Catherine Walma, as well as my brothers, Alex, Jonny, and Nate Cruz Walma. You are all, without a doubt, the most loving, generous, and patient individuals I have ever known. You have encouraged me to pursue whatever path I chose and have been an unwavering support throughout numerous surprises, both good and bad. I would not be here without your support and love. With my entire being, I love you.

IMPACT OF COVID ON STUDIES

Planned work prior to building closure

Prior to the closure, I was characterising *in vitro* 3D cell culture phenotype variations between SIMS wild-type and SIMS BTBD7 knockout cells. The inhibitor/growth factor and proteomic assays performed after the lockdown would have been completed earlier if the pandemic had not occurred. Follow up proteomic assays enriching for specific pathways (e.g., ubiquitin pathways) would have been performed. I would have created lentiviral BTBD7 rescue cell lines and performed 3D *in vitro* rescue assays to ensure the observed phenotype differences are related to BTBD7 expression and not clonal variation.

Work performed during closure

During workspace closure, I first planned all experiments to be performed upon regaining workspace access. I then published a review in Development (Walma and Yamada, 2020) as well as an article in the Journal of Dental Education (Aitken et al., 2020), and worked on reviews for the Journal of Dental Research (Cruz Walma and Yamada, 2022), and Nature Reviews Molecular Cell Biology (Cruz Walma et al., 2022). I am an Associate Editor for Oral Diseases and a reviewer for several journals for which I handled manuscripts throughout the lockdown. During the pandemic, I volunteered for the NIH Covid Response Team, served as a peer supporter for NIH trainees, served as a UNIQ+ mentor for Oxford, helped with the 2020 Teddy Hall Graduate Access Summer School, served as a faculty member teaching online courses for the FAES at the NIH, and served as the Nuffield Department of Medicine Student Committee Chair, the Oxford Representative of the NIH-OxCam Student Leadership Board, and the Teddy Hall MCR Sports representative.

Continued impact of COVID on studies

Following the lab lockdown and in the middle of the pandemic, I moved from the National Institutes of Health to Oxford. I had to spend several weeks in quarantine, thus delaying my ability to begin working in my Oxford-based lab. Following the quarantine, it took several weeks to complete all in-person trainings required to perform experiments since administrative members of the

department were not all on site. Shortly after beginning experiments at Oxford, my lab moved buildings from the Old Road Campus Research Building to the Biochemistry Building. This lab move involved several months of packing, moving, and unpacking during which experiments could not be performed. Fortunately, many of the COVID-induced restrictions regarding lab access were lifted following this move. During the subsequent months, work for my thesis progressed swiftly. Towards the end of my DPhil studies, the lab once again moved buildings back to the Old Road Campus site. Such a move once again involved several months of halted experiments. Altogether, an estimated eight to ten months of lab work was missed secondary to lab moves and the COVID pandemic.

TABLE OF CONTENTS

ABSTRACT 2
DECLARATION 3
ACKNOWLEDGEMENTS 4
IMPACT OF COVID ON STUDIES 6
TABLE OF CONTENTS 8
LIST OF FIGURES 12
LIST OF TABLES 14
1 CHAPTER ONE – Introduction and aims of the study 15
1.1 The BTB domain 15
1.1.1 Background 15
1.1.2 BTB domain fold and oligomerisation 16
1.1.3 Biological functions 18
1.1.3.1 Transcriptional regulators 18
1.1.3.2 Voltage-gated ion channels 20
1.1.3.3 E3 ubiquitin ligase substrate adaptors 21
1.2 Atypical BTBs 23
1.2.1 The tandem BTB domain 23
1.2.2 The KCTD family 25
1.3 BTBs in human disease 27
1.3.1 BTBD7 27
1.3.2 RHOBTB1 28
1.3.3 LZTR1 30
1.3.4 KCTD15 and KCTD1 32
1.4 Aims of this thesis 33
1.5 References 36

2 CHAPTER TWO – Materials and methods 47
2.1 General cell culture 47
2.1.1 Cell lines and growth conditions 47
2.1.2 Cell counting 47
2.2 2D cell culture assays 48
2.2.1 Coverslip coating with extracellular matrix proteins 48
2.2.2 Colocalisation assays 48
2.3 3D cell culture assays 49
2.3.1 Activation of glass imaging chambers 49
2.3.2 Matrigel gel formation and cell culture 49
2.3.3 Collagen gel formation and cell culture 50
2.3.4 Ubiquitin pathway inhibition and growth factor supplementation assays 51
2.4 Microscopy and imaging 52
2.4.1 Automated brightfield microscopy 52
2.4.2 Immunostaining light microscopy 52
2.4.3 Image processing and analysis 53
2.5 Animal studies 54
2.5.1 Mouse breeding 54
2.5.2 Mouse dissections 54
2.6 Cloning 55
2.6.1 Restriction enzyme digestion 55

2.6.2 Ligation independent cloning (LIC) 56
2.6.3 Site-directed mutagenesis 58
2.6.4 Transformations 59
2.7 Lentiviral assays 60
2.7.1 Lentivirus packaging 60
2.7.2 Lentivirus titration 61
2.7.3 Lentivirus transduction 61
2.8 Protein expression 61
2.8.1 *E. coli* expression 61
2.9 Protein purification 63
2.9.1 Buffers 63
2.9.2 Cell lysis 63
2.9.3 Affinity purification of glutathione s-transferase and hexahistidine fusion proteins 64
2.9.4 Size exclusion chromatography 65
2.9.5 Ion-exchange chromatography 66
2.9.6 Protein handling 67
2.10 Western blotting 68
2.11 Co-immunoprecipitation 69
2.12 Size exclusion chromatography/multi-angle light scattering (SEC-MALS) 70
2.13 Differential scanning fluorimetry 71
2.14 X-ray crystallography 72
2.14.1 Crystallisation 72
2.14.2 Structure determination 73
2.15 Structural modelling 75
2.15.1 Modelling of CUL3 binding to tandem BTB AlphaFold models 75
2.15.2 Homology modelling 76
2.16 Mass spectrometry 77
2.16.1 Intact mass spectrometry (LC/MS) 77
2.16.2 Native mass spectrometry 78
2.16.3 Phosphoproteomics 79
2.17 Analytical ultracentrifugation 81
2.18 Biolayer interferometry 83
2.19 References 84

3 CHAPTER THREE – Characterising the morphogenic role of BTBD7 using 3D *in vitro* culture models 90
3.1 Introduction 90
3.2 Results 92
3.2.1 New polyclonal and monoclonal antibodies to BTBD7 are applicable for western blot assays 92
3.2.2 Novel 3D cultures as tools to characterise the 3D *in vitro* biologic function of target proteins 94
3.2.3 BTBD7 exhibited a diffuse cytoplasmic distribution and did not co-localise to adherens junctions, endoplasmic reticula, endosomes, nor proteasomes in 2D 98

3.2.4 BTBD7 knockout 3D cultures formed less organised, smaller, and more numerous protrusions compared to wild-type cultures 100
3.2.5 Ubiquitin signalling pathway inhibition exacerbated the BTBD7-associated 3D culture phenotype 101
3.2.6 A preliminary large-scale proteomic investigation showed no significant differences between BTBD7 wild-type and knockout 3D culture proteomes 104
3.2.7 Stable tetracycline-inducible BTBD7 expression cell lines were produced for BTBD7 rescue assays 106
3.2.8 BTBD7 knockout mice grew to become healthy adults and showed no phenotypic difference compared to control mice 106
3.3 Discussion 108
3.4 References 114

4 CHAPTER FOUR – Molecular mechanisms of tandem BTB proteins 118
4.1 Introduction 118
4.2 Results 119
4.2.1 Construct design and cloning 119
4.2.2 Construct test expression and test purification 122
4.2.3 Optimisation of large-scale protein production 123
4.2.4 Only a subset of the purified tandem BTB proteins bind CUL3 127
4.2.5 SEC-MALS indicates that tandem BTBs exhibit different stoichiometries and bind CUL3 in different ratios 129
4.2.6 RHOBTB1 folding is stabilised by CUL3 binding 132
4.2.7 Crystallisation of tandem BTB proteins 134
4.2.7.1 LZTR1 crystallisation trials 134
4.2.7.2 RHOBTB1 crystallisation trials 137
4.2.7.3 BTBD7 crystallisation trials 139
4.2.8 Compatibility of CUL3 binding to AlphaFold models of BTBD7, RHOBTB1, and LZTR1 141
4.3 Discussion 145
4.4 References 151

5 CHAPTER FIVE – The pathogenic roles of BTB domain mutations in craniofacial disease 154
5.1 Introduction 154
5.2 Results 156
5.2.1 KCTD15 wild type and variants exhibit differing recombinant expression levels and stability 156
5.2.2 Homology models predict the KCTD15 substitution Asp104His disrupts BTB domain oligomerisation 159
5.2.3 Crystallographic analysis of KCTD15 wild type and variants 162
5.2.4 Native mass spectrometry analysis of KCTD15 wild type and variants 167

5.2.5 Additional biophysical analyses confirm human mutations in KCTD15 perturb protein oligomerisation 172
5.2.6 Human variant KCTD15 Asp104His displays altered thermal stability compared to wild-type KCTD15 173
5.2.7 Biolayer interferometry indicates KCTD15 substitutions may perturb KCTD15 binding to TFAP2 175
5.3 Discussion 177
5.4 References 182

6 CHAPTER SIX – Conclusions and future directions 186
6.1 Approach 1 – the morphogenic role of BTBD7 in 3D culture models 187
6.2 Approach 2 – molecular mechanisms of the tandem BTB domain 189
6.3 Approach 3 – pathogenic mechanisms of KCTD15 mutations in craniofacial disease 193
6.4 References 196

APPENDICES 200

LIST OF FIGURES

CHAPTER ONE

Figure 1.1 BTB fold topology and oligomerisation states.
Figure 1.2 Examples of BTB domain-containing proteins serving as transcription factors and E3 ubiquitin ligases.
Figure 1.3 The KCTD protein family including an overview of KCTD1, KCTD15, and their pathologic variants.
Figure 1.4 Domain maps of BTBD7, RHOBTB1, and LZTR1.
Figure 1.5 Expression profiles and example biological functions of BTBD7, RHOBTB1, and LZTR1.
Figure 1.6 Schematic overview of the three approaches used to achieve the aims of this thesis.

CHAPTER THREE

Figure 3.1 Mouse monoclonal antibodies specific to BTBD7 are applicable for western blot assays.
Figure 3.2 SMG-HU1 cells exhibited interesting 3D culture phenotypes useful for characterising salivary gland cell migration.
Figure 3.3 3D collagen matrix cultures of mouse submandibular salivary gland cells are useful *in vitro* tools to investigate protein function.
Figure 3.4 In SIMS cells, fluorescently tagged BTBD7 was diffusely cytoplasmic and did not co-localise with target organelles in 2D.
Figure 3.5 SIMS BTBD7 knockout 3D cell cultures exhibited altered tubular networks compared to wild-type cell cultures, though no significant differences in cytoskeletal and adherens junction architectures were observed between knockout and wild-type cultures.
Figure 3.6 Inhibiting the ubiquitin signalling system selectively altered the 3D culture phenotype of SIMS BTBD7 knockout cultures compared to SIMS BTBD7 wild-type cultures.
Figure 3.7 Preliminary mass spectrometry assays detected similar proteomic profiles between SIMS BTBD7 wild-type and knockout 3D cultures.
Figure 3.8 Knockout of the BTB domains of BTBD7 in C57BL/6 mice showed no phenotypic differences compared to wild-type C57BL/6 mice and knockout mice grew to become healthy viable adult mice.

CHAPTER FOUR

Figure 4.1 Construct design and PCR screen of ligation independent cloning (LIC) inserts of the tandem BTB domain proteins prior to ligation into pNIC28-Bsa4 vectors.
Figure 4.2 Test expression and nickel-affinity purification of the successfully cloned and transformed tandem BTB protein constructs.
Figure 4.3 Optimising the large-scale protein production of $BTBD7_{118\text{-}483}$, $RHOBTB1_{252\text{-}591}$, and $LZTR1_{424\text{-}766}$.
Figure 4.4 Co-immunoprecipitation of $BTBD7_{118\text{-}483}$, $RHOBTB1_{252\text{-}591}$, and $LZTR1_{424\text{-}766}$ with Flag-tagged $CUL3_{1\text{-}388}$.

Figure 4.5 SEC-MALS and DSF of $BTBD7_{118-483}$, $RHOBTB1_{252-591}$, and $LZTR1_{424-766}$ with $CUL3_{1-388}$.
Figure 4.6 Crystallisation trials of $LZTR1_{424-766}$.
Figure 4.7 Crystallisation trials of $BTBD7_{118-483}$ and $RHOBTB1_{252-591}$.
Figure 4.8 Modelling of CUL3 binding to tandem BTB AlphaFold models.

CHAPTER FIVE

Figure 5.1 The two families affected by missense substitutions in KCTD15.
Figure 5.2 Optimising the expression and purification of KCTD15 constructs.
Figure 5.3 Published structures of KCTD15 homologues alongside homology modelling of KCTD15 wild type and variants.
Figure 5.4 Crystal forms of KCTD15 Gly88Asp BTB domain and crystallisation trials of KCTD15 Asp104His.
Figure 5.5 Crystal structure of the KCTD15 Gly88Asp variant BTB domain.
Figure 5.6 Native mass spectrometry of KCTD15 wild-type and variant BTB domains.
Figure 5.7 Native mass spectrometry of KCTD15 wild-type and variant BTB+CTD domains.
Figure 5.8 AUC, SEC-MALS, and DSF analyses of KCTD15 wild type and variants.
Figure 5.9 Biolayer interferometry of KCTD1, KCTD15 wild type, and KCTD15 variants.

LIST OF TABLES

CHAPTER FOUR

Table 4.1 SEC-MALS results of tandem BTB proteins alone and in complex with CUL3.

CHAPTER FIVE

Table 5.1 KCTD15 G88D crystallographic data collection and refinement statistics.

Table 5.2 Native mass spectrometry results of KCTD15 wild type and two human variants.

Table 5.3 SEC-MALS and AUC results of KCTD15 wild type and two human variants.

Table 5.4 Differential scanning fluorimetry apparent *Tm* values of KCTD15 wild type and two human variants.

APPENDIX

Table A.1 Key resources.

Table A.2 Recombinant protein constructs.

Table A.3 Recombinant protein cloning primers.

CHAPTER ONE

Introduction and aims of the study

1.1 The BTB domain

1.1.1 Background

The BTB (or POZ) domain is a highly conserved versatile protein-protein interaction motif initially identified in bric-à-brac, tramtrack and broad (BTB) complex transcription regulators of Drosophila melanogaster as well as pox virus zinc finger proteins (POZ) (1). Since then, approximately 200 BTB-containing proteins have been identified in the human genome performing functions as diverse as transcriptional regulators, voltage-gated ion channels, and E3 ubiquitin ligase substrate adaptors. Proteins containing the BTB domain have been categorised into families based on the similarity of their sequences, structural elements, and biological functions. The overall number and distribution of BTB protein families varies between species. In the human genome, BTB-containing proteins are categorised into families dependent on the conserved domains surrounding their BTB domains. The three largest families include the BTB-ZF, T1-Kv, and BTB-BACK-Kelch families whose members tend to serve as transcription regulators, voltage-gated ion channels, and E3 ubiquitin ligase substrate adaptors, respectively. Smaller families include the MATH-BTB, RhoBTB, BTB-BACK-PHR, BTB-ankyrin, BTB-bZip, and BTB with no other identified domain protein families (2).

A common characteristic among the structural classes of BTB domains is their ability to oligomerise. As discussed in the following section, each protein class tends to follow a specific pattern of hetero- or homo-oligomerisation to produce functional protein complexes.

1.1.2 BTB domain fold and oligomerisation

The core BTB fold was first defined by the structure of the 'T1 domain' of Shaker potassium channel AKv1.1a and is shared by many other voltage-gated potassium channel proteins (3). Further studies have shown this domain is not limited to potassium channel proteins but is also found in soluble proteins. The core component of the BTB domain fold contains five alpha helices organised into two alpha-helical hairpins (A1-A2 and A4-A5) interposed within a three-stranded solvent-exposed beta sheet (B1-B3). Alpha helix A3 links the B1-B2-A1-A2 folds to the A4-A5 hairpin (Figure 1.1A). Beyond this core fold, small amino- and carboxy-terminal decorations are found in some BTB proteins dependent on their subfamily (Figure 1.1A).

BTB domain-containing proteins are most commonly observed forming functional homodimers as a result of a β-strand and α-helix at the amino terminus of the domain (2) (Figure 1.1A). Nevertheless, the BTB domain is also able to adopt monomeric or various higher order oligomeric states specific to protein function (4) (Figure 1.1A). For example, proteins containing the related T1 domain adopt homotetrameric assemblies (Figure 1.1D) (2). BTB domains in the KCTD family have been shown forming tetramers with four-fold or two-fold rotational symmetry as well as closed and open pentamers (Figure 1.1E) (4). Interestingly, the

oligomerisation of some BTB domains is dependent on the presence of binding partners exemplified by SHKBP1 failing to oligomerise and instead forming monomers in the absence of CUL3 (4). For these higher order assemblies, oligomerisation is closely linked to function. For example, the KCTD member KCTD16 forms functional open pentameric assemblies to bind $GABA_B$ receptors. Perturbation of the oligomeric state can disrupt function as demonstrated by the incorporation of a sixth BTB subunit into the KCTD16 assembly which results in the formation of an inhibitory closed hexamer (5).

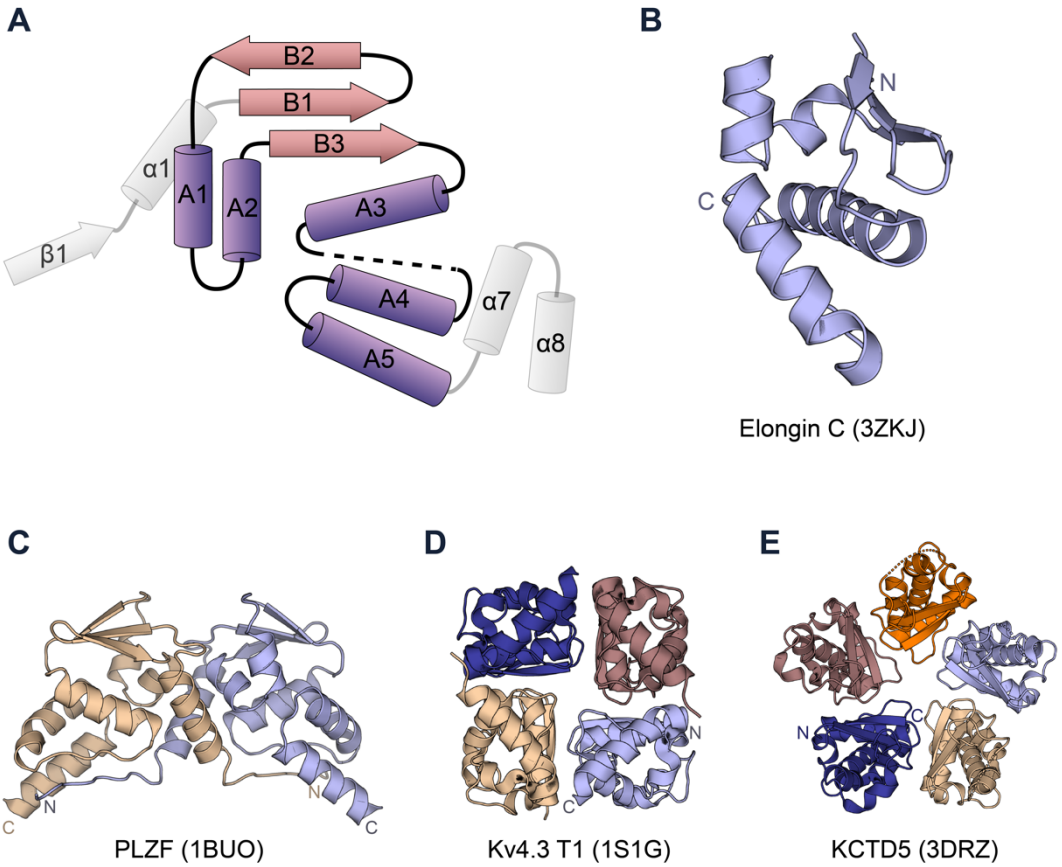


Figure 1.1 BTB fold topology and oligomerisation states. (A) Schematic of the BTB fold. The core components of the conventional BTB fold are labelled B1 to B3 (salmon-coloured arrows) for the three conserved beta-strands, and A1 to A5 (violet-coloured cylinders) for the five conserved alpha-helices. Some BTB proteins contain an amino-terminal extension of α1 and β1 or two additional alpha-helices at the carboxyl terminus, labelled α7 and α8. These amino- and carboxy-terminal extensions are coloured a faded grey in the image. The dashed

line between A3 and A4 represents a segment of the core BTB fold that can be observed as an alpha-helix in Skp1 proteins or a β5 strand in select BTB domain-containing proteins. (B) Ribbon structure of the Elongin C BTB domain (PDB ID 3ZKJ) as an example of monomeric BTB domains. The carboxyl and amino terminus of the domain is labelled. (C) Ribbon structure of the PLZF homodimer (PDB ID 1BUO). The BTB domain of PLZF homodimerizes to form a functional transcription factor capable of recruiting DNA histone deacetylases and regulating chromatin remodelling. The carboxyl and amino terminus of the BTB domains are labelled. (D) Ribbon structure of the Kv4.3 T1 domain (PDB ID 1S1G) as an example of BTB domains that oligomerise into function tetramers. The Kv4.3 tetramer serves as a voltage-gated ion channel. (E) Ribbon structure of the KCTD5 complex (PDB ID 3DRZ) as an example of BTB domains that oligomerise into functional pentamers. KCTD5 acts as a pentameric CUL3-dependent E3 ligase to regulate the ubiquitination of various proteins such as components of the Gβγ signalling pathway. For (D) and (E), the carboxyl and amino terminus of one BTB domain in the oligomer is labelled.

1.1.3 Biological functions

BTB domain-containing proteins have been implicated in a wide range of cellular functions including, but not limited to, transcriptional regulation, ion channel assembly and gating, as well as Cullin-RING ligase (CRL) mediated protein ubiquitination (2).

1.1.3.1 Transcriptional regulators

Transcription factors are proteins that bind specific sequences of DNA to regulate chromatin remodelling and transcription. New protein motifs capable of binding DNA in a sequence-specific manner continue to be identified. However, the initial transcription factor families identified in the 1980s include the C_2H_2 zinc finger (ZF), homeodomain, basic helix-loop-helix, basic leucine zipper, and nuclear hormone receptor proteins (6).

The BTB-Zinc Finger (BTB-ZF) proteins (also known as “POK” proteins for “POZ/ Krüppel-like”) possess a series of C_2H_2 zinc finger motifs and many are

considered zinc-finger transcription factors. For these BTB-ZF transcription factors, the ZF motif binds DNA in a sequence-specific manner while the BTB domain recruits additional proteins such as transcriptional repressors (e.g., the homodimeric BTB domain of BCL6 interacting with corepressors N-CoR and SMRT (Figure 1.2A,B) (7)) and activators (e.g., Miz-1 recruiting p300 (8)). Transcriptional regulation by BTB-ZFs has been shown to regulate musculoskeletal development, neurological homeostasis, haematopoiesis, fertility, immune system maintenance, and several other physiologic processes (9, 10).

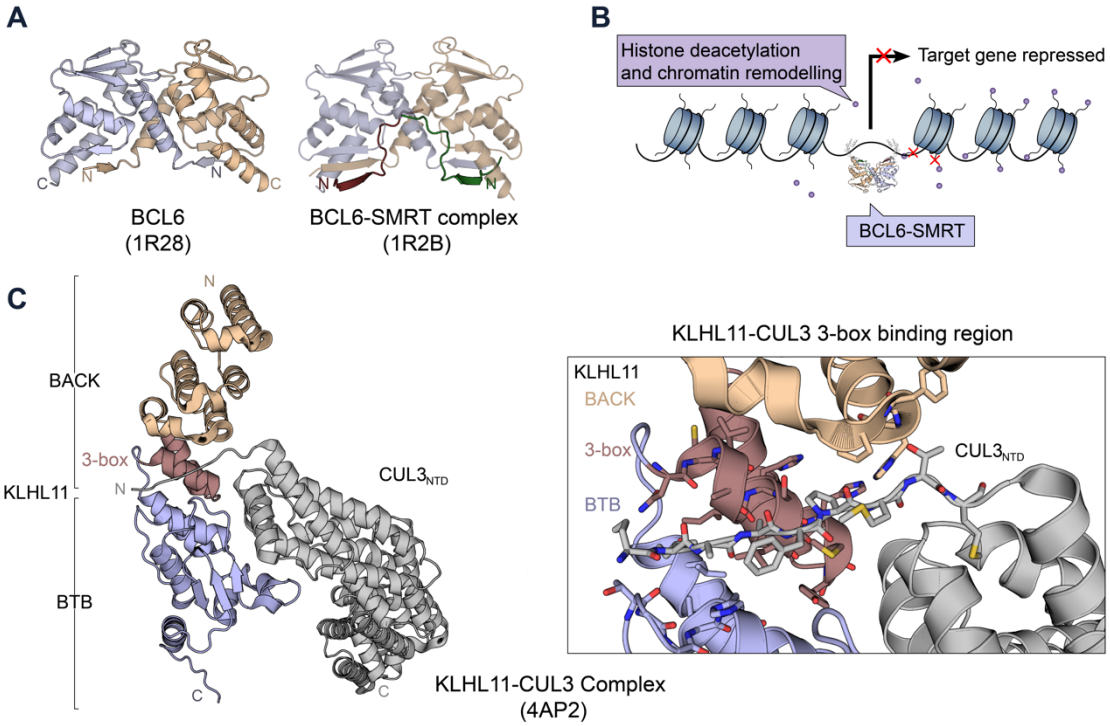


Figure 1.2 Examples of BTB domain-containing proteins serving as transcription factors and E3 ubiquitin ligases. (A) Ribbon diagram of the BCL6 BTB dimer alone (PDB ID 1R28) and in complex with two SMRT peptides (PDB ID 1R2B). The BTB domains of BCL6 form a homodimer with each BTB domain interacting with one SMRT molecule. The two chains of the BCL6 homodimer are coloured light blue and wheat, the two SMRT chains are coloured deep violet and dark green. The amino and carboxy termini of the two BCL6 BTB domains are labelled. The amino termini of the two SMRT chains are labelled. (B) Schematic illustrating the biological mechanism of the BCL6-SMRT complex. BCL6-SMRT binds to DNA via the zinc finger domain of BCL6. The complex promotes histone deacetylation and chromatin compaction to repress

gene expression. (C) Ribbon diagram of the human KLHL11-CUL3 structure (PDB ID 4AP2) highlighting the functional domains of the complex. Physiologically, KLHL11 forms a homodimer to recruit two CUL3 molecules. A single protamer of the KLHL11-CUL3 dimer is depicted. The amino-terminal extension of CUL3 binds the 3-box in a hydrophobic groove between the BTB and BACK domains of KLHL11. This amino-terminal extension of CUL3 and the hydrophobic groove of KLHL11 are depicted as sticks in the zoomed image of panel C. Amino and carboxy termini of CUL3 and KLHL11 are labelled.

1.1.3.2 Voltage-gated ion channels

Voltage-gated ion channels are transmembrane proteins responsible for the generation of electrical signals across cell membranes. These transmembrane channels undergo voltage-dependent conformational changes to permit or prevent the passage of ions across the cell membrane. These channels are frequently ion specific and therefore may be selectively permeable to ions such as potassium (K_V channels), sodium (Na_V channels), or calcium (Ca_V channels) (11). All three of these ion channels consist of four homologous units and are considered tetrameric ion channels. Each unit contains six transmembrane α-helices and the four units are circularly arranged around a central pore (12). In sodium and calcium channels, the individual units are connected by flexible loops. In contrast, the four units of potassium channels are not covalently linked and instead exist as separate subunits.

The approximately 40 K_V channel proteins in the human genome are organised into twelve subfamilies with different families having distinct tissue distributions, physiologic functions, and activation/inactivation kinetics (13). Common to the K_V channel proteins is a highly conserved sequence in the α-subunit called the “T1 domain,” named as such for being an amino-terminal tetramerisation domain. Structurally, the T1 domain consists of only the core BTB fold and lies at the

amino-terminus of each α-subunit (2). This cytoplasmic T1 domain is responsible for subfamily-specific subunit tetramerisation – members of the same K_V subfamily tend to co-assemble to form functional tetrameric ion channels (14). Beyond regulating tetramerisation, the T1 domain is also responsible for channel localisation to the plasma membrane and the association of regulatory K_V β-subunits (15).

Mutations in the T1 domain have been linked to a variety of human diseases (e.g., *de novo* mutations in *KCNC1* causing progressive myoclonic epilepsy [16]) and ion channels are popular pharmacologic targets due to their key biological functions such as regulating action potential initiation and propagation (17). As a result, the biophysical properties of the T1 domain and its roles in K_V channel dynamics have become a popular area of research. Indeed, several studies have investigated the mechanisms by which the cytoplasmic T1 domain modulates K_V channel gating (18-21). Of note, Chi et al. used structural analyses and electrophysiological data to highlight K_V3.1a activation and deactivation kinetics are modulated by interactions between the helical S4/S5 linker that joins the pore-forming and transmembrane domains of K_V channels and the α-helices of the T1 domain tetramer (21). The T1 domain fold is also shared by the BTB domain of the KCTD family of non-membrane proteins described below in section 1.2.2.

1.1.3.3 E3 ubiquitin ligase substrate adaptors

One of the most well-characterised roles of BTB domain-containing proteins is as substrate-specific subunits of CUL3-containing Cullin-RING ligase (CRL3)

complexes mediating protein ubiquitination. In this context, the core BTB domain is similar in structure and function to Skp1 and Elongin C, which serve as adaptors of CUL1 and CUL2/5, respectively (22, 23). In the CRL3 complex, the RING-domain protein Rbx1 binds CUL3's carboxy-terminal domain and recruits the E2 conjugating enzyme while the BTB domain protein binds CUL3's amino-terminal domain to recruit specific substrates to the complex. The interactions between BTB domain proteins and CUL3 have been attributed to the presence of a "3-box" motif consisting of two α-helices at the amino terminus of the BACK domain (Figure 1.2C) (24). Such interactions permit the formation of functional CRLs mediating the ubiquitination of a variety of substrates in numerous biological processes. Substrate capture is enabled by other domains fused to the amino- or carboxy-terminus of the BTB/3-box region. Some of the best-characterised examples include the MATH-BTB, BTB-BACK-Kelch, and KCTD proteins. The mammalian MATH-BTB protein SPOP (Speckle-type POZ protein) ubiquitinates oncoproteins PTEN (phosphatase and tensin homolog) and GLI2 to regulate cancer progression (25, 26). Of the BTB-BACK-Kelch proteins, KEAP1 (Kelch-like ECH-associated protein 1) has been associated with cancer progression and chemotherapeutic resistance (27, 28). Other prominent members of the family and their roles in human physiology include KLHL3 (Kelch-like protein 3) in cardiovascular health (29), KLHL9 in musculoskeletal homeostasis (30), as well as KLHL7 and KLHL12 in autoimmune diseases such as Sjögren's syndrome (31). Finally, members of the KCTD family are implicated in muscle development (32), heart morphogenesis (33), psychiatric disorders (34), neurological movement disorders (35), and several cancers (36, 37).

1.2 Atypical BTBs

1.2.1 The tandem BTB domain

Of the two hundred human BTB domain-containing proteins, eight have been reported to harbour two sequential BTB domains, generally termed tandem BTB domains. Proteins predicted to contain back-to-back copies of the BTB domain include BTBD7, BTBD8, RHOBTB1, RHOBTB2, RHOBTB3, LZTR1, IBTK, and ABTB1. Much uncertainty exists regarding the folding, oligomerisation, and function of these tandem BTB proteins. For example, are the two domains redundant? Is protein function mediated primarily through one BTB domain and not the other? BTB domains have been reported to form dimers, tetramers, and pentamers depending on the associated protein's function. Do the two BTB domains of a single tandem BTB domain protein form an intramolecular pair "pseudodimer"? Do two distinct tandem BTB proteins homodimerise or heterodimerise to form functional tetramers of BTB domains?

A common biological function for many of the better-characterised tandem BTB domain-containing proteins is the ability to interact with CUL3 to form E3 ligase complexes. LZTR1 and all three RHOBTB proteins have been documented as adaptor proteins for CUL3 (38, 39, 40). ABTB1 contains a series of two ankryin repeats amino-terminal to its two BTB domains and has also been reported to interact with CUL3 in proteome-wide binary interactome maps (41). Furthermore, the three related *S. pombe* proteins with a similar domain series of two ankyrin repeats and two BTB domains (Btb1p, Btb2p, and Btb3p) all interact with the CUL3 homologue Pcu3p (42).

Conventionally, CRL3 adaptor proteins containing single copies of the BTB domain typically dimerise through their BTB domains to recruit two CUL3 subunits – forming a functional CRL3 complex of two BTB proteins and two CUL3 subunits. Many questions remain regarding how tandem BTB proteins interact with CUL3. For example, can a single tandem BTB protein recruit two CUL3 subunits? If only one of the two BTB domains interacts with CUL3, what is the role of the second BTB domain – does it facilitate a scaffolding role for the complex? Similar to their single BTB domain counterparts, not all tandem BTB containing proteins interact with CUL3 and serve as E3 ubiquitin ligases. Highlighted in the results of this thesis, BTBD7 does not appear to interact with CUL3. As another example, instead of forming a CRL, Inhibitor of Bruton's Tyrosine Kinase (IBTK) serves as an inhibitor of Bruton's tyrosine kinase (BTK) and plays a role in B cell development. IBTK downregulates BTK activity through directly binding and repressing the function of BTK's PH domain, an amino-terminal domain critical to BTK's kinase activity (43). Finally, BTBD8 is one of the least characterised tandem BTB proteins, but has been reported to be a neuron-specific protein that interacts with adaptor protein-2 (AP2) to regulate clathrin-dependent endocytosis of synaptic vesicles (44).

The structure of the tandem BTB domain has not been solved and the biological relevance for a protein to contain two sequential copies of the BTB domain is unknown. As discussed in section 1.3 of this thesis, several tandem BTB domain-containing proteins have been linked to human disease. Characterising the biophysical properties and functions of tandem BTB domain-containing proteins will address a gap in our existing knowledge of the BTB domain and its

critical biological roles. Accordingly, chapter four of this thesis focuses on the biophysical and functional characterisation of proteins harbouring tandem BTB domains.

1.2.2 The KCTD family

Several of the 25 members of the potassium (K+) channel tetramerisation domain (KCTD) family are considered “atypical” BTB-domain-containing proteins as they assemble into pentamers instead of conventional BTB-domain dimers. These non-membrane-bound proteins share an amino-terminal BTB domain homologous to the T1 tetramerisation domain of voltage-gated potassium (Kv) channels alongside a variable carboxy-terminal domain (CTD) (Figure 1.3A) (45, 46). Members of the KCTD family members typically oligomerise into functional homopentamers (4) but have also shown great structural diversity with monomeric, tetrameric, pentameric, and hexameric crystal forms reported (4, 47). The KCTD family is separated into several phylogenetic clades based on similarity in BTB regions (Figure 1.3B) (4, 48). An unusual feature of the KCTD protein family is their diversity outside the shared BTB domain. Barring closely related family members of the same clade, KCTD proteins lack significant sequence similarity in their CTDs (49). This variability reflects the prominent role of KCTD family members as CUL3-dependent E3 ubiquitin ligases to mediate ubiquitination and degradation of target proteins. As adaptor molecules for CRLs, KCTD proteins use their variable CTDs to bind and recruit a vast repertoire of cellular proteins destined for degradation (e.g., KCTD2 and KCTD5 mediating the ubiquitination and degradation of Gβγ (50)). However, not all KCTD family proteins function as E3 ligases. For example, KCTD8, 12, and 16 contribute to

mood disorders via acting as auxiliary subunits to GABAB receptors in a CUL3-independent manner (4). Such variety also reflects the assortment of KCTD-associated human diseases as well as their diverse roles in a variety of biological processes (reviewed in 48).

Numerous KCTD family members have been implicated in human diseases including cancer (KCTD10, KCTD11; 51, 52) neurodevelopmental, neurocognitive, and neuropsychiatric disorders (KCTD7, KCTD3, KCTD12, KCTD13, KCTD17; 53-55, 48), movement disorders (KCTD17; 35), obesity (KCTD15; 56), and craniofacial disease (KCTD1; 57, 58) among others.

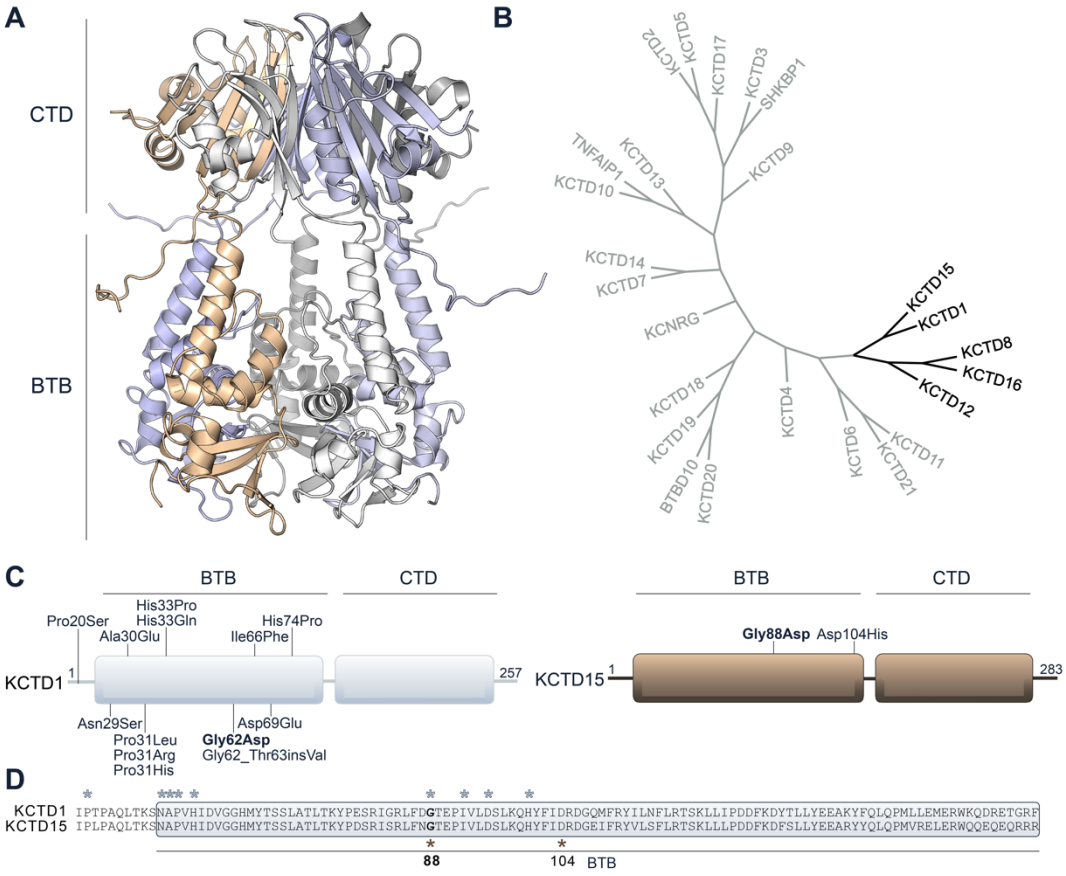


Figure 1.3 The KCTD protein family including an overview of KCTD1, KCTD15, and their pathologic variants. (A) Homology model of a KCTD15 closed pentamer based on the KCTD1 structure (PDB ID 6s4l) showing the BTB and C-terminal domains. Different colours denote different KCTD15 subunits of

the pentamer. (B) Phylogenetic tree of the KCTD family BTB domains. The cluster containing paralogues KCTD1, KCTD8, KCTD12, KCTD15, and KCTD16 is highlighted in black. (C) Domain graphics of KCTD1 and KCTD15 depicting the 13 variants in KCTD1 causing SEN and the two novel *de novo* missense substitutions in KCTD15 causing a frontonasal malformation syndrome similar to SEN. The substitutions in KCTD15 and KCTD1 occurring at the equivalent positions (Gly88Asp and Gly62Asp, respectively) are in bold. (D) Sequence alignment of KCTD1 and KCTD15 BTB domains. The BTB domain is boxed and labelled. Known substitution sites in KCTD15 and KCTD1 are marked with asterisks and locations of the two novel KCTD15 substitutions are labelled.

1.3 BTBs in human disease

As discussed throughout this introductory chapter, numerous BTB domain-containing proteins have been associated with human disease. To date, most research has focused on the BTB proteins that serve as transcription factors or adaptors for E3 ubiquitin ligases. Members of these two families have been linked to altered reproductive health, compromised musculoskeletal and immune systems, defects in embryogenesis, and cancer progression (9, 59). The following section highlights BTB domain-containing proteins most pertinent to this thesis and their roles in human physiology. Detailed reviews of other BTB domain-containing proteins can be found elsewhere (9, 60).

1.3.1 BTBD7

BTBD7 has a domain architecture unlike any other annotated human protein and contains two BTB domains, two BACK-like domains, and a large intrinsically disordered carboxy-terminal region (Figure 1.4). BTBD7 has been linked to several biological processes including epithelial-to-mesenchymal-transition (EMT), which involves epithelial cells losing their polarity and cell-cell adhesions to become migratory mesenchymal cells (61, 62). EMT is a fundamental process underlying embryogenesis, tissue/organ development and homeostasis, as well

as cancer progression (62). BTBD7 has been reported to regulate EMT in both tissue development (61) and tumour metastasis (for example, in lung cancer [63], salivary gland adenoid cystic carcinoma [64], prostate cancer [65], and breast cancer [66], among others). Beyond these reported roles regulating cell migration, BTBD7 has also been linked to the heat stress response (67) and human dental pulp cell behaviours (68). An overview of BTBD7's expression patterns and biological functions are provided in figure 1.5.

BTBD7's biological roles have been reported to be in part through altering levels of the cell-cell adhesion protein E-cadherin (63, 69) and SNAI2/SLUG, a transcriptional repressor of E-cadherin and other cell-adhesion proteins (69). However, the specific molecular mechanisms involved in such regulation have not been determined. Preliminary large-scale proteomic experiments suggested BTBD7 interacts with CUL3, potentially forming an E3 ubiquitin ligase complex to mediate protein degradation (70). However, no other reports confirmed or refuted such an interaction.

With such uncertainty surrounding BTBD7's potentially critical roles regulating tissue development and homeostasis, this thesis aimed to characterise BTBD7's molecular mechanisms of biological function. Results of such work are reported in chapter 3.

1.3.2 RHOBTB1

RHOBTB1 is one of three RHOBTB proteins (RHOBTB1-3) that constitute a subfamily of the RHO family of small guanosine triphosphatases (GTPases).

RHOBTB1 (as well as RHOBTB2 and RHOBTB3) contains an amino-terminal GTPase domain followed by two BTB domains and a conserved carboxy-terminal BACK domain (Figure 1.4) (40). Unlike LZTR1, RHOBTB1 contains a sequence of approximately 13 amino acids at the amino terminus of its BACK domain predicted to form the characteristic “3-box” motif mediating interactions between BTB proteins and CUL3.

Human missense variants in RHOBTB2 cause neurological disorders (71) and RHOBTB2 is a proposed tumour suppressor homozygously deleted in breast cancer samples (72). RHOBTB1 has been reported to serve similar functions as a tumour suppressor (73) and all three RHOBTB proteins have been reported to interact with CUL3 (40). Through its interactions with CUL3, RHOBTB1 has been closely linked to vascular smooth muscle and cardiovascular function through serving as both a substrate (74) and adaptor for CUL3 E3 ligases. RHOBTB1 has been reported to deliver phosphodiesterase 5 (PDE5) to the CUL3 E3 ligase complex for ubiquitination (75). Through such restriction in PDE5 activity, RHOBTB1 augments vascular dilation, reduces arterial stiffness, and protects against hypertension (75, 76). An overview of RHOBTB1’s expression patterns and biological functions are provided in figure 1.5.

Similar to LZTR1 discussed below, biophysical details of RHOBTB1 and the RHOBTB1-CUL3 complex have not been reported. To fill this gap in our knowledge and shed light on the importance of the tandem BTB domain in human physiology, RHOBTB1 was included with BTBD7 and LZTR1 in the

biochemical and structural characterisations reported in this thesis. Results of such work are reported in chapter 4.

1.3.3 LZTR1

Leucine zipper-like transcription regulator 1 (LZTR1) contains six Kelch domains at its amino terminus followed by two BTB domains and a BACK domain (Figure 1.4). Human mutations in LZTR1 have been linked to Noonan syndrome, glioblastoma, schwannomatosis, and chronic myeloid leukaemia (77-81). LZTR1 has been reported to regulate the RAS/MAPK pathways through serving as a CUL3-adaptor mediating the polyubiquitination and subsequent degradation of various RAS-superfamily proteins (e.g., KRAS, MRAS, NRAS, and RAF1 [38]).

LZTR1's roles in the pathogenesis of Noonan Syndrome and schwannomatosis have been closely linked to its regulation of RAS/MAPK signalling (80). LZTR1 has been reported to inhibit RAS/MAPK signalling through both binding the RAF1/SHOC2/PP1CB complex to promote RAF1 phosphorylation (79) as well as mediating the polyubiquitination and degradation of RAS (77, 39). Nevertheless, it is clear LZTR1's mechanisms of function are complex and extend beyond the RAS/MAPK pathway. For example, cardiovascular dysfunction is a routine finding among individuals affected by the relatively common genetic disorder Noonan Syndrome (NS). General and vascular-specific *Lztr1* knockout in mice results in a cardiovascular phenotype similar to that of individuals with NS (82). This cardiovascular phenotype has been linked to failed recycling of VEGFR2 (vascular endothelial growth factor receptor 2) to the cell surface secondary to altered LZTR1-CUL3 E3 ligase-mediated non-degradative ubiquitination of a

member of the endosomal sorting complex, CHMP1B (charged multivesicular protein 1B) (82). An overview of LZTR1's expression patterns and biological functions are provided in figure 1.5.

Although multiple studies have concluded altered LZTR1-CUL3 complex function drives human disease, details of the LZTR1-CUL3 interaction remain to be discovered. Accordingly, this thesis aimed to characterise the structural and biochemical nature of LZTR1 and its interactions with CUL3. Results of such work are reported in chapter 4.

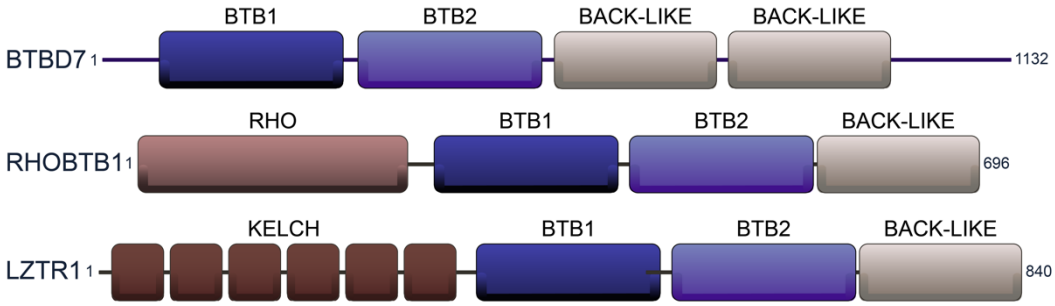


Figure 1.4 Domain maps of BTBD7, RHOBTB1, and LZTR1. Domain maps of BTBD7, RHOBTB1, and LZTR1 showing the shared tandem BTB (labelled BTB1 and BTB2) and BACK-LIKE domains. Beyond these shared domains, each protein has distinct accompanying protein domains. Domains are colour coded by similarity. Solid black lines represent regions of the proteins predicted to be disordered.

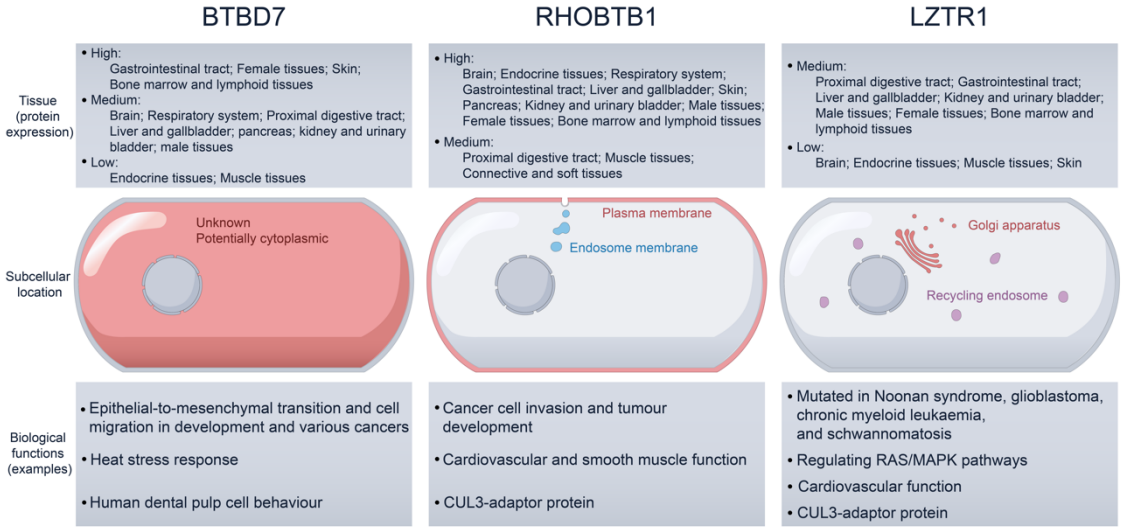


Figure 1.5 Expression profiles and example biological functions of BTBD7, RHOBTB1, and LZTR1. Tissues in which each protein is expressed in high, medium, or low levels are listed in the top panels of the figure. Schematics of cells in the middle panel depict the subcellular localisation of each protein – the coloured (red, blue, or purple) components of the cells represent protein expression locations. The subcellular localisation of BTBD7 protein is unconfirmed, but preliminary studies suggest it has a diffusely cytoplasmic localisation. The bottom panel of the figure lists example biological functions of each protein.

1.3.4 KCTD15 and KCTD1

Of the 25 potassium (K+) channel tetramerisation domain (KCTD) proteins, KCTD15 and its closely related paralogue KCTD1 are most pertinent to the work reported in this thesis and are further discussed in chapter 5. Structural predictions and primary sequence analysis cluster KCTD15 with paralogues KCTD1, KCTD8, KCTD12, and KCTD16 (4) (Figure 1.3B). Of these, KCTD15 is most closely related to KCTD1 (Figure 1.3) (overall sequence identity of about 80%) and the two proteins are involved in several analogous biological functions. KCTD15 has been linked to obesity as well as Wnt/beta catenin and TFAP2 signalling regulation (83-86). Similar to KCTD15, KCTD1 regulates the Wnt/beta catenin pathway and has been linked to adipogenesis (87). However, unlike the lack of ties between KCTD15 and mendelian disease, twelve mutations and one

in frame insertion in the BTB domain of KCTD1 are reported to cause Scalp-Ear-Nipple syndrome (SEN) (Figure 1.3C,D) (57, 58) characterised by craniofacial features including cutis aplasia of the scalp, hypertelorism, frontal bossing, and others (58). Discussed in chapter 5 of this thesis, a collaborating geneticist identified two *de novo* substitutions in human KCTD15 causing a craniofacial syndrome similar to SEN (Figure 1.3C,D). Work from this thesis was the first to characterise these two newly identified *de novo* mutations in KCTD15.

1.4 Aims of this thesis

This dissertation aimed to expand our understanding of the critical biological roles and biophysical properties of the BTB protein domain through characterising a subset of “atypical” BTB domain-containing proteins linked to developmental biology and how these proteins may determine function and disease, particularly of the craniofacial complex. In this context, “atypical” refers to BTB domains mutated in human disease and the select few proteins with two back-to-back BTB domains (tandem BTB) for which the biological relevance and biophysical properties are unknown, or the KCTD family in which the BTB domain appears to function as a pentamer rather than the canonical dimer. The three approaches used to achieve these aims included characterising 1) the morphogenic role of the tandem BTB protein BTBD7 in 3D culture models, 2) the biophysical properties and molecular mechanisms of BTBD7 and related tandem BTB proteins, and 3) the pathogenic mechanisms by which BTB domain mutations in KCTD15 cause human disease (Figure 1.6). Work presented herein initially focused on the tandem BTB domain-containing protein BTBD7 with the aim to characterise the molecular mechanisms through which BTBD7 drives

tissue morphogenesis (chapter 3). Results obtained using novel 3D cell culture as well as various microscopy and proteomic techniques presented in chapter 3 prompted me to expand this characterisation to several other tandem BTB domain-containing proteins. Accordingly, chapter 4 used mass-spectrometry, size-exclusion chromatography coupled with multi-angle light scattering (SEC-MALS), and several other biophysical approaches to characterise the biophysical properties and functional interactions of the tandem BTB domain using BTBD7 and two additional tandem BTB domain-containing proteins linked to critical biological functions; RHOBTB1 and LZTR1. Finally, chapter 5 aimed to link biological insights with clinical data and used X-ray crystallography, native mass-spectrometry, bio-layer interferometry, and other biophysical assays to characterise how human mutations in the BTB domain influence protein function. Ultimately, this work catalyses new discussions of the functional relevance of the tandem BTB domain and provides significant new insight into how human mutations in the BTB domain abrogate the formation of functional protein assemblies.

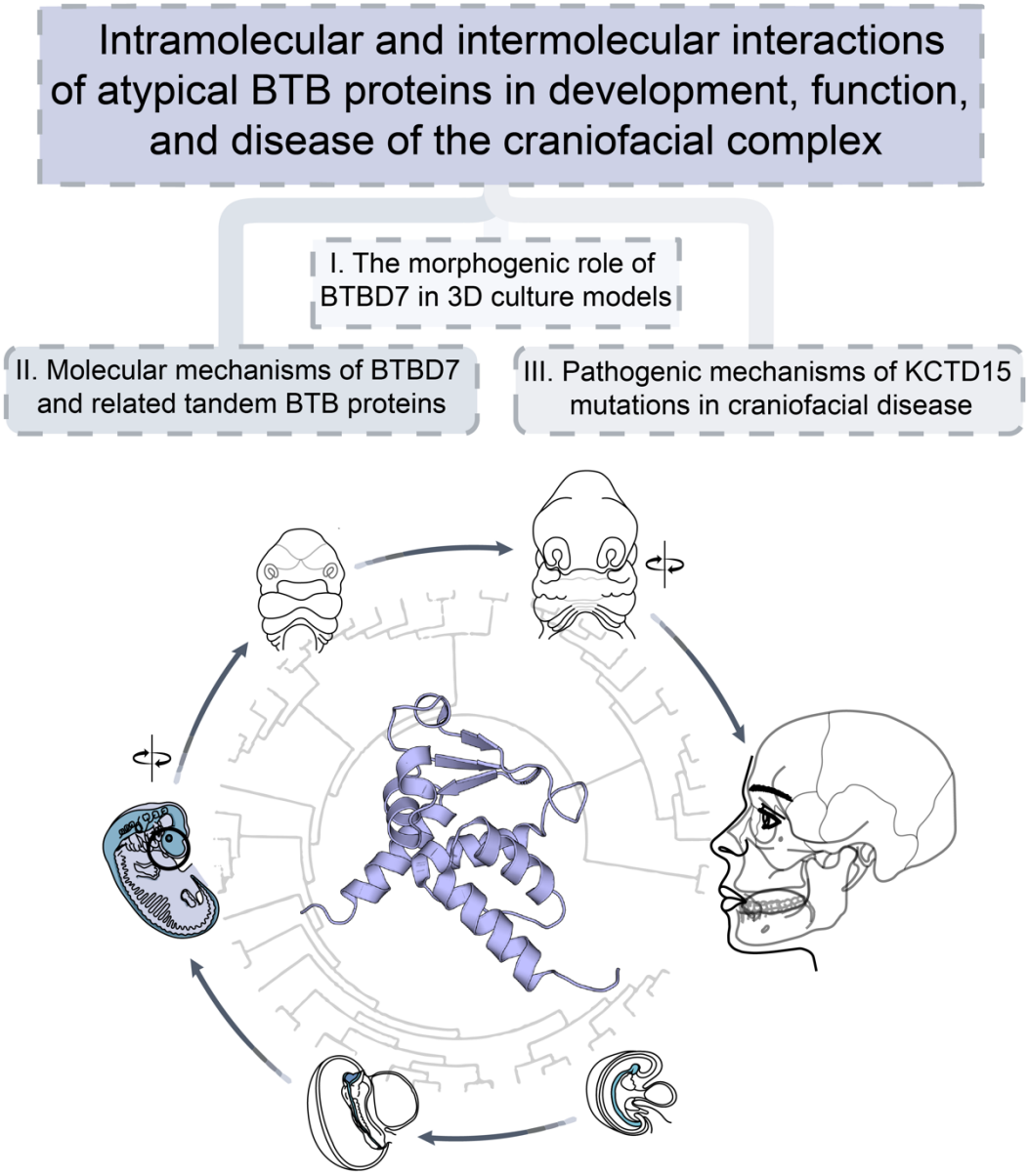


Figure 1.6 Schematic overview of the three approaches used to achieve the aims of this thesis. This thesis aimed to characterise the intramolecular and intermolecular interactions of atypical BTB proteins in development, function, and disease, with a focus on the craniofacial complex. Figure 1.6 provides a schematic overview of the three approaches used to achieve this aim.

1.5 References

1. Zollman S, Godt D, Privé GG, Couderc JL, Laski FA. The BTB domain, found primarily in zinc finger proteins, defines an evolutionarily conserved family that includes several developmentally regulated genes in Drosophila. Proc Natl Acad Sci U S A. 1994 Oct 25;91(22):10717-21. doi: 10.1073/pnas.91.22.10717. PMID: 7938017; PMCID: PMC45093.
2. Stogios PJ, Downs GS, Jauhal JJ, Nandra SK, Privé GG. Sequence and structural analysis of BTB domain proteins. Genome Biol. 2005;6(10):R82. doi: 10.1186/gb-2005-6-10-r82. Epub 2005 Sep 15. PMID: 16207353; PMCID: PMC1257465.
3. Kreusch A, Pfaffinger PJ, Stevens CF, Choe S. Crystal structure of the tetramerization domain of the Shaker potassium channel. Nature. 1998 Apr 30;392(6679):945-8. doi: 10.1038/31978. PMID: 9582078.
4. Pinkas DM, Sanvitale CE, Bufton JC, Sorrell FJ, Solcan N, Chalk R, Doutch J, Bullock AN. Structural complexity in the KCTD family of Cullin3-dependent E3 ubiquitin ligases. Biochem J. 2017 Nov 1;474(22):3747-3761. doi: 10.1042/BCJ20170527. PMID: 28963344; PMCID: PMC5664961.
5. Zuo H, Glaaser I, Zhao Y, Kurinov I, Mosyak L, Wang H, Liu J, Park J, Frangaj A, Sturchler E, Zhou M, McDonald P, Geng Y, Slesinger PA, Fan QR. Structural basis for auxiliary subunit KCTD16 regulation of the GABAB receptor. Proc Natl Acad Sci U S A. 2019 Apr 23;116(17):8370-8379. doi: 10.1073/pnas.1903024116. Epub 2019 Apr 10. PMID: 30971491; PMCID: PMC6486783.
6. Lambert SA, Jolma A, Campitelli LF, Das PK, Yin Y, Albu M, Chen X, Taipale J, Hughes TR, Weirauch MT. The Human Transcription Factors. Cell. 2018 Feb 8;172(4):650-665. doi: 10.1016/j.cell.2018.01.029. Erratum in: Cell. 2018 Oct 4;175(2):598-599. PMID: 29425488.
7. Huynh KD, Bardwell VJ. The BCL-6 POZ domain and other POZ domains interact with the co-repressors N-CoR and SMRT. Oncogene. 1998 Nov 12;17(19):2473-84. doi: 10.1038/sj.onc.1202197. PMID: 9824158.
8. Staller P, Peukert K, Kiermaier A, Seoane J, Lukas J, Karsunky H, Möröy T, Bartek J, Massagué J, Hänel F, Eilers M. Repression of p15INK4b expression by Myc through association with Miz-1. Nat Cell Biol. 2001 Apr;3(4):392-9. doi: 10.1038/35070076. PMID: 11283613.
9. Siggs OM, Beutler B. The BTB-ZF transcription factors. Cell Cycle. 2012 Sep 15;11(18):3358-69. doi: 10.4161/cc.21277. Epub 2012 Aug 16. PMID: 22894929; PMCID: PMC3466544.
10. Cheng ZY, He TT, Gao XM, Zhao Y, Wang J. ZBTB Transcription Factors: Key Regulators of the Development, Differentiation and Effector Function of T Cells. Front Immunol. 2021 Jul 19;12:713294. doi: 10.3389/fimmu.2021.713294. PMID: 34349770; PMCID: PMC8326903.
11. Loussouarn G, Tarek M. Editorial: Molecular Mechanisms of Voltage-Gating in Ion Channels. Front Pharmacol. 2021 Sep 15;12:768153. doi: 10.3389/fphar.2021.768153. PMID: 34603066; PMCID: PMC8479100.

12. Zhang XC, Yang H, Liu Z, Sun F. Thermodynamics of voltage-gated ion channels. Biophys Rep. 2018;4(6):300-319. doi: 10.1007/s41048-018-0074-y. Epub 2018 Nov 16. PMID: 30596139; PMCID: PMC6276078.
13. Gutman GA, Chandy KG, Grissmer S, Lazdunski M, McKinnon D, Pardo LA, Robertson GA, Rudy B, Sanguinetti MC, Stühmer W, Wang X. International Union of Pharmacology. LIII. Nomenclature and molecular relationships of voltage-gated potassium channels. Pharmacol Rev. 2005 Dec;57(4):473-508. doi: 10.1124/pr.57.4.10. PMID: 16382104.
14. Robinson JM, Deutsch C. Coupled tertiary folding and oligomerization of the T1 domain of Kv channels. Neuron. 2005 Jan 20;45(2):223-32. doi: 10.1016/j.neuron.2004.12.043. PMID: 15664174.
15. Burg ED, Platoshyn O, Tsigelny IF, Lozano-Ruiz B, Rana BK, Yuan JX. Tetramerization domain mutations in KCNA5 affect channel kinetics and cause abnormal trafficking patterns. Am J Physiol Cell Physiol. 2010 Mar;298(3):C496-509. doi: 10.1152/ajpcell.00464.2009. Epub 2009 Dec 16. PMID: 20018952; PMCID: PMC2838577.
16. Poirier K, Viot G, Lombardi L, Jauny C, Billuart P, Bienvenu T. Loss of Function of KCNC1 is associated with intellectual disability without seizures. Eur J Hum Genet. 2017 May;25(5):560-564. doi: 10.1038/ejhg.2017.3. Epub 2017 Feb 1. PMID: 28145425; PMCID: PMC5437909.
17. Wulff H, Castle NA, Pardo LA. Voltage-gated potassium channels as therapeutic targets. Nat Rev Drug Discov. 2009 Dec;8(12):982-1001. doi: 10.1038/nrd2983. PMID: 19949402; PMCID: PMC2790170.
18. Wang G, Strang C, Pfaffinger PJ, Covarrubias M. Zn2+-dependent redox switch in the intracellular T1-T1 interface of a Kv channel. J Biol Chem. 2007 May 4;282(18):13637-47. doi: 10.1074/jbc.M609182200. Epub 2007 Mar 1. PMID: 17331952; PMCID: PMC2211274.
19. Wang G, Covarrubias M. Voltage-dependent gating rearrangements in the intracellular T1-T1 interface of a K+ channel. J Gen Physiol. 2006 Apr;127(4):391-400. doi: 10.1085/jgp.200509442. Epub 2006 Mar 13. PMID: 16533897; PMCID: PMC2151515.
20. Kise Y, Kasuya G, Okamoto HH, Yamanouchi D, Kobayashi K, Kusakizako T, Nishizawa T, Nakajo K, Nureki O. Structural basis of gating modulation of Kv4 channel complexes. Nature. 2021 Nov;599(7883):158-164. doi: 10.1038/s41586-021-03935-z. Epub 2021 Sep 22. PMID: 34552243; PMCID: PMC8566240.
21. Chi G, Liang Q, Sridhar A, Cowgill JB, Sader K, Radjainia M, Qian P, Castro-Hartmann P, Venkaya S, Singh NK, McKinley G, Fernandez-Cid A, Mukhopadhyay SMM, Burgess-Brown NA, Delemotte L, Covarrubias M, Dürr KL. Cryo-EM structure of the human Kv3.1 channel reveals gating control by the cytoplasmic T1 domain. Nat Commun. 2022 Jul 15;13(1):4087. doi: 10.1038/s41467-022-29594-w. PMID: 35840580; PMCID: PMC9287412.
22. Zheng N, Schulman BA, Song L, Miller JJ, Jeffrey PD, Wang P, Chu C, Koepp DM, Elledge SJ, Pagano M, Conaway RC, Conaway JW, Harper JW, Pavletich NP. Structure of the Cul1-Rbx1-Skp1-F boxSkp2 SCF ubiquitin

ligase complex. Nature. 2002 Apr 18;416(6882):703-9. doi: 10.1038/416703a. PMID: 11961546.
23. Errington WJ, Khan MQ, Bueler SA, Rubinstein JL, Chakrabartty A, Privé GG. Adaptor protein self-assembly drives the control of a cullin-RING ubiquitin ligase. Structure. 2012 Jul 3;20(7):1141-53. doi: 10.1016/j.str.2012.04.009. Epub 2012 May 24. PMID: 22632832.
24. Canning P, Cooper CDO, Krojer T, Murray JW, Pike ACW, Chaikuad A, Keates T, Thangaratnarajah C, Hojzan V, Marsden BD, Gileadi O, Knapp S, von Delft F, Bullock AN. Structural basis for Cul3 protein assembly with the BTB-Kelch family of E3 ubiquitin ligases. J Biol Chem. 2013 Mar 15;288(11):7803-7814. doi: 10.1074/jbc.M112.437996. Epub 2013 Jan 24. Erratum in: J Biol Chem. 2013 Sep 27;388(39):28304. Ayinampudi, Vikram [added]. PMID: 23349464; PMCID: PMC3597819.
25. Han B, Sun Z, Yu T, Wang Y, Kuang L, Li T, Cai J, Cao Q, Xu Y, Gao B, Cheng SY, Yue S, Liu C. SPOP-PTEN-SUFU axis promotes progression of clear cell renal cell carcinoma via activating SHH and WNT pathway. Cell Death Discov. 2021 May 21;7(1):120. doi: 10.1038/s41420-021-00484-2. PMID: 34021128; PMCID: PMC8140158.
26. Coquenlorge S, Yin WC, Yung T, Pan J, Zhang X, Mo R, Belik J, Hui CC, Kim TH. GLI2 Modulated by SUFU and SPOP Induces Intestinal Stem Cell Niche Signals in Development and Tumorigenesis. Cell Rep. 2019 Jun 4;27(10):3006-3018.e4. doi: 10.1016/j.celrep.2019.05.016. PMID: 31167144.
27. Padmanabhan B, Tong KI, Ohta T, Nakamura Y, Scharlock M, Ohtsuji M, Kang MI, Kobayashi A, Yokoyama S, Yamamoto M. Structural basis for defects of Keap1 activity provoked by its point mutations in lung cancer. Mol Cell. 2006 Mar 3;21(5):689-700. doi: 10.1016/j.molcel.2006.01.013. PMID: 16507366.
28. Islam SS, Qassem K, Islam S, Parag RR, Rahman MZ, Farhat WA, Yeger H, Aboussekhra A, Karakas B, Noman ASM. Genetic alterations of Keap1 confers chemotherapeutic resistance through functional activation of Nrf2 and Notch pathway in head and neck squamous cell carcinoma. Cell Death Dis. 2022 Aug 9;13(8):696. doi: 10.1038/s41419-022-05126-8. PMID: 35945195; PMCID: PMC9363464.
29. Boyden LM, Choi M, Choate KA, Nelson-Williams CJ, Farhi A, Toka HR, Tikhonova IR, Bjornson R, Mane SM, Colussi G, Lebel M, Gordon RD, Semmekrot BA, Poujol A, Välimäki MJ, De Ferrari ME, Sanjad SA, Gutkin M, Karet FE, Tucci JR, Stockigt JR, Keppler-Noreuil KM, Porter CC, Anand SK, Whiteford ML, Davis ID, Dewar SB, Bettinelli A, Fadrowski JJ, Belsha CW, Hunley TE, Nelson RD, Trachtman H, Cole TR, Pinsk M, Bockenhauer D, Shenoy M, Vaidyanathan P, Foreman JW, Rasoulpour M, Thameem F, Al-Shahrouri HZ, Radhakrishnan J, Gharavi AG, Goilav B, Lifton RP. Mutations in kelch-like 3 and cullin 3 cause hypertension and electrolyte abnormalities. Nature. 2012 Jan 22;482(7383):98-102. doi: 10.1038/nature10814. PMID: 22266938; PMCID: PMC3278668.
30. Cirak S, von Deimling F, Sachdev S, Errington WJ, Herrmann R, Bönnemann C, Brockmann K, Hinderlich S, Lindner TH, Steinbrecher A, Hoffmann K,

Privé GG, Hannink M, Nürnberg P, Voit T. Kelch-like homologue 9 mutation is associated with an early onset autosomal dominant distal myopathy. Brain. 2010 Jul;133(Pt 7):2123-35. doi: 10.1093/brain/awq108. Epub 2010 Jun 16. Erratum in: Brain. 2020 Jun 1;143(6):e52. PMID: 20554658; PMCID: PMC2892937.
31. Uchida K, Akita Y, Matsuo K, Fujiwara S, Nakagawa A, Kazaoka Y, Hachiya H, Naganawa Y, Oh-Iwa I, Ohura K, Saga S, Kawai T, Matsumoto Y, Shimozato K, Kozaki K. Identification of specific autoantigens in Sjögren's syndrome by SEREX. Immunology. 2005 Sep;116(1):53-63. doi: 10.1111/j.1365-2567.2005.02197.x. PMID: 16108817; PMCID: PMC1802401.
32. Rodríguez-Pérez F, Manford AG, Pogson A, Ingersoll AJ, Martínez-González B, Rape M. Ubiquitin-dependent remodeling of the actin cytoskeleton drives cell fusion. Dev Cell. 2021 Mar 8;56(5):588-601.e9. doi: 10.1016/j.devcel.2021.01.016. Epub 2021 Feb 19. PMID: 33609460.
33. Ren K, Yuan J, Yang M, Gao X, Ding X, Zhou J, Hu X, Cao J, Deng X, Xiang S, Zhang J. KCTD10 is involved in the cardiovascular system and Notch signaling during early embryonic development. PLoS One. 2014 Nov 17;9(11):e112275. doi: 10.1371/journal.pone.0112275. PMID: 25401743; PMCID: PMC4234411.
34. Golzio C, Willer J, Talkowski ME, Oh EC, Taniguchi Y, Jacquemont S, Reymond A, Sun M, Sawa A, Gusella JF, Kamiya A, Beckmann JS, Katsanis N. KCTD13 is a major driver of mirrored neuroanatomical phenotypes of the 16p11.2 copy number variant. Nature. 2012 May 16;485(7398):363-7. doi: 10.1038/nature11091. PMID: 22596160; PMCID: PMC3366115.
35. Mencacci NE, Rubio-Agusti I, Zdebik A, Asmus F, Ludtmann MH, Ryten M, Plagnol V, Hauser AK, Bandres-Ciga S, Bettencourt C, Forabosco P, Hughes D, Soutar MM, Peall K, Morris HR, Trabzuni D, Tekman M, Stanescu HC, Kleta R, Carecchio M, Zorzi G, Nardocci N, Garavaglia B, Lohmann E, Weissbach A, Klein C, Hardy J, Pittman AM, Foltynie T, Abramov AY, Gasser T, Bhatia KP, Wood NW. A missense mutation in KCTD17 causes autosomal dominant myoclonus-dystonia. Am J Hum Genet. 2015 Jun 4;96(6):938-47. doi: 10.1016/j.ajhg.2015.04.008. Epub 2015 May 14. PMID: 25983243; PMCID: PMC4457957.
36. Cancer Genome Atlas Research Network; Albert Einstein College of Medicine; Analytical Biological Services; Barretos Cancer Hospital; Baylor College of Medicine; Beckman Research Institute of City of Hope; Buck Institute for Research on Aging; Canada's Michael Smith Genome Sciences Centre; Harvard Medical School; Helen F. Graham Cancer Center &Research Institute at Christiana Care Health Services; HudsonAlpha Institute for Biotechnology; ILSbio, LLC; Indiana University School of Medicine; Institute of Human Virology; Institute for Systems Biology; International Genomics Consortium; Leidos Biomedical; Massachusetts General Hospital; McDonnell Genome Institute at Washington University; Medical College of Wisconsin; Medical University of South Carolina; Memorial Sloan Kettering Cancer Center; Montefiore Medical Center; NantOmics; National Cancer Institute; National Hospital, Abuja, Nigeria; National Human Genome Research

Institute; National Institute of Environmental Health Sciences; National Institute on Deafness &Other Communication Disorders; Ontario Tumour Bank, London Health Sciences Centre; Ontario Tumour Bank, Ontario Institute for Cancer Research; Ontario Tumour Bank, The Ottawa Hospital; Oregon Health &Science University; Samuel Oschin Comprehensive Cancer Institute, Cedars-Sinai Medical Center; SRA International; St Joseph's Candler Health System; Eli &Edythe L. Broad Institute of Massachusetts Institute of Technology &Harvard University; Research Institute at Nationwide Children's Hospital; Sidney Kimmel Comprehensive Cancer Center at Johns Hopkins University; University of Bergen; University of Texas MD Anderson Cancer Center; University of Abuja Teaching Hospital; University of Alabama at Birmingham; University of California, Irvine; University of California Santa Cruz; University of Kansas Medical Center; University of Lausanne; University of New Mexico Health Sciences Center; University of North Carolina at Chapel Hill; University of Oklahoma Health Sciences Center; University of Pittsburgh; University of São Paulo, Ribeir ão Preto Medical School; University of Southern California; University of Washington; University of Wisconsin School of Medicine &Public Health; Van Andel Research Institute; Washington University in St Louis. Integrated genomic and molecular characterization of cervical cancer. Nature. 2017 Mar 16;543(7645):378-384. doi: 10.1038/nature21386. Epub 2017 Jan 23. PMID: 28112728; PMCID: PMC5354998.

37. Greif PA, Eck SH, Konstandin NP, Benet-Pagès A, Ksienzyk B, Dufour A, Vetter AT, Popp HD, Lorenz-Depiereux B, Meitinger T, Bohlander SK, Strom TM. Identification of recurring tumor-specific somatic mutations in acute myeloid leukemia by transcriptome sequencing. Leukemia. 2011 May;25(5):821-7. doi: 10.1038/leu.2011.19. Epub 2011 Feb 22. PMID: 21339757.
38. Zhang H, Cao X, Wang J, Li Q, Zhao Y, Jin X. LZTR1: A promising adaptor of the CUL3 family. Oncol Lett. 2021 Jul;22(1):564. doi: 10.3892/ol.2021.12825. Epub 2021 May 29. PMID: 34113392; PMCID: PMC8185703.
39. Abe T, Umeki I, Kanno SI, Inoue SI, Niihori T, Aoki Y. LZTR1 facilitates polyubiquitination and degradation of RAS-GTPases. Cell Death Differ. 2020 Mar;27(3):1023-1035. doi: 10.1038/s41418-019-0395-5. Epub 2019 Jul 23. PMID: 31337872; PMCID: PMC7206011.
40. Berthold J, Schenková K, Ramos S, Miura Y, Furukawa M, Aspenström P, Rivero F. Characterization of RhoBTB-dependent Cul3 ubiquitin ligase complexes--evidence for an autoregulatory mechanism. Exp Cell Res. 2008 Nov 15;314(19):3453-65. doi: 10.1016/j.yexcr.2008.09.005. Epub 2008 Sep 20. PMID: 18835386; PMCID: PMC2749729.
41. Rolland T, Taşan M, Charloteaux B, Pevzner SJ, Zhong Q, Sahni N, Yi S, Lemmens I, Fontanillo C, Mosca R, Kamburov A, Ghiassian SD, Yang X, Ghamsari L, Balcha D, Begg BE, Braun P, Brehme M, Broly MP, Carvunis AR, Convery-Zupan D, Corominas R, Coulombe-Huntington J, Dann E, Dreze M, Dricot A, Fan C, Franzosa E, Gebreab F, Gutierrez BJ, Hardy MF, Jin M, Kang S, Kiros R, Lin GN, Luck K, MacWilliams A, Menche J, Murray RR,

Palagi A, Poulin MM, Rambout X, Rasla J, Reichert P, Romero V, Ruyssinck E, Sahalie JM, Scholz A, Shah AA, Sharma A, Shen Y, Spirohn K, Tam S, Tejeda AO, Wanamaker SA, Twizere JC, Vega K, Walsh J, Cusick ME, Xia Y, Barabási AL, Iakoucheva LM, Aloy P, De Las Rivas J, Tavernier J, Calderwood MA, Hill DE, Hao T, Roth FP, Vidal M. A proteome-scale map of the human interactome network. Cell. 2014 Nov 20;159(5):1212-1226. doi: 10.1016/j.cell.2014.10.050. PMID: 25416956; PMCID: PMC4266588.

42. Geyer R, Wee S, Anderson S, Yates J, Wolf DA. BTB/POZ domain proteins are putative substrate adaptors for cullin 3 ubiquitin ligases. Mol Cell. 2003 Sep;12(3):783-90. doi: 10.1016/s1097-2765(03)00341-1. PMID: 14527422.
43. Liu W, Quinto I, Chen X, Palmieri C, Rabin RL, Schwartz OM, Nelson DL, Scala G. Direct inhibition of Bruton's tyrosine kinase by IBtk, a Btk-binding protein. Nat Immunol. 2001 Oct;2(10):939-46. doi: 10.1038/ni1001-939. PMID: 11577348.
44. Piccini A, Castroflorio E, Valente P, Guarnieri FC, Aprile D, Michetti C, Bramini M, Giansante G, Pinto B, Savardi A, Cesca F, Bachi A, Cattaneo A, Wren JD, Fassio A, Valtorta F, Benfenati F, Giovedì S. APache Is an AP2-Interacting Protein Involved in Synaptic Vesicle Trafficking and Neuronal Development. Cell Rep. 2017 Dec 19;21(12):3596-3611. doi: 10.1016/j.celrep.2017.11.073. PMID: 29262337.
45. Angrisani A, Di Fiore A, De Smaele E, Moretti M. The emerging role of the KCTD proteins in cancer. Cell Commun Signal. 2021 May 17;19(1):56. doi: 10.1186/s12964-021-00737-8. PMID: 34001146; PMCID: PMC8127222.
46. Ji AX, Chu A, Nielsen TK, Benlekbir S, Rubinstein JL, Privé GG. Structural Insights into KCTD Protein Assembly and Cullin3 Recognition. J Mol Biol. 2016 Jan 16;428(1):92-107. doi: 10.1016/j.jmb.2015.08.019. Epub 2015 Aug 31. PMID: 26334369.
47. Sereikaite V, Fritzius T, Kasaragod VB, Bader N, Maric HM, Schindelin H, Bettler B, Strømgaard K. Targeting the γ-Aminobutyric Acid Type B (GABAB) Receptor Complex: Development of Inhibitors Targeting the K+ Channel Tetramerization Domain (KCTD) Containing Proteins/GABAB Receptor Protein-Protein Interaction. J Med Chem. 2019 Oct 10;62(19):8819-8830. doi: 10.1021/acs.jmedchem.9b01087. Epub 2019 Sep 25. PMID: 31509708.
48. Teng X, Aouacheria A, Lionnard L, Metz KA, Soane L, Kamiya A, Hardwick JM. KCTD: A new gene family involved in neurodevelopmental and neuropsychiatric disorders. CNS Neurosci Ther. 2019 Jul;25(7):887-902. doi: 10.1111/cns.13156. PMID: 31197948; PMCID: PMC6566181.
49. Liu Z, Xiang Y, Sun G. The KCTD family of proteins: structure, function, disease relevance. Cell Biosci. 2013 Nov 24;3(1):45. doi: 10.1186/2045-3701-3-45. PMID: 24268103; PMCID: PMC3882106.
50. Young BD, Sha J, Vashisht AA, Wohlschlegel JA. Human Multisubunit E3 Ubiquitin Ligase Required for Heterotrimeric G-Protein β-Subunit Ubiquitination and Downstream Signaling. J Proteome Res. 2021 Sep 3;20(9):4318-4330. doi: 10.1021/acs.jproteome.1c00292. Epub 2021 Aug 3. PMID: 34342229.

51. Kubota D, Yoshida A, Tsuda H, Suehara Y, Okubo T, Saito T, Orita H, Sato K, Taguchi T, Yao T, Kaneko K, Katai H, Kawai A, Kondo T. Gene expression network analysis of ETV1 reveals KCTD10 as a novel prognostic biomarker in gastrointestinal stromal tumor. PLoS One. 2013 Aug 19;8(8):e73896. doi: 10.1371/journal.pone.0073896. PMID: 23977394; PMCID: PMC3747077.
52. Di Marcotullio L, Ferretti E, De Smaele E, Argenti B, Mincione C, Zazzeroni F, Gallo R, Masuelli L, Napolitano M, Maroder M, Modesti A, Giangaspero F, Screpanti I, Alesse E, Gulino A. REN(KCTD11) is a suppressor of Hedgehog signaling and is deleted in human medulloblastoma. Proc Natl Acad Sci U S A. 2004 Jul 20;101(29):10833-8. doi: 10.1073/pnas.0400690101. Epub 2004 Jul 12. PMID: 15249678; PMCID: PMC490020.
53. Metz KA, Teng X, Coppens I, Lamb HM, Wagner BE, Rosenfeld JA, Chen X, Zhang Y, Kim HJ, Meadow ME, Wang TS, Haberlandt ED, Anderson GW, Leshinsky-Silver E, Bi W, Markello TC, Pratt M, Makhseed N, Garnica A, Danylchuk NR, Burrow TA, Jayakar P, McKnight D, Agadi S, Gbedawo H, Stanley C, Alber M, Prehl I, Peariso K, Ong MT, Mordekar SR, Parker MJ, Crooks D, Agrawal PB, Berry GT, Loddenkemper T, Yang Y, Maegawa GHB, Aouacheria A, Markle JG, Wohlschlegel JA, Hartman AL, Hardwick JM. KCTD7 deficiency defines a distinct neurodegenerative disorder with a conserved autophagy-lysosome defect. Ann Neurol. 2018 Nov;84(5):766-780. doi: 10.1002/ana.25351. Epub 2018 Nov 8. PMID: 30295347; PMCID: PMC6295419.
54. Faqeih EA, Almannai M, Saleh MM, AlWadei AH, Samman MM, Alkuraya FS. Phenotypic characterization of KCTD3-related developmental epileptic encephalopathy. Clin Genet. 2018 May;93(5):1081-1086. doi: 10.1111/cge.13227. Epub 2018 Mar 15. PMID: 29406573.
55. Golzio C, Willer J, Talkowski ME, Oh EC, Taniguchi Y, Jacquemont S, Reymond A, Sun M, Sawa A, Gusella JF, Kamiya A, Beckmann JS, Katsanis N. KCTD13 is a major driver of mirrored neuroanatomical phenotypes of the 16p11.2 copy number variant. Nature. 2012 May 16;485(7398):363-7. doi: 10.1038/nature11091. PMID: 22596160; PMCID: PMC3366115.
56. Willer CJ, Speliotes EK, Loos RJ, Li S, Lindgren CM, Heid IM, Berndt SI, Elliott AL, Jackson AU, Lamina C, Lettre G, Lim N, Lyon HN, McCarroll SA, Papadakis K, Qi L, Randall JC, Roccasecca RM, Sanna S, Scheet P, Weedon MN, Wheeler E, Zhao JH, Jacobs LC, Prokopenko I, Soranzo N, Tanaka T, Timpson NJ, Almgren P, Bennett A, Bergman RN, Bingham SA, Bonnycastle LL, Brown M, Burtt NP, Chines P, Coin L, Collins FS, Connell JM, Cooper C, Smith GD, Dennison EM, Deodhar P, Elliott P, Erdos MR, Estrada K, Evans DM, Gianniny L, Gieger C, Gillson CJ, Guiducci C, Hackett R, Hadley D, Hall AS, Havulinna AS, Hebebrand J, Hofman A, Isomaa B, Jacobs KB, Johnson T, Jousilahti P, Jovanovic Z, Khaw KT, Kraft P, Kuokkanen M, Kuusisto J, Laitinen J, Lakatta EG, Luan J, Luben RN, Mangino M, McArdle WL, Meitinger T, Mulas A, Munroe PB, Narisu N, Ness AR, Northstone K, O'Rahilly S, Purmann C, Rees MG, Ridderstråle M, Ring SM, Rivadeneira F, Ruokonen A, Sandhu MS, Saramies J, Scott LJ, Scuteri A, Silander K, Sims MA, Song K, Stephens J, Stevens S, Stringham HM,

Tung YC, Valle TT, Van Duijn CM, Vimaleswaran KS, Vollenweider P, Waeber G, Wallace C, Watanabe RM, Waterworth DM, Watkins N; Wellcome Trust Case Control Consortium; Witteman JC, Zeggini E, Zhai G, Zillikens MC, Altshuler D, Caulfield MJ, Chanock SJ, Farooqi IS, Ferrucci L, Guralnik JM, Hattersley AT, Hu FB, Jarvelin MR, Laakso M, Mooser V, Ong KK, Ouwehand WH, Salomaa V, Samani NJ, Spector TD, Tuomi T, Tuomilehto J, Uda M, Uitterlinden AG, Wareham NJ, Deloukas P, Frayling TM, Groop LC, Hayes RB, Hunter DJ, Mohlke KL, Peltonen L, Schlessinger D, Strachan DP, Wichmann HE, McCarthy MI, Boehnke M, Barroso I, Abecasis GR, Hirschhorn JN; Genetic Investigation of ANthropometric Traits Consortium. Six new loci associated with body mass index highlight a neuronal influence on body weight regulation. Nat Genet. 2009 Jan;41(1):25-34. doi: 10.1038/ng.287. Epub 2008 Dec 14. PMID: 19079261; PMCID: PMC2695662.

57. Marneros AG, Beck AE, Turner EH, McMillin MJ, Edwards MJ, Field M, de Macena Sobreira NL, Perez AB, Fortes JA, Lampe AK, Giovannucci Uzielli ML, Gordon CT, Plessis G, Le Merrer M, Amiel J, Reichenberger E, Shively KM, Cerrato F, Labow BI, Tabor HK, Smith JD, Shendure J, Nickerson DA, Bamshad MJ; University of Washington Center for Mendelian Genomics. Mutations in KCTD1 cause scalp-ear-nipple syndrome. Am J Hum Genet. 2013 Apr 4;92(4):621-6. doi: 10.1016/j.ajhg.2013.03.002. Epub 2013 Mar 28. PMID: 23541344; PMCID: PMC3617379.
58. Butler KM, Bahrambeigi V, Merrihew A, Friez MJ, Cathey SS. Scalp-Ear-Nipple syndrome: first report of a Potassium channel tetramerization domain-containing 1 in-frame insertion and review of the literature. Clin Dysmorphol. 2021 Oct 1;30(4):167-172. doi: 10.1097/MCD.0000000000000387. PMID: 34456244.
59. Genschik P, Sumara I, Lechner E. The emerging family of CULLIN3-RING ubiquitin ligases (CRL3s): cellular functions and disease implications. EMBO J. 2013 Aug 28;32(17):2307-20. doi: 10.1038/emboj.2013.173. Epub 2013 Aug 2. PMID: 23912815; PMCID: PMC3770339.
60. Dhanoa BS, Cogliati T, Satish AG, Bruford EA, Friedman JS. Update on the Kelch-like (KLHL) gene family. Hum Genomics. 2013 May 15;7(1):13. doi: 10.1186/1479-7364-7-13. PMID: 23676014; PMCID: PMC3658946.
61. Onodera T, Sakai T, Hsu JC, Matsumoto K, Chiorini JA, Yamada KM. Btbd7 regulates epithelial cell dynamics and branching morphogenesis. Science. 2010 Jul 30;329(5991):562-5. doi: 10.1126/science.1191880. PMID: 20671187; PMCID: PMC3412157.
62. Kalluri R, Weinberg RA. The basics of epithelial-mesenchymal transition. J Clin Invest. 2009 Jun;119(6):1420-8. doi: 10.1172/JCI39104. Erratum in: J Clin Invest. 2010 May 3;120(5):1786. PMID: 19487818; PMCID: PMC2689101.
63. Shu J, Wang L, Han F, Chen Y, Wang S, Luo F. BTBD7 Downregulates E-Cadherin and Promotes Epithelial-Mesenchymal Transition in Lung Cancer. Biomed Res Int. 2019 Nov 27;2019:5937635. doi: 10.1155/2019/5937635. PMID: 31886230; PMCID: PMC6900955.

64. Yang L, Wang T, Zhang J, Wang X. BTBD7 silencing inhibited epithelial-mesenchymal transition (EMT) via regulating Slug expression in human salivary adenoid cystic carcinoma. Cancer Biomark. 2017 Dec 6;20(4):461-468. doi: 10.3233/CBM-170262. PMID: 28946551.
65. Chen B, Liu C, Bai G, Zhu Y, Xu H. BTBD7 accelerates the epithelial-mesenchymal transition, proliferation and invasion of prostate cancer cells. J BUON. 2021 Sep-Oct;26(5):2111-2116. PMID: 34761624.
66. Li ZX, Huang ZN, Luo H, Yang XB, Wang YL, Chen JX, Ma XK, Xu F, Wang TT, Lin L. High BTBD7 expression positive is correlated with SLUG-predicted poor prognosis in hormone receptor-negative breast cancer. Ann Transl Med. 2021 Aug;9(15):1252. doi: 10.21037/atm-21-3409. PMID: 34532389; PMCID: PMC8421947.
67. Dou J, Luo H, Sammad A, Lou W, Wang D, Schenkel F, Yu Y, Fang L, Wang Y. Epigenomics of rats' liver and its cross-species functional annotation reveals key regulatory genes underlying short term heat-stress response. Genomics. 2022 Sep;114(5):110449. doi: 10.1016/j.ygeno.2022.110449. Epub 2022 Aug 17. PMID: 35985612.
68. Bao Q, Zhang J, Wang XX. Effects of Btbd7 knockdown on the proliferation of human dental pulp cells and expression of Dspp. Int J Clin Exp Pathol. 2018 Mar 1;11(3):1460-1465. PMID: 31938244; PMCID: PMC6958179.
69. Fan C, Miao Y, Zhang X, Liu D, Jiang G, Lin X, Han Q, Luan L, Xu Z, Wang E. Btbd7 contributes to reduced E-cadherin expression and predicts poor prognosis in non-small cell lung cancer. BMC Cancer. 2014 Sep 24;14:704. doi: 10.1186/1471-2407-14-704. PMID: 25253020; PMCID: PMC4189533.
70. Bennett EJ, Rush J, Gygi SP, Harper JW. Dynamics of cullin-RING ubiquitin ligase network revealed by systematic quantitative proteomics. Cell. 2010 Dec 10;143(6):951-65. doi: 10.1016/j.cell.2010.11.017. PMID: 21145461; PMCID: PMC3008586.
71. Straub J, Konrad EDH, Grüner J, Toutain A, Bok LA, Cho MT, Crawford HP, Dubbs H, Douglas G, Jobling R, Johnson D, Krock B, Mikati MA, Nesbitt A, Nicolai J, Phillips M, Poduri A, Ortiz-Gonzalez XR, Powis Z, Santani A, Smith L, Stegmann APA, Stumpel C, Vreeburg M; Deciphering Developmental Disorders Study; Fliedner A, Gregor A, Sticht H, Zweier C. Missense Variants in RHOBTB2 Cause a Developmental and Epileptic Encephalopathy in Humans, and Altered Levels Cause Neurological Defects in Drosophila. Am J Hum Genet. 2018 Jan 4;102(1):44-57. doi: 10.1016/j.ajhg.2017.11.008. Epub 2017 Dec 21. PMID: 29276004; PMCID: PMC5777381.
72. Hamaguchi M, Meth JL, von Klitzing C, Wei W, Esposito D, Rodgers L, Walsh T, Welcsh P, King MC, Wigler MH. DBC2, a candidate for a tumor suppressor gene involved in breast cancer. Proc Natl Acad Sci U S A. 2002 Oct 15;99(21):13647-52. doi: 10.1073/pnas.212516099. Epub 2002 Oct 7. PMID: 12370419; PMCID: PMC129730.
73. Beder LB, Gunduz M, Ouchida M, Gunduz E, Sakai A, Fukushima K, Nagatsuka H, Ito S, Honjo N, Nishizaki K, Shimizu K. Identification of a candidate tumor suppressor gene RHOBTB1 located at a novel allelic loss region 10q21 in head and neck cancer. J Cancer Res Clin Oncol. 2006

Jan;132(1):19-27. doi: 10.1007/s00432-005-0033-0. Epub 2005 Sep 17. PMID: 16170569.
74. Ibeawuchi SR, Agbor LN, Quelle FW, Sigmund CD. Hypertension-causing Mutations in Cullin3 Protein Impair RhoA Protein Ubiquitination and Augment the Association with Substrate Adaptors. J Biol Chem. 2015 Jul 31;290(31):19208-17. doi: 10.1074/jbc.M115.645358. Epub 2015 Jun 22. PMID: 26100637; PMCID: PMC4521042.
75. Kumar G, Fang S, Golosova D, Lu KT, Brozoski DT, Vazirabad I, Sigmund CD. Structure and Function of RhoBTB1 Required for Substrate Specificity and Cullin-3 Ubiquitination. Function (Oxf). 2023 Jul 3;4(5):zqad034. doi: 10.1093/function/zqad034. PMID: 37575477; PMCID: PMC10413933.
76. Mukohda M, Fang S, Wu J, Agbor LN, Nair AR, Ibeawuchi SC, Hu C, Liu X, Lu KT, Guo DF, Davis DR, Keen HL, Quelle FW, Sigmund CD. RhoBTB1 protects against hypertension and arterial stiffness by restraining phosphodiesterase 5 activity. J Clin Invest. 2019 Mar 21;129(6):2318-2332. doi: 10.1172/JCI123462. PMID: 30896450; PMCID: PMC6546477.
77. Steklov M, Pandolfi S, Baietti MF, Batiuk A, Carai P, Najm P, Zhang M, Jang H, Renzi F, Cai Y, Abbasi Asbagh L, Pastor T, De Troyer M, Simicek M, Radaelli E, Brems H, Legius E, Tavernier J, Gevaert K, Impens F, Messiaen L, Nussinov R, Heymans S, Eyckerman S, Sablina AA. Mutations in LZTR1 drive human disease by dysregulating RAS ubiquitination. Science. 2018 Dec 7;362(6419):1177-1182. doi: 10.1126/science.aap7607. Epub 2018 Nov 15. PMID: 30442762; PMCID: PMC8058620.
78. Frattini V, Trifonov V, Chan JM, Castano A, Lia M, Abate F, Keir ST, Ji AX, Zoppoli P, Niola F, Danussi C, Dolgalev I, Porrati P, Pellegatta S, Heguy A, Gupta G, Pisapia DJ, Canoll P, Bruce JN, McLendon RE, Yan H, Aldape K, Finocchiaro G, Mikkelsen T, Privé GG, Bigner DD, Lasorella A, Rabadan R, Iavarone A. The integrated landscape of driver genomic alterations in glioblastoma. Nat Genet. 2013 Oct;45(10):1141-9. doi: 10.1038/ng.2734. Epub 2013 Aug 5. PMID: 23917401; PMCID: PMC3799953.
79. Umeki I, Niihori T, Abe T, Kanno SI, Okamoto N, Mizuno S, Kurosawa K, Nagasaki K, Yoshida M, Ohashi H, Inoue SI, Matsubara Y, Fujiwara I, Kure S, Aoki Y. Delineation of LZTR1 mutation-positive patients with Noonan syndrome and identification of LZTR1 binding to RAF1-PPP1CB complexes. Hum Genet. 2019 Jan;138(1):21-35. doi: 10.1007/s00439-018-1951-7. Epub 2018 Oct 27. PMID: 30368668.
80. Farncombe KM, Thain E, Barnett-Tapia C, Sadeghian H, Kim RH. LZTR1 molecular genetic overlap with clinical implications for Noonan syndrome and schwannomatosis. BMC Med Genomics. 2022 Jul 15;15(1):160. doi: 10.1186/s12920-022-01304-x. PMID: 35840934; PMCID: PMC9288044.
81. Bigenzahn JW, Collu GM, Kartnig F, Pieraks M, Vladimer GI, Heinz LX, Sedlyarov V, Schischlik F, Fauster A, Rebsamen M, Parapatics K, Blomen VA, Müller AC, Winter GE, Kralovics R, Brummelkamp TR, Mlodzik M, Superti-Furga G. LZTR1 is a regulator of RAS ubiquitination and signaling. Science. 2018 Dec 7;362(6419):1171-1177. doi: 10.1126/science.aap8210. Epub 2018 Nov 15. PMID: 30442766; PMCID: PMC6794158.

82. Sewduth RN, Pandolfi S, Steklov M, Sheryazdanova A, Zhao P, Criem N, Baietti MF, Lechat B, Quarck R, Impens F, Sablina AA. The Noonan Syndrome Gene Lztr1 Controls Cardiovascular Function by Regulating Vesicular Trafficking. Circ Res. 2020 May 8;126(10):1379-1393. doi: 10.1161/CIRCRESAHA.119.315730. Epub 2020 Mar 16. PMID: 32175818; PMCID: PMC8575076.
83. Lamiquiz-Moneo I, Mateo-Gallego R, Bea AM, Dehesa-García B, Pérez-Calahorra S, Marco-Benedí V, Baila-Rueda L, Laclaustra M, Civeira F, Cenarro A. Genetic predictors of weight loss in overweight and obese subjects. Sci Rep. 2019 Jul 24;9(1):10770. doi: 10.1038/s41598-019-47283-5. PMID: 31341224; PMCID: PMC6656717.
84. Dutta S, Dawid IB. Kctd15 inhibits neural crest formation by attenuating Wnt/beta-catenin signaling output. Development. 2010 Sep;137(18):3013-8. doi: 10.1242/dev.047548. Epub 2010 Aug 4. PMID: 20685732; PMCID: PMC2926954.
85. Zarelli VE, Dawid IB. Inhibition of neural crest formation by Kctd15 involves regulation of transcription factor AP-2. Proc Natl Acad Sci U S A. 2013 Feb 19;110(8):2870-5. doi: 10.1073/pnas.1300203110. Epub 2013 Feb 4. PMID: 23382213; PMCID: PMC3581937.
86. Spiombi E, Angrisani A, Fonte S, De Feudis G, Fabretti F, Cucchi D, Izzo M, Infante P, Miele E, Po A, Di Magno L, Magliozzi R, Guardavaccaro D, Maroder M, Canettieri G, Giannini G, Ferretti E, Gulino A, Di Marcotullio L, Moretti M, De Smaele E. KCTD15 inhibits the Hedgehog pathway in Medulloblastoma cells by increasing protein levels of the oncosuppressor KCASH2. Oncogenesis. 2019 Nov 4;8(11):64. doi: 10.1038/s41389-019-0175-6. PMID: 31685809; PMCID: PMC6828672.
87. Pirone L, Smaldone G, Spinelli R, Barberisi M, Beguinot F, Vitagliano L, Miele C, Di Gaetano S, Raciti GA, Pedone E. KCTD1: A novel modulator of adipogenesis through the interaction with the transcription factor AP2α. Biochim Biophys Acta Mol Cell Biol Lipids. 2019 Dec;1864(12):158514. doi: 10.1016/j.bbalip.2019.08.010. Epub 2019 Aug 26. PMID: 31465887.

CHAPTER TWO

Materials and methods

2.1 General cell culture

2.1.1 Cell lines and growth conditions

All media were supplemented with 10% FBS (Hyclone) supplemented with 100 U ml^{-1} penicillin, 100 µg ml^{-1} streptomycin, and 2.5 mM L-glutamine (Gibco) to create respective complete media. Cell lines used in this thesis included SIMS cells (ductal epithelial cells isolated from an adult mouse submandibular salivary gland), HEK293T cells (epithelial-like cells derived from human embryonic kidney cells), A549 cells (pulmonary epithelial cells isolated from a human with alveolar cell carcinoma), SMG-HU1 cells (epithelial cells isolated from human submandibular salivary glands), and MDA-MB-231 cells (epithelial cells isolated from the pleural effusion of a human with invasive ductal carcinoma of the breast). SIMS, SIMS derived, and HEK293T cells were cultured in DMEM complete medium at 37°C in 10% CO_2 incubators. A549 and derived cells were cultured in DMEM/F-12 complete medium at 37°C in 5% CO_2 incubators. SMG-HU1 cells were cultured in either MEGM, KGM2, or Epimax complete medium at 37°C in 10% CO_2 incubators. MDA-MB-231 and derived cells were cultured in Leibovitz's L-15 complete medium at 37°C in 5% CO_2 incubators. For passage, cells were rinsed with HBSS prior to detachment with trypsin-EDTA.

2.1.2 Cell counting

Cell densities were determined using an automated cell counter (Nexcelom Cellometer Auto 2000).

2.2 2D cell culture assays

2.2.1 Coverslip coating with extracellular matrix proteins

Extracellular matrix coatings were created as previously described by Lu et al. (1) with modification. Briefly, Matrigel was diluted to 50 µg/mL, aliquoted onto MatTek dishes to cover the glass surface, and incubated at 37°C for 1 hour. After incubation, excess solution was removed, dishes were washed once with 1XPBS, and blocked with BSA (10 µg/mL) for 30 minutes at 37°C.

2.2.2 Colocalisation assays

12 mm diameter glass coverslips were placed into labelled wells of a 12-well tissue culture dish and 1 mL culture media was placed into each well. Culturing SIMS wild-type and BTBD7 knockout cells were resuspended to a concentration of $1x10^5$ cells/mL. 1 mL of cell suspension was plated into 1 mL culture media in labelled wells of the 12-well dish containing glass coverslips and cells were cultured for 24 hours at 37°C. After 24 hours, cells were rinsed with PBS containing calcium and magnesium then fixed in PBS containing 4% paraformaldehyde with 5% sucrose for 30 minutes at 37°C, rinsed four times with PBS containing calcium and magnesium, and permeabilised with 0.5% Triton X-100 in PBS for 30 minutes at 37°C. Non-specific sites were blocked with 10% donkey serum for 1 hour at 37°C. Primary and secondary antibodies were prepared in PBS containing 10% donkey serum and placed on samples for 1 hour at room temperature, washing six times with PBS after each round of

antibody incubation. Samples on coverslips were mounted on slides using ProLong Gold Antifade Mountant (Invitrogen). Images were acquired using a Nikon A1R-MP confocal microscope with laser lines 405, 488, 561, and 642 and a 60X oil (N.A. 1.4) objective.

2.3 3D cell culture and assays

2.3.1 Activation of glass imaging chambers

The term “activation” in this context refers to conjugating a reactive aldehyde group directly to the glass surface via silanes. This conjugated aldehyde group can then react with the hydroxyl groups of collagen and covalently attach collagen matrices to the glass surface. Glass imaging chambers were activated by Andrew D. Doyle as described in Doyle et al. (2). In brief, 1.5 thickness coverglass bottomed MatTek dishes were acid washed with 68% nitric acid for 25 minutes, rinsed with distilled water for 60 minutes, treated with 200 mM NaOH for 15 minutes, rinsed with distilled water, and dried. Glass surfaces were coated in 2% triethoxysilylbutraldehyde (Gelest Inc.) diluted in 100% ethanol and incubated for 5 minutes. Solutions were aspirated, the coverglass was rinsed once with 100% ethanol and once with water. The treated surfaces were dried, cured for 2 hours at 65°C and stored at 4°C.

2.3.2 Matrigel gel formation and cell culture

Matrigel (Corning) solutions were prepared by diluting thawed 9-10 mg/mL growth factor-reduced Matrigel in complete media containing $1x10^5$ or $1x10^3$ cells/mL to obtain 0.45 mg/mL Matrigel solutions. 100 µL of diluted Matrigel solutions containing cells were plated into ultra-low attachment 96-well U-bottom

dishes, centrifuged at 300 rpm for 5 minutes, and cultured in 37°C 10% CO_2 incubators. 24 hours after plating, 100 µL of fresh 0.45 mg/ml Matrigel/complete media was added to each well. After 3 days, cell-spheres were collected and embedded in collagen matrices or allowed to continue culturing in Matrigel after replenishing wells with 100 µL of fresh 0.45 mg/mL Matrigel/complete media.

2.3.3 Collagen gel formation and cell culture

Rat tail collagen was made by Andrew D. Doyle in a manner similar to Chandrakasan et al. (3). Briefly, rat tail tendons were dissected, removing tendon sheaths, bone, cartilage, and blood vessels. Tendon fibres were resuspended in 0.5 M acetic acid, stirred at 4°C for 48 hours, and filtered through gauze at 14,000xg for 1 hour at room temperature. The acquired supernatant was dialysed against three changes of 0.02 M acetic acid. Protein concentration was determined by comparing pre- and post-lyophilisation weights of 5-6 tubes containing 1 mL of solution. Concentration was confirmed using a Sircol collagen assay kit (Biocolor).

Collagen was fluorescently labelled by Andrew D. Doyle as described in Doyle et al. (2). In brief, polymerised collagen was incubated with 50 mM borate buffer pH 9.0 for 10 minutes then aspirated and replaced by Atto-565 NHS-ester dye (Sigma-Aldrich) and incubated in the dark at room temperature for 1 hour. Dye solution was aspirated and residual NHS-esters were quenched with 50 mM Tris buffer pH 7.5 for 10 minutes. Collagen gels were then rinsed with PBS containing calcium and magnesium 10 times over several hours then acidified in 200 mM HCl until solubilised. Collagen solutions were dialysed against 20 mM glacial

acetic acid for 4 hours at a 1:1000 ratio then stored as stock solutions of fluorescently labelled collagen. For experiments, fluorescently labelled collagen was mixed with unlabelled collagen such that the final percentage of labelled collagen was approximately 4%.

Collagen solutions were prepared as described by Doyle (4). Briefly, stock collagen was prepared on ice by mixing 6.0 mg/mL rat tail collagen, 10XDMEM and 10Xreconstitution buffer in a 10:1:1 ratio. 1 M NaOH was used to adjust the pH to 7.4. PBS containing calcium and magnesium and cells were added to solutions to bring the final gel concentration to 2 mg/mL. 250 µL of gel solutions were added to 35 mm MatTek dishes and gels containing cells were allowed to polymerise at 22°C for 45 minutes. After 45 minutes, 2 mL of complete media were carefully added to the dishes and cells were cultured in 37°C 10% CO_2 incubators.

2.3.4 Ubiquitin pathway inhibition and growth factor supplementation assays

The NEDD8-activating enzyme inhibitor MLN4924 (Sigma) and the COP9 signalosome inhibitor that prevents deneddylation of NEDD8-modified CRLs, CSN5i-3 (FisherScientific) were prepared to 100 µM in DMSO. FGF10 (ThermoFisher) and HGF (ThermoFisher) were prepared to 500 ng/mL in 0.1% BSA in media. Matrigel solutions were prepared by diluting thawed 9-10 mg/mL growth factor-reduced Matrigel in complete media containing $1x10^5$ cells/mL to obtain 0.45 mg/mL Matrigel solutions. 100 µL of diluted Matrigel solutions containing cells were plated into ultra-low attachment 96-well U-bottom dishes

centrifuged at 300 rpm for 5 minutes and cultured in 37°C 10% CO_2 incubators. 24 hours after plating, 100 µL of fresh 0.45 mg/mL Matrigel/complete media containing inhibitor, growth factor, or control solutions at the designated final concentrations were added to each well: for MLN4924 and CSN5i-3, 10 µM and 5 µM; for FGF10, 250 ng/mL and 50 ng/mL; for HGF 40 ng/mL and 20 ng/mL. Cells were cultured for 1 week in 37°C 10% CO_2 incubators and images were acquired every 24 hours. After 3 days, wells were replenished with 100 µL of fresh 0.45 mg/mL Matrigel/complete media containing inhibitor, growth factor, or control solutions. All ubiquitin pathway inhibition and growth factor supplementation assays were performed with greater than three replicates.

2.4 Microscopy and imaging

2.4.1 Automated brightfield microscopy

Brightfield imaging of 3D and 2D cell cultures was performed on a Nikon Ti-E brightfield microscope system with a Hamamatsu Orca Flash 4.0 V3 sCMOS camera. 3D cultures were imaged in the same 96-well U-bottom or 35 mm MatTek dishes used for culture. Nikon NIS-Elements software was used to control image acquisition. The JOBS module of the NIS-Elements software was used to automatically set up multiple positions in a 96 well plate for the inhibitor and growth factor assays.

2.4.2 Immunostaining light microscopy

For two-dimension staining, cells were fixed in 4% paraformaldehyde with 5% sucrose for 30 minutes at 37°C, rinsed four times with PBS containing calcium and magnesium, and permeabilised with 0.5% Triton X-100 in PBS for 30

minutes at 37°C. Non-specific sites were blocked with 10% donkey serum for 1 hour at 37°C. Primary and secondary antibodies were prepared in PBS containing 10% donkey serum and placed on samples for 1 hour at room temperature, washing six times with PBS after each round of antibody incubation. Samples on coverslips were mounted on slides using ProLong Gold Antifade Mountant (Invitrogen). Images were acquired using a Nikon A1R-MP confocal microscope with laser lines 405, 488, 561, and 642 and a 60X oil (N.A. 1.4) objective.

For three-dimensional staining, cells were fixed in 4% paraformaldehyde with 5% sucrose for 1 hour at 37°C, rinsed four times with PBS containing calcium and magnesium and 0.5% (v/v) Triton X-100, and permeabilised with 0.5% (v/v) Triton X-100 in PBS for 1 hour at 37°C. Non-specific sites were blocked with 10% donkey serum for 1 hour at 37°C. Primary and secondary antibodies were prepared in PBS containing 10% donkey serum and 0.5% (v/v) Triton X-100 and placed on samples for 48 hours at 4°C, washing six times with PBS with 0.5% (v/v) Triton X-100 after each round of antibody incubation. 3 mL of PBS were placed on samples and samples were stored at 4°C in the dark until imaging by laser scanning confocal microscopy using Nikon 5x, 10x, 20x, or 40x objectives on a Nikon A1R Confocal Microscope.

2.4.3 Image processing and analysis

All images acquired on the Nikon A1R Confocal System were denoised using the Nikon NIS-Elements software's Denoise.ai function. ImageJ, Fiji, and Imaris 9.5.0 were used for all other image processing. Imaris 9.5.0 was used to

reconstruct 3D surface renderings. Custom ImageJ Macro scripts were used to facilitate manual image analysis.

2.5 Animal studies

2.5.1 Mouse breeding

Animal study protocols were approved by the NIDCR Animal Care and Use Committee. All mouse experiments were performed under the approved animal study protocols 14-745 and 17-845. Homozygous BTBD7 knockout C57BL/6 congenic mice were created by Kazue Matsumoto and Ken Holmbeck and outcrossing was performed by William Daley. In brief, W4/129S6 embryonic stem cells were grown and injected into C57BL/6 mouse blastocysts then implanted into C57BL/6 pseudopregnant females. The resulting floxed mice were crossed to a cre-recombinase line in C57BL/6 background to generate the knockout in a mixed background. The mice were finally outcrossed into a pure C57BL/6 background six times prior to characterising phenotype via gross anatomical dissections. Mouse genotyping was performed by Kazue Matsumoto, William Daley, and Shaohe Wang using DNA from tail biopsies.

2.5.2 Mouse dissections

After six outcrossings, a litter of eight five-month-old mice were euthanized and genotyped in accordance with the NIDCR's Veterinary Resources Core guidelines. Mice were dissected for systematic phenotype characterisation as described in Antal et al. (5) with minor deviations in the protocol due to COVID-19 social distancing guidelines. Mouse tissues were disposed of in accordance with the NIDCR's Veterinary Resources Core guidelines.

2.6 Cloning

2.6.1 Restriction enzyme digestion

Restriction endonucleases create double strand breaks at different locations on each DNA strand to produce 3' or 5' overhangs of approximately 1-4 nucleotides. To produce compatible ends for ligating target inserts into cloning vectors, both cloning vectors and target inserts must be treated with restriction enzymes. Ligation of inserts into cloning vectors requires T4 ligase.

Restriction enzymes were selected based on the desired cloning vector and insert sequences and NEBcutter (6; https://nc3.neb.com/NEBcutter/) was used to ensure no in-frame cutting sites were present and NEBcloner (https://nebcloner.neb.com/#!/) was used to model and assess digestion with the selected enzymes. Forward and reverse primers were designed around the selected restriction sites alongside a random 6 base pair sequence at the 5' end to ensure sufficient DNA cleavage. PCR was performed using Herculase II Fusion DNA polymerase (Agilent) with touchdown PCR (7) as follows:

95°C, 10 min

(95°C, 30 sec; 68°C, 30 sec; 68°C, 1-3 min*)x5 cycles

(95°C, 30 sec; 60°C, 30 sec; 68°C, 1-3 min*)x5 cycles

(95°C, 30 sec; 55°C, 30 sec; 68°C, 1-3 min*)x5 cycles

(95°C, 30 sec; 50°C, 30 sec; 68°C, 1-3 min*)x10 cycles

68°C, 10 min

15°C hold

Where * denotes that extension time is determined by the length of the PCR product with 30 seconds used per 1 kb.

PCR products were purified and both vectors as well as purified inserts were treated with restriction enzymes following instructions from NEBcloner appropriate for the chosen enzymes. Digested inserts and vectors were purified using gel extraction and ligated using a 3:1 molar ratio of vector:insert with T4 ligase in a compatible buffer for 30 to 90 minutes at room temperature.

2.6.2 Ligation independent cloning (LIC)

Ligation independent cloning makes use of the 3' to 5' exonuclease activity of T4 DNA polymerase. Linearised inserts and vectors are treated with T4 DNA polymerase in the presence of a single deoxynucleotide (dNTP; this dNTP is a dGTP or dCTP and limits the extent of exonuclease activity) to create complementary overhangs of approximately 10-12 base pairs. The annealed fragments contain several nicks that are then repaired by *E. coli* upon transformation. The LIC compatible vectors used in this thesis were previously produced by the Structural Genomics Consortium. PCR fragments of the gene of interest with overhangs complementary to their target vectors were generated by adding 5' extensions into the LIC primers then treating the amplified fragments with T4 DNA polymerase in the presence of the appropriate dNTP.

Prior to beginning cloning, forward and reverse primers were mixed and prepared to 5 μM and DNA templates containing genes of interest were diluted to 2.5 ng/μL. Inserts containing the gene of interest with LIC-compatible overhangs

were produced using PCR with Herculase II Fusion DNA polymerase (Agilent) and the touch-down PCR conditions described in 2.6.1. 3 µL PCR products were analysed on Invitrogen pre-cast ethidium bromide gels against a Low Range Quantitative DNA Ladder (Invitrogen). For any constructs unsuccessfully cloned in the preliminary PCR reactions, DMSO was added to the PCR mix at a final concentration of 3% to facilitate primer-template annealing and fixed annealing temperatures representative of the failed reactions were used instead of the touch-down PCR method. In cases where the template construct and LIC vector shared the same antibiotic resistance sequence, PCR products were treated with 20 units of the restriction endonuclease DpnI (which only cleaves methylated DNA) for 1 hour at 37°C. The *E. coli* strains used in this protocol produce methylated DNA, thus DpnI treating a PCR product will remove any contaminating DNA from the template constructs. Final PCR products were purified using Qiagen's PCR purification kit (Qiagen) to remove any unincorporated dNTPs that could inhibit resection of the 3' ends during T4 DNA polymerase treatment. Target LIC vectors were digested with the appropriate restriction enzyme (BsaI in all LIC vectors used in this thesis) for 2 hours at 37°C, analysed on a 1.5% TAE-agarose gel to confirm digestion, and purified as stated previously.

To produce complementary overhangs, T4 DNA polymerase (NEB) was added following the manufacturer's instructions to purified vectors (with 25 mM dGTP) and to purified inserts (with 25 mM dCTP) then placed in a thermocycler with the following conditions: 22°C for 30 minutes, heat inactivation at 75°C for 20 minutes, 15°C hold. T4 treated inserts were added in a ratio of 2:1 to T4 treated

vectors and allowed to incubate at room temperature for 20 to 60 minutes. Annealed vectors were transformed into 50 µL of chemically competent MACH1 *E. coli* cells with 45 seconds of heat shock at 42°C. Transformed cells were plated onto LB agar containing the appropriate antibiotics (50 µg/mL kanamycin for pNIC28-Bsa4, pGTVL2, and pNIC-NHT-cTStII vectors or streptomycin for pCDF-LIC vectors) as well as 5% sucrose for *sacB* gene selection (the *sacB* gene product is expressed from the LIC vectors and converts sucrose to a toxic by-product. Cloning the gene of interest into the vector removes the *sacB* gene thus the presence of sucrose in the LB selects for recombinant plasmids lacking the *sacB* gene) then incubated at 37°C for 16 hours. When transformations yielded no bacterial colonies, the ratio of insert to vector was increased, the annealing time was extended, and/or a larger volume of MACH1 cells were used during transformation.

2.6.3 Site-directed mutagenesis

Mutagenesis was performed using an overlapping PCR workflow. One set of mostly complementary primers with the target mismatched DNA in the middle of the primers were used to amplify the entire wild-type cDNA template plasmids (this method is not suitable for plasmids larger than 10 kb). Primers were designed with the designated human KCTD15 substitutions with 15-20 bases flanking the substitution sites. Additional guidelines while designing primers included the following; the 3’ end should end with one or two G/C nucleotides, the terminal 5 base pairs of the 3’ end should contain no more than 3 G/C nucleotides, and the 5’ end should not contain G/C nucleotides. Mutagenesis

PCR was performed using Q5 High-fidelity DNA polymerase (NEB) and the following cycling conditions:

98°C, 10 sec

(98°C, 10 sec; 62-68°C*, 30 sec; 72°C, 1-3 min**)x25 cycles

72°C, 2 min

15°C hold

Where * denotes the temperature is based on the calculated primer *Tm* using NEB Tm calculator and ** denotes that extension time is determined by the length of the PCR product with 30 sec used per 1 kb.

PCR products were treated with DpnI as designated above to remove wild-type template cDNA. Mutated plasmids were transformed into MACH1 competent cells. LIC methods described previously were used to clone mutant cDNA into desired LIC vectors.

2.6.4 Transformations

LB agar plates were prepared by dissolving 25 grams Luria Broth powder and 15 grams Agar powder in 1 L ddH_2O and autoclaving. Heated LB-agar was allowed to cool to 40°C then antibiotics were added and the LB-agar antibiotic solutions were poured into petri dishes and allowed to cool. Competent cells were thawed on ice and 1 µL purified plasmids or 5-10 µL ligation products were placed in sterile 1.5 mL tubes and allowed to incubate with 50 µL competent cells on ice for 30 minutes. The cell-plasmid mixtures were heat-shocked in a 42°C water bath for 45 seconds then incubated on ice for 2 minutes. 500 µL Super Optimal

broth with Catabolite repression (SOC) media (2% tryptone, 0.5% yeast extract, 10 mM NaOH, 2.5 mM KCl, 10 mM $MgCl_2$, 20 mM glucose, pH 7.0) was added to heat-shocked cells and the cultures were incubated at 37°C shaking at 500 rpm for 1-2 hours. Cells were plated on LB agar with appropriate antibiotics and incubated at 37°C in a stationary incubator overnight.

2.7 Lentiviral assays

2.7.1 Lentivirus packaging

All lentivirus work occurred in a BSL2/3 room with a dedicated tissue culture hood and incubator using BSL3 practices. Infectious lentiviral particles were generated by co-transfecting 10 µg of pDCW101 or pDCW102 with 10 µg pMD2t.G and 10 µg psPAX2 into HEK293T cells using calcium co-precipitation. In brief, 4 million cells were plated in 10 cm dishes 24 hours prior to transfection. The day of transfection, DMEM complete media was replaced with culture media supplemented with 25 µM chloroquine. 10 µg of each plasmid was added to 1 mL 0.3M $CaCl_2$ and pipetted to mix. DNA-$CaCl_2$ mixes were sequentially added to 1 mL 2xHBS (50 mM HEPES, 280 mM NaCl, 1.5 mM Na_2HPO_4, pH 7.10) and mixed. The complete transfection mix was then added dropwise to 10 cm dishes of cells. Culture media was replaced at approximately 12 and 36 hours post transfection and lentivirus-containing supernatants were collected at 36 and 60 hours post transfection. Pooled lentivirus supernatants were passed through a 0.45 µm filter prior to concentrating the virus. To concentrate, 5xPEG reagent was added to the virus-containing supernatant, incubated at 4°C for 48 hours, and pelleted by centrifugation at 1,500xg for 30 min at 4°C. The pellet was

resuspended in 300 µL DMEM with 1xPenStrep and stored at -80°C until transduction.

2.7.2 Lentivirus titration

Concentrated lentivirus was diluted 100x and titre was estimated using Lenti-X GoStix Plus (Tamara). A GoStix Value of 50 was empirically considered to be the equivalent of a lentivirus titre of approximately $5x10^5$ IFU/mL.

2.7.3 Lentivirus transduction

The day prior to transduction, $1x10^5$ cells were plated in a well of a 12-well plate. On the day of transduction, cell culture media was replaced with 1 mL complete media containing 2 µL 4 mg/mL polybrene. 100 µL concentrated lentivirus was added to the appropriate cell cultures and incubated for 24 hours. After 24 hours, the virus-containing medium was replaced with regular complete medium after 8 washes with HBSS and re-plated to a 75 cm^2 flask in culture medium supplemented with 2 µg/mL puromycin to begin antibiotic selection.

2.8 Protein expression

2.8.1 *E. coli* expression

All recombinant proteins discussed in this thesis were expressed from *E. coli*. Other common expression systems used to produce recombinant protein include baculovirus insect cell expression, yeast expression, and various mammalian cell expression systems. Each expression system differs regarding ease of use and types of post-translational modifications introduced onto the expressed protein. *E. coli* expression was selected for this work due to the large amount of protein

required for structural studies as well as the presence of an established high-throughput workflow for *E. coli* expression in my research department. Target constructs cloned into pNIC28-Bsa4, pGTVL2, pCDF-LIC, or pNIC-NHT-cTStII vectors were transformed into the expressing strain BL21(DE3)-R3-pRARE2. To produce glycerol stocks for future inoculations, a single colony of BL21(DE3)-R3-pRARE2 cells was inoculated in 5 mL Luria Broth (LB) containing 34 µg/mL chloramphenicol and 50 µg/mL kanamycin (for pNIC28-Bsa4, pGTVL2, and pNIC-NHT-cTStII vectors) or streptomycin (for pCDF-LIC vectors) and grown overnight at 250 rpm in 37°C. Glycerol stocks were produced via mixing 50% overnight culture with 50% autoclaved glycerol then stored in -80°C. For 1 litre expressions, auto-induction Terrific Broth containing 50 µg/mL kanamycin (for pNIC28-Bsa4, pGTVL2, and pNIC-NHT-cTStII vectors) or streptomycin (for pCDF-LIC vectors) were inoculated with 5 mL overnight cultures and grown shaking at 180 rpm in 37°C until an optical density at 600 nm wavelength reached 0.6. Using auto-induction Terrific Broth, there was no need to add additional β-D-1thiogalactopyranoside (IPTG) to the cells, but the culture temperature was lowered to 18°C and cultures were grown overnight. In the three expression vectors used in this thesis, target genes were inserted at the 3' end of a lac operator. IPTG binds to, and allosterically releases, the lac repressor from the lac operator allowing for gene transcription (8). Cells were collected and centrifuged at 5000 rpm in 4°C for 15 minutes then resuspended in binding buffer supplemented with 0.5 mM TCEP and SET III protease inhibitor cocktail (Calbiochem) (binding buffer recipe is reported in section 2.9.1).

2.9 Protein purification

2.9.1 Buffers

Binding buffer: 500 mM NaCl, 50 mM HEPES pH 7.5, 5% (v/v) glycerol, 5 mM imidazole, with 0.5 mM TCEP and SET III protease inhibitor cocktail (Calbiochem) added day of use

Wash buffer: 500 mM NaCl, 50 mM HEPES pH 7.5, 5% (v/v) glycerol, 30 mM imidazole

Elution buffers for nickel affinity resin purification: 500 mM NaCl, 50 mM HEPES pH 7.5, 5% (v/v) glycerol, 50-250 mM imidazole

Elution buffer for glutathione Sepharose affinity resin purification: 500 mM NaCl, 50 mM HEPES pH 7.5, 5% (v/v) glycerol, 5 mM imidazole, 10 mM reduced glutathione

Size exclusion chromatography buffer: 300 mM NaCl, 50 mM HEPES pH 7.5, 0.5 mM TCEP

Ion exchange low salt buffer: 20 mM Tris pH 8.0, 50 mM NaCl, 0.5 mM TCEP

Ion exchange high salt buffer: 20 mM Tris pH 8.0, 1 M NaCl, 0.5 mM TCEP

2.9.2 Cell lysis

E. Coli cell pellets were resuspended in binding buffer with fresh 0.5 mM TCEP and SET III protease inhibitors. 20 mL of binding buffer was used for every 1 L cell culture. Cells were sonicated on ice for 15 to 30 minutes at 35% amplitude pulsing for 5 seconds on 10 seconds off (Qsonica). Following sonication, polyethylenimine (PEI) was added at a final concentration of 0.15% (v/v) to precipitate DNA. Cell debris was pelleted by centrifugation at 21000 rpm for 30 minutes at 4°C. The cleared supernatant was collected and filtered using 0.22 µm filters.

2.9.3 Affinity purification of glutathione s-transferase and hexahistidine fusion proteins

Glutathione S-transferase (GST) is a 26 kDa eukaryotic protein that binds with high affinity to glutathione. Histidine is a roughly 2.5 kDa motif that chelates metal ions such as Nickel. Hence, glutathione resin columns can be used for the purification of GST-tagged proteins and nickel Sepharose resin columns can be used for the purification of polyhistidine (hexahistidine)-tagged proteins.

The filtered supernatant from section 2.9.2 was batch bound to 50% Nickel resin or glutathione resin slurries pre-equilibrated with binding buffer in 50 mL tubes under gentle rotation at 4°C for 30-60 minutes. 1 mL bed volume of resin was used for every 1 L of cell culture. Resin was washed with 10 column volumes (CVs) binding buffer followed by 20 CV wash buffer. Between washes, resin was pelleted by gentle centrifugation of 400xg for 5 minutes at 4°C and the supernatant was removed and discarded.

For nickel resin affinity purifications, bound protein was eluted with 2 column volumes of the appropriate elution buffer containing a gradient of imidazole ranging from 50 to 250 mM. For the first attempts at glutathione Sepharose resin affinity purifications, bound protein was eluted with 2 column volumes of the appropriate elution buffer containing reduced glutathione. Proteins from each fraction were analysed by SDS-PAGE.

Due to low yields of eluted GST-tagged protein (described in chapter 4), subsequent glutathione Sepharose purifications involved on-column cleavage of protein. Following washes, resin was resuspended in 3 column volumes wash buffer containing TEV protease in a ratio of 1:100 protease:protein (w/w) and incubated overnight at 4°C under gentle rotation. The following morning, supernatant containing cleaved protein was collected and analysed by SDS-PAGE.

2.9.4 Size exclusion chromatography

Size exclusion chromatography (SEC) is a liquid chromatography technique used to separate macromolecules of varying sizes and shapes using a column filled with spherical beads that create pores of a specific size distribution. Separation is caused by molecules of different size/shape being either included or excluded from the pores of the resin matrix as the sample traverses the column length (9).

Protein samples were concentrated using centrifugal ultrafiltration to a volume of 5 mL and concentration of 1-2 mg/mL, filtered using 0.22 µm filters, and loaded onto a size-exclusion chromatography column (HiLoad 16/600 Superdex 200 or 75 preparatory grade column [GE Healthcare]) pre-equilibrated in gel filtration buffer. Column length and pore size were taken into consideration when selecting the column to use for protein purifications. In general, longer (e.g., 60 cm) columns allow for better separation of “dirty” protein samples compared to shorter columns and the optimal pore size depends on the predicted size/shape of the proteins being purified (e.g., the 75 pg column is generally suitable for 3-

70 kDa proteins and the 200 pg column for 10-600 kDa proteins). Protein fractions were analysed by SDS-PAGE and concentrated using centrifugal ultrafiltration. Sample identity was verified by mass spectrometry (LC-MS). Protein was used fresh or flash frozen in liquid nitrogen and stored at -80°C.

2.9.5 Ion-exchange chromatography

Ion-exchange chromatography is a technique used to separate biological molecules by their charge. Dependant on the pH of its microenvironmental, a protein may carry a net positive charge, a negative charge, or may lack a charge. The pH at which a protein has no net charge is referred to as its isoelectric point (pI) and is determined by the electrical properties of its amino acids (10). At pHs above their pIs, proteins will carry a net negative charge and at pHs below their pIs, a net positive charge. Proteins with different pIs will have different charges at the same pH. Ion-exchange chromatography takes advantage of this charge discrepancy to separate proteins of differing pIs. For example, a protein with a pI of 6 will have a net negative charge when in a buffer of pH 7 and will bind to a positively charged anion exchange resin. In contrast, a protein with a pI of 8 will have a net positive charge in that same buffer and will not bind the positively charged anion exchange resin. This principle allows one to bind a protein of interest to an appropriately selected ion exchange chromatography column, wash the column to remove impurities, then elute the purified target protein using either a salt gradient or a change in pH.

The pIs of target proteins and protein complexes were predicted using Expasy Compute pI/Mw (11) and ranged from approximately 4.7 to 6. Thus, an anion

exchange resin (HighTrap Q HP column [GE Healthcare]) and a tris-based buffer of pH 8.0 were chosen for anion exchange chromatography experiments. Proteins were prepared to 1 mg/ml in a low salt buffer (20 mM Tris, pH 8.0, 50 mM NaCl, 0.5 mM TCEP) and bound to a HighTrap Q 5 mL column pre-equilibrated with low salt buffer. After binding proteins to the column, a gradient of 50 mM to 500 mM NaCl buffer was passed over the column for 25 column volumes at a rate of 2.5 mL/minute. After 25 column volumes, a buffer containing 1 M NaCl was used to remove any residual bound protein. Fractions were collected and analysed with SDS-PAGE.

2.9.6 Protein handling

Between each stage of protein purification, 0.5 mM TCEP was added to protein solutions to prevent oxidation. Protein solutions were kept on ice or handled in 4°C environments throughout purification. Following purifications, proteins were concentrated using centrifugal concentrators to greater than 1 mg/ml and either used fresh or flash-frozen in liquid nitrogen and stored at -80°C. Protein identity and purity were confirmed by intact mass spectrometry.

The ligation independent cloning (LIC) vectors used in chapters 4 and 5 of this thesis include a tobacco etch virus (TEV) protease cleavage site (ENLYFQ*SM, with '*' denoting the cleavage locus) between the tag and protein target. To remove the tag, protein could be incubated with TEV protease in a ratio of 1:100 protease:protein (w/w) at 4°C overnight or for 2 hours at room temperature. The TEV protease used in this thesis is histidine tagged, thus allowing residual TEV

to be removed using nickel affinity resin alongside other conventional purification methods.

2.10 Western blotting

Western blotting is an analytical technique used to detect specific targets among heterogeneous protein samples (e.g., a tissue homogenate). Denatured protein samples are subjected to electrophoresis using a polyacrylamide gel and separated by their apparent molecular masses. Separated proteins are then transferred to a membrane, detected using appropriately selected antibodies, visualised, and analysed (13).

Protein samples were denatured by boiling in sample buffer (Bio-Rad) for 5 minutes then subjected to gel electrophoresis (SDS-PAGE in all cases discussed in this thesis). Proteins were transferred from the gel to either a nitrocellulose or polyvinylidene difluoride (PVDF) membrane using a Bio-Rad Trans-Blot Turbo Transfer System (Bio-Rad). Following transfer, membranes were incubated for 30 minutes at room temperature in blocking buffer (Tris-buffered saline with 0.5% (v/v) Tween-20 (TBST) and 5% (w/v) non-fat dried milk powder) to block sites of potential nonspecific protein binding. Membranes were probed with target-specific primary antibodies diluted in blocking buffer for 30-60 minutes at room temperature. Membranes were washed five to ten times using TBST, incubating one to three minutes for each wash, then probed with species-specific secondary antibodies conjugated to Horseradish Peroxidase (HRP). HRP can catalyse the oxidation of the chemiluminescent reagent luminol to create an excited state product called 3-aminopthalate. Upon decaying to a lower energy state, 3-

aminopthalate releases photons of light that can be detected at 425-428 nm. Following another round of washes, membranes were incubated with SuperSignal™ West Femto Maximum Sensitivity chemiluminescence substrate (Thermofisher) for 1-2 minutes and imaged by GE Healthcare's Amersham Imager 680 (GE Healthcare).

When required, this general western blotting workflow was optimised for working with extremely limited sources of antibody. This modified workflow was predominantly used to screen candidate animal sera and hybridoma cell supernatant while producing antibodies to BTBD7, as described in chapter 3. Details of this modified workflow can be found in Cruz Walma et al. (13).

2.11 Co-immunoprecipitation

Immunoprecipitation involves precipitating a target protein out of solution (e.g., cellular lysate) using a specific antibody coupled to a solid-state material (e.g., agarose resin). Protein complex immunoprecipitation (Co-IP) is a common technique to assess protein-protein interactions. Co-IP is similar to IP with the exception that all proteins associated with the protein antigen are similarly precipitated (14). As a result, a protein complex can be isolated by Co-IP using an antibody for only one of the proteins in the complex and subsequently analysed by SDS-PAGE or Mass Spectrometry.

Samples were kept on ice throughout Flag co-immunoprecipitation. Flag M2 affinity resin (Sigma Aldrich) was washed with milliQ water and pre-equilibrated with gel filtration buffer (300 mM NaCl, 50 mM HEPES pH 7.5, 0.5 mM TCEP). 1

µL Flag resin was prepared for every 1 µg of purified protein. All proteins were purified via affinity purification and size exclusion chromatography prior to Co-IP experiments. Flag-tagged and cleaved test proteins were prepared to 0.1 mg/mL in buffer containing 300 mM NaCl, 50 mM HEPES pH 7.5, 0.5 mM TCEP, mixed, and incubated for 30 minutes with rotation at 4°C. After 30 minutes, Flag M2 affinity resin was added to the protein mixtures and samples continued to incubate with rotation at 4°C overnight. Flag resin was pelleted via centrifugation at 2000 rpm for 2 minutes at 4°C and supernatants were kept for downstream analysis. Resin was washed twice with buffer containing 50 mM HEPES pH 7.5, 150 mM NaCl, 10% glycerol, 0.5 mM TCEP, 0.05% Tween-20. Protein complexes were eluted off resin via boiling in sample buffer then subjected to SDS-PAGE and Coomassie staining.

2.12 Size exclusion chromatography/multi-angle light scattering (SEC-MALS)

Size exclusion chromatography/multi-angle light scattering (SEC-MALS) allows for the analysis of a molecule’s molar mass in solution. The SEC column separates molecules by hydrodynamic volume while MALS measures the intensity of light scattered by the separated molecules (15). A single frequency polarised light beam illuminates macromolecules in solution and the intensity of the scattered light is proportional to the weight-averaged molar mass of a molecule in solution while the angle of scattered light carries information about the molecule’s shape. Mass estimation by SEC alone can be inaccurate as a molecule's retention time depends on both its molecular mass and hydrodynamic radius. When an analytical SEC column is coupled with MALS, molecular mass

can be accurately calculated and oligomeric states, aggregation states, alongside other properties of native molecules in solution can be analysed (15).

SEC was performed using an analytical grade Superose 6 10/300 GL column (GE Healthcare) pre-equilibrated with Phosphate Buffered Saline at a flow rate of 0.5 mL/min. Protein samples were prepared at 1 mg/mL in buffer containing 300 mM NaCl, 50 mM HEPES pH 7.5, and 0.5 mM TCEP. Experiments were performed at a flow rate of 0.5 mL/min. Elution was monitored via online light scattering (DAWN-HELEOS 8+, Wyatt Technology) and UV (SPD-20A, Shimadzu) detectors. The ASTRA software package (Wyatt Technology) was used to analyse data.

2.13 Differential scanning fluorimetry

Differential scanning fluorimetry (DSF) is a technique that measures protein unfolding by monitoring changes in a protein's fluorescence emission as a function of temperature. The measured fluorescence can be caused by either a hydrophobic fluorescent dye that binds to proteins as they unfold (conventional DSF) or from the intrinsic fluorescence of a protein's tryptophan residues (nanoDSF) (16).

Samples were diluted to 5, 2.5, and 1.25 μM in gel filtration buffer (300 mM NaCl, 50 mM HEPES, pH 8.0, 0.5 mM TCEP) containing the hydrophobic fluorescent dye SYPRO Orange. Protein thermal stability was determined by heating samples from 25°C to 95°C in a Mx3005P real-time PCR instrument (Stratagene) and measuring fluorescence with excitation and emission filters set to 465 nm

and 590 nm, respectively. Resulting fluorescence measurements as a function of time were exported to Graphpad Prism and apparent T_m values were calculated by fitting data to a Boltzmann equation (17).

2.14 X-ray crystallography

2.14.1 Crystallisation

Vapour diffusion is one of the most widely used methods for protein crystallisation (18). Vapour diffusion experiments can be performed using either a hanging drop or sitting drop workflow. In both methods, a sample of protein is mixed with a “mother-liquor” solution typically containing a precipitant, buffer, and salt (although other compounds can be included) then placed in a sealed chamber containing a reservoir of mother liquor of significantly greater volume than the protein drop. In such conditions, the significantly higher concentration of precipitant in the reservoir drives water from the drop to the reservoir via net vapour diffusion. As the ratio of protein-to-precipitant in the drop increases, protein is pushed to a supersaturated state in which it will either crystallise or precipitate (18).

Unless otherwise stated in the relevant results sections of this thesis, proteins were concentrated to 10 mg/mL using a 10 kDa centrifugal concentrator (Millipore). Crystallisation was performed using a sitting drop vapour diffusion method. During preliminary crystal coarse screens, the following four sparse matrix course screens were used: Ligand Friendly Screen (LFS), Joint Centre for Structural Genomics (JCSG) screen, Basic Chemical Space (BCS) screen, and

the Morpheus screen (details of which screen was used for each protein are found in the relevant results sections of this thesis).

Crystallisation fine screens were designed following the Structural Genomics Consortium's optimisation guidelines (19). In brief, when a coarse screen condition contained three components (a detergent, a buffer, and a salt), a 96 well plate was divided into quadrants. Each quadrant of the fine screen contains a different molarity of the salt from the coarse screen hit, buffer pH is varied along the four rows of each quadrant, and detergent concentration is varied along the six columns of each quadrant.

Details of crystallisation trials for each protein discussed in this thesis are included in the following results sections; 4.2.7 for LZTR1, RHOBTB1, and BTBD7; 5.2.3 for KCTD15 wild type as well as Gly88Asp and Asp104His variants.

2.14.2 Structure determination

Following diffraction data collection, a protein's structure can be determined via using two fundamental stages of data processing: "integration" and "scaling and merging." Integration involves extracting intensity information from diffraction spots on diffraction images and consists of selecting diffraction spots from background signals, assigning a 3D index to define each reflection in the dataset, and measuring reflection spot intensity. Scaling and merging then places the measured intensities onto a uniform scale and merges symmetry-related measurements.

Diffraction data were collected at the Diamond Light Source beamline I03 then processed in Xia2 (20), dials (21), or Staraniso (22). For KCTD15Z-x046 (crystal form II), data were auto processed with Xia2 dials and molecular replacement was performed using the AlphaFold KCTD15 model by the downstream processor Mr Bump (23). PDB files of three KCTD1 crystal structures (5BXB, 6S4L, and 5BXD) as well as the AlphaFold KCTD15 model were uploaded to the ISPYB server to enable molecular replacement performed by Mr Bump (23). Mr Bump internally ranked each uploaded PDB and attempted to perform molecular replacement with each PDB file. Mr Bump used the AlphaFold KCTD15 model for the final molecular replacement output. For KCTD15Z-x046 (form II), due to an indexing solution indicative of higher symmetry ($a \approx b$, $\alpha \approx 90°$, $\gamma \approx 60°$), the data were reprocessed with dials (21). No higher symmetry solution could be found, so space group P1 was used. For KCTD15Z-x038 (crystal form I), data were auto processed in Xia2 dials and molecular replacement was performed with Phaser (24) in PHENIX (25) using the refined KCTD15Z-x046 structure as the search model. COOT (26) was used for manual model building and refinement, whereas PHENIX.REFINE was used for automated refinement (25). Geometry and real space parameters were restrained in the first few rounds of refinement and locating NCS and TLS parameters were included in the latter stages of refinement. The final rounds of KCTD15Z-x046 (form II) refinement, automated refinements were performed using MTZ files from Staraniso auto processing to improve the structure's B-factors (Debye-Waller factors). Refined models were validated using MolProbity (27). Following a final round of manual and automated refinements correcting for warnings flagged by the PDB

validation report, structure co-ordinates and factors were deposited in the PDB with accession codes 8PNR (KCTD15Z-x038, form I) and 8PNM (KCTD15Z-x046, form II). Structure figures were prepared using Pymol (28).

2.15 Structural modelling

2.15.1 Modelling of CUL3 binding to tandem BTB AlphaFold models

AlphaFold, a machine-learning based artificial intelligence system, has predicted the structures of over 200 million proteins and has become a powerful tool to help solve diverse challenges in structural biology. AlphaFold models have been used to predict the structural effects of mutations on protein stability and folding, detect protein pockets to assist in targeted drug discovery, predict protein complexes and protein disorder, as well as provide structural models for molecular replacement in X-ray crystallography, alongside various other applications (29). As AlphaFold predictions continue to improve, this computational tool will continue to have a transformative impact on structural biology. Future versions of AlphaFold may provide more accurate predictions of protein disorder and thus key insights into the functional importance of such disorder (at present, AlphaFold is trained primarily on X-ray data and therefore predicted regions of disorder are mainly regions not solved by X-ray crystallography). Similarly, AlphaFold's ability to accurately predict protein oligomerisation and complex formation will continue to improve. With continued refinement, it will be intriguing to see if the tool will become capable of predicting obligate cofactors and/or metal ions in protein structures as well as new protein-protein interactions. Although artificial intelligence-based modelling will continue to transform the field of structural biology, it will not do away with experimental

studies. Instead, the combined use of both artificial intelligence and experimental data to answer challenging questions will become an increasingly common trend.

Protein structure predictions of BTBD7, RHOBTB1, and LZTR1 were downloaded from the AlphaFold Protein Structure Database (30). Structures of each BTB domain of BTBD7, RHOBTB1, and LZTR1 were superimposed on the BTB domain of KLHL11 in the CUL3-KLHL11 complex (PDB ID 4AP2) using sequence-independent structure-based dynamic programming alignment followed by a series of refinement cycles in Pymol (28). RMSD values for the superimposition were calculated and images of the tandem BTB protein-CUL3 complex were ray traced and exported. With recent improvements in AlphaFold, the tandem BTB protein-CUL3 complexes could have been modelled with an AlphaFold multimer prediction algorithm. Due to time constraints and limited access to the computational resources needed for such modelling, this approach was unable to be completed.

2.15.2 Homology modelling

Homology models of human KCTD15 full length and BTB domain were prepared in ICM-Pro software package (Molsoft) using KCTD1 PDB codes 6S4L (for full length modelling) and 5BXB (for BTB domain modelling). KCTD15 substitutions Asp104His and Gly88Asp were modelled by *in silico* mutation in Pymol (28). For comparison, models of KCTD15 were also produced using AlphaFold. Minimal differences between the AlphaFold KCTD15 models and KCTD1 crystal structures were noted in this region of the BTB domain. Images were exported as ray-traced PNGs from Pymol.

2.16 Mass spectrometry

2.16.1 Intact mass spectrometry (LC/MS)

Intact mass spectrometry uses a combination of liquid chromatography (LC) and mass spectrometry (MS) to provide information about protein mass (31).

Intact protein masses were determined using the liquid chromatography and mass analyser interface provided by the Agilent LC/MS ToF system. Reversed-phase chromatography was performed in-line prior to mass spectrometry using an Agilent 1100 HPLC system (Agilent Technologies Inc.). Concentrated protein samples were diluted to 0.02 mg/mL in 0.1% formic acid and 50 µL was injected on to a 2.1 mm x 12.5 mm Zorbax 5um 300SB-C3 guard column housed in a column oven set at 40°C. The solvent system used consisted of 0.1% formic acid in ultra-high purity water (Millipore) (solvent A) and 0.1% formic acid in methanol (LC-MS grade, Chromasolve) (solvent B). Chromatography was performed as follows: Initial conditions were 90% A and 10% B and a flow rate of 1.0 mL/min. After 15 seconds at 10% B, a two-stage linear gradient from 10% B to 80% B was applied over 45 seconds and then from 80% B to 95% B over 3 seconds. Elution proceeded isocratically at 95% B for 1 minute 12 seconds followed by equilibration at initial conditions for 45 seconds. Protein intact mass was determined using a 1969 MSD-ToF electrospray ionisation orthogonal time-of-flight mass spectrometer (Agilent Technologies Inc.). The instrument was configured with the standard ESI source and operated in positive ion mode. The ion source was operated with the capillary voltage at 4000 V, nebulizer pressure at 60 psig, drying gas at 350°C and drying gas flow rate at 12 L/min. The

instrument ion optic voltages were as follows: fragmentor 250 V, skimmer 60 V and octopole RF 250 V. Protein samples were prepared and provided to Rod Chalk who ran all mass spectrometry analyses reported in this thesis.

2.16.2 Native mass spectrometry

Native mass spectrometry involves “soft” electrospray ionisation (ESI) using biologically and ESI compatible native buffer systems. It preserves all the native features of macromolecules while allowing for measurement of masses, charge states, and their relative ion abundances (32). During electrospray ionisation, large biomolecules are transferred from the liquid to the gas phase. Ionisation itself must occur at or before the desolvation point (when the gas phase is achieved). While *m/z* measurement occurs in the gas phase, charge state determination occurs during the liquid phase. It therefore follows that native MS charge distributions reflect the molecular conditions in the liquid phase, not the gas phase as commonly assumed. This is immensely important as it allows biologically relevant measurements to be derived in the absence of artifice such immobilization, conjugation, or fluorophores. Native MS provides both structural and functional information. Conventionally, native MS can determine complex stoichiometry, protein-protein interaction, and protein-ligand interaction. More recently it has been used to determine molecular size, shape, functional activity, conformation, and thermal stability (32).

Protein samples were prepared to 1 mg/mL then desalted via applying to a Micro BioSpin 6 size-exclusion column pre-equilibrated with 50 mM ammonium acetate pH 6.5. Eluents were collected and subsequently subjected to two further rounds

of size exclusion then held on ice until MS analysis. MS was performed using an Agilent 6530 QToF mass spectrometer with the following acquisition parameters: ion mode positive; detector mode 1 GHz; scan range 100 m/z to 20,000 m/z; collision cell off; capillary 3500V; fragmentor 430 V; skimmer 65 V; octopole rf 750 V; drying gas 325°C; drying gas 5 L/min; nebuliser 15 psi. The instrument was configured using a standard ESI source and a 30-gauge stainless steel nebuliser needle. Samples for analysis were transferred to 500 µL gas tight syringes (Hamilton) and directly infused into the mass spectrometer at 6 µL/min. Multimer assignment was achieved using an ion table and charge radius of the complex was calculated using the method of Testa et al. (33) and the most abundant charge states.

2.16.3 Phosphoproteomics

With over two-thirds of cellular proteins containing phosphorylation sites (34), the study of protein phosphorylation (phosphoproteomics) has become a major focus of the scientific community. Traditionally, analysing protein phosphorylation with mass spectrometry has proved challenging due the complex low-throughput workflows required to handle the poor ionisation, high hydrophilicity, and incomplete digestion of phosphopeptides (35). To combat these issues, strategies to enrich samples for phosphopeptides have been developed (36). When prepared in the appropriate buffers (e.g., 2,5-dihydroxybenzoic acid or phthalic acid), TiO_2 selectively binds phosphopeptides (37) and in acidic conditions, the negatively charged phosphate groups preferentially bind positively charged metal ions (e.g., Fe^{3+}) (38). Accordingly, a prominent strategy

to enrich for phosphorylated peptides includes the use of titanium dioxide (TiO_2) and iron-chelate resin (Fe-NTA) spin columns (ThermoFisher).

3D cultures of SIMS cells in Matrigel solutions, were grown for 7 days prior to harvesting for lysis. After 7 days, the 60 replicate cultures of SIMS BTBD7 WT and KO cells were rinsed with PBS, collected into 200 µL of a 10 mM sodium phosphate 2% (v/v) SDS solution supplemented with protease and phosphatase inhibitors in 15 mL centrifuge tubes, homogenised, and immediately boiled in water for 5 minutes. A four times volume of cold acetone was added to the protein lysate, vortexed to mix, and incubated for 24 hours at -20°C to precipitate proteins. After 24 hours, proteins were pelleted by centrifugation at 15,000xg for 10 minutes, supernatant was discarded, and residual acetone was allowed to evaporate. The protein pellet was resuspended in 22.5 µL 8 M urea/50 mM TEAB (Triethylammonium bicarbonate) and protein concentration was determined via Bradford Assay. 2.5 µL of 50 mM DTT/50 mM TEAB was added and samples were incubated 1 hour at 37°C to reduce the proteins. 500 mM MMTS (methyl methanethiosulfonate)/50 mM TEAB at a final MMTS concentration of 40 mM was added to block free sulfhydryl groups (present on cysteine side chains). Following incubation for 40 minutes at room temperature, 1 µg Trypsin/LysC per 25 µg starting protein was added to samples and incubated for 2 hours at room temperature. 50 mM TEAB was added to dilute samples to less than 1 M urea and samples were further incubated overnight at 37°C. Digestion was terminated using 1.0% final concentration of TFA (trifluoroacetic acid) and samples were loaded onto a C18 micro spin column to desalt the peptide mixture. Samples were washed using a 2.5% acetonitrile/0.1%

TFA solution, eluted into 1.5 mL centrifuge tubes using a 60% acetonitrile/0.1% TFA solution, and concentrated using a speedvac vacuum concentrator. The lyophilized protein pellets were suspended in 150 µL 5% TFA/70% acetonitrile/15% lactic solution and protein concentration was determined using Bradford Assay. Input aliquots were set aside and the remaining solution was subjected to phosphopeptide enrichment using first TiO_2 spins columns then Fe-NTA spin columns (ThermoFisher). Enrichment was performed using the protocol provided by the manufacturer (ThermoFisher). Peptides were eluted over a linear gradient of acetonitrile/water/0.1% formic acid, ionised by electrospray ionisation, and analysed on an Orbitrap Fusion Tribrid Mass Spectrometer (ThermoFisher). MS data was analysed with the Proteome Discoverer 2.4 software (ThermoFisher). Peptide and protein identifications were obtained through searching against the mammalian Swiss-Prot protein database with trypsin specified as the digestion enzyme.

2.17 Analytical ultracentrifugation

Analytical ultracentrifugation is a technique to study the behaviour of macromolecules in solution as they sediment secondary to centrifugal force. Two complementary methods of AUC can be used to characterise either the dynamic behaviours of macromolecules in solution (sedimentation velocity) or their behaviours in equilibrium (sedimentation equilibrium) (39). Sedimentation velocity can provide information about the size and shape of a molecule and sedimentation equilibrium can provide insight about a molecules molar mass, association constants, and stoichiometries (40, 41). A typical AUC is equipped with systems to detect both absorbance and interference and contains a central

chamber with a rotor and optic system of a lamp, reflector, lens, and photomultiplier tube. Sample protein solutions and matched buffer references without proteins are placed in a specially designed centrifuge cell. Samples are centrifuged at a designated speed and temperature and optical density or a refractive index is measured along the cell radius over time. Upon subjection to centrifugal forces, buoyant and diffusion forces counteract the applied centrifugal force and the solutions sedimentation is opposite the rotor's centre of rotation (41).

During sedimentation velocity, the high speeds of the rotor move macromolecules away from the centre of the rotor to create a sedimented pellet at the outer edge of the cell. Optical density is measured throughout such sedimentation and a series of wavelength scans are produced, with wavelengths flattening as the solution sediments (40, 41). The sedimentation coefficient, diffusion coefficient, molecular weight, and predicted shape can then be calculated from the distribution of wavelengths over time (40, 41).

In contrast to sedimentation velocity, sedimentation equilibrium is performed at lower speeds thus does not cause a pellet of macromolecules to form at the edge of the cell. The counteracting sedimentation and diffusion forces cause the system to eventually reach an equilibrium in which the sedimentation of the proteins in solution reaches a steady state. Sample absorbance versus radial distance from the centre of the rotor is plotted. This distribution movement over time can be used to provide information about a sample's molecular weight, and the slope of the curve provides information related to the macromolecules

aggregation states, molecular weight, homogeneity, and association constants (41, 42).

Sedimentation velocity experiments were used to calculate molecular weights of proteins in their native state. Experiments were performed in a Beckman Optima XL-1 analytic centrifuge with a Beckman An-60 Ti rotor at 20°C with a rotor speed of 40,000 rpm. Proteins were prepared at 1 mg/mL in a buffer containing 300 mM NaCl, 50 mM HEPES pH 7.5, and 0.5 mM TCEP. Filter flowthroughs produced during centrifugal concentration of protein samples were used as buffer-matched reference samples. Radial absorbance scans were recorded with absorbance optics at 280 nm in continuous scan mode. SEDNTERP (43) was used to calculate buffer density and viscosity as well as partial specific volumes from amino acids sequences and SEDFIT (44) was used to fit scans to a continuous size distribution and calculate molecular weights.

2.18 Biolayer interferometry

Biolayer Interferometry (BLI) can be used to determine the binding kinetics and affinity between molecules (45). During a BLI experiment, one target molecule is immobilised on the tip of a biosensor. The coated sensor tip is then dipped into a solution containing the second target molecule. Binding between the two molecules will manifest as an increase in the number of molecules bound to the biosensor tip. The biosensor can then be placed into a well containing only buffer and the second bound molecule can dissociate from the immobilized first molecule. Interference patterns of white light reflected from the surface of the biosensor tip are measured and a change in the number of molecules bound to

the biosensor tip will manifest as a shift in the interference patterns (45). BLI experiments can be used to analyse the association and dissociation between two molecules of interest to calculate binding affinities and dissociation constants.

Binding affinities between TFAP2 peptide and KCTD15 wild type as well as Asp104His and Gly88Asp variants were determined using an Octet RED384 system (FortéBio). A 14 amino acid biotinylated TFAP2 peptide (sequence: Biotin-NADFQPPYFPPPYQ) was designed based on the PY motif of TFAP2 reported to interact with KCTD1 (46) and synthesised by (LifeTein). Biotin-TFAP2 peptides were immobilised onto four superstreptavidin-coated sensors (one for each KCTD15 and KCTD1 construct) to saturation of the sensor. An additional four “free” reference sensors were used and did not harbour immobilised peptide. Proteins were prepared in buffer containing 100 mM NaCl, 25 mM HEPES pH 7.5, 0.05% (v/v) Tween-20 and titrated in 1:2 dilutions from 10 µM down to 100 nM (7 data points plus one “blank” of no protein). Each peptide sensor was sequentially dipped into its respective protein from low to high concentrations (baseline in buffer 60 sec, association in protein 240 sec, dissociation in buffer 240 sec). Data were analysed using the FortéBio Data Analysis software (version 9.0).

2.19 References

1. Lu J, Doyle AD, Shinsato Y, Wang S, Bodendorfer MA, Zheng M, Yamada KM. Basement Membrane Regulates Fibronectin Organization Using Sliding Focal Adhesions Driven by a Contractile Winch. Dev Cell. 2020 Mar 9;52(5):631-646.e4. doi: 10.1016/j.devcel.2020.01.007. Epub 2020 Jan 30. PMID: 32004443; PMCID: PMC8335633.

2. Doyle AD, Sykora DJ, Pacheco GG, Kutys ML, Yamada KM. 3D mesenchymal cell migration is driven by anterior cellular contraction that generates an extracellular matrix prestrain. Dev Cell. 2021 Mar 22;56(6):826-841.e4. doi: 10.1016/j.devcel.2021.02.017. Epub 2021 Mar 10. PMID: 33705692; PMCID: PMC8082573.
3. Chandrakasan G, Torchia DA, Piez KA. Preparation of intact monomeric collagen from rat tail tendon and skin and the structure of the nonhelical ends in solution. J Biol Chem. 1976 Oct 10;251(19):6062-7. PMID: 972153.
4. Doyle AD. Generation of 3D Collagen Gels with Controlled Diverse Architectures. Curr Protoc Cell Biol. 2016 Sep 1;72:10.20.1-10.20.16. doi: 10.1002/cpcb.9. PMID: 27580704; PMCID: PMC5030718.
5. Antal C, Teletin M, Wendling O, Dgheem M, Auwerx J, Mark M. Tissue collection for systematic phenotyping in the mouse. Curr Protoc Mol Biol. 2007 Oct;Chapter 29:Unit 29A.4. doi: 10.1002/0471142727.mb29a04s80. PMID: 18265401.
6. Vincze T, Posfai J, Roberts RJ. NEBcutter: A program to cleave DNA with restriction enzymes. Nucleic Acids Res. 2003 Jul 1;31(13):3688-91. doi: 10.1093/nar/gkg526. PMID: 12824395; PMCID: PMC168933.
7. Korbie DJ, Mattick JS. Touchdown PCR for increased specificity and sensitivity in PCR amplification. Nat Protoc. 2008;3(9):1452-6. doi: 10.1038/nprot.2008.133. PMID: 18772872.
8. Rosano GL, Ceccarelli EA. Recombinant protein expression in Escherichia coli: advances and challenges. Front Microbiol. 2014 Apr 17;5:172. doi: 10.3389/fmicb.2014.00172. PMID: 24860555; PMCID: PMC4029002.
9. Hong P, Koza S, Bouvier ES. Size-Exclusion Chromatography for the Analysis of Protein Biotherapeutics and their Aggregates. J Liq Chromatogr Relat Technol. 2012 Nov;35(20):2923-2950. doi: 10.1080/10826076.2012.743724. Epub 2012 Nov 30. PMID: 23378719; PMCID: PMC3556795.
10. Cummins PM, Rochfort KD, O'Connor BF. Ion-Exchange Chromatography: Basic Principles and Application. Methods Mol Biol. 2017;1485:209-223. doi: 10.1007/978-1-4939-6412-3_11. PMID: 27730555.
11. Wilkins MR, Gasteiger E, Bairoch A, Sanchez JC, Williams KL, Appel RD, Hochstrasser DF. Protein identification and analysis tools in the ExPASy server. Methods Mol Biol. 1999;112:531-52. doi: 10.1385/1-59259-584-7:531. PMID: 10027275.
12. Mahmood T, Yang PC. Western blot: technique, theory, and trouble shooting. N Am J Med Sci. 2012 Sep;4(9):429-34. doi: 10.4103/1947-2714.100998. PMID: 23050259; PMCID: PMC3456489.
13. Cruz Walma DA, Collins JW. Western Blotting with Solutions containing Nanoliter Volumes of Antibody. Curr Protoc Cell Biol. 2019 Sep;84(1):e87. doi: 10.1002/cpcb.87. PMID: 31483112; PMCID: PMC6727981.
14. Lin JS, Lai EM. Protein-Protein Interactions: Co-Immunoprecipitation. Methods Mol Biol. 2017;1615:211-219. doi: 10.1007/978-1-4939-7033-9_17. PMID: 28667615.

15. Some D, Amartely H, Tsadok A, Lebendiker M. Characterization of Proteins by Size-Exclusion Chromatography Coupled to Multi-Angle Light Scattering (SEC-MALS). J Vis Exp. 2019 Jun 20;(148). doi: 10.3791/59615. PMID: 31282880.
16. Gao K, Oerlemans R, Groves MR. Theory and applications of differential scanning fluorimetry in early-stage drug discovery. Biophys Rev. 2020 Feb;12(1):85-104. doi: 10.1007/s12551-020-00619-2. Epub 2020 Jan 31. PMID: 32006251; PMCID: PMC7040159.
17. Niesen FH, Berglund H, Vedadi M. The use of differential scanning fluorimetry to detect ligand interactions that promote protein stability. Nat Protoc. 2007;2(9):2212-21. doi: 10.1038/nprot.2007.321. PMID: 17853878.
18. McPherson A, Gavira JA. Introduction to protein crystallization. Acta Crystallogr F Struct Biol Commun. 2014 Jan;70(Pt 1):2-20. doi: 10.1107/S2053230X13033141. Epub 2013 Dec 24. PMID: 24419610; PMCID: PMC3943105.
19. Ng JT, Dekker C, Reardon P, von Delft F. Lessons from ten years of crystallization experiments at the SGC. Acta Crystallogr D Struct Biol. 2016 Feb;72(Pt 2):224-35. doi: 10.1107/S2059798315024687. Epub 2016 Jan 22. PMID: 26894670; PMCID: PMC4756611.
20. Winter G, Lobley CM, Prince SM. Decision making in xia2. Acta Crystallogr D Biol Crystallogr. 2013 Jul;69(Pt 7):1260-73. doi: 10.1107/S0907444913015308. Epub 2013 Jun 18. PMID: 23793152; PMCID: PMC3689529.
21. Winter G, Waterman DG, Parkhurst JM, Brewster AS, Gildea RJ, Gerstel M, Fuentes-Montero L, Vollmar M, Michels-Clark T, Young ID, Sauter NK, Evans G. DIALS: implementation and evaluation of a new integration package. Acta Crystallogr D Struct Biol. 2018 Feb 1;74(Pt 2):85-97. doi: 10.1107/S2059798317017235. Epub 2018 Feb 1. PMID: 29533234; PMCID: PMC5947772.
22. Tickle IJ, Flensburg C, Keller P, et al. STARANISO (http://staraniso.globalphasing.org/cgi-bin/staraniso.cgi). Global Phasing Ltd; Cambridge, United Kingdom 2018
23. Keegan RM, Winn MD. Automated search-model discovery and preparation for structure solution by molecular replacement. Acta Crystallogr D Biol Crystallogr. 2007 Apr;63(Pt 4):447-57. doi: 10.1107/S0907444907002661. Epub 2007 Mar 16. PMID: 17372348.
24. McCoy AJ, Grosse-Kunstleve RW, Adams PD, Winn MD, Storoni LC, Read RJ. Phaser crystallographic software. J Appl Crystallogr. 2007 Aug 1;40(Pt 4):658-674. doi: 10.1107/S0021889807021206. Epub 2007 Jul 13. PMID: 19461840; PMCID: PMC2483472.
25. Liebschner D, Afonine PV, Baker ML, Bunkóczi G, Chen VB, Croll TI, Hintze B, Hung LW, Jain S, McCoy AJ, Moriarty NW, Oeffner RD, Poon BK, Prisant MG, Read RJ, Richardson JS, Richardson DC, Sammito MD, Sobolev OV, Stockwell DH, Terwilliger TC, Urzhumtsev AG, Videau LL, Williams CJ, Adams PD. Macromolecular structure determination using X-rays, neutrons and electrons: recent developments in Phenix. Acta Crystallogr D Struct Biol.

2019 Oct 1;75(Pt 10):861-877. doi: 10.1107/S2059798319011471. Epub 2019 Oct 2. PMID: 31588918; PMCID: PMC6778852.
26. Emsley P, Cowtan K. Coot: model-building tools for molecular graphics. Acta Crystallogr D Biol Crystallogr. 2004 Dec;60(Pt 12 Pt 1):2126-32. doi: 10.1107/S0907444904019158. Epub 2004 Nov 26. PMID: 15572765.
27. Chen VB, Arendall WB 3rd, Headd JJ, Keedy DA, Immormino RM, Kapral GJ, Murray LW, Richardson JS, Richardson DC. MolProbity: all-atom structure validation for macromolecular crystallography. Acta Crystallogr D Biol Crystallogr. 2010 Jan;66(Pt 1):12-21. doi: 10.1107/S0907444909042073. Epub 2009 Dec 21. PMID: 20057044; PMCID: PMC2803126.
28. Schrödinger L, DeLano W. PyMOL, Available at: http://www.pymol.org/pymol. 2020
29. Akdel M, Pires DEV, Pardo EP, Jänes J, Zalevsky AO, Mészáros B, Bryant P, Good LL, Laskowski RA, Pozzati G, Shenoy A, Zhu W, Kundrotas P, Serra VR, Rodrigues CHM, Dunham AS, Burke D, Borkakoti N, Velankar S, Frost A, Basquin J, Lindorff-Larsen K, Bateman A, Kajava AV, Valencia A, Ovchinnikov S, Durairaj J, Ascher DB, Thornton JM, Davey NE, Stein A, Elofsson A, Croll TI, Beltrao P. A structural biology community assessment of AlphaFold2 applications. Nat Struct Mol Biol. 2022 Nov;29(11):1056-1067. doi: 10.1038/s41594-022-00849-w. Epub 2022 Nov 7. PMID: 36344848; PMCID: PMC9663297.
30. Jumper J, Evans R, Pritzel A, Green T, Figurnov M, Ronneberger O, Tunyasuvunakool K, Bates R, Žídek A, Potapenko A, Bridgland A, Meyer C, Kohl SAA, Ballard AJ, Cowie A, Romera-Paredes B, Nikolov S, Jain R, Adler J, Back T, Petersen S, Reiman D, Clancy E, Zielinski M, Steinegger M, Pacholska M, Berghammer T, Bodenstein S, Silver D, Vinyals O, Senior AW, Kavukcuoglu K, Kohli P, Hassabis D. Highly accurate protein structure prediction with AlphaFold. Nature. 2021 Aug;596(7873):583-589. doi: 10.1038/s41586-021-03819-2. Epub 2021 Jul 15. PMID: 34265844; PMCID: PMC8371605.
31. Donnelly DP, Rawlins CM, DeHart CJ, Fornelli L, Schachner LF, Lin Z, Lippens JL, Aluri KC, Sarin R, Chen B, Lantz C, Jung W, Johnson KR, Koller A, Wolff JJ, Campuzano IDG, Auclair JR, Ivanov AR, Whitelegge JP, Paša-Tolić L, Chamot-Rooke J, Danis PO, Smith LM, Tsybin YO, Loo JA, Ge Y, Kelleher NL, Agar JN. Best practices and benchmarks for intact protein analysis for top-down mass spectrometry. Nat Methods. 2019 Jul;16(7):587-594. doi: 10.1038/s41592-019-0457-0. Epub 2019 Jun 27. PMID: 31249407; PMCID: PMC6719561.
32. Tamara S, den Boer MA, Heck AJR. High-Resolution Native Mass Spectrometry. Chem Rev. 2022 Apr 27;122(8):7269-7326. doi: 10.1021/acs.chemrev.1c00212. Epub 2021 Aug 20. PMID: 34415162; PMCID: PMC9052423.
33. Testa L, Brocca S, Grandori R. Charge-surface correlation in electrospray ionization of folded and unfolded proteins. Anal Chem. 2011 Sep 1;83(17):6459-63. doi: 10.1021/ac201740z. Epub 2011 Aug 5. PMID: 21800882.

34. Sharma K, D'Souza RC, Tyanova S, Schaab C, Wiśniewski JR, Cox J, Mann M. Ultradeep human phosphoproteome reveals a distinct regulatory nature of Tyr and Ser/Thr-based signaling. Cell Rep. 2014 Sep 11;8(5):1583-94. doi: 10.1016/j.celrep.2014.07.036. Epub 2014 Aug 21. PMID: 25159151.
35. Humphrey SJ, Azimifar SB, Mann M. High-throughput phosphoproteomics reveals in vivo insulin signaling dynamics. Nat Biotechnol. 2015 Sep;33(9):990-5. doi: 10.1038/nbt.3327. Epub 2015 Aug 17. PMID: 26280412.
36. Humphrey SJ, Karayel O, James DE, Mann M. High-throughput and high-sensitivity phosphoproteomics with the EasyPhos platform. Nat Protoc. 2018 Sep;13(9):1897-1916. doi: 10.1038/s41596-018-0014-9. PMID: 30190555.
37. Thingholm TE, Jørgensen TJ, Jensen ON, Larsen MR. Highly selective enrichment of phosphorylated peptides using titanium dioxide. Nat Protoc. 2006;1(4):1929-35. doi: 10.1038/nprot.2006.185. PMID: 17487178.
38. Swaney DL, Villén J. Enrichment of Phosphopeptides via Immobilized Metal Affinity Chromatography. Cold Spring Harb Protoc. 2016 Mar 1;2016(3):pdb.prot088005. doi: 10.1101/pdb.prot088005. PMID: 26933247.
39. Cole JL, Lary JW, P Moody T, Laue TM. Analytical ultracentrifugation: sedimentation velocity and sedimentation equilibrium. Methods Cell Biol. 2008;84:143-79. doi: 10.1016/S0091-679X(07)84006-4. PMID: 17964931; PMCID: PMC2711687.
40. Stafford W. Analytical ultracentrifugation: sedimentation velocity analysis. Curr Protoc Protein Sci. 2003 May;Chapter 20:Unit 20.7. doi: 10.1002/0471140864.ps2007s31. PMID: 18429240.
41. Cole JL, Lary JW, P Moody T, Laue TM. Analytical ultracentrifugation: sedimentation velocity and sedimentation equilibrium. Methods Cell Biol. 2008;84:143-79. doi: 10.1016/S0091-679X(07)84006-4. PMID: 17964931; PMCID: PMC2711687.
42. Harding SE, Gillis RB, Adams GG. Assessing sedimentation equilibrium profiles in analytical ultracentrifugation experiments on macromolecules: from simple average molecular weight analysis to molecular weight distribution and interaction analysis. Biophys Rev. 2016;8(4):299-308. doi: 10.1007/s12551-016-0232-8. Epub 2016 Nov 22. PMID: 28003857; PMCID: PMC5135724.
43. Philo JS. SEDNTERP: a calculation and database utility to aid interpretation of analytical ultracentrifugation and light scattering data. Eur Biophys J. 2023 Jul;52(4-5):233-266. doi: 10.1007/s00249-023-01629-0. Epub 2023 Feb 15. PMID: 36792822.
44. Zhao H, Brautigam CA, Ghirlando R, Schuck P. Overview of current methods in sedimentation velocity and sedimentation equilibrium analytical ultracentrifugation. Curr Protoc Protein Sci. 2013 Feb;Chapter 20:Unit20.12. doi: 10.1002/0471140864.ps2012s71. PMID: 23377850; PMCID: PMC3652391.
45. Shah NB, Duncan TM. Bio-layer interferometry for measuring kinetics of protein-protein interactions and allosteric ligand effects. J Vis Exp. 2014 Feb

18;(84):e51383. doi: 10.3791/51383. PMID: 24638157; PMCID: PMC4089413.
46. Hu L, Chen L, Yang L, Ye Z, Huang W, Li X, Liu Q, Qiu J, Ding X. KCTD1 mutants in scalp-ear-nipple syndrome and AP-2α P59A in Char syndrome reciprocally abrogate their interactions, but can regulate Wnt/β-catenin signaling. Mol Med Rep. 2020 Nov;22(5):3895-3903. doi: 10.3892/mmr.2020.11457. Epub 2020 Aug 24. PMID: 33000225; PMCID: PMC7533495

CHAPTER THREE

Characterising the morphogenic role of BTBD7 using 3D *in vitro* culture models

3.1 INTRODUCTION

As one of the twenty "BTBD" family members, BTBD7 has been reported to be a critical regulator of cell dynamics, organogenesis, and tumour metastasis (1-3). Other proteins containing the BTB domain serve various biological roles including transcriptional regulators (exemplified by PLZF and BCL6 [4-6], cellular stress sensors (seen with KEAP1 [7]), and substrate adaptors to Cullin RING ubiquitin ligases (exemplified by KEAP1 and SPOP [8, 9]). The BTBD, KCTD, and BTB-Kelch families are three major classes of BTB E3 ligases with the potential to be exploited for targeted protein degradation in disease/disorder (10). BTBD7 is hypothesized to serve as a regulator of branching morphogenesis in several organ systems (3, 11). BTBD7's mechanism of biologic function and biophysical characteristics are unknown. Reports suggest BTBD7 regulates intracellular E-cadherin levels to control branching in salivary gland morphogenesis and the epithelial-to-mesenchymal cellular transition (EMT) in cancer (2, 11-13). Several signalling pathways (e.g., growth factor and ubiquitin signalling) regulate salivary gland morphogenesis (14) and EMT (15).

I began my DPhil studies with the central hypothesis that BTBD7 drives tissue morphogenesis through currently unknown mechanisms that require elucidation. Accordingly, my overriding project aim was to critically evaluate the molecular mechanisms of BTBD7's role in tissue morphogenesis using *in vitro* cell and 3D cultures, targeted biophysical assays, and *in silico* modelling. The first key aim for my project thesis was to elucidate the morphogenic role of BTBD7 using 3D culture models. Prior to beginning my studies, there was a lack of accurate commercially available antibodies specific to BTBD7. Accordingly, I produced polyclonal and monoclonal antibodies to BTBD7. Due to BTBD7's reported involvement in salivary gland development, I used two salivary gland cell lines to create novel 3D *in vitro* culture systems to characterise BTBD7's biological mechanisms of function. To verify the reported *in vivo* phenotype associated with BTBD7 knockout, I performed several gross anatomical investigations using BTBD7 wild-type and knockout mice. Using 2D and novel 3D *in vitro* culture systems, several microscopy imaging techniques, and a variety of proteomic assays, the results of this chapter reveal BTBD7 may play a role in cell proliferation/degradation through the ubiquitin-proteasome pathway. These results support my initial hypothesis that BTBD7 drives tissue morphogenesis. However, the data reported herein does not confirm the result of prior studies that claim BTBD7s biological role involves regulating cell-cell and cell-matrix interactions. During my first year of studies, I helped disprove the reported *in vivo* roles of BTBD7's BTB domains. Due to this lack of *in vivo* phenotype associated with the BTB domains of BTBD7 and because proteomics analyses are more powerful with counter screens to assess selectivity, the subsequent chapters of

my thesis expanded the planned characterisation of BTBD7 to include the investigation of several additional BTB domain-containing proteins.

3.2 RESULTS

3.2.1 New polyclonal and monoclonal antibodies to BTBD7 are applicable for western blot assays

Antibodies specific to BTBD7 are not commercially available. Custom rabbit polyclonal and mouse monoclonal antibodies were produced with the assistance of Covance and Genscript, respectively. Covance was provided with purified BTBD7 protein for rabbit immunizations. This GST-tagged protein was produced, cleaved, and purified by a technician in our group at the NIH. The peptide antigen *CSPSKPDFLYKKSAL* was designed based on BTBD7 amino acids 1119-1132 with Genscript for mouse immunisations. Western blot and immunofluorescence screens of animal sera and hybridoma supernatants were performed with immortalized mouse submandibular salivary gland cells expressing (SIMS WT) or not expressing BTBD7 via CRISPR-mediated knockout (SIMS BTBD7 KO) to test antibody specificity. The construct used to generate the SIMS BTBD7 KO cell line is reported in Daley et al. (16). It is important to note this construct deleted exons 3 and 4 of BTBD7, but re-initiation of translation at an internal start site producing a truncated form of BTBD7 (represented by a 68 kDa band in the in western blots of SIMS KO cells with the produced BTBD7 antibodies Figure 3.1A) could not be ruled out. The rabbit anti-human BTBD7 polyclonal antibody (rabbit 7745) finished production prior to the monoclonal antibody and was used as a positive control to select mouse B cells for hybridoma production (Figure. 3.1A). To maximise the number of western

blots screens performed with the 15 µL sample mouse anti-serum, I developed a novel micro-western blotting technique. Details of the technique are described in Cruz Walma et al., 2019. In brief, after subjecting isolated proteins to gel electrophoresis and transferring the gel to a PVDF or nitrocellulose membrane, membranes were sectioned and incubated with minimal volumes of primary and secondary antibody solutions (with intervening blocking and washing steps) in custom miniature incubation chambers that prevented the membranes from drying out and maximised the antibody solution-membrane contact area (17).

Upon request, Genscript provided the original mixed hybridoma populations. After receiving these heterogeneous cell populations, I no longer interacted with the company and produced clonal hybridoma populations as well as concentrated, purified, and characterised the secreted monoclonal antibodies. After culturing hybridomas in multiple bioreactor systems (e.g., CELLine Classic and FiberCell Systems) and testing several purification methods (e.g., protein A vs. G beads, various buffers and pHs, etc.), the optimal purification parameters were found to be protein A purification eluting with 0.1M glycine-HCl at a pH of 4.5 (Figure 3.1B).

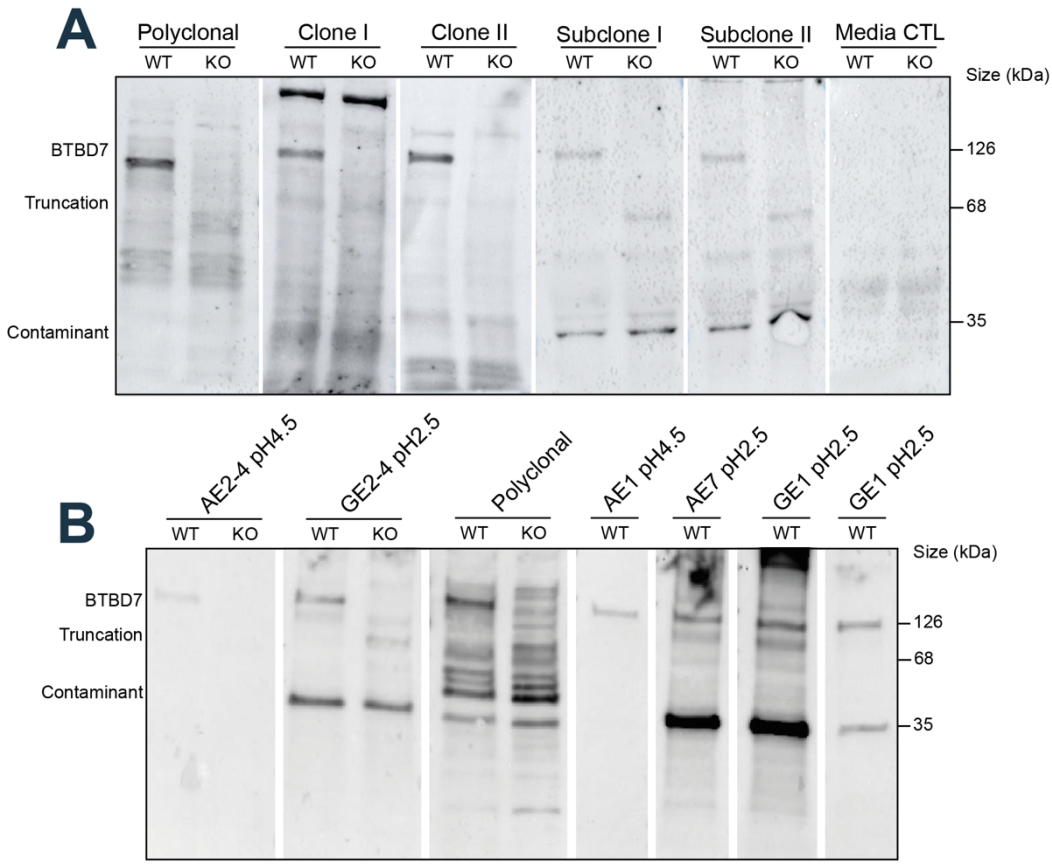


Figure 3.1 Mouse monoclonal antibodies specific to BTBD7 are applicable for western blot assays. (A) SIMS wild-type and BTBD7 knockout cell lysates were used to screen hybridoma clone and subclone supernatants. Initial subclone supernatants provided by Genscript were non-specific to BTBD7 and tagged an approximately 35 kDa contaminant protein. SIMS BTBD7 knockout cells expressed a potentially truncated BTBD7 variant that migrated at around 68 kDa on SDS-PAGE gels. (B) Mouse IgG2a antibodies specific to BTBD7 were produced using protein A agarose purification eluting with 0.1M glycine-HCl at a pH of 4.5. Protein A versus G agarose purifications are denoted by “A” or “G”. Elutions are denoted by “EX” with “X” being the elution number. For example, “AE1 pH4.5” signifies protein A agarose purification eluting once with 0.1M glycine-HCl at a pH of 4.5.

3.2.2 Novel 3D cultures as tools to characterise the 3D *in vitro* biologic function of target proteins

Various cell lines and culture methods were tested for their use in characterising BTBD7’s biologic function. Several cell lines (e.g., A549, MDA-MB-231,

HEK293T) and culture methods were ruled out due to slow proliferation rate, low lentiviral transduction rate, or lack of useful *in vitro* cell culture phenotypes.

In collaboration with the Simon Tran lab, I characterised the newly created human submandibular salivary gland cell line (SMG-HU1). With the only human salivary gland cell line (HSG) reported to be contaminated by HeLa cells (18), this new line has potential as a useful salivary gland biology tool. Although the SMG-HU1 cell's migratory phenotype in 3D cultures may prove useful for characterising salivary gland cell migration and ECM interactions (Figure 3.2) their slow proliferation rate made them non-ideal for characterising BTBD7's biologic function in this project.

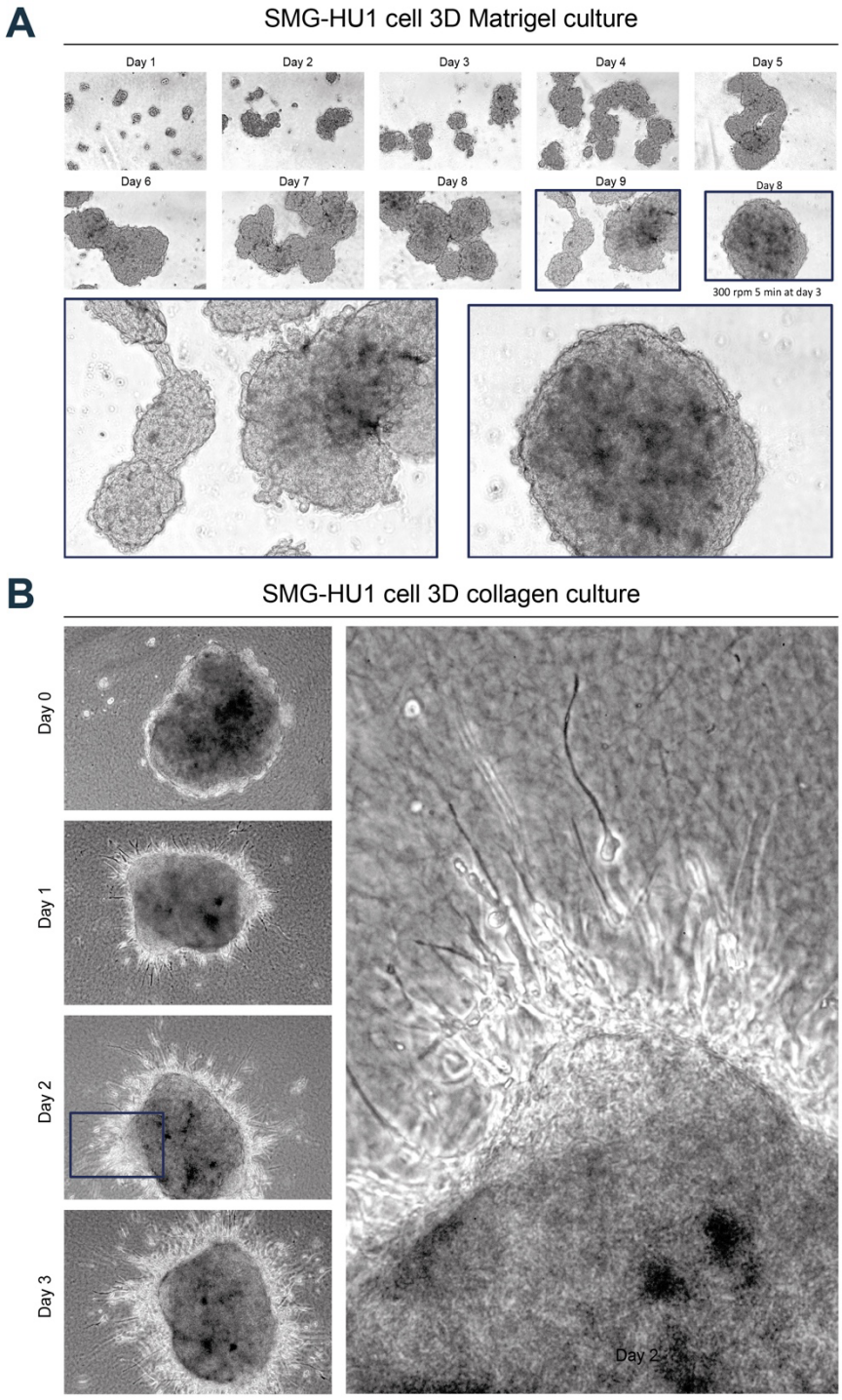


Figure 3.2 SMG-HU1 cells exhibited interesting 3D culture phenotypes useful for characterising salivary gland cell migration. (A) SMG-HU1 cells cultured for nine days in 0.45 mg/mL Matrigel matrices aggregated into spheroids of varying shapes and can be centrifuged early in the culture timeline to form more discrete spheroids. (B) SMG-HU1 spheroids can be embedded in 2 mg/mL collagen matrices after eight days of culture in Matrigel. After one day of culture in collagen matrices, SMG-HU1 cells displayed a migrating leader-follower strategy of collective cell migration.

Given the drawbacks of the human-derived cell lines alongside our initial successes with the mouse-derived SIMS cell line, I characterised SIMS cell behaviour in 3D *in vitro* cell cultures. With a rapid proliferation rate, SIMS WT cells cultured in a 0.45 mg/mL 3D extracellular matrix extract (Matrigel) solution aggregated into spheroids in less than 48 hours. These spheroids can either be left to culture in Matrigel or isolated and embedded in a collagen matrix (Figure 3.3). SIMS WT cells formed an intricate tubular network over a period of 7 days in a 2 mg/mL collagen matrix polymerised at 22ºC (Figures 3.3A,B). The proteome of cells cultured in these *in vivo*-mimicking conditions was characterised with immunofluorescence confocal microscopy (Figure 3.3C) and other methods.

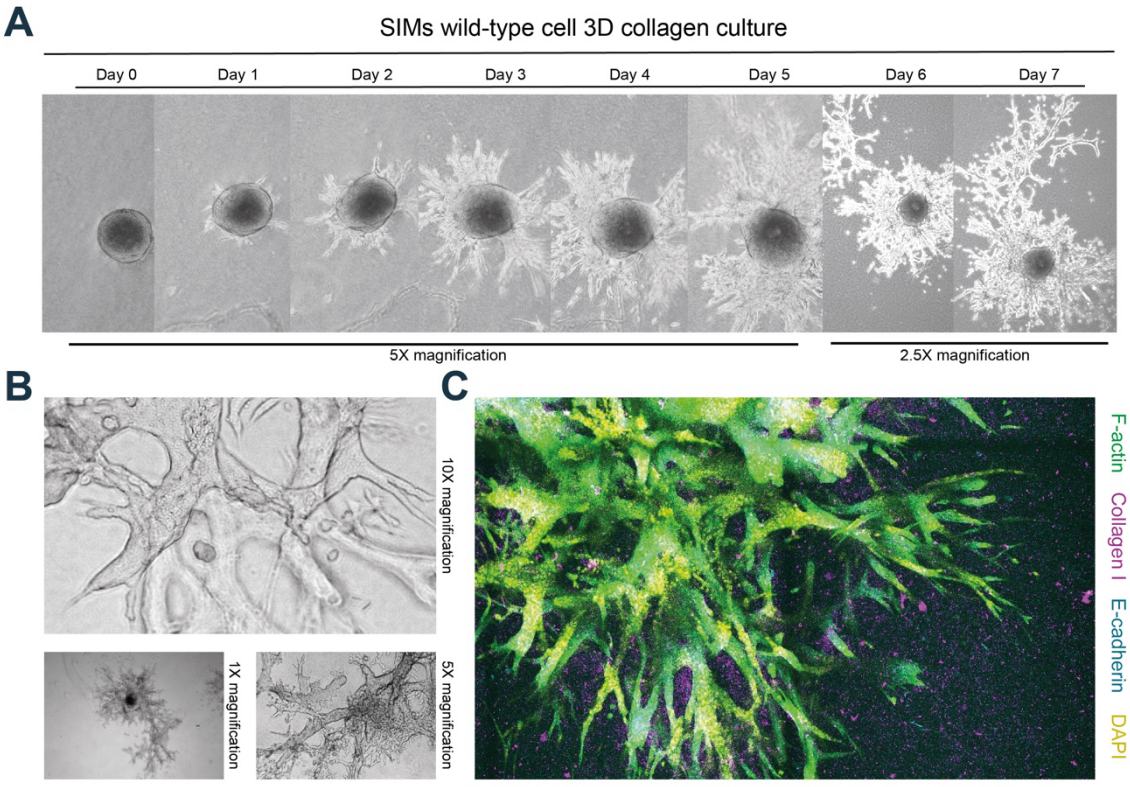


Figure 3.3 3D collagen matrix cultures of mouse submandibular salivary gland cells are useful *in vitro* tools to investigate protein function. (A,B) SIMS wild-type cell spheroids cultured for seven days in a 2 mg/mL collagen

matrix polymerised at 22°C formed an intricate tubular network. (C) Confocal microscopy immunostaining for the cytoskeletal marker F-actin and the adherens junction protein E-cadherin highlighted the intricate 3D tubular network formed by SIMS wild-type cells. F-actin is depicted in green, E-cadherin in turquoise, Collagen I in magenta, and DAPI (representing nuclei) in yellow.

3.2.3 BTBD7 exhibited a diffuse cytoplasmic distribution and did not co-localise to adherens junctions, endoplasmic reticula, endosomes, nor proteasomes in 2D

A SIMS cell line expressing fluorescently tagged BTBD7 was used to determine BTBD7's intracellular localisation (Figure 3.4). BTBD7 labelled with the green fluorescent marker "mNeonGreen" exhibited a diffuse cytoplasmic distribution and did not co-localise with the endoplasmic reticulum (PDI), early endosome (EEA1), nor proteasome (Figure 3.4).

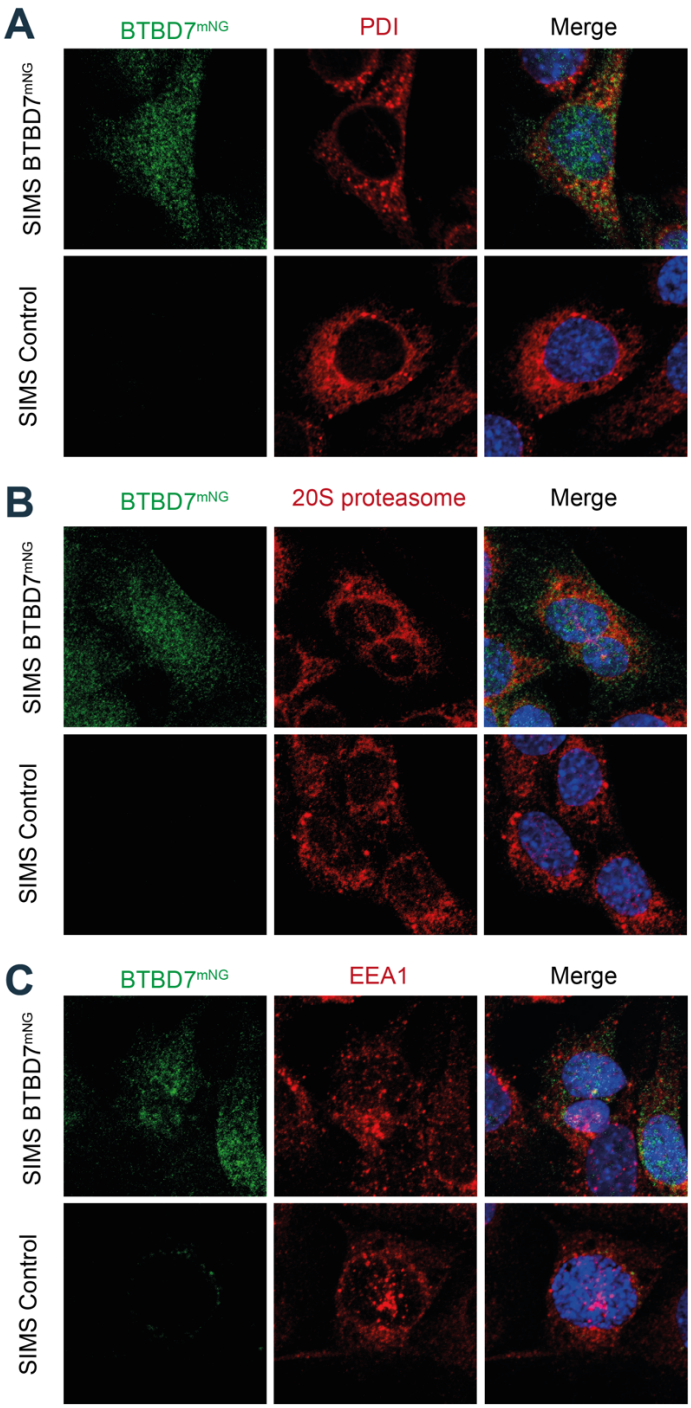


Figure 3.4 In SIMS cells, fluorescently tagged BTBD7 was diffusely cytoplasmic and did not co-localise with target organelles in 2D. (A-C) BTBD7mNG ("mNeonGreen") did not co-localise to the endoplasmic reticulum (PDI; A), proteasome (20S proteasome; B), or early endosome (EEA1; C) in 2D cultures. BTBD7 fluoresced green, each labelled organelle fluoresced red, and DAPI (representing the nuclei) fluoresced blue.

With prior reports suggesting BTBD7 regulates cell-cell and cell-ECM dynamics (1-3), cytoskeletal and adherens junction variations associated with BTBD7 expression were characterised in 2D and 3D cultures (Figure 3.5). On 2D glass or Matrigel coated surfaces, BTBD7 did not co-localise to adherens junctions in SIMS BTBD7^{mNeonGreen} cells (Figure 3.5A). On these same surfaces, both SIMS WT and BTBD7 KO cells showed similar expression patterns of E-cadherin and F-actin (Figure 3.5B).

3.2.4 BTBD7 knockout 3D cultures formed less organised, smaller, and more numerous protrusions compared to wild-type cultures

Although no unique BTBD7-associated phenotype was observed in 2D cell cultures, I characterised BTBD7's function in 3D *in vitro* cultures since 3D systems provide a more biologically relevant cellular environment. Compared to SIMS WT, SIMS BTBD7 KO cells in collagen matrices formed less-organised, smaller, and more numerous protrusions. Immunofluorescence imaging of the 3D cultures depicted an increased staining intensity of F-actin and E-cadherin in BTBD7 knockout cells (Figure 3.5C). Using DAPI to stain cell nuclei, 3D cultures of SIMS BTBD7 KO cells appeared to contain a greater number of cells than SIMS WT cultures (Fig. 3.5C). These results suggested BTBD7 may be responsible for the observed altered cell protrusions, although this phenotype may be due to altered cell abundance, not necessarily altered cytoskeletal dynamics.

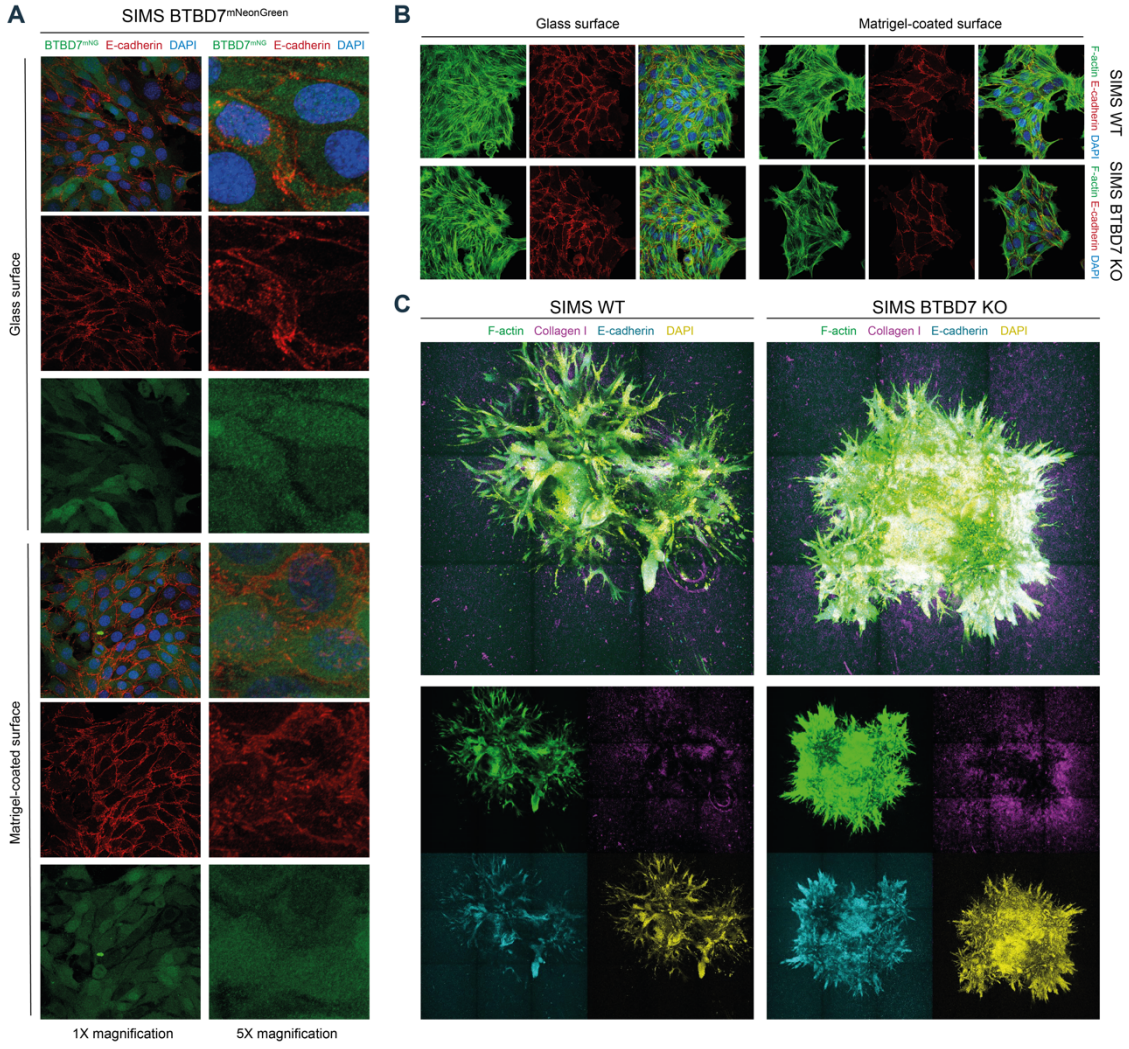


Figure 3.5 SIMS BTBD7 knockout 3D cell cultures exhibited altered tubular networks compared to wild-type cell cultures, though no significant differences in cytoskeletal and adherens junction architectures were observed between knockout and wild-type cultures. (A) Fluorescently tagged BTBD7 (green) did not co-localise to adherens junctions (E-cadherin; red) on 2D glass or Matrigel surfaces. (B) The abundance and distribution of F-actin (green) and E-cadherin (red) were similar between BTBD7 wild-type and knockout cultures on 2D glass and Matrigel surfaces. (C) SIMS BTBD7 knockout cells cultured in 3D collagen matrices formed less organised tubular networks and exhibited a greater staining intensity of F-actin (green), E-cadherin (turquoise), and DAPI (yellow) compared to BTBD7 wild-type cultures. Collagen fibres are coloured magenta. Top panels depict a superimposition of all four stained components (F-actin, collagen, E-cadherin, and the nucleus [DAPI]). Bottom panels depict each component individually.

3.2.5 Ubiquitin signalling pathway inhibition exacerbated the BTBD7-associated 3D culture phenotype

With BTB proteins known to serve as CRL adaptor proteins and specific growth factors (e.g., FGF10 and HGF) known to regulate branching morphogenesis (19-22), I characterised the phenotypic variation between wild-type and BTBD7-knockout 3D cultures containing different concentrations of growth factors and inhibitors (Figure 3.6). When treated with the neddylation inhibitor MLN4924 and deneddylation inhibitor CSN5i-3, 3D cultures of SIMS wild-type cells showed minimal variations from DMSO and media controls (Figure 3.6). In comparison, SIMS BTBD7 knockout cells in the same conditions portrayed a significant difference in culture size and architecture versus controls, with knockout cells forming larger cultures with more numerous outgrowths of cells (Figure 3.6). In the presence of FGF10 and HGF, SIMS wild-type and BTBD7 knockout 3D cell cultures displayed a similar increase in cell abundance compared to BSA carrier and media controls (Figure 3.6). These results suggested BTBD7 may contribute to the observed phenotype through involvement of ubiquitin signalling.

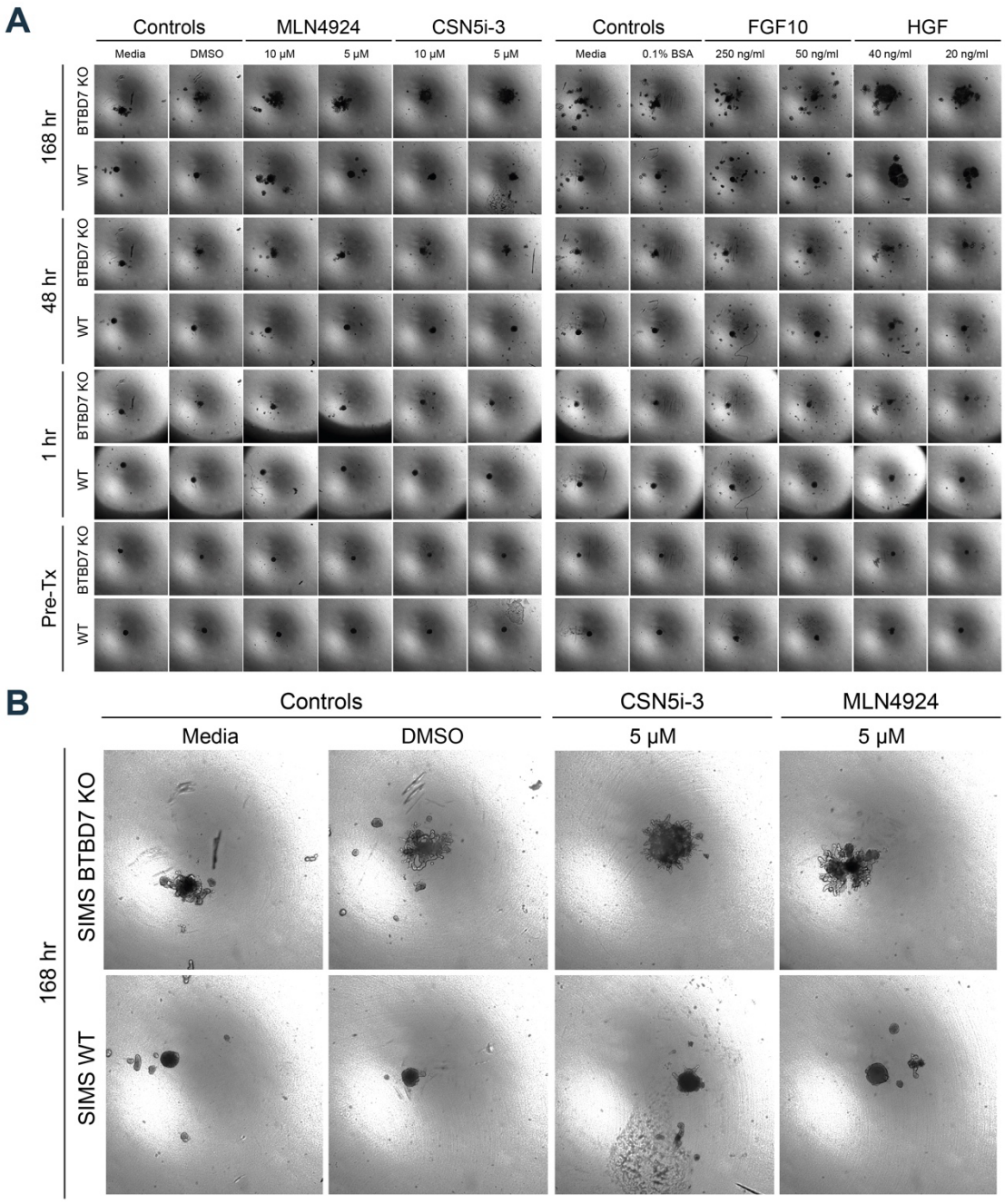


Figure 3.6 Inhibiting the ubiquitin signalling system selectively altered the 3D culture phenotype of SIMS BTBD7 knockout cultures compared to SIMS BTBD7 wild-type cultures. (A) SIMS BTBD7 wild-type and knockout 3D cell cultures supplemented with FGF10 and HGF showed similarly increased proliferation rates compared to controls over 168 hours. In contrast, SIMS BTBD7 knockout cells cultured with neddylation and de-neddylation inhibitors (MLN4924 and CSN5i-3) achieved significantly larger culture dimensions than SIMS wild-type cells over 168 hours. (B) Expanded images of SIMS wild-type and BTBD7 knockout 3D cultures after 168 hours supplemented with 5 μM CSN5i-3 and MLN4924 compared to controls. Assays were performed with greater than three replicates and the provided images are representative of each condition.

3.2.6 A preliminary large-scale proteomic investigation showed no significant differences between BTBD7 wild-type and knockout 3D culture proteomes

To characterise phosphoproteomic variations between SIMS wild-type and BTBD7 knockout cells in 3D cultures, a series of mass spectrometry experiments enriching for phosphorylated peptides was performed. Using two different enrichment methods, the total number of phosphorylated and non-phosphorylated proteins were similar between wild-type and BTBD7 knockout cultures (Figure 3.7). Analysing biologic processes and KEGG pathways, similar distributions of proteins across the reported pathways were observed in 3D cultures expressing and not expressing BTBD7 (Figure 3.7).

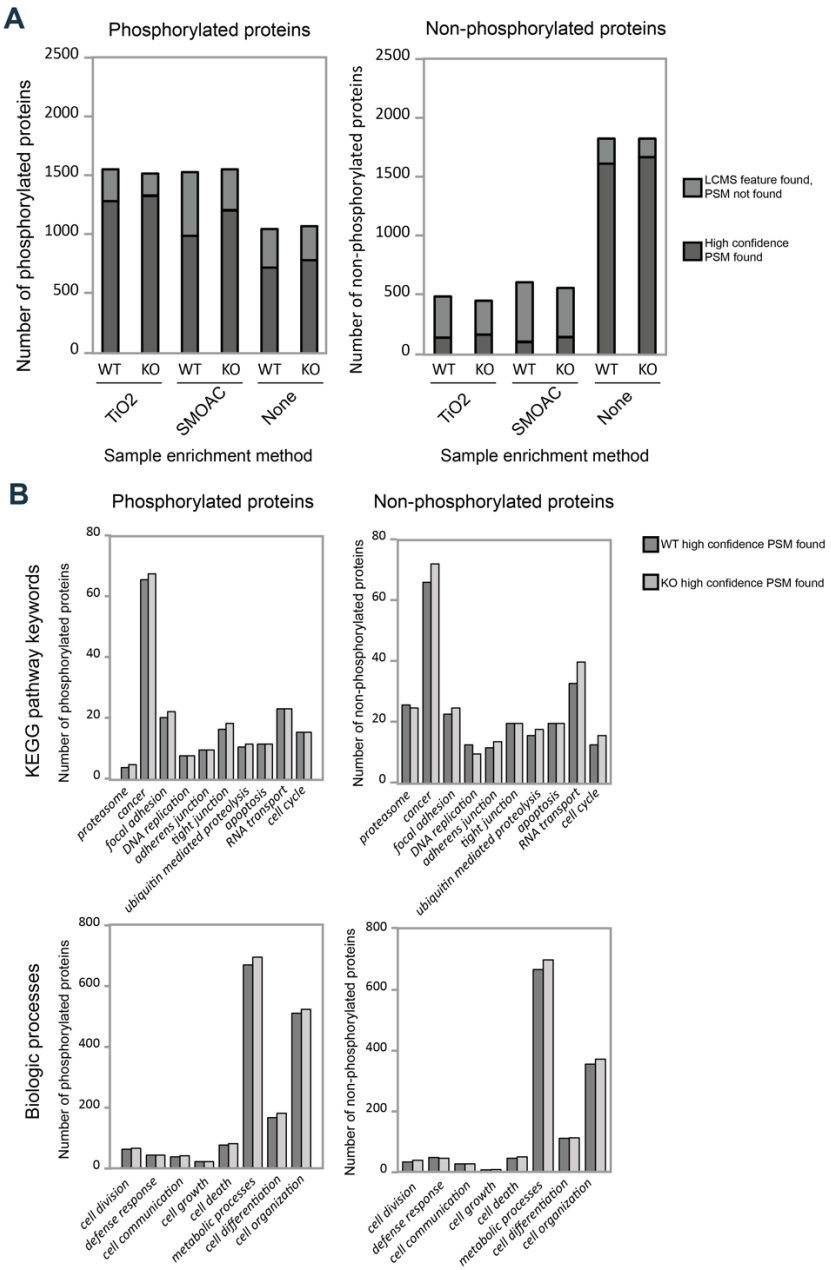


Figure 3.7 Preliminary mass spectrometry assays detected similar proteomic profiles between SIMS BTBD7 wild-type and knockout 3D cultures. (A) SIMS BTBD7 wild-type and knockout 3D cell cultures contained a similar number of non-phosphorylated and phosphorylated proteins when enriched for phosphorylated proteins using either TiO_2 containing columns (TiO_2) or Fe-NTA containing columns (SMOAC). (B) SIMS BTBD7 wild-type and knockout 3D cell cultures contained a similar number of proteins involved in the portrayed KEGG pathways and biologic processes. PSM denotes “peptide-spectrum match.” LCMS denotes “liquid chromatography mass spectrometry.”

3.2.7 Stable tetracycline-inducible BTBD7 expression cell lines were produced for BTBD7 rescue assays

To produce stable tetracycline-regulated BTBD7 expressing cell lines for BTBD7 rescue assays, I created two lentiviral vectors; one containing the BTBD7 coding sequence alone (pDCW102) and the other a BTBD7 coding sequence followed by a BFP fluorescence reporter sequence (pDCW101). After cloning the plasmids, preliminary transformations into *E. coli* failed – likely due to the large coding sequence insert (23). Upon modifying the transformation workflow (24), transformations were successful and Sanger sequencing results verified the plasmid sequence. After packaging and concentrating lentiviral particles, SIMS BTBD7 KO cells were infected with lentivirus. Following 6 days of puromycin selection, resistant cells were cryopreserved for future experiments. 3D culture rescue assays with these cells capable of tetracycline-regulated BTBD7 expression will help verify the observed 3D phenotype is due to BTBD7 expression and not clonal variation.

3.2.8 BTBD7 knockout mice grew to become healthy adults and showed no phenotypic difference compared to control mice

A litter of eight C57BL/6 BTBD7 homozygous and hemizygous BTBD7 knockout mutants were euthanized, genotyped, and dissected to determine phenotypic variations associated with BTBD7 expression. Of the litter, six mice were heterozygous BTBD7 knockouts (326-329, 331, and 333) and two mice were homozygous BTBD7 knockouts (330 and 332). Mice 326-328 were males, and 329-333 were females. All mice were healthy, showed no developmental abnormalities, and were of similar size upon euthanasia at the age of five months

(Figure 3.8). Such results suggested the *in vivo* BTBD7 knockout phenotype reported by Daley et al. in 2017 was incorrect and supported initial concerns in the laboratory that the conclusion was not correct (see discussion below).

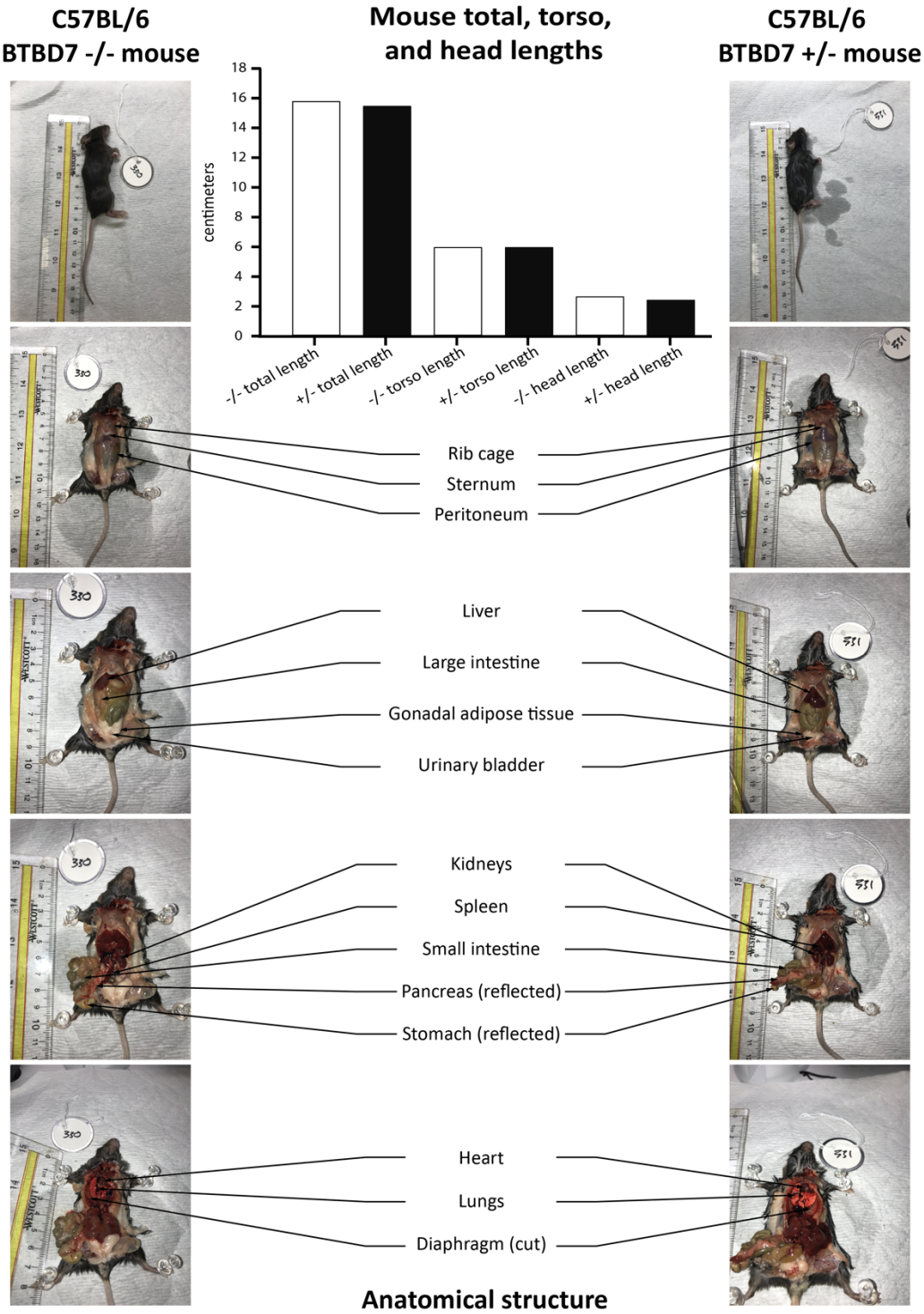


Figure 3.8 Knockout of the BTB domains of BTBD7 in C57BL/6 mice showed no phenotypic differences compared to wild-type C57BL/6 mice

and knockout mice grew to become healthy viable adult mice.
Representative anatomical dissections of the eight dissected homozygous (-/-) and hemizygous (+/-) BTBD7 knockout mice with major organs and tissues labelled. Average total, torso, and head lengths of the eight dissected homozygous (-/-) and hemizygous (+/-) BTBD7 knockout mice are shown in the top of the middle column of the figure. Six homozygous (-/-) and two hemizygous (+/-) BTBD7 knockout mice were examined with representative images shown. Only gross anatomical dissections were performed. Tissues were not stained to analyse select molecules.

3.3 DISCUSSION

Initially, this project sought to characterise the mechanism through which BTBD7 regulates branching morphogenesis (11). To achieve this goal, the project's first aim focused on developing *in vitro* cell and 3D culture models to characterise BTBD7's biologic function.

Antibodies specific to BTBD7 were essential tools to monitor BTBD7 in these cellular experiments. Accordingly, polyclonal and monoclonal antibodies targeting BTBD7 were generated. After verifying the IgG2a subtype of the monoclonal antibody, optimal protein A purification parameters were determined and are consistent with prior reports (25). Several cell lines were tested in a variety of 2D and 3D culture methods for applicability to study BTBD7's biologic function. The optimal cell lines would 1) be of human or mouse origin to facilitate reagent compatibility, 2) have a doubling rate of approximately 24-48 hours to facilitate experiment workflow, 3) express BTBD7, 4) have a high transduction and/or transfection rate, and 5) exhibit unique/interesting 2D or 3D phenotypes with which BTBD7 can be investigated. A549, MDA-MB-231, and HEK293T cells were ruled out mainly due to lack of an interesting 3D cell culture phenotype. SMG-HU1 cells showed promise as a new human salivary gland cell line with an

interesting 3D phenotype. However, due to slow proliferation rate, the SMG-HU1 cells were ill-suited for this project. Though not human in origin, SIMS cells doubled in approximately 24 hours, portrayed a unique and interesting phenotype in several 3D culture methods, were readily transduced with virus, and were easily transfected using cationic lipids. The SIMS cells were selected to characterise BTBD7's biologic function.

Though initially hypothesised to control cell-cell dynamics through ubiquitination and resulting degradation of E-cadherin (11), BTBD7 did not co-localise with E-cadherin and both E-cadherin and F-actin portrayed similar expression patterns in 2D SIMS cell cultures. In 3D SIMS cell cultures, BTBD7 knockout cultures showed an increased staining intensity of E-cadherin and F-actin, but the knockout cultures also proliferated more rapidly to contain greater numbers of cells at the time of imaging. Thus, it was unclear if the increased fluorescence of E-cadherin and F-actin was due to elevated expression levels or increased cellular abundance. Several endocytic pathways regulate E-cadherin turnover, the majority of which result in lysosomal degradation of E-cadherin (26). Labelled BTBD7 did not co-localise with E-cadherin nor any specific organelle and portrayed a diffuse cytoplasmic dispersion, suggesting BTBD7 may not play a direct role in E-cadherin degradation. Nevertheless, these results must be interpreted with the understanding that fluorescent tags may alter protein function and localization (27).

In 3D cultures, SIMS BTBD7 KO cells exhibited a unique phenotype compared to SIMS WT cells. In both 3D Matrigel and collagen matrices, SIMS BTBD7 KO

cultures achieved greater dimensions compared to WT. The increased staining intensity of E-cadherin, F-actin, and DAPI in BTBD7 KO collagen cultures may be due to increased cell number; potentially caused by differential cell division or cell death/apoptosis (28). A variety of signalling pathways regulate cell division and proliferation (e.g., ubiquitin-mediated control of cyclins and CDK inhibitors, growth factor signalling, etc. [28, 29]). Ubiquitin pathway inhibitors (MLN4924 and CSN5i-3) and growth factors known to regulate tubulogenesis and branching morphogenesis (FGF10 and HGF [19, 20]) were used in these 3D SIMS cell cultures. MLN4924 prevents cullin-RING E3 ligase (CRL) neddylation via inhibiting the activity of neddylation-activating enzymes (NAEs [21]). CSN5i-3 prevents CRL de-neddylation through inhibiting the activity of the COP9 signalosome (22). No significant variation in phenotype was observed between BTBD7 KO and WT cells when treated with growth factors. However, altering CRL activity through preventing NEDD8 binding and release resulted in further increased dimensions of BTBD7 KO cultures compared to control and WT. Inhibiting CRL activity diminishes ubiquitin-mediated proteolysis and results in the accumulation of numerous proteins (30). Many of these proteins are involved in cell proliferation, apoptosis, and cycle progression (31, 32). With CRL inhibition exerting a greater effect on BTBD7 KO cells, BTBD7 may play a role in a negative-feedback pathway to prevent excess accumulation of proteins involved in cell proliferation, apoptosis, and cycle progression (33, 34). A quantitative analysis of the collagen and Matrigel 3D cell cultures reported in this chapter could help provide a better representation of how BTBD7 knockout influences cell behaviour. General dimensions of Matrigel cultures alongside average heights, widths, lengths, and numbers of cellular protrusions in collagen

cultures could be measured and compared. Such analyses were planned to occur following BTBD7 rescue assays using the newly created cell lines. As described below, such rescue assays were unable to be performed due to time constraints exerted by the pandemic and the lack of an *in vivo* phenotype associated with BTBD7.

It is important to note the BTBD7 knockout and BTBD7 wild-type SIMS cell lines are monoclonal cell populations. As such, the observed variations in 3D *in vitro* phenotype may be due to clonal variability and not BTBD7 expression. Accordingly, I created stable SIMS BTBD7 KO cell lines endogenously expressing either BTBD7 alone or BTBD7 with a blue fluorescent reporter protein under tetracycline-inducible promoters to help determine if the observed 3D *in vitro* phenotypes of BTBD7 KO cell cultures are related to BTBD7 protein expression and not results of clonal variation in the SIMS cell line. Due to time constraints exerted by the pandemic and the lack of an *in vivo* phenotype associated with BTBD7, the various 3D culture assays reported herein were unable to be performed with these newly created cell lines.

Proteomic analysis of SIMS BTBD7 KO and WT 3D cell cultures showed no significant difference in the numbers of proteins associated with apoptosis, cell growth, cell cycle, ubiquitin, and proteasome pathways. These results may be due to lack of enrichment for the ubiquitin pathway during the proteomic experiment series (35, 36). To analyse the ubiquitin pathway using quantitative mass spectrometry, reagents such as 1,10 phenanthroline, MLN4924, CSN5i-3, and other deubiquitinase and neddylation/de-neddylation inhibitors should be

added to the buffers (35, 22). Due to time constraints with the pandemic and the lack of an *in vivo* phenotype associated with BTBD7, additional shotgun mass spectrometry experiments could not be performed to follow up on these preliminary results.

In 2017, Daley et al. initially reported BTBD7 as a critical regulator of salivary gland, lung, and kidney branching morphogenesis *in vivo* (11). Unfortunately, intensive inbreeding and backcrossing of the original mouse line exhibiting this phenotype revealed a loss of the phenotype. During the first year of my DPhil studies, a postdoc in the Yamada lab inbred and outcrossed the mouse model to cleanse the line of a closely linked passenger mutation and create the homozygous BTBD7 model with both BTB domains ablated (16). I performed a series of gross anatomy dissections with the re-created BTBD7 knockout model. Several litters of hemizygous and homozygous BTBD7 knockout mice grew to be viable healthy adult mice. Physical characterisation of the eight mice in a 5-month-old litter showed no significant difference in physical characteristics of hemizygous and homozygous BTBD7 knockout mice. Unfortunately, there were no wild-type mice in the litter. However, the dissected hemizygous and homozygous knockout mice portrayed no significant physical differences compared to wild-type C57BL/6 mice.

Experiments performed in this first chapter of my DPhil thesis sought to test the central hypothesis that BTBD7 drives tissue morphogenesis through unknown mechanisms requiring elucidation. In both 2D and 3D culture models, I explored BTBD7's biological function testing for variations in protein phosphorylation, cell-

cell and cell-matrix components, as well as ubiquitin signalling. The collected results suggest BTBD7 may play a role in tissue morphogenesis through regulating cell behaviours in 3D. Results suggest the ubiquitin signalling pathway may be involved, however, the precise molecular mechanisms of action remain to be determined due to the negative phosphoproteomics data, limitations mediated by the pandemic, and the change in project directions due to the concern that BTBD7's BTB domains were not involved in tissue development *in vivo*.

The initial aims of this project sought to characterise BTBD7 protein interactions that can be exploited to modify BTBD7s reported *in vivo* function regulating branching morphogenesis. Though results produced by the Yamada lab with small contributions from the data obtained for this first thesis chapter proved the initial *in vivo* phenotype associated with BTBD7's BTB domains is unfounded (16), BTBD7 may yet serve a critical biologic role. Accordingly, subsequent chapters do not focus exclusively on BTBD7, but the protein's function continued to be characterised in relation to several paralogues.

Due to domain similarity and critical biological roles, I selected several other BTB domain-containing proteins to investigate alongside BTBD7. The biophysical properties of select proteins and their interactions were characterised in parallel to BTBD7 to understand common and distinct mechanisms in different BTB protein subfamilies. In chapter four, I characterise the structural and biophysical importance of the tandem BTB domain and expand my studies to include RHOBTB1 and LZTR1, two proteins which, similar to BTBD7, harbour two

consecutive BTB domains. The central hypothesis, aims, and results of this work are provided in the subsequent chapter.

3.4 REFERENCES

1. Chen J, Lai YH, Ooi S, Song Y, Li L, Liu TY. BTB domain-containing 7 predicts low recurrence and suppresses tumor progression by deactivating Notch1 signaling in breast cancer. Breast Cancer Res Treat. 2020 Nov;184(2):287-300. doi: 10.1007/s10549-020-05857-2. Epub 2020 Aug 8. PMID: 32772271.
2. Shu J, Wang L, Han F, Chen Y, Wang S, Luo F. BTBD7 Downregulates E-Cadherin and Promotes Epithelial-Mesenchymal Transition in Lung Cancer. Biomed Res Int. 2019 Nov 27;2019:5937635. doi: 10.1155/2019/5937635. PMID: 31886230; PMCID: PMC6900955.
3. Onodera T, Sakai T, Hsu JC, Matsumoto K, Chiorini JA, Yamada KM. Btbd7 regulates epithelial cell dynamics and branching morphogenesis. Science. 2010 Jul 30;329(5991):562-5. doi: 10.1126/science.1191880. PMID: 20671187; PMCID: PMC3412157.
4. Savage AK, Constantinides MG, Han J, Picard D, Martin E, Li B, Lantz O, Bendelac A. The transcription factor PLZF directs the effector program of the NKT cell lineage. Immunity. 2008 Sep 19;29(3):391-403. doi: 10.1016/j.immuni.2008.07.011. Epub 2008 Aug 14. PMID: 18703361; PMCID: PMC2613001.
5. Pasqualucci L, Migliazza A, Basso K, Houldsworth J, Chaganti RS, Dalla-Favera R. Mutations of the BCL6 proto-oncogene disrupt its negative autoregulation in diffuse large B-cell lymphoma. Blood. 2003 Apr 15;101(8):2914-23. doi: 10.1182/blood-2002-11-3387. Epub 2002 Dec 19. PMID: 12515714.
6. Słabicki M, Yoon H, Koeppel J, Nitsch L, Roy Burman SS, Di Genua C, Donovan KA, Sperling AS, Hunkeler M, Tsai JM, Sharma R, Guirguis A, Zou C, Chudasama P, Gasser JA, Miller PG, Scholl C, Fröhling S, Nowak RP, Fischer ES, Ebert BL. Small-molecule-induced polymerization triggers degradation of BCL6. Nature. 2020 Nov 18. doi: 10.1038/s41586-020-2925-1. Epub ahead of print. PMID: 33208943.
7. Kang MI, Kobayashi A, Wakabayashi N, Kim SG, Yamamoto M. Scaffolding of Keap1 to the actin cytoskeleton controls the function of Nrf2 as key regulator of cytoprotective phase 2 genes. Proc Natl Acad Sci U S A. 2004 Feb 17;101(7):2046-51. doi: 10.1073/pnas.0308347100. Epub 2004 Feb 5. PMID: 14764898; PMCID: PMC357049.
8. Stogios PJ, Privé GG. The BACK domain in BTB-kelch proteins. Trends Biochem Sci. 2004 Dec;29(12):634-7. doi: 10.1016/j.tibs.2004.10.003. PMID: 15544948.

9. Canning P, Cooper CD, Krojer T, Murray JW, Pike AC, Chaikuad A, Keates T, Thangaratnarajah C, Hojzan V, Ayinampudi V, Marsden BD, Gileadi O, Knapp S, von Delft F, Bullock AN. Structural basis for Cul3 protein assembly with the BTB-Kelch family of E3 ubiquitin ligases. J Biol Chem. 2013 Mar 15;288(11):7803-14. doi: 10.1074/jbc.M112.437996. Epub 2013 Jan 24. Erratum in: J Biol Chem. 2013 Sep 27;388(39):28304. Ayinampudi, Vikram [added]. PMID: 23349464; PMCID: PMC3597819.
10. Schapira M, Calabrese MF, Bullock AN, Crews CM. Targeted protein degradation: expanding the toolbox. Nat Rev Drug Discov. 2019 Dec;18(12):949-963. doi: 10.1038/s41573-019-0047-y. Epub 2019 Oct 30. PMID: 31666732.
11. Daley WP, Matsumoto K, Doyle AD, Wang S, DuChez BJ, Holmbeck K, Yamada KM. Btbd7 is essential for region-specific epithelial cell dynamics and branching morphogenesis in vivo. Development. 2017 Jun 15;144(12):2200-2211. doi: 10.1242/dev.146894. Epub 2017 May 15. Retraction in: Development. 2020 Aug 12;147(15): PMID: 28506999; PMCID: PMC5482991.
12. Hayashi K, Ikari T, Sugiyama G, Sugiura T, Ohyama Y, Kumamaru W, Shirasuna K, Mori Y. Involvement of the T-box transcription factor Brachyury in early-stage embryonic mouse salivary gland. Biochem Biophys Res Commun. 2016 Sep 2;477(4):814-819. doi: 10.1016/j.bbrc.2016.06.140. Epub 2016 Jun 29. PMID: 27369076.
13. Wang JS, Wang MJ, Lu X, Zhang J, Liu QX, Zhou D, Dai JG, Zheng H. Artesunate inhibits epithelial-mesenchymal transition in non-small-cell lung cancer (NSCLC) cells by down-regulating the expression of BTBD7. Bioengineered. 2020 Dec;11(1):1197-1207. doi: 10.1080/21655979.2020.1834727. PMID: 33108235.
14. Harunaga J, Hsu JC, Yamada KM. Dynamics of salivary gland morphogenesis. J Dent Res. 2011 Sep;90(9):1070-7. doi: 10.1177/0022034511405330. Epub 2011 Apr 12. PMID: 21487116; PMCID: PMC3318079.
15. Gonzalez DM, Medici D. Signaling mechanisms of the epithelial-mesenchymal transition. Sci Signal. 2014 Sep 23;7(344):re8. doi: 10.1126/scisignal.2005189. PMID: 25249658; PMCID: PMC4372086.
16. Daley WP, Matsumoto K, Doyle AD, Wang S, DuChez BJ, Holmbeck K, Yamada KM. Retraction: Btbd7 is essential for region-specific epithelial cell dynamics and branching morphogenesis in vivo. Development. 2020 Aug 12;147(15):dev195560. doi: 10.1242/dev.195560. PMID: 32792339.
17. Cruz Walma DA, Collins JW. Western Blotting with Solutions containing Nanoliter Volumes of Antibody. Curr Protoc Cell Biol. 2019 Sep;84(1):e87. doi: 10.1002/cpcb.87. PMID: 31483112; PMCID: PMC6727981.
18. Lin LC, Elkashty O, Ramamoorthi M, Trinh N, Liu Y, Sunavala-Dossabhoy G, Pranzatelli T, Michael DG, Chivasso C, Perret J, Chiorini JA, Delporte C, Tran SD. Cross-contamination of the human salivary gland HSG cell line with HeLa cells: A STR analysis study. Oral Dis. 2018 Nov;24(8):1477-1483. doi: 10.1111/odi.12920. Epub 2018 Jul 10. PMID: 29923277.

19. Bellusci S, Grindley J, Emoto H, Itoh N, Hogan BL. Fibroblast growth factor 10 (FGF10) and branching morphogenesis in the embryonic mouse lung. Development. 1997 Dec;124(23):4867-78. PMID: 9428423.
20. Zhang YW, Vande Woude GF. HGF/SF-met signaling in the control of branching morphogenesis and invasion. J Cell Biochem. 2003 Feb 1;88(2):408-17. doi: 10.1002/jcb.10358. PMID: 12520544.
21. Schlierf A, Altmann E, Quancard J, Jefferson AB, Assenberg R, Renatus M, Jones M, Hassiepen U, Schaefer M, Kiffe M, Weiss A, Wiesmann C, Sedrani R, Eder J, Martoglio B. Targeted inhibition of the COP9 signalosome for treatment of cancer. Nat Commun. 2016 Oct 24;7:13166. doi: 10.1038/ncomms13166. PMID: 27774986; PMCID: PMC5078989.
22. Majolée J, Pronk MCA, Jim KK, van Bezu JSM, van der Sar AM, Hordijk PL, Kovačević I. CSN5 inhibition triggers inflammatory signaling and Rho/ROCK-dependent loss of endothelial integrity. Sci Rep. 2019 May 31;9(1):8131. doi: 10.1038/s41598-019-44595-4. PMID: 31148579; PMCID: PMC6544660.
23. Ohse M, Takahashi K, Kadowaki Y, Kusaoke H. Effects of plasmid DNA sizes and several other factors on transformation of Bacillus subtilis ISW1214 with plasmid DNA by electroporation. Biosci Biotechnol Biochem. 1995 Aug;59(8):1433-7. doi: 10.1271/bbb.59.1433. PMID: 7549093.
24. Zhou J, Li X, Xia J, Wen Y, Zhou J, Yu Z, Tian B. The role of temperature and bivalent ions in preparing competent Escherichia coli. 3 Biotech. 2018 May;8(5):222. doi: 10.1007/s13205-018-1243-x. Epub 2018 Apr 17. PMID: 29682441; PMCID: PMC5904042.
25. Ey PL, Prowse SJ, Jenkin CR. Isolation of pure IgG1, IgG2a and IgG2b immunoglobulins from mouse serum using protein A-sepharose. Immunochemistry. 1978 Jul;15(7):429-36. doi: 10.1016/0161-5890(78)90070-6. PMID: 30693.
26. Kowalczyk AP, Nanes BA. Adherens junction turnover: regulating adhesion through cadherin endocytosis, degradation, and recycling. Subcell Biochem. 2012;60:197-222. doi: 10.1007/978-94-007-4186-7_9. PMID: 22674073; PMCID: PMC4074012.
27. Weill U, Krieger G, Avihou Z, Milo R, Schuldiner M, Davidi D. Assessment of GFP Tag Position on Protein Localization and Growth Fitness in Yeast. J Mol Biol. 2019 Feb 1;431(3):636-641. doi: 10.1016/j.jmb.2018.12.004. Epub 2018 Dec 12. PMID: 30550779; PMCID: PMC7611381.
28. Vermeulen K, Van Bockstaele DR, Berneman ZN. The cell cycle: a review of regulation, deregulation and therapeutic targets in cancer. Cell Prolif. 2003 Jun;36(3):131-49. doi: 10.1046/j.1365-2184.2003.00266.x. PMID: 12814430; PMCID: PMC6496723.
29. Duronio RJ, Xiong Y. Signaling pathways that control cell proliferation. Cold Spring Harb Perspect Biol. 2013 Mar 1;5(3):a008904. doi: 10.1101/cshperspect.a008904. PMID: 23457258; PMCID: PMC3578363.
30. Tong S, Si Y, Yu H, Zhang L, Xie P, Jiang W. MLN4924 (Pevonedistat), a protein neddylation inhibitor, suppresses proliferation and migration of human clear cell renal cell carcinoma. Sci Rep. 2017 Jul 17;7(1):5599. doi: 10.1038/s41598-017-06098-y. PMID: 28717191; PMCID: PMC5514088.

31. Nakayama KI, Nakayama K. Ubiquitin ligases: cell-cycle control and cancer. Nat Rev Cancer. 2006 May;6(5):369-81. doi: 10.1038/nrc1881. PMID: 16633365.
32. Jang SM, Redon CE, Thakur BL, Bahta MK, Aladjem MI. Regulation of cell cycle drivers by Cullin-RING ubiquitin ligases. Exp Mol Med. 2020 Oct;52(10):1637-1651. doi: 10.1038/s12276-020-00508-4. Epub 2020 Oct 2. PMID: 33005013.
33. Chen X, Barton LF, Chi Y, Clurman BE, Roberts JM. Ubiquitin-independent degradation of cell-cycle inhibitors by the REGgamma proteasome. Mol Cell. 2007 Jun 22;26(6):843-52. doi: 10.1016/j.molcel.2007.05.022. PMID: 17588519; PMCID: PMC2031223.
34. Kalejta RF, Shenk T. Proteasome-dependent, ubiquitin-independent degradation of the Rb family of tumor suppressors by the human cytomegalovirus pp71 protein. Proc Natl Acad Sci U S A. 2003 Mar 18;100(6):3263-8. doi: 10.1073/pnas.0538058100. Epub 2003 Mar 7. PMID: 12626766; PMCID: PMC152280.
35. Udeshi ND, Mertins P, Svinkina T, Carr SA. Large-scale identification of ubiquitination sites by mass spectrometry. Nat Protoc. 2013 Oct;8(10):1950-60. doi: 10.1038/nprot.2013.120. Epub 2013 Sep 19. PMID: 24051958; PMCID: PMC4725055.
36. Hristova V, Sun S, Zhang H, Chan DW. Proteomic analysis of degradation ubiquitin signaling by ubiquitin occupancy changes responding to 26S proteasome inhibition. Clin Proteomics. 2020 Jan 25;17:2. doi: 10.1186/s12014-020-9265-x. Erratum in: Clin Proteomics. 2020 Feb 21;17:6. PMID: 31997977; PMCID: PMC6982382.

CHAPTER FOUR

Molecular mechanisms of tandem BTB proteins

4.1 INTRODUCTION

Introduced in chapter 1, a subset of proteins is annotated as containing tandem BTB domains. Proteins predicted to include two sequential copies of the BTB domain include BTBD7, BTBD8, RHOBTB1, RHOBTB2, RHOBTB3, LZTR1, IBTK, and ABTB1. The biological relevance for a single protein to harbour two evolutionarily conserved BTB domains is unknown. To date, no structure of a tandem BTB domain-containing protein has been solved and the biophysical and structural relationships between tandem BTB proteins and CUL3 have not been characterised. With the intent to produce a soluble recombinant tandem BTB protein for structural and functional assays, I designed constructs for, and attempted to produce, recombinant proteins of seven tandem BTB proteins (RHOBTB2 was not cloned due to an extensive number of existing RHOBTB2 constructs produced by the department alongside its similarity to RHOBTB1 and RHOBTB3). Based on their tractability, I then focused my analyses on three of the eight tandem BTB proteins; RHOBTB1, LZTR1, and BTBD7. The domain architecture and biological relevance of these three proteins is introduced in Chapter 1.

Considering existing knowledge of the BTB domain, I developed the following hypotheses: 1) Similar to proteins containing a single BTB domain, tandem BTB

proteins may exhibit differing affinities for CUL3. 2) The BTB domains of tandem BTB proteins will dimerise with a second copy of the tandem BTB to form a tetramer of BTB domains. 3) The two BTB domains of tandem BTB proteins are not redundant: one of the two BTB domains serves as the primary functional BTB domain and loss of function in this primary domain cannot be compensated for by the non-primary BTB domain. For the tandem BTB proteins that serve as CUL3 adaptors, this functional discrepancy in the BTB domains manifests as only one of the two BTB domains capable of recruiting a CUL3 subunit and the other facilitating a scaffolding role.

Co-immunoprecipitation, SEC-MALS, and thermal shift assays were used to characterise tandem BTB-CUL3 binding. Crystallisation trials supplemented these assays to characterise the oligomeric state of tandem BTB proteins. Structural modelling of the tandem BTB proteins complemented structural assays to provide further insight into the nature of the tandem BTB domain. Results of this chapter have improved our understanding of the biophysical properties of the tandem BTB fold and prompted several revised hypotheses.

4.2 RESULTS

4.2.1 Construct design and cloning

Not all recombinant proteins exhibit sufficient solubility, homogeneity, and stability for biophysical assays and structure determination by X-ray crystallography. With the aim of producing protein constructs encompassing a tandem BTB domain suitable for biophysical characterisation and structural analysis, full-length and truncated constructs of seven different tandem BTB

domain-containing proteins (BTBD7, BTBD8, RHOBTB1, RHOBTB3, LZTR1, ABTB1, and IBTKA) were designed and cloned based on available cDNA templates. Truncated constructs were designed using domain boundary, disorder, and secondary structure predictions, as well as sequence alignments to other BTB proteins. Approximately 2-5 boundaries on the amino- and carboxy-terminals of each protein were selected yielding 18 constructs for BTBD7 (Figure 4.1A), 12 constructs for RHOBTB1 (Figure 4.1B), 9 constructs for BTBD8, 6 constructs for LZTR1 (Figure 4.1C), 4 constructs for RHOBTB3, 6 constructs for ABTB1, and 31 constructs for IBTKA. These constructs were designed prior to the release of the AlphaFold artificial intelligence system and were aided by the use of GlobPlot (1) and Expasy SIM alignment tool (2). Construct designs were re-assessed following the publication of the AlphaFold algorithm. Expression clones were generated by polymerase chain reaction and ligation-independent cloning into the pNIC28-Bsa4 vector that fused a 23-residue amino-terminal tag (MHHHHHHSSGVDLGTENLYFQ*SM) comprised of hexahistidine and a TEV-protease cleavage site (marked by *) to the construct inserts. Constructs were transformed first into MACH1 *E. coli* to produce colonies for plasmid DNA preparation and subsequently into phage-resistant BL21(DE3)-R3 *E. coli* for protein production. MACH1 *E. coli* were used to produce plasmid DNA because the strain exhibits several advantageous traits such as minimal nonspecific recombination of cloned DNA (due to the expression of heat-stable recA protein which catalyses the pairing of homologous DNA sequences), T1 and T5 phage resistance, and rapid growth rate, among others. Thirty of the 86 constructs from the initial rounds of insert cloning, ligation into pNIC28-Bsa4, and transformation into MACH1 *E. coli* failed to yield bacterial colonies, even though a PCR screen

showed the DNA inserts had been successfully produced (Figure 4.1D). Through modifying the cloning parameters (e.g., increasing ratio of insert to vector and utilizing a DNA ligase enzyme), an additional 19 constructs were successfully cloned into MACH 1. The 75 successfully transformed constructs were isolated from MACH1 cells and transformed into BL21 (DE3)-R3 cells.

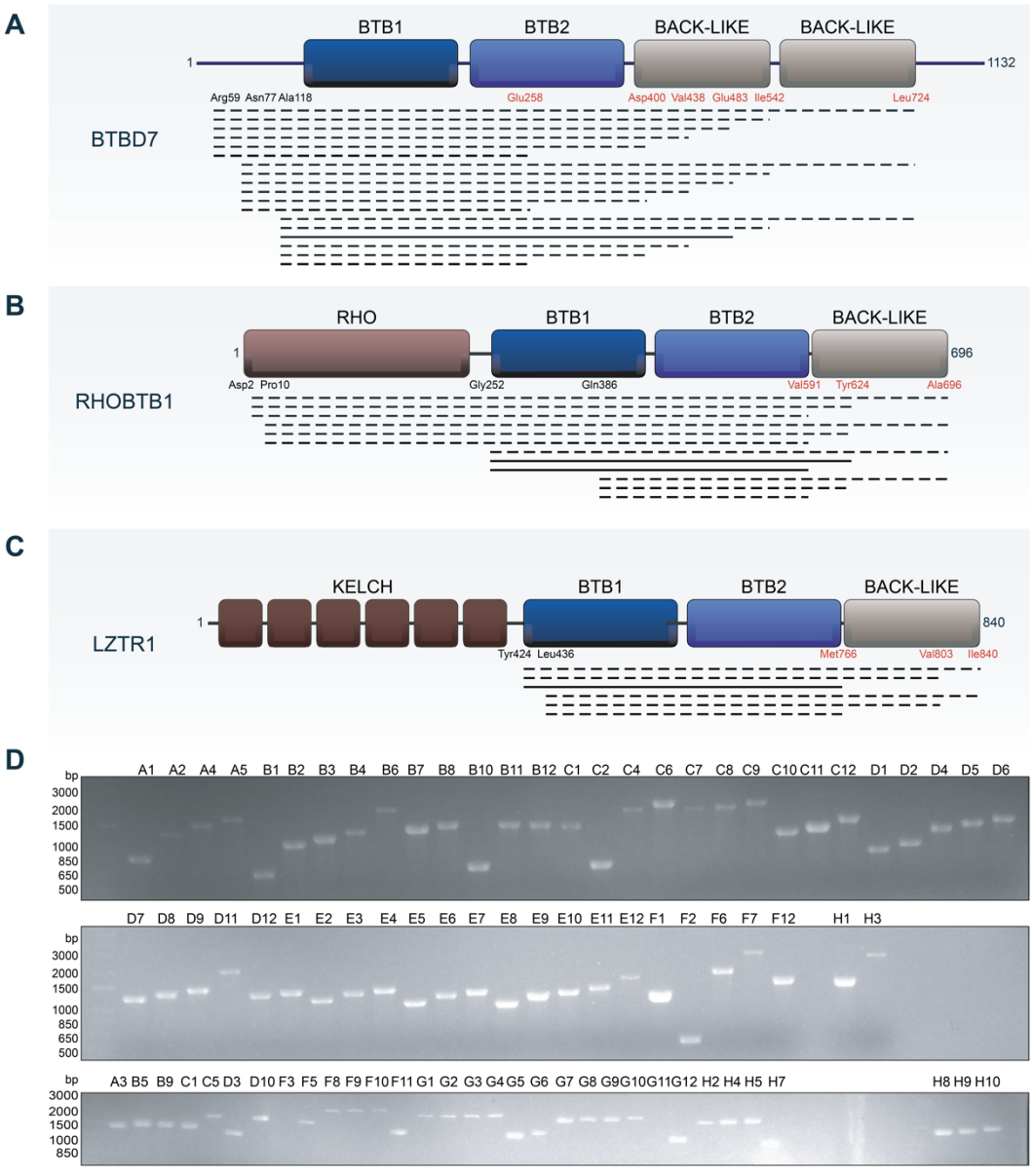


Figure 4.1 Construct design and PCR screen of ligation independent cloning (LIC) inserts of the tandem BTB domain proteins prior to ligation into pNIC28-Bsa4 vectors. (A-C) Domain maps and construct boundaries depicting the 18 constructs designed for BTBD7, 12 constructs for RHOBTB1,

and 6 constructs for LZTR1. Constructs that yielded soluble protein are depicted as solid black lines and constructs that did not yield soluble protein as dashed black lines. (D) Image of the initial PCRs performed in a 96-well format using an E-Gel. Wells of the cloned inserts are labelled. The top two gels depict the first cloning attempt. The bottom gel depicts the second cloning attempt of inserts that failed to be cloned in the first attempt.

4.2.2 Construct test expression and test purification

To determine which of the 75 constructs were likely to yield sufficient soluble protein for large-scale experiments, small-scale 1 mL expression cultures were prepared and Ni-affinity test protein purifications were performed to detect soluble protein expression (Figure 4.2). From these experiments, four protein constructs containing tandem BTB domains yielded soluble protein, including BTBD7 Ala118-Glu483 ($BTBD7_{118-483}$), LZTR1 Try424-Met766 ($LZTR1_{424-766}$), RHOBTB1 Gly252-Val591 ($RHOBTB1_{252-591}$), and RHOBTB1 Gly252-Tyr624 ($RHOBTB1_{252-624}$) (Figures 4.1A-C, 4.2). A further construct of RHOBTB1 encompassing the full carboxy-terminus of the protein (Gly252-Ala696) also appeared to yield soluble protein but suffered degradation (Figures 4.1B, 4.2). Of these three RHOBTB1 constructs, $RHOBTB1_{252-591}$ was selected for biophysical and structural studies due to its relatively high expression levels and purity. $BTBD7_{118-483}$ encompasses the two BTB domains and part of the first BACK domain, but removes the subsequent BACK domain and terminal disordered domains (Figure 4.1A). $RHOBTB1_{252-591}$ encompasses two BTB domains but removes the amino-terminal RHO domain and carboxy-terminal BACK domain (Figure 4.1B) while $LZTR1_{424-766}$ encompasses the two BTB domains and removes the amino-terminal Kelch repeat domain and the carboxy-terminal BACK domain (Figure 4.1C). $BTBD7_{118-483}$, $RHOBTB1_{252-591}$, and $LZTR1_{424-766}$, were selected for large-scale expressions and purifications to enable biophysical and structural studies.

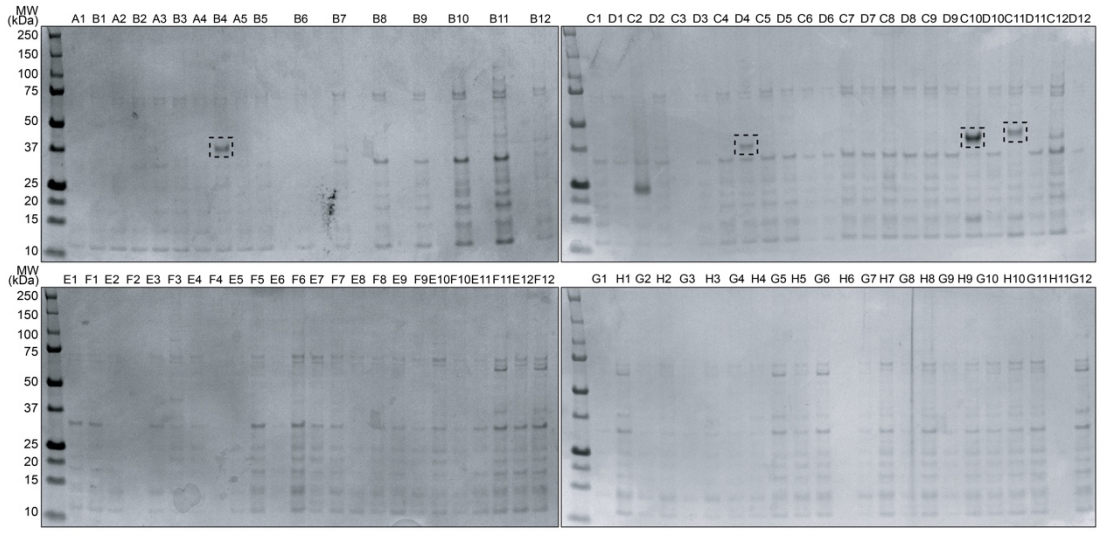


Figure 4.2 Test expression and nickel-affinity purification of the successfully cloned and transformed tandem BTB protein constructs. SDS-PAGE Coomassie gels of small-scale nickel affinity purifications of the tandem BTB domain protein constructs showed four protein constructs yielded soluble protein (dashed boxes). Wells of the cloned constructs from the initial 96 well sample plate are designated. Wells are interweaved due to spacing of pipette tips in the multichannel pipette. Well B4 is BTBD7$_{118-483}$, D4 is LZTR1$_{424-766}$, C10 is RHOBTB1$_{252-591}$, and C11 is RHOBTB1$_{252-624}$. The degraded RHOBTB1$_{252-696}$ construct is observed in lane C12.

4.2.3 Optimisation of large-scale protein production

My first large-scale protein purifications were performed using both BTBD7$_{118-483}$ and RHOBTB1$_{252-591}$. Due to the large number of contaminants following nickel Sepharose affinity purification, BTBD7$_{118-483}$ elutions were subjected to an initial round of size-exclusion chromatography (SEC) prior to tag cleavage (Figure 4.3A). Following SEC, elution fractions containing the smallest number of contaminants were selected for TEV-mediated tag cleavage and further purification. Following cleavage, a second round of SEC removed most of a higher molecular weight (approximately 60 kDa) contaminant alongside any residual TEV (Figure 4.3A). While this first round of purification yielded protein of sufficient quality for biophysical experiments, the continued presence of lower

(13 kDa, 20 kDa, and 25 kDa) and higher molecular weight (60 kDa) contaminants was sub-optimal for any attempts at crystallisation.

Interestingly, cleaved $BTBD7_{118-483}$ has an expected mass of 42,025 daltons, yet purified $BTBD7_{118-483}$ consistently ran below the 37 kDa marker on SDS-PAGE gels (Figure 4.3A,B). Purified $BTBD7_{118-483}$ was verified by mass spectrometry to be the designated construct of interest. Nevertheless, this discrepancy between denatured mass and SDS-PAGE gel migration was consistent in all subsequent purifications and is reminiscent of the discrepancy in SEC retention volume and predicted molecular weight of $BTBD7_{118-483}$ from MALS data described in subsequent sections.

With the goal of removing these remaining contaminants and producing protein of sufficient purity for crystallisation, I modified the $BTBD7_{118-483}$ purification workflow. Notable differences in subsequent purifications included 1) tagged $BTBD7_{118-483}$ was batch bound to nickel Sepharose resin and washed in Falcon tubes instead of on gravity flow drip columns, 2) eluted $BTBD7_{118-483}$ was immediately cleaved prior to size exclusion chromatography, 3) size-exclusion chromatography was performed using a HiLoad 16/600 Superdex 200 pg column instead of a 75 pg column to determine if a larger pore size assisted purification since SEC-MALS data suggested $BTBD7_{118-483}$ may be forming higher order species, and 4) a nickel rebind was performed to remove residual His-tagged TEV protease and the cleaved His tag following size-exclusion chromatography. While these modifications aided purification, small amounts of lower molecular weight contaminants (25 kDa and 13 kDa) remained (Figure 4.3B).

Compared to BTBD7$_{118-483}$, RHOBTB1$_{252-591}$ exhibited significantly higher expression levels of soluble protein. I performed my first large-scale purification of RHOBTB1$_{252-591}$ simultaneously with the preliminary BTBD7$_{118-483}$ nickel-affinity resin purifications described previously. Accordingly, this first RHOBTB1$_{252-591}$ purification involved a drip column instead of batch binding to nickel Sepharose affinity resin, washing, and eluting in Falcon tubes. This initial large-scale purification yielded protein with several lower molecular weight contaminants that could not be removed following SEC, nickel rebinding, and anion exchange. In subsequent purifications, the nickel Sepharose affinity resin purification was modified per insights gained troubleshooting BTBD7$_{118-483}$ purifications. In subsequent purifications of RHOBTB1$_{252-591}$, expressed protein was batch bound to nickel Sepharose resin, washed, and eluted in 50 mL Falcon tubes at 4°C. Elutions were separated based on purity and sequentially subjected to SEC on a HiLoad 16/600 Superdex 200 pg column. This workflow consistently produced greater than 10 mg of soluble protein from 2 L of cell cultures of sufficient purity for biophysical assays and crystallisation screens (Figure 4.3C).

Implementing insights gained trouble-shooting BTBD7$_{118-483}$ and RHOBTB1$_{252-591}$ purifications, LZTR1$_{424-766}$ purifications were streamlined to minimize purification time and improve the likelihood of producing soluble purified protein. Tagged LZTR1$_{424-766}$ was batch bound to nickel Sepharose resin in 50 mL Falcon tubes, washed, eluted, cleaved overnight, subjected to SEC on a HiLoad 16/600 Superdex 200 pg column, and verified by mass spectrometry. This workflow

yielded LZTR1$_{424-766}$ fractions of sufficient purity for biophysical assays as well as crystallisation screens (Figure 4.3D). Further discussed in the LZTR1 crystallisation trial section of this chapter, LZTR1$_{424-766}$ consistently precipitated upon reaching concentrations of 2 mg/mL. Described in section 4.2.8, the purification workflow was modified with the aim to minimise this precipitation. However, even with such modifications, LZTR1$_{424-766}$ continued to precipitate upon reaching a concentration of 2 mg/ml.

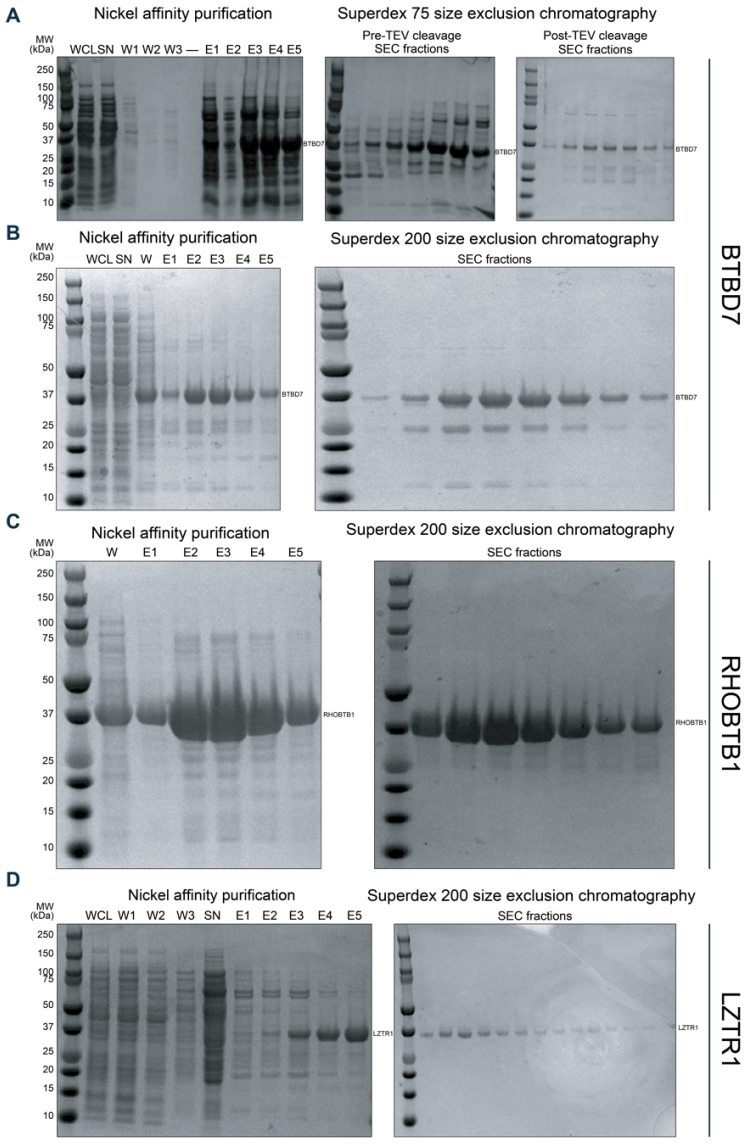


Figure 4.3 Optimising the large-scale protein production of BTBD7$_{118-483}$, RHOBTB1$_{252-591}$, and LZTR1$_{424-766}$. (A-D) SDS-PAGE Coomassie gels of nickel

affinity purifications (left panels) and SEC fractions (right panels and middle panel of A) as the protein purification parameters were optimised. Lanes of nickel affinity purification gels are labelled as whole cell lysate (WCL), supernatant (SN), wash (W), or elution (E). (A) The first attempt purifying a His-tagged tandem BTB protein ($BTBD7_{118-483}$) showing contaminated elutions (left panel) that was subjected to preparatory SEC before (middle panel) and after (right panel) TEV cleavage of the His tag. (B) An example purification of the same His-tagged $BTBD7_{118-483}$ construct after refining the purification workflow as outlined in section 4.2.3. The SEC fractions depicted were pooled, concentrated, and used for biophysical experiments. (C,D) Example purifications of $RHOBTB1_{252-591}$ (C) and $LZTR1_{424-766}$ (D) using the same optimised purification workflow noted in B of this figure and described in section 4.2.3. The depicted SEC fractions were pooled, concentrated, and used for biophysical experiments.

4.2.4 Only a subset of the purified tandem BTB proteins bind CUL3

Many BTB domain-containing proteins are known to serve as substrate-specific adaptors for the Cullin-RING ligase (CRL) CRL3 subclass of E3 ubiquitin ligases. Several previous reports suggest RHOBTB1 and LZTR1 interact with CUL3 (3, 4). While BTBD7 has been reported to be a CUL3 interacting protein by large scale proteomics (5), no subsequent reports have confirmed this result. To verify which tandem BTB domain-containing proteins interact with CUL3, I performed a series of co-immunoprecipitation assays with purified $BTBD7_{118-483}$, $LZTR1_{424-766}$, $RHOBTB1_{252-591}$, and $CUL3_{1-388}$.

Purified $BTBD7_{118-483}$, $LZTR1_{424-766}$, and $RHOBTB1_{252-591}$ were incubated with purified C-terminally Flag-tagged $CUL3_{1-388}$. KCTD15 is a BTB domain-containing protein that does not bind to CUL3 (6, 7), hence was used as a negative control. Protein solutions including isolated proteins and protein mixtures were passed over a Flag M2 affinity agarose resin resulting in immobilisation of 6His-Flag-CUL3 and any proteins bound to CUL3. Following two washes (see materials and methods for details), proteins were eluted with sample buffer, subjected to SDS-PAGE, and stained with Coomassie stain.

BTBD7$_{118-483}$ and negative control KCTD15 failed to co-immunoprecipitate with Flag-tagged CUL3$_{1-388}$ (Figure 4.4). In contrast, both RHOBTB1$_{252-591}$ and LZTR1$_{424-766}$ co-immunoprecipitated with Flag-tagged CUL3$_{1-388}$ (Figure 4.4). To further verify the differential ability of tandem BTB domain-containing proteins to bind to CUL3 and better characterise the stoichiometry of such interactions, SEC-MALS experiments were performed.

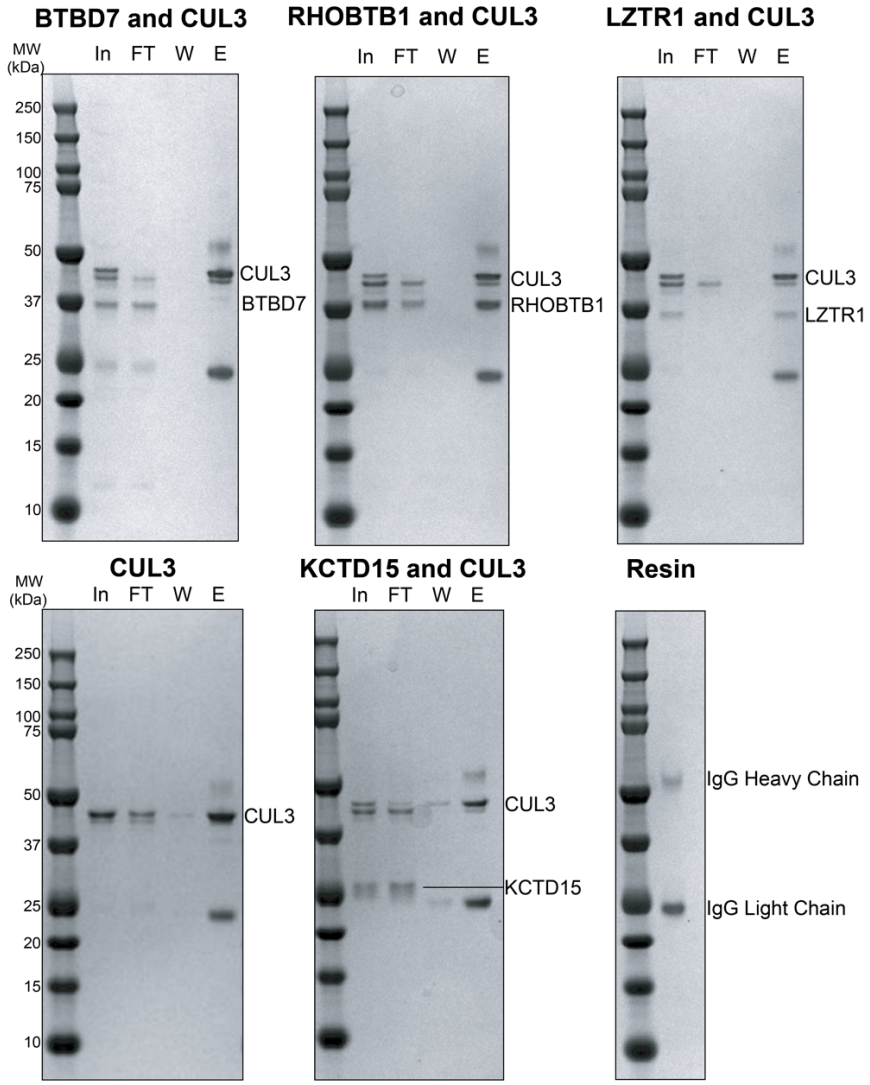


Figure 4.4 Co-immunoprecipitation of BTBD7$_{118-483}$, RHOBTB1$_{252-591}$, and LZTR1$_{424-766}$ with Flag-tagged CUL3$_{1-388}$. SDS-PAGE Coomassie gels of co-immunoprecipitation experiments of tandem BTB proteins with Flag-tagged CUL3. BTBD7$_{118-483}$ did not co-immunoprecipitate with CUL3 (top left panel)

whereas RHOBTB1$_{252-591}$ and LZTR1$_{424-766}$, did co-immunoprecipitate with CUL3 (top middle and right panels, respectively). Bottom panels show controls - immunoprecipitation of CUL3 alone (left panel), co-immunoprecipitation of CUL3 with a protein known to not interact with CUL3 (KCTD15; middle panel), and an image of the Flag M2 affinity resin alone showing the IgG heavy and light chains being eluted off the resin. Each gel, with the exception of the resin gel, shows lanes of input (In) prior to adding resin, flow through (FT) of solutions not bound to resin, washes (W), and elution via directly boiling in sample buffer (E). Proteins are labelled. CUL3 existed as two bands representing neddylated and non-neddylated CUL3. The IgG heavy and light chains can be seen in each gel.

4.2.5 SEC-MALS indicates that tandem BTBs exhibit different stoichiometries and bind CUL3 in different ratios

BTB adaptor proteins typically dimerise through their BTB domains to recruit two CUL3 subunits into a CRL3 complex. Unanswered questions relating to proteins harbouring tandem BTB domains include; do proteins with two BTB domains exist predominantly as monomers or do they dimerise to form the equivalent of a "tetramer" of BTB domains? Do tandem BTB domains recruit one or two CUL3 subunits? To explore these questions and to characterise the oligomeric states of LZTR1, RHOBTB1, and BTBD7 in isolation alongside their stoichiometric ratios when complexed with CUL3, I performed a series of experiments using size-exclusion chromatography coupled with multi-angle light scattering (SEC-MALS).

Isolated BTBD7$_{118-483}$ (42.0 kDa), RHOBTB1$_{252-591}$ (38.2 kDa), and LZTR1$_{424-766}$ (39.8 kDa) as well as mixtures of the three recombinant proteins with CUL3$_{1-388}$ (48.1 kDa) were analysed by SEC-MALS. Protein complexes were mixed in a ratio of 10 μM:25 μM tandem BTB protein:CUL3 to account for the hypothesis that a tandem BTB protein may bind two CUL3 subunits. RHOBTB1 alone eluted as a single monomeric species with a retention volume of 15.4 mL and an

average MALS measurement of 35.2 kDa (Figure 4.5A, Table 4.1). The mixture of RHOBTB1 with CUL3 eluted as two species. Data suggested the predominant species in the mixture was a RHOBTB1:CUL3 complex with a 1:1 stoichiometry (retention volume:14.0 mL, average MALS measurement: 73.1 kDa). The isolated monomers were comparatively less abundant (retention volume: 15.6 mL, average MALS measurement: 40.6 kDa) (Figure 4.5A, Table 4.1).

LZTR1 alone eluted as a dimeric species as evidenced by a 14.1 mL retention volume and an average MALS measurement of 87.6 kDa (Figure 4.5A, Table 4.1). Complexes of LZTR1 and CUL3 eluted as two species; a complex with a retention volume of 12.8 mL and an average MALS measurement of 117.7 kDa (suggesting three protein subunits were present) as well as the isolated proteins with retention volumes of 15.4 mL and average MALS measurements of 44.8 kDa (suggesting an excess of unbound CUL3). In contrast to the RHOBTB1-CUL3 sample in which the predominant species was the complex, the LZTR1 and CUL3 mixture less efficiently formed a complex and existed predominantly as isolated species (Figure 4.5A, Table 4.1).

BTBD7 alone eluted as a single species with a retention volume similar to the LZTR1 dimer (14.1 mL), but displayed an average MALS measurement of only 55.5 kDa (less than the predicted 84.0 kDa of a BTBD7 dimer) (Figure 4.5A, Table 4.1). Of note, the elution peak showed some tailing suggesting non-specific interaction with the column matrix. When mixed with CUL3, a shift in BTBD7 elution to a higher molecular weight was not observed, suggesting that a BTBD7-CUL3 complex was not formed (confirming the results of the co-

immunoprecipitation experiments). Somewhat surprisingly, when mixed with CUL3, BTBD7 showed a delayed elution with both BTBD7 and CUL3 eluting as a single SEC peak at retention volume 15.3 mL and an average MALS measurement of 45.3 kDa (Figure 4.5A, Table 4.1). Thus, while no complex was apparent, the presence of CUL3 appeared to induce a more compact BTBD7 species and limited its tailing.

In summary, SEC-MALS experiments showed 1) LZTR1 alone eluted as an apparent dimer and the LZTR1-CUL3 complex contained three protein subunits (due to the similarity in molecular weight of the LZTR1 and CUL3 constructs, the ratio of LZTR1:CUL3 could not be determined from the SEC-MALS data – a single LZTR1 protein may be recruiting two CUL3 proteins, one to each BTB domain, or the LZTR1 subunits may be dimerising and recruiting only a single CUL3), 2) RHOBTB1 alone eluted as a monomer and the RHOBTB1-CUL3 complex contained two protein subunits (likely 1:1 RHOBTB1:CUL3 subunits), 3) BTBD7 alone eluted at a retention volume similar to the LZTR1 dimer but displayed a MALS value less than that of a BTBD7 dimer (suggesting isolated BTBD7 may exist as a monomer that interacts non-specifically with the column matrix) and the BTBD7-CUL3 mixture did not form a complexed protein species (confirming the lack of interaction between the purified BTBD7 and CUL3 constructs) and 4) purified LZTR1 and RHOBTB1 constructs bound to CUL3 while purified BTBD7 constructs did not.

Table 4.1 SEC-MALS results of tandem BTB proteins alone and in complex with CUL3.

	Denatured Mass [1:1 complex mass] (kDa)	MALS Mass [range] (kDa)	Retention volume (mL)	Hypothesised Observed Species
RHOBTB1	38.2	35.2 [33.3-44.6]	15.4	Monomer
LZTR1	39.8	87.6 [82.2-126.3]	14.1	Dimer
BTBD7	42.0	55.5 [49.8-59.5]	14.1	Poorly behaved monomer
CUL3	48.1	42.4 [39.6-48.8]	15.2	Monomer
RHOBTB1-CUL3	38.2, 46.2 [84.4]	73.1 [69.5-80.0](Peak 1), 40.6 [35.4-44.1](Peak 2)	14.0 (Peak 1), 15.6 (Peak 2)	1:1 RHOBTB1:CUL3, Individual monomers
LZTR1-CUL3	39.8, 46.2 [86.0]	117.7 [104.8-134.4](Peak1), 44.8 [42.8-50.7](Peak 2)	12.8 (Peak 1), 15.4 (Peak 2)	2:1 CUL3:LZTR1 or LZTR1:CUL3, individual monomers
BTBD7-CUL3	42.0, 46.2 [88.2]	45.3 [41.0-55.8]	15.3	Individual monomers

4.2.6 RHOBTB1 folding is stabilised by CUL3 binding

The CUL3 binding interactions observed in the SEC-MALS experiments may be expected to stabilise the folding of RHOBTB1 and LZTR1. To assess differences in thermal stability between isolated proteins and their CUL3 complexes, I mixed isolated proteins and protein complexes with SYPRO Orange fluorescent dye and performed thermal denaturation experiments in an RT-PCR thermocycler. Using this fluorescence-based thermal shift assay, a relative increase in the complexed protein's melting temperature (*Tm* shift) would suggest the complexed protein is more stable than the isolated protein species.

Isolated CUL3, LZTR1, and the LZTR1-CUL3 complex all displayed similar thermal shift curves indicating similar stabilities and no stabilisation of the complex, perhaps reflecting only weak sub-stoichiometric CUL3 binding (apparent *Tm* values of 53°C, 55°C, and 54°C, respectively) (Figure 4.5B). In contrast, isolated RHOBTB1 showed high SYPRO Orange binding, indicative of

exposed hydrophobic surfaces, even at low temperatures and a shallow unfolding transition close to physiological temperature (apparent *Tm* of 37°C) (Figure 4.5B). When mixed with CUL3, the RHOBTB1-CUL3 complex showed low SYPRO Orange binding at low temperatures and became more thermally stable with a well-defined unfolding transition and melting temperature similar to CUL3 alone (apparent *Tm* of 53°C). BTBD7 alone also showed high initial SYPRO Orange binding and no obvious unfolding transition as the decreased fluorescence observed at higher temperatures could have occurred from precipitation, as well as from the reduced fluorescence quantum yield at higher temperatures. Upon addition of CUL3, the fluorescence of the mixture resembled an average of the melting curves of the two individual proteins as expected for a protein pair without binding.

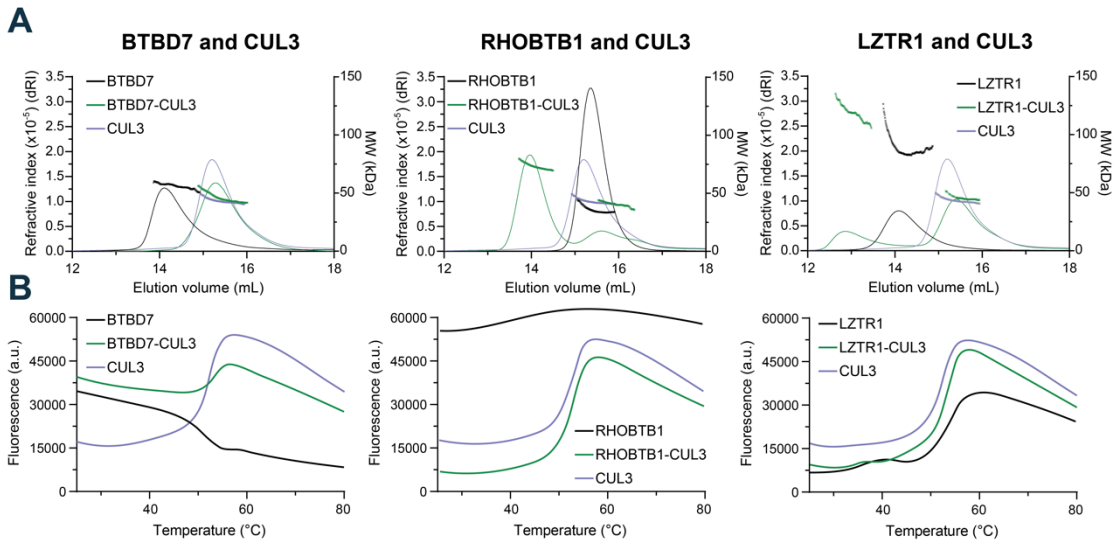


Figure 4.5 SEC-MALS and DSF of BTBD7$_{118-483}$, RHOBTB1$_{252-591}$, and LZTR1$_{424-766}$ with CUL3$_{1-388}$. (A) SEC-MALS of tandem BTB proteins in isolation and mixed with CUL3 depicted BTBD7$_{118-483}$ eluted at a volume suggestive of a dimer (14.1 mL), but has a predicted MALS measurement less than the predicted 84 kDa of a BTBD7$_{118-483}$ dimer (left panel). When mixed with CUL3, a shift in elution peak was not observed, suggesting the proteins do not interact. RHOBTB1$_{252-591}$ SEC volume and MALS data suggested the protein exists as a monomer (middle panel) and when mixed with CUL3, exists predominantly as a complexed species with one RHOBTB1$_{252-591}$ species binding one CUL3 species. SEC and MALS data suggested LZTR1$_{424-766}$ alone eluted as a dimer (right

panel). SEC and MALS data of LZTR1$_{424-766}$ complexed with CUL3 suggested the complex consists of three proteins. (B) Thermal denaturation of tandem BTB proteins alone and with CUL3 detected using the SYPRO Orange fluorescent dye. BTBD7$_{118-483}$ alone showed high initial SYPRO Orange binding indicative of exposed hydrophobic surfaces and no obvious unfolding transition (left panel). Fluorescence of the BTBD7$_{118-483}$ and CUL3 mixture resembled an averaging of each individual protein. RHOBTB1$_{252-591}$ alone similarly showed high initial SYPRO Orange binding with a shallow unfolding transition (middle panel). When mixed with CUL3, the RHOBTB-CUL3 complex was more thermally stable with a well-defined unfolding transition and an apparent *Tm* similar to CUL3 alone (53°C), suggesting RHOBTB1$_{252-591}$ may be stabilised by CUL3. Isolated CUL3, LZTR1$_{424-766}$, and the LZTR1$_{424-766}$-CUL3 complex all displayed similar thermal shift curves and apparent *Tm* values (53°C and 54°C, respectively) indicative of similar stabilities (right panel). Experiments were performed in triplicate.

4.2.7 Crystallisation of tandem BTB proteins

Crystal structures of the tandem BTB domain alone and in complex with interacting proteins would provide critical insight into the folding and functions of this poorly characterised protein motif. Accordingly, I performed crystallisation trials using LZTR1$_{424-766}$, RHOBTB1$_{252-591}$, and BTBD7$_{118-483}$. The greatest effort was placed on LZTR1$_{424-766}$ since preliminary coarse screens yielded crystals. Relatively less time was spent attempting to crystallise BTBD7$_{118-483}$ due to the inability to remove protein contaminants and the more promising preliminary screen results from LZTR1$_{424-766}$ and RHOBTB1$_{252-591}$ trials.

4.2.7.1 LZTR1 crystallisation trials

To set up crystal screens, SEC fractions of LZTR1$_{424-766}$ from purifications described in 4.2.3 were concentrated using a 10 kDa molecular weight cutoff centrifugal filtration device. LZTR1$_{424-766}$ precipitated upon reaching a concentration of 2 mg/mL (Figure 4.6A,B). This low protein solubility could be due to properties of the solvent and/or intrinsic properties of the protein construct (e.g., structural flexibility of the folded protein as well as residue-residue

interactions including salt bridges, hydrogen bonds, and electrostatic forces). Precipitated protein was resolubilised in gel filtration buffer with 20 mM arginine/20 mM glutamic acid mix to enhance protein solubility (8) and re-concentrated. However, the protein continued to precipitate as it neared 2 mg/mL. Accordingly, soluble protein at a concentration of 1.5 mg/mL was used to set up two crystallisation coarse screens (LFS and JCSG7) at 20°C.

After 48 hours, crystal tray wells began showing preliminary signs of crystallisation. After 28 days, several conditions in the JCSG7 screen exhibited phase separation and one condition of the LFS screen (Well A3a: 0.1M SPG, pH 8.0, 30% PEG 1K) showed signs of protein crystals with a fine needle morphology (Figure 4.6B). Nine small crystals from this LFS well A3a were mounted and sent to the Diamond Light Source beamline I03 for diffraction data collection. However, none of the nine crystals diffracted. Remaining non-mounted crystals were resuspended in 20uL of mother liquor from LFS coarse screen well A3a, placed in a microcentrifuge tube containing a seed bead, and vortexed to produce a crystal seed stock for future crystallisation trials.

For follow up crystal screens, a fine screen around the conditions of LFS-A3a (called LFS-A3a Custom) was designed in ROCK MAKER crystallisation software (Formulatrix) and created using a FORMULATOR screen builder (Formulatrix) (Figure 4.6C). $LZTR1_{424-766}$ was freshly purified and several modifications to the purification workflow were made to minimise protein precipitation. For example, 20 mM arginine/20 mM glutamic acid mix was added to $LZTR1_{424-766}$ prior to concentrating for SEC and again prior to concentrating for

crystal trays. The protein was also concentrated slowly while regularly checking for precipitation. Similar to the first protein preparation for coarse screens, the newly purified $LZTR1_{424-766}$ continued to precipitate when nearing a concentration of 2 mg/mL. Therefore, a concentration of 1.5 mg/mL was repeated to set up four crystallisation screens: LFS-A3a Custom with seed stock at 20°C, LFS-A3a Custom without seed stock at 20°C, LFS with seed stock at 20°C, and LFS without seed stock at 20°C. The LFS without seed stock at 20°C condition was repeated to ensure the $LZTR1_{424-766}$ crystals were reproducible. At 4 days, crystals were observed in all four crystal trays, with the LFS coarse screen with LZTR1 seed stock showing the most prolific crystal growth. At 42 days, 16 crystals from wells E8a, E9c, and E12c (4, 7, and 5 crystals, respectively) of the LFS coarse screen with seed stock were mounted and sent to the I03 beamline for diffraction data collection (Figure 4.6D). Unfortunately, departmental colleagues misread the number on my puck of crystals and discarded them before they could be sent to the Diamond Light Source beamline for diffraction data collection. The puck was discarded in my final week at Oxford, thus there was no further time remaining to repeat the crystals.

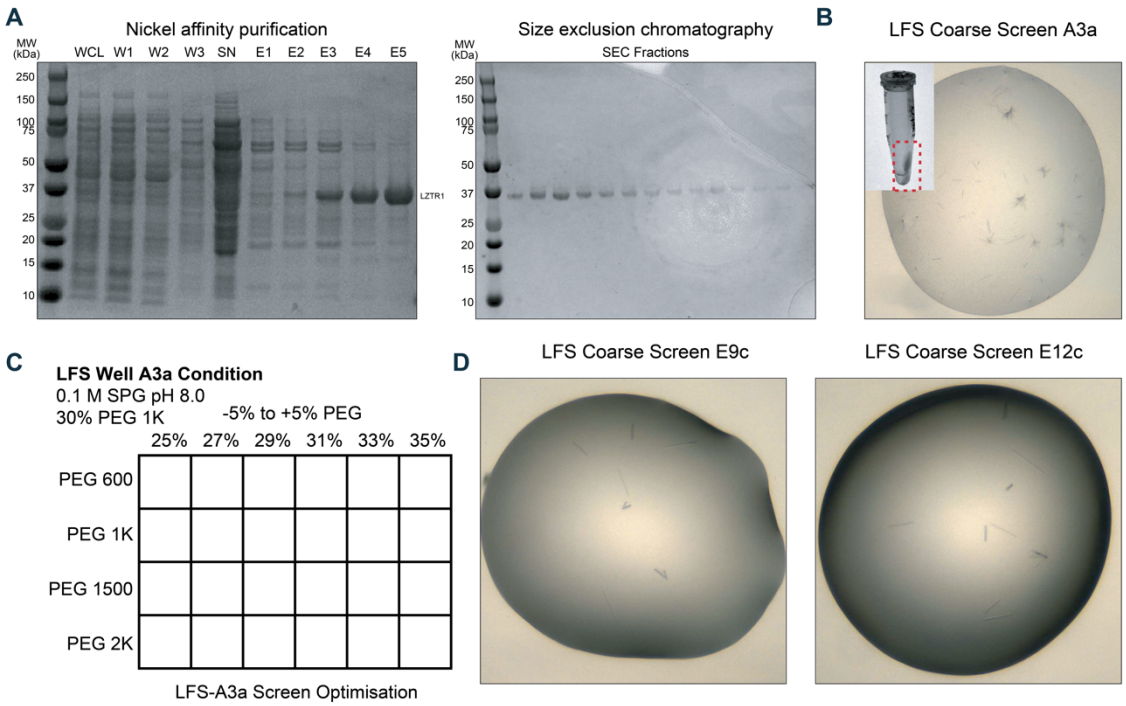


Figure 4.6 Crystallisation trials of LZTR1$_{424-766}$. (A,B) Preliminary crystallisation trials of LZTR1 depicting SDS-PAGE Coomassie gels of the protein preparation for crystallisation trials (A) and a representative photograph of protein crystals formed (B). (A) Nickel affinity purification gels (left panels) are labelled with whole cell lysate (WCL), washes (W1-W3), supernatant (SN) and elutions 1-5 (E1-E5). SEC gels (middle panels) show the SEC fractions that were collected and concentrated for setting up crystal trays. (B) A representative image of the crystals formed in well A3a of the LFS crystallisation coarse screen. A photograph of the protein precipitate that formed when the protein was concentrated above 1.5 mg/mL is shown in the top left of B with the precipitate boxed in red. (C) A schematic of the crystallisation optimisation screen designed around LFS coarse screen well A3a as described in section 4.2.7.1. (D,E) Photographic images of LZTR1 crystals that formed from LZTR1 seed stock in LFS coarse screens.

4.2.7.2 RHOBTB1 crystallisation trials

To set up crystallisation coarse screens of isolated RHOBTB1$_{252-591}$, the optimised purification workflow described in section 4.2.3 was used to produce 12 mg of purified RHOBTB1$_{252-591}$ (Figure 4.7A). Of these 12 mg, 5 mg was concentrated to 10 mg/mL and used to set up five crystal coarse screens (LFS and JCSG7 at 20°C as well as LFS, Morpheus, and BCS at 4°C). Of these

coarse screens, no conditions yielded crystals, but heavy precipitate formed in several of the wells (Figure 4.7A).

Although no crystallisation trials of RHOBTB1$_{252-591}$ yielded crystals, results of SEC-MALS experiments and thermal shift assays suggested RHOBTB1 may be stabilised in the presence of CUL3. Accordingly, I performed crystallisation trials with the RHOBTB1-CUL3 complex with the hypothesis that the presence of CUL3 would stabilise the protein mixture to a sufficient degree for crystallisation and promote new potential crystal contacts.

RHOBTB1$_{252-591}$ and CUL3$_{23-388}$ were purified separately using the optimised nickel Sepharose purification workflow described above. Individually purified RHOBTB1$_{252-591}$ and CUL3$_{23-388}$ were incubated for 60 minutes at 4°C then subjected to SEC on a HiLoad 16/600 Superdex 200 pg column to isolate the RHOBTB1-CUL3 protein complex from the individual RHOBTB1 and CUL3 species (Figure 4.7B). SEC fractions containing the complexed protein were pooled, concentrated to 11 mg/mL, and used to set up four crystallisation coarse screens (LFS and BCS at 20°C as well as JCSG7 and Morpheus at 4°C). After 14 days, several conditions showed signs of granular species (Figure 4.7B). However, none of these conditions produced crystals suitable for mounting and subjecting to X-ray diffraction.

In a second attempt at crystallising the RHOBTB1-CUL3 complex, proteins were mixed and SEC was performed as described above. Protein fractions from SEC were then pooled and subjected to anion exchange using a HiTrap Q HP

column. This additional purification step was used to remove any residual non-complexed proteins and contaminants that could prevent crystal lattice formation (Figure 4.7C). Anion (rather than cation) exchange was performed due to RHOBTB1$_{252-591}$'s and CUL3$_{23-388}$'s predicted isoelectric (PI) values of 5.41 and 4.90, respectively. These PI values are less than the ion exchange buffer's pH (low salt buffer 20 mM Tris pH 8.0, 50 mM NaCl, 0.5 mM TCEP). After diluting in the low salt ion exchange buffer, the protein solution was bound to the column and a salt gradient from 50 mM NaCl to 500 mM NaCl was passed over the column for 25X column volumes. A high salt buffer (20 mM Tris pH 8.0, 1 M NaCl, 0.5 mM TCEP) was used to elute any remaining protein from the column. Anion exchange produced four peaks – potentially reflecting one contaminant protein, one protein complex, and two peaks of individual proteins (Figure 4.7C). The fractions containing protein complex were pooled, concentrated to 10 mg/mL, and used to set up three crystal coarse screens (LFS and BCS at 20°C as well as JCSG7 at 4°C). After 4 days, several conditions began showing signs of protein crystallisation with an apparent crystalline ring forming around the outer edge of the drop where the ratio of protein to precipitant was most rapidly changing due to evaporation (Figure 4.7C). After 11 days, 13 crystals were mounted and sent to the I03 beamline for diffraction; eight crystals were from LFS-A7a, one crystal was from BCS-A4d, and four crystals were from BCS-A4a. None of the crystals diffracted.

4.2.7.3 BTBD7 crystallisation trials

Described in section 4.2.3, several lower molecular weight contaminants could not be removed during BTBD7$_{118-483}$ purifications. Nevertheless, to test if

BTBD7$_{118-483}$ could form crystals in the presence of these lower molecular weight contaminants, purified BTBD7 protein was concentrated to 10 mg/mL using a 10 kDa molecular weight cutoff centrifugal filtration device and a trial Ligand-Friendly Screen (LFS) coarse screen was set up at 4°C. After 56 days, BTBD7$_{118-483}$ failed to crystallise in these conditions and instead formed a precipitate (Figure 4.7D). Due to the inability to remove contaminants from purified BTBD7 constructs and better crystallisation leads from RHOBTB1 and LZTR1 trials, further screens of BTBD7 were not performed.

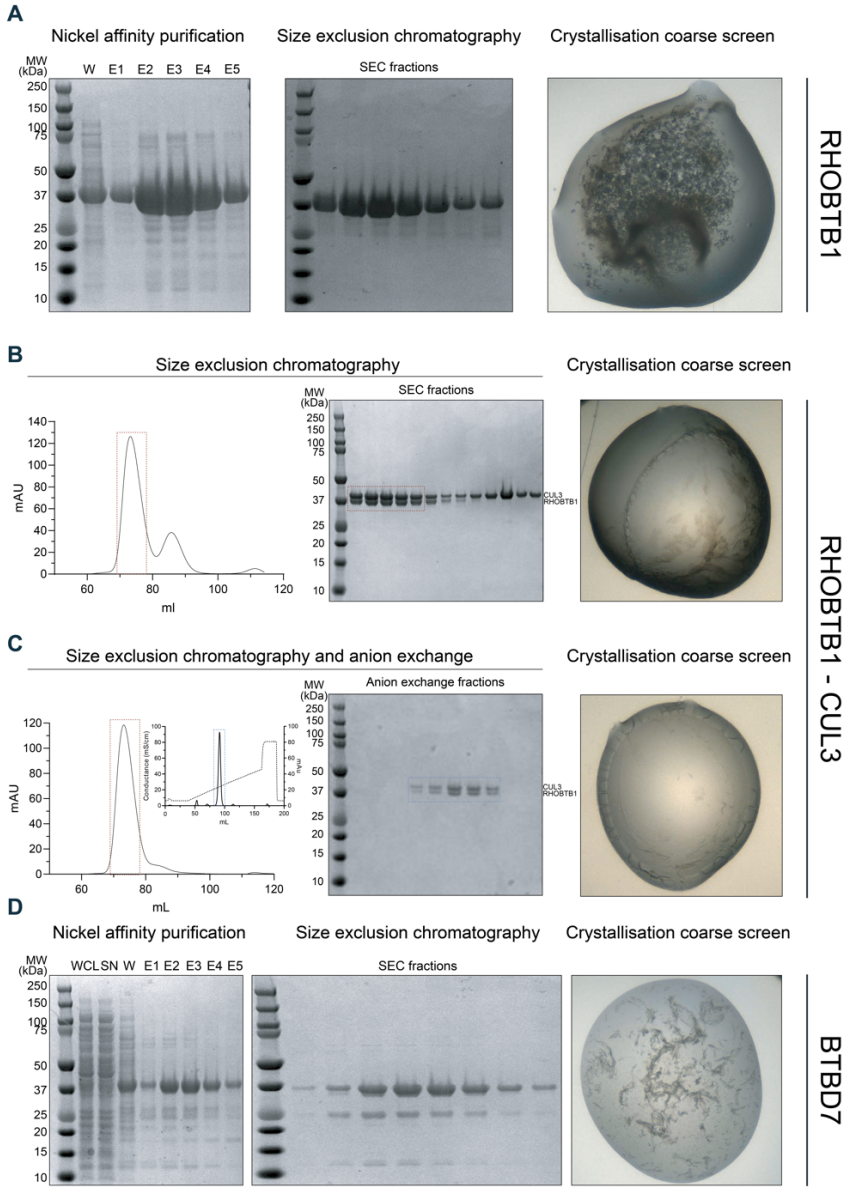


Figure 4.7 Crystallisation trials of BTBD7$_{118-483}$ and RHOBTB1$_{252-591}$. (A,D) Crystallisation trials of isolated RHOBTB1$_{252-591}$ (A) and BTBD7$_{118-483}$ (D) depicting SDS-PAGE Coomassie gels of the protein preparation for crystallisation trials (left two panels) and a representative photograph of protein precipitates that formed in crystallisation coarse screens (right panel). Nickel affinity purification gels (left panels) are labelled with whole cell lysate (WCL), supernatant (SN), washes (W), and elutions 1-5 (E1-E5). SEC gels (middle panels) show the SEC fractions that were collected and concentrated for setting up crystal trays. (B,C) Chromatograms (left panels), SDS-PAGE Coomassie gels (middle panels), and photographic images (right panels) depicting two different purification workflows of the RHOBTB1$_{252-591}$-CUL3 complex for crystallisation trials. Purified RHOBTB1$_{252-591}$ was mixed with CUL3, subjected to SEC, and the bracketed SEC fractions were pooled and concentrated for crystal trays (B). Indistinct crystal rings were observed in several wells. In a subsequent attempt at purifying the RHOBTB1$_{252-591}$-CUL3 complex (C), SEC fractions of the complex were pooled and subjected to anion exchange (inset of SEC chromatogram), the bracketed anion exchange fractions were pooled and concentrated to set up crystal trays. Indistinct crystal rings were once again observed.

4.2.8 Compatibility of CUL3 binding to AlphaFold models of BTBD7, RHOBTB1, and LZTR1

For reasons described above and in the discussion section of chapter 4, crystal structures of the tandem BTB domain or in complex with CUL3 were not obtained. Accordingly, I modelled AlphaFold protein structure predictions of BTBD7, RHOBTB1, and LZTR1 with the expected CUL3 interface. As described in methods section 2.15.1, each BTB domain of these three tandem BTB domain proteins was superimposed on the BTB domain of KLHL11 in the KLHL11-CUL3 complex (PDB ID 4AP2). In the KLHL11-CUL3 complex, the amino-terminal extension of CUL3 interacts with a hydrophobic groove in the amino-terminal portion of KLHL11's BACK domain known as a 3-box motif (Figure 4.8A). The resulting BTB-CUL3 interfaces of each BTB domain of BTBD7, RHOBTB1, and LZTR1 were evaluated to determine if 1) the models support the obtained results showing that BTBD7 failed to bind to CUL3 while RHOBTB1 and LZTR1 bound to CUL3; and 2) whether one or both of the tandem BTB domains of the

RHOBTB1 and LZTR1 models were compatible with the CUL3 binding surface – thus providing hints regarding the functionality of each tandem BTB domain.

Superimposing BTBD7's BTB domains (BTB1 and BTB2) on the KLHL11 BTB domain in the KLHL11-CUL3 complex yielded an RMSD value of 18.6 $Å^2$ (suggesting a poor fit of the BTB domain superimposition) (Figure 4.8B). Clashes were noted between the amino-terminus of CUL3 and B1-B3 of BTBD7's BTB1 domain and A1-A2 of BTBD7's BTB2 domain (Figure 4.8B). Superimposing the BTB2 and BACK-LIKE domain of BTBD7 with the BTB domain of KLHL11 in the KLHL11-CUL3 complex yielded an improved RMSD value of 6.8 $Å^2$, however major clashes existed between the alpha helices of BTBD7's BACK-LIKE domain and CUL3 (Figure 4.8B). Such results suggested BTBD7 is unlikely to bind CUL3 in a manner similar to KLHL11 and supported the co-immunoprecipitation and SEC-MALS data showing BTBD7 failed to bind CUL3.

Superimposing BTB1 of RHOBTB1 with the BTB domain of KLHL11 in the KLHL11-CUL3 complex yielded an RMSD value of 1.3 $Å^2$. Depicted in Figure 4.8C, BTB1 of RHOBTB1 does not contain the final alpha helices of the conventional BTB domain and superimposed best on the amino-terminal portion of KLHL11's BTB domain that is situated far from the BTB-CUL3 interface, suggesting BTB1 is unlikely to mediate interactions between RHOBTB1 and CUL3. Superimposing the BTB2-BACK domains as well as the BTB1-BTB2-BACK domains of RHOBTB1 with the BTB domain of KLHL11 in the KLHL11-CUL3 complex both yielded RMSD values of 2.6 $Å^2$, suggesting that both BTB domains of RHOBTB1 superimposed better with KLHL11 compared to BTBD7

superimposed with KLHL11. The 3-box motif mediating the interaction between KLHL11 and CUL3 was also present in RHOBTB1 (Figure 4.8C). In both models of RHOBTB1 with CUL3, the amino-terminus of CUL3 fitted within the 3-box between the BTB2 and BACK domains of RHOBTB1 in a manner similar to that of KLHL11 (Figure 4.8C). Such results suggested the second BTB domain of RHOBTB1 mediated the interaction between RHOBTB1 and CUL3.

Superimposing BTB1 of LZTR1 with the BTB domain of KLHL11 in the KLHL11-CUL3 complex yielded an RMSD value of 3.4 $Å^2$. Similar superimposition of the BTB2 and BACK domains of LZTR1 yielded an RMSD value of 6.0 $Å^2$. In contrast to the RHOBTB1-CUL3 models, both BTB1 and BTB2 of LZTR1 modelled well with CUL3 (Figure 4.8D). In such models, one CUL3 molecule fits between the BTB2 and BACK domains of LZTR1 and another CUL3 molecule could interact with the carboxy-terminus of LZTR1's BTB1 domain (Figure 4.8D). Modelling the two CUL3 molecules with the BTB1-BTB2-BACK and KELCH domains of LZTR1 showed a long flexible region linking the KELCH and BTB1 domain of LZTR1. The KELCH domain is known to be a substrate recruitment domain of the CRL complex (9). In this model of LZTR1 with CUL3, the KELCH domain of LZTR1 is positioned such that it could alternate between providing substrates to each of the two CUL3 molecules (Figure 4.8D). This model in which LZTR1 interacts with two CUL3 molecules is supported by the SEC-MALS data that suggested the LZTR1-CUL3 complex was comprised of three molecules (Table 4.1).

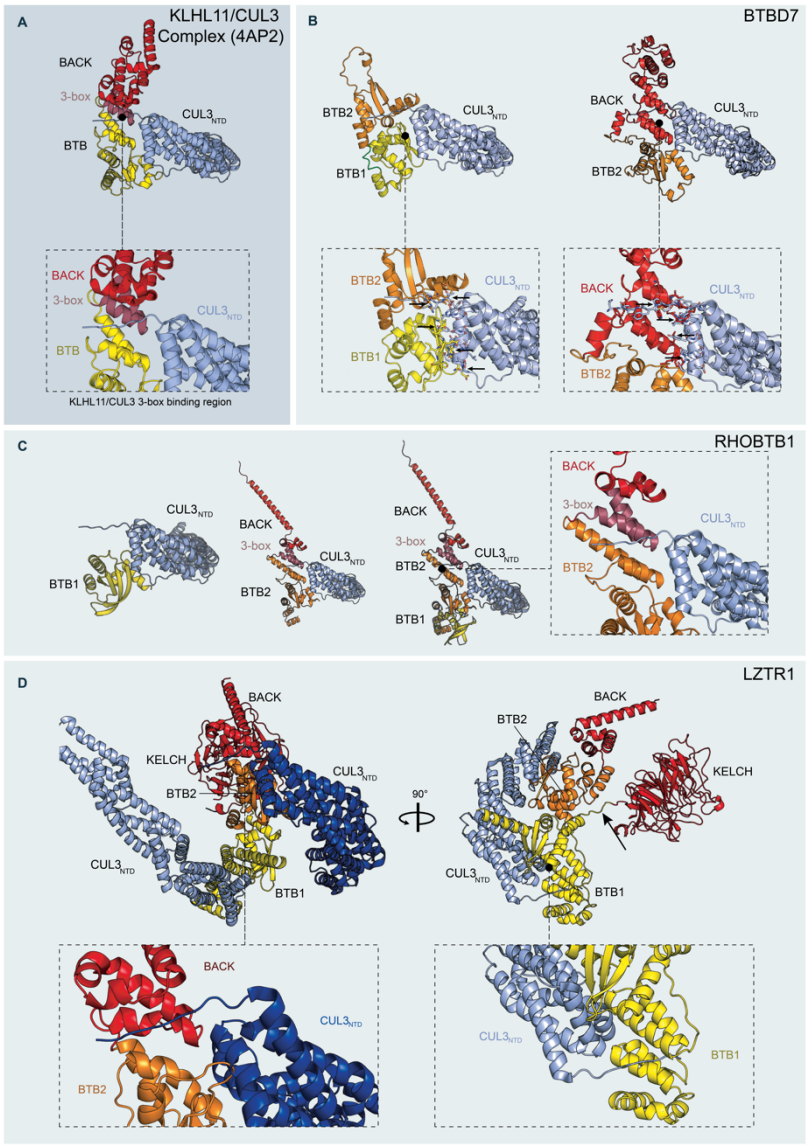


Figure 4.8 Modelling of CUL3 binding to tandem BTB AlphaFold models. (A) Ribbon diagram of the human KLHL11-CUL3 structure (PDB ID 4AP2) highlighting the functional domains of the complex. As described in B-D, AlphaFold protein structure predictions of the BTB domains of BTBD7, RHOBTB1, and LZTR1 were superimposed on the BTB domain of KLHL11 in the KLHL11-CUL3 complex to model structure predictions of these three tandem BTB proteins with the expected CUL3 interface. *In vivo*, KLHL11 forms a homodimer to recruit two CUL3 molecules. A single protamer of the KLHL11-CUL3 dimer is depicted. (B) Models of the BTB1 and BTB2 domains (left) and BTB2 and BACK domains (right) of BTBD7 with CUL3 created by superimposing each BTB domain of BTBD7 on the BTB domain of KLHL11 in the KLHL11-CUL3 complex. Clashes were noted between each BTB and BACK domain of BTBD7 with the amino terminus of CUL3 (general regions of clashes are shown as sticks with example clashes demarcated by black arrows in the zoomed panels). (C) Models of the BTB1, BTB2-BACK, and BTB1-BTB2-BACK domains of RHOBTB1 with CUL3 created by superimposing each BTB domain of

RHOBTB1 on the BTB domain of KLHL11 in the KLHL11-CUL3 complex. The first BTB domain of RHOBTB1 superimposed on KLHL11 far from the CUL3 interface and did not contain a carboxy-terminal alpha helix typically present in the BTB domain. The second BTB domain of RHOBTB1 does contain this carboxy-terminal helix as well as the 3-box motif noted for its interaction with CUL3. The modelled binding interface between the second BTB domain of RHOBTB1 and CUL3 is in the close-up panel to the right of C. (D) Models of the KELCH-BTB1-BTB2-BACK domains of LZTR1 with CUL3 created by superimposing each BTB domain of LZTR1 on the BTB domain of KLHL11 in the KLHL11-CUL3 complex. Both BTB domains of LZTR1 resemble the conventional BTB domain and fit well with CUL3. Modelling two CUL3 units onto a single LZTR1 molecule places the substrate-recruiting KELCH repeat domain of LZTR1 in a position that allows it to interact with both CUL3 proteins. In the right panel, the dark blue CUL3 molecule has been removed to show the flexible linker joining the KELCH repeat domains and BTB1 domains of LZTR1 (a black arrow points to this flexible linker). Bottom panels depict zoomed versions of the CUL3 interfaces of each BTB domain of LZTR1. To create figure 4.8, ribbon structures of the AlphaFold models of BTBD7, RHOBTB1, and LZTR1 were modified in Pymol (28) as follows: 1) some regions predicted to have intrinsic disorder were removed (to aid in visualisation of the protein complex), 2) BTB1 domains were coloured yellow, BTB2 domains orange, and all other domains red, and 3) CUL3 molecules were coloured light blue and dark blue.

4.3 DISCUSSION

In this chapter, I characterised the oligomerisation of tandem BTB domain-containing proteins as well as their ability to assemble into CUL3-based Cullin-RING Ligases. Reflected by only four of the 75 successfully cloned and transformed constructs producing soluble protein, the tandem BTB domain proteins were challenging to make as recombinant protein. The Structural Genomics Consortium (SGC) has been attempting to produce these tandem BTB proteins for several years with no success. Indeed, the SGC had previously cloned 47 different constructs of LZTR1 and tried several expression systems, none of which produced soluble protein. Thus, the success of my construct represents a small breakthrough. As noted in section 2.8, different expression strategies can be used in future works to attempt to produce the tandem BTB constructs designed herein. Mammalian expression systems that introduce

proper post-translational modifications onto the expressed protein may offer improved success in producing properly folded and stable soluble protein. Although BTBD7, RHOBTB1, and LZTR1 each contain tandem BTB domains, their surrounding domain architectures vary, with BTBD7 containing several large, disordered regions, RHOBTB1 containing an amino-terminal GTPase domain, and LZTR1 containing six amino-terminal Kelch repeat motifs (Figure 1.4). The constructs used in this chapter isolated the tandem BTB domains of these proteins (a potential limitation discussed later in this section).

This is one of the first reports discussing the oligomerisation potential of the tandem BTB domain. Although Stogios et al. proposed the tandem BTB domains of RHOBTB1 may form an intramolecular dimer (10), studies exploring the biophysical nature of the tandem BTB domain have been limited. Berthold et al. used a yeast two-hybrid approach to report RHOBTB2 homodimerises with itself and heterodimerises with RHOBTB3 (11). Similarly, Abe et al. reported LZTR1 is capable of homodimerising with a second copy of LZTR1 to form a complex of two LZTR1 proteins, one CUL3 subunit, and one RAS substrate (12). The SEC-MALS data in this report supported such a model of the LZTR1-CUL3 complex with MALS data suggesting three protein subunits were present in the LZTR1-CUL3 complex. However, it is unclear from the data reported herein if there are two LZTR1 and one CUL3, or one LZTR1 and two CUL3 proteins in the LZTR1-CUL3 complex. To help shed light on the structural nature of LZTR1's regulation of RAS/MAPK signalling, Paladino et al. modelled LZTR1 in complex with interacting protein RIT1 (9). However, such modelling has limitations in that it did not consider LZTR1 oligomerisation and focused predominantly on LZTR1's

substrate-binding Kelch domain (9). SEC-MALS results depicted the three tandem BTB proteins characterised in this study may each adopt different oligomeric states. It was clear that RHOBTB1 formed a predominantly monomeric species in solution, in contrast to the homodimerisation Berthold et al. observed with RHOBTB2 and RHOBTB3 (11). Haga et al. expanded these findings to show RHOBTB1 similarly homodimerises using constructs encompassing amino acids 1-210 of RHOBTB1 (13). The discrepancy between this report and those reporting RHOBTB1 dimerisation may be due to the differences in RHOBTB1 construct boundaries. Haga et al. used residues 1-210 of RHOBTB1 which includes the amino-terminal GTPase domain but excludes the two BTB domains and conserved carboxy-terminal domain. This report excluded the first 252 residues encompassing the GTPase domain of RHOBTB1 and thus may have removed additional residues critical for dimerisation. This monomeric species of RHOBTB1 also contrasts with the predominantly dimeric species formed by LZTR1. Structural modelling of RHOBTB1 and LZTR1 depicts the flexible linker joining the two BTB domains of RHOBTB1 is approximately half that of LZTR1 (a flexible linker of 8 versus 16 residues). This difference in flexible linker length may influence the ability of the BTB domains to dimerise, whether as an intramolecular pseudodimer or intermolecularly with a second copy of the tandem BTB protein. The presence of intramolecular BTB-BTB domain interactions as a pseudodimer cannot be determined by SEC-MALS and would require structural information from X-ray crystallography or another technique. The oligomeric nature of BTBD7 could not be accurately determined by SEC-MALS, with observed elution volumes suggesting the presence of a potentially dimeric species but observed MALS data failing to confirm such a

dimeric species. These results may be due in part to the observed non-specific interactions of BTBD7 with the column matrix. Future experiments could use site directed mutagenesis to assess protein folding interfaces of BTBD7. Additional methods that could be used to characterise the oligomeric status of BTBD7 and other tandem BTB proteins include native polyacrylamide gel electrophoresis, circular dichroism spectroscopy, and nuclear magnetic resonance spectroscopy, among others.

SEC-MALS, co-immunoprecipitation, and differential scanning fluorimetry results all suggested the three tandem BTB proteins exhibit different binding characteristics with CUL3. Functional characterisations of proteins containing tandem BTB domains has highlighted their roles as CUL3-based E3 ubiquitin ligases. However, results from this chapter confirm that not all tandem BTB proteins interact with CUL3. Interactions between LZTR1 as well as RHOBTB1 with CUL3 have been extensively investigated (11, 14-16) and findings from this chapter confirm such an interaction. SEC-MALS data suggested the complex of LZTR1 and CUL3 contained a different number of protein subunits compared to the RHOBTB1-CUL3 complex, with the LZTR1-CUL3 complex containing three subunits and the RHOBTB1-CUL3 complex two. Modelling the LZTR1-CUL3 complex by superimposing each BTB domain of LZTR1 onto the BTB domain of KLHL11 in the KLHL11-CUL3 complex (PDB ID 4AP2) suggested CUL3 may be able to bind to both BTB domains of LZTR1. In such a complex, the KELCH domain is linked to the amino terminus of BTB1 via a flexible linker and is positioned such that it could bring protein substrates into proximity of either CUL3 molecule for ubiquitination (Figure 4.8D). Due to the similarity in molecular

weight of the LZTR1 and CUL3 constructs, the ratio of LZTR1:CUL3 cannot be determined from the results of this thesis – a single LZTR1 protein may be recruiting two CUL3 proteins, one to each BTB domain, or the LZTR1 subunits may be dimerising and recruiting only a single CUL3. Regardless of final stoichiometry, the binding affinity between LZTR1 and CUL3 appears to be less than that of RHOBTB1 and CUL3. Such an observation can be witnessed in both the large elution peak of the RHOBTB1-CUL3 complex from SEC-MALS as well as the shift in T_m observed in the differential scanning fluorimetry experiments when RHOBTB1 is mixed with CUL3 compared to solutions of isolated RHOBTB1. Superimposing each of the BTB domains of RHOBTB1's AlphaFold structure on the BTB domain of KLHL11 in the KLHL11-CUL3 complex (PDB ID 4AP2) suggested the second BTB domain of RHOBTB1 is more likely to serve as the CUL3 interaction domain (Figure 4.8C). In this model, RHOBTB1 contained the 3-box motif noted to be critical for CUL3 interactions. LZTR1 is not predicted to contain such a 3-box motif, thus explaining the comparatively greater binding affinity between RHOBTB1 and CUL3 versus LZTR1 and CUL3.

In contrast to RHOBTB1 and LZTR1, co-immunoprecipitation, SEC-MALS, and differential scanning fluorimetry all suggested BTBD7 does not interact with CUL3. In 2010, Bennett et al., used a large-scale proteomic approach to propose CUL3 interacted with BTBD7 (5). However, no report since has confirmed such an interaction. Results from this thesis using several methods failed to support this initially reported interaction. Similarly, in contrast to RHOBTB1 and LZTR1, plausible models of BTBD7 in complex with CUL3 could not be modelled using the AlphaFold structure of BTBD7 and the KLHL11-CUL3 complex (PDB ID

4AP2). Nevertheless, it is important to note that the lack of BTBD7-CUL3 interaction may be an artefact of the truncated clones used in this study.

As noted in the paragraphs above, the truncated nature of the constructs used in this thesis must be considered when interpreting results pertaining to tandem BTB domain oligomerisation and CUL3 interactions. The 3-box motif consists of two α-helices at the amino terminus of the BACK domain and has been reported to be critical for CUL3 interactions (17, 18). Structural models of RHOBTB1 suggest the presence of this 3-box motif. Although data from this report show strong CUL3 interactions with $RHOBTB1_{252\text{-}591}$, this construct does not contain the predicted 3-box motif which appears to comprise residues V590-N623 of RHOBTB1. A similar double α-helix motif in the BACK domain was not observed in the models of LZTR1 and BTBD7. Truncations of the BTBD7, RHOBTB1, and LZTR1 constructs, in addition to potentially removing residues mediating protein oligomerisation and CUL3 binding, may cause exposure of hydrophobic surfaces that would be otherwise buried in protein folds. The high SYPRO Orange binding observed in differential scanning fluorimetry with the RHOBTB1 and BTBD7 constructs suggests these two constructs indeed may contain large hydrophobic surface areas. Cellular thermal shift assay (CETSA) which quantifies changes in a protein's thermal stability upon binding ligands in intact cells (19) could be performed to further assess stability of RHOBTB1 and BTBD7 constructs. Results of differential scanning fluorimetry and crystallisation trials of BTBD7 and RHOBTB1 suggested the protein quality of these two proteins must be improved to achieve any future success in crystallisation. Locating ligands capable of binding and stabilising the proteins as well as screening buffer in which the

proteins are most stable could enhance protein stability and improve the likelihood of crystallisation. To further characterise the interactions between RHOBTB1 or LZTRZ1 with CUL3, targeted mutations could be introduced in each BTB domain to probe for critical CUL3 binding residues.

4.4 REFERENCES

1. Linding R, Russell RB, Neduva V, Gibson TJ. GlobPlot: Exploring protein sequences for globularity and disorder. Nucleic Acids Res. 2003 Jul 1;31(13):3701-8. doi: 10.1093/nar/gkg519. PMID: 12824398; PMCID: PMC169197.
2. Duvaud S, Gabella C, Lisacek F, Stockinger H, Ioannidis V, Durinx C. Expasy, the Swiss Bioinformatics Resource Portal, as designed by its users. Nucleic Acids Res. 2021 Jul 2;49(W1):W216-W227. doi: 10.1093/nar/gkab225. PMID: 33849055; PMCID: PMC8265094.
3. Berthold J, Schenková K, Ramos S, Miura Y, Furukawa M, Aspenström P, Rivero F. Characterization of RhoBTB-dependent Cul3 ubiquitin ligase complexes--evidence for an autoregulatory mechanism. Exp Cell Res. 2008 Nov 15;314(19):3453-65. doi: 10.1016/j.yexcr.2008.09.005. Epub 2008 Sep 20. PMID: 18835386; PMCID: PMC2749729.
4. Kumar G, Fang S, Golosova D, Lu KT, Brozoski DT, Vazirabad I, Sigmund CD. Structure and Function of RhoBTB1 Required for Substrate Specificity and Cullin-3 Ubiquitination. Function (Oxf). 2023 Jul 3;4(5):zqad034. doi: 10.1093/function/zqad034. PMID: 37575477; PMCID: PMC10413933.
5. Bennett EJ, Rush J, Gygi SP, Harper JW. Dynamics of cullin-RING ubiquitin ligase network revealed by systematic quantitative proteomics. Cell. 2010 Dec 10;143(6):951-65. doi: 10.1016/j.cell.2010.11.017. PMID: 21145461; PMCID: PMC3008586.
6. Smaldone G, Pirone L, Balasco N, Di Gaetano S, Pedone EM, Vitagliano L. Cullin 3 Recognition Is Not a Universal Property among KCTD Proteins. PLoS One. 2015 May 14;10(5):e0126808. doi: 10.1371/journal.pone.0126808. PMID: 25974686; PMCID: PMC4431850.
7. Spiombi E, Angrisani A, Fonte S, De Feudis G, Fabretti F, Cucchi D, Izzo M, Infante P, Miele E, Po A, Di Magno L, Magliozzi R, Guardavaccaro D, Maroder M, Canettieri G, Giannini G, Ferretti E, Gulino A, Di Marcotullio L, Moretti M, De Smaele E. KCTD15 inhibits the Hedgehog pathway in Medulloblastoma cells by increasing protein levels of the oncosuppressor KCASH2. Oncogenesis. 2019 Nov 4;8(11):64. doi: 10.1038/s41389-019-0175-6. PMID: 31685809; PMCID: PMC6828672.
8. Golovanov AP, Hautbergue GM, Wilson SA, Lian LY. A simple method for improving protein solubility and long-term stability. J Am Chem Soc. 2004 Jul 28;126(29):8933-9. doi: 10.1021/ja049297h. PMID: 15264823.

9. Paladino A, D'Angelo F, Noviello TMR, Iavarone A, Ceccarelli M. Structural Model for Recruitment of RIT1 to the LZTR1 E3 Ligase: Evidences from an Integrated Computational Approach. J Chem Inf Model. 2021 Apr 26;61(4):1875-1888. doi: 10.1021/acs.jcim.1c00296. Epub 2021 Apr 1. PMID: 33792302; PMCID: PMC8154269.
10. Stogios PJ, Downs GS, Jauhal JJ, Nandra SK, Privé GG. Sequence and structural analysis of BTB domain proteins. Genome Biol. 2005;6(10):R82. doi: 10.1186/gb-2005-6-10-r82. Epub 2005 Sep 15. PMID: 16207353; PMCID: PMC1257465.
11. Berthold J, Schenková K, Ramos S, Miura Y, Furukawa M, Aspenström P, Rivero F. Characterization of RhoBTB-dependent Cul3 ubiquitin ligase complexes--evidence for an autoregulatory mechanism. Exp Cell Res. 2008 Nov 15;314(19):3453-65. doi: 10.1016/j.yexcr.2008.09.005. Epub 2008 Sep 20. PMID: 18835386; PMCID: PMC2749729.
12. Abe T, Umeki I, Kanno SI, Inoue SI, Niihori T, Aoki Y. LZTR1 facilitates polyubiquitination and degradation of RAS-GTPases. Cell Death Differ. 2020 Mar;27(3):1023-1035. doi: 10.1038/s41418-019-0395-5. Epub 2019 Jul 23. PMID: 31337872; PMCID: PMC7206011.
13. Haga RB, Garg R, Collu F, Borda D'Agua B, Menéndez ST, Colomba A, Fraternali F, Ridley AJ. RhoBTB1 interacts with ROCKs and inhibits invasion. Biochem J. 2019 Sep 13;476(17):2499-2514. doi: 10.1042/BCJ20190203. PMID: 31431478; PMCID: PMC6744581.
14. Zhang H, Cao X, Wang J, Li Q, Zhao Y, Jin X. LZTR1: A promising adaptor of the CUL3 family. Oncol Lett. 2021 Jul;22(1):564. doi: 10.3892/ol.2021.12825. Epub 2021 May 29. PMID: 34113392; PMCID: PMC8185703.
15. Berthold J, Schenkova K, Rivero F. Rho GTPases of the RhoBTB subfamily and tumorigenesis. Acta Pharmacol Sin. 2008 Mar;29(3):285-95. doi: 10.1111/j.1745-7254.2008.00773.x. PMID: 18298893.
16. Ji W, Rivero F. Atypical Rho GTPases of the RhoBTB Subfamily: Roles in Vesicle Trafficking and Tumorigenesis. Cells. 2016 Jun 14;5(2):28. doi: 10.3390/cells5020028. PMID: 27314390; PMCID: PMC4931677.
17. Canning P, Cooper CDO, Krojer T, Murray JW, Pike ACW, Chaikuad A, Keates T, Thangaratnarajah C, Hojzan V, Marsden BD, Gileadi O, Knapp S, von Delft F, Bullock AN. Structural basis for Cul3 protein assembly with the BTB-Kelch family of E3 ubiquitin ligases. J Biol Chem. 2013 Mar 15;288(11):7803-7814. doi: 10.1074/jbc.M112.437996. Epub 2013 Jan 24. Erratum in: J Biol Chem. 2013 Sep 27;388(39):28304. Ayinampudi, Vikram [added]. PMID: 23349464; PMCID: PMC3597819.
18. Adamson RJ, Payne NC, Bartual SG, Mazitschek R, Bullock AN. Structural and biochemical characterization establishes a detailed understanding of KEAP1-CUL3 complex assembly. Free Radic Biol Med. 2023 Aug 1;204:215-225. doi: 10.1016/j.freeradbiomed.2023.04.021. Epub 2023 May 6. PMID: 37156295; PMCID: PMC10564622.
19. Martinez NJ, Asawa RR, Cyr MG, Zakharov A, Urban DJ, Roth JS, Wallgren E, Klumpp-Thomas C, Coussens NP, Rai G, Yang SM, Hall MD, Marugan JJ, Simeonov A, Henderson MJ. A widely-applicable high-throughput cellular

thermal shift assay (CETSA) using split Nano Luciferase. Sci Rep. 2018 Jun 21;8(1):9472. doi: 10.1038/s41598-018-27834-y. PMID: 29930256; PMCID: PMC6013488.

CHAPTER FIVE

The pathogenic roles of BTB domain mutations in craniofacial disease

5.1 INTRODUCTION

The first and second results chapters of my DPhil studies allowed me to characterise BTB domain-containing proteins from basic cell biology and structural biology perspectives, respectively. In this third results chapter, I focused on the BTB domain-containing protein KCTD15 to link basic biological insights with clinical data and human disease. KCTD15 has been linked to cancer progression (1, 2), obesity (3, 4), neural crest development (5, 6), and Wnt/beta-catenin signalling via transcription factor TFAP2 transactivation (6). Although flanking non-coding single nucleotide polymorphisms have been tied to body weight (4), no links between *KCTD15* and Mendelian disease have been reported.

A collaborator in the John Radcliffe hospital (clinical geneticist Andrew Wilkie) met a father and daughter (Family 1) affected by a similar combination of fronto-nasal lipoma, cutis aplasia of the scalp, and congenital heart defects (Figure 5.1A). Andrew Wilkie's group performed trio-based exome sequencing of the affected father and the father's unaffected parents to reveal a single high-confidence non-synonymous *de novo* variant c.310G>C in *KCTD15*, encoding a

p.Asp104His substitution in the protein's BTB domain (Figures 1.3C,D, 5.1A). A second family (Family 2) later presented to Andrew's group with a female proband similarly affected by these distinctive craniofacial conditions (Figure 5.1B). Targeted dideoxy-sequencing of *KCTD15* in the proband and her unaffected parents revealed a *de novo* heterozygous c.263G>A variant predicted to encode p.Gly88Asp also in the BTB domain of the protein (Figures 1.3C,D, 5.1B). The p.Gly88Asp mutation occurs at the equivalent position of a p.Gly62Asp mutation in KCTD1 that is reported to cause SEN (Figure 1.3C,D). No non-synonymous variants in either Asp104 or Gly88 of KCTD15 are recorded in either the gnomADv.2.1.1 or v.3.1.1 databases of normal allelic variation.

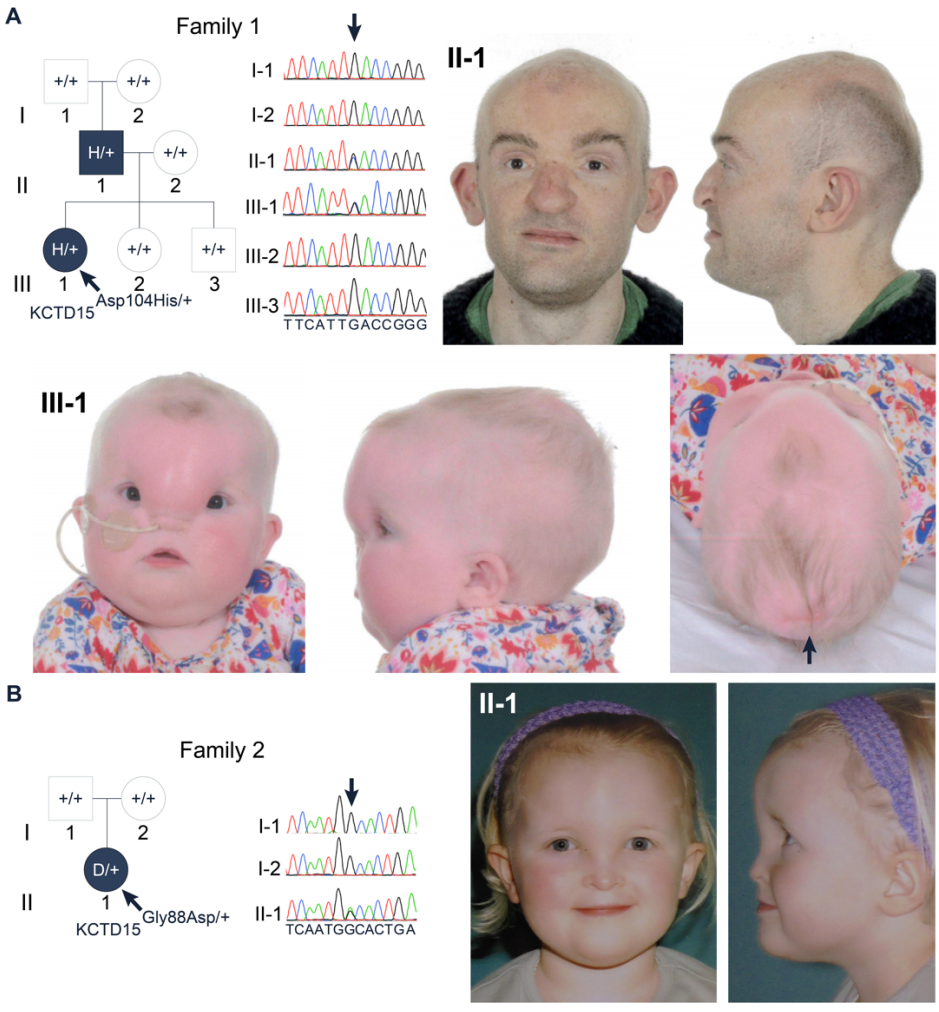


Figure 5.1 The two families affected by missense substitutions in KCTD15. (A) Analysis of Family 1, showing pedigree (left), dideoxy-sequencing of KCTD15 exon 5 (centre), and craniofacial features of two affected family members (right and bottom). Photographs show the affected child III-1 aged 6 months (pre-operative) and her affected father II-1 aged 35 years (post-operative). Both individuals presented with hypertelorism and sparse hair and the child exhibited a large frontonasal lipoma and a region of aplasia cutis posteriorly located on the scalp (black arrow). The sequence showed a heterozygous c.310G>C in II-1 and III-1 (black arrow), which arose *de novo* in II-1. (B) Family 2 showing pedigree (left), dideoxy-sequencing of KCTD15 exon 5 (centre), and preoperative craniofacial features of II-1 aged 3 years (right). Note hypertelorism and midline frontonasal swelling, which showed less lateral extension and nasal involvement compared to the proband in Family 1. The sequence chromatogram showed a heterozygous c.263G>A transition in II-1, absent in both her parents (black arrow).

The association of these two *de novo* missense variants in the same domain of KCTD15 with a clinically similar rare phenotype suggested the variants are causative for the distinct frontonasal dysplasia reminiscent of phenotypes observed in SEN caused by KCTD1 mutations. It was hypothesised the Asp104His and Gly88Asp variants alter protein oligomerisation, stability, and thus biological function. To investigate the underlying mechanism of disease, I designed, cloned, expressed, and purified these pathogenic mutant proteins and performed structural, biophysical, and functional analyses.

5.2 RESULTS

5.2.1 KCTD15 wild type and variants exhibit differing recombinant expression levels and stability

To test the hypothesis that KCTD15 mutations abrogate protein oligomerisation, stability, and function, I initially designed 6 constructs of each KCTD15 wild type, Asp104His, and Gly88Asp encompassing either the BTB domain alone or both the BTB and CTD (Figure 5.2A). Six KCTD1 constructs with matching domain

boundaries were designed as control proteins. Constructs were cloned from template wild-type KCTD15 and KCTD1 cDNA using ligation independent cloning. Site-directed mutagenesis was performed by PCR with mutations incorporated into the cloning primers (see methods for details). KCTD15 constructs were cloned into a pCDF-LIC vector with an amino-terminal 6xHis tag and KCTD1 constructs were cloned into a pNIC-NHT-cTStII vector that incorporated an amino-terminal 6xHis tag and a carboxy-terminal twin-strep tag. Small-scale 50 mL test expressions and purifications of the 24 constructs were performed to assess the production of pure soluble protein (Figure 5.2B). Due to low expression and the presence of several protein contaminants following nickel-NTA affinity purification, the 18 KCTD15 inserts were recloned into a pGTVL2 vector that incorporated an amino-terminal 6xHis-GST tag with a TEV cleavage site. After attempting several different methods of purification (nickel resin purification, size exclusion chromatography using HiLoad 16/600 Superdex 75 and 200 preparatory grade columns, anion exchange, nickel rebinding), the purification workflow that consistently produced the highest yield of purified protein involved binding GST-tagged protein to glutathione Sepharose resin, TEV cleaving protein from the resin overnight, collecting the cleaved proteins in the morning and purifying the proteins with size-exclusion chromatography (SEC) on a HiLoad 16/600 Superdex 200 pg column (Figure 5.2C). This workflow produced significantly higher yields of cleaved soluble pure protein compared to eluting GST-tagged protein from the resin with glutathione prior to SEC (Figure 5.2C).

Large-scale expressions and purifications of the KCTD15 constructs provided preliminary insights into protein stability. KCTD15 Gly88Asp constructs encompassing both the BTB and CTD regions (aa52-283 [designated $KCTD15_{BTB+CTD}$]) were significantly less stable than the isolated BTB domain (aa52-165 [designated $KCTD15_{BTB}$]), with $KCTD15_{BTB+CTD}$ Gly88Asp, but not $KCTD15_{BTB}$ Gly88Asp, forming a precipitate upon concentrating (Figure 5.2D). Similar results were observed with KCTD15 WT and the Asp104His variant; didomain constructs exhibited significantly decreased yield and more readily precipitated at higher concentrations compared to their isolated BTB domain counterparts. Comparing overall protein yields among the three KCTD15 proteins, Gly88Asp variant proteins exhibited a significantly higher yield than WT and Asp104His variant proteins, with Asp104His variant constructs producing the lowest yield.

After optimising expression and purification workflows as described above, I succeeded in producing pure soluble protein of KCTD15 wild type, Asp104His, and Gly88Asp for use in biophysical experiments (Figure 5.2E). However, the aforementioned variations in protein yield and stability upon concentrating resulted in some constructs failing to form crystals for structural analysis, as described in the following sections.

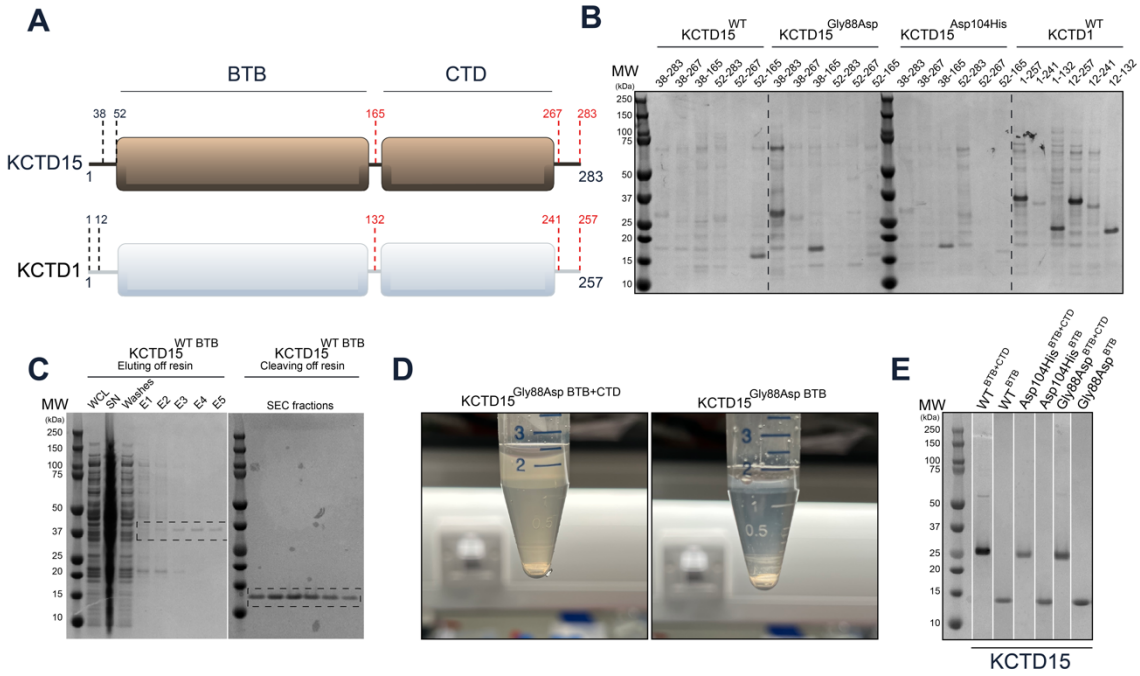


Figure 5.2 Optimising the expression and purification of KCTD15 constructs. An overview of the design (A) and purification (B-E) of KCTD15 wild type and variants. (A) A domain map graphic of KCTD15 and KCTD1 showing the amino termini (black numbers) and carboxy termini (red numbers) of the 24 cloned KCTD15 and KCTD1 constructs. (B) SDS-PAGE Coomassie gel of test purifications of the 24 constructs after cloning into the pCDF-LIC (KCTD15) and pNIC-NHT-cTStII (KCTD1) vectors showing the poor expression levels of the KCTD15 constructs. (C) SDS-PAGE Coomassie gel of KCTD15 BTB wild type after recloning into a pGTVL2 vector showing the variation in protein yield with eluting off resin (left image) versus cleaving off resin (right image). (D) Photographs showing the variations in stability of the KCTD15 BTB+CTD versus KCTD15 BTB constructs, with the multidomain construct forming a precipitate at room temperature (left image). (E) SDS-PAGE Coomassie gels of the purified KCTD15 BTB and KCTD15 BTB+CTD constructs used for experiments in this chapter.

5.2.2 Homology models predict the KCTD15 substitution Asp104His disrupts BTB domain oligomerisation

The structure of KCTD15 has not been previously determined. However, crystal structures of KCTD15's paralogues KCTD1 and KCTD16 have been solved and show they can assemble into open and closed pentameric oligomers (Figure 5.3A). KCTD16 was reported to function in $GABA_B$ receptor signalling by forming an open pentameric assembly to bind the carboxy-terminal region of the

intracellular component of the $GABA_{B2}$ receptor, thus stabilising the receptor at the cell membrane (7) (Figure 5.3A). This open KCTD16 pentamer was also reported to bind a sixth BTB domain to form an inhibitory hexamer (7) (Figure 5.3A). Low resolution observations from negative stain electron microscopy (EM) showed the BTB domain of KCTD15 can similarly adopt open and closed pentamers (8).

To gain preliminary insights testing the hypothesis that the two missense substitutions in KCTD15 alter protein oligomerisation, I built homology models of wild-type and variant BTB domains in the ICM-Pro (Molsoft) software package using the available KCTD1 structure PDB 5BXB. The KCTD15 Asp104His substitution mapped to the oligomerisation interface where the side chain of aspartate 104 was predicted to form a salt bridge to Arg118 and hydrogen bonds with Ser69 and Thr73 on the neighbouring BTB domain subunit (Figure 5.3B,C). The Asp104His substitution was predicted to ablate these inter-subunit interactions thus preventing protein oligomerisation (Figure 5.3C,D). In contrast, the KCTD15 Gly88Asp substitution did not map to an oligomerisation interface but instead to the solvent exposed α2-β3 loop of the BTB domain (Figure 5.3E). Accordingly, it was unclear from homology modelling how the Gly88Asp variant could be disrupting protein oligomerisation.

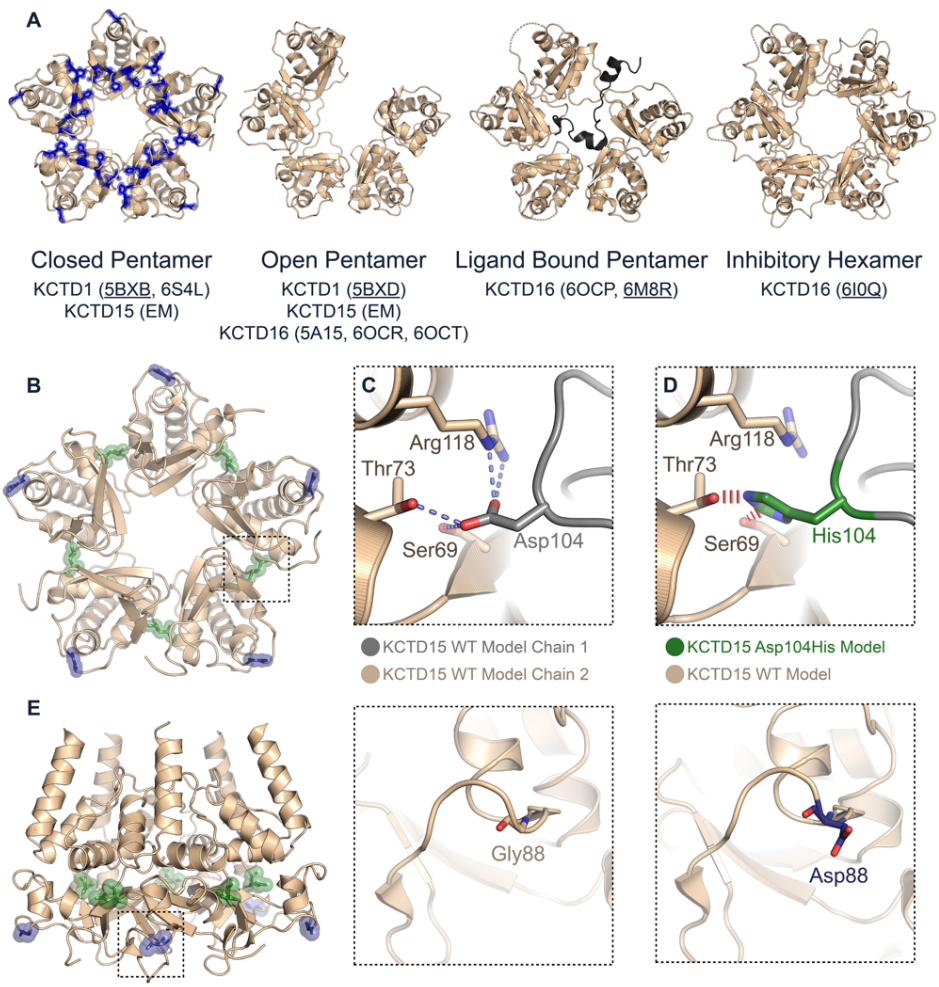


Figure 5.3 Published structures of KCTD15 homologues alongside homology modelling of KCTD15 wild type and variants. (A) Previously published structural assemblies of the BTB domains of KCTD1, KCTD15, and KCTD16; crystal structure PDB codes are given in parenthesis (PDBs used for figures are underlined), while EM denotes negative stain electron microscopy imaging. KCTD1 and KCTD15 can form open and closed pentameric rings. Blue sticks in the closed pentamer model of KCTD1 indicate residues with substitutions in SEN. KCTD16 adopts a similar open pentameric ring to bind a $GABAB_2$-derived peptide. This binding is inhibited if a sixth BTB domain is incorporated into the complex. (B) Homology model of wild-type KCTD15 BTB domain shown as a closed pentamer with the Gly88 and Asp104 side chain positions highlighted in blue and green, respectively. (C) Model of the wild-type KCTD15 BTB domain oligomerisation interface showing the critical inter-subunit interactions (blue dashed lines) mediated by Asp104 of one BTB subunit (grey) with Arg118, Ser69, and Thr73 of the neighbouring BTB subunit (light brown). (D) Model depicting how the Asp104His substitution (green) will abrogate oligomerisation by breaking the inter-subunit salt bridge with Arg118 and introducing steric clashes (red lines) with Ser69 and Thr73. (E) Model depicting Gly88 lying in the solvent exposed α2-β3 loop of KCTD15, away from the inter-subunit oligomerisation interface.

5.2.3 Crystallographic analysis of KCTD15 wild type and variants

I attempted to purify and obtain crystals of the isolated BTB domains (residues 52-165) and BTB+CTD domains (residues 52-283) of KCTD15 wild type and the two KCTD15 variants. Of these attempts, only the Gly88Asp variant BTB domain yielded diffracting crystals. Two distinct crystal morphologies were obtained and yielded two distinct X-ray diffraction datasets for the two crystal structures (Figure 5.4A-D). One crystal structure dataset was solved in space group $P4_32_12$ at 2.25 Å resolution and the other in space group $P1$ at 1.96 Å resolution (Figure 5.4A,B, Table 5.1). In both structures, the KCTD15 Gly88Asp BTB domain variant was observed to form closed hexameric rings (Figure 5.5), reminiscent of the previously reported inhibitory hexamer of KCTD16 (Figure 5.3A, Figure 5.5A). In contrast to the KCTD16 hexamer which contained a poor fitting out of plane sixth subunit (Figure 5.5A), the KCTD15 mutant hexameric ring was completely planar, suggesting a more stable packing arrangement of the KCTD15 variant (Figure 5.5B).

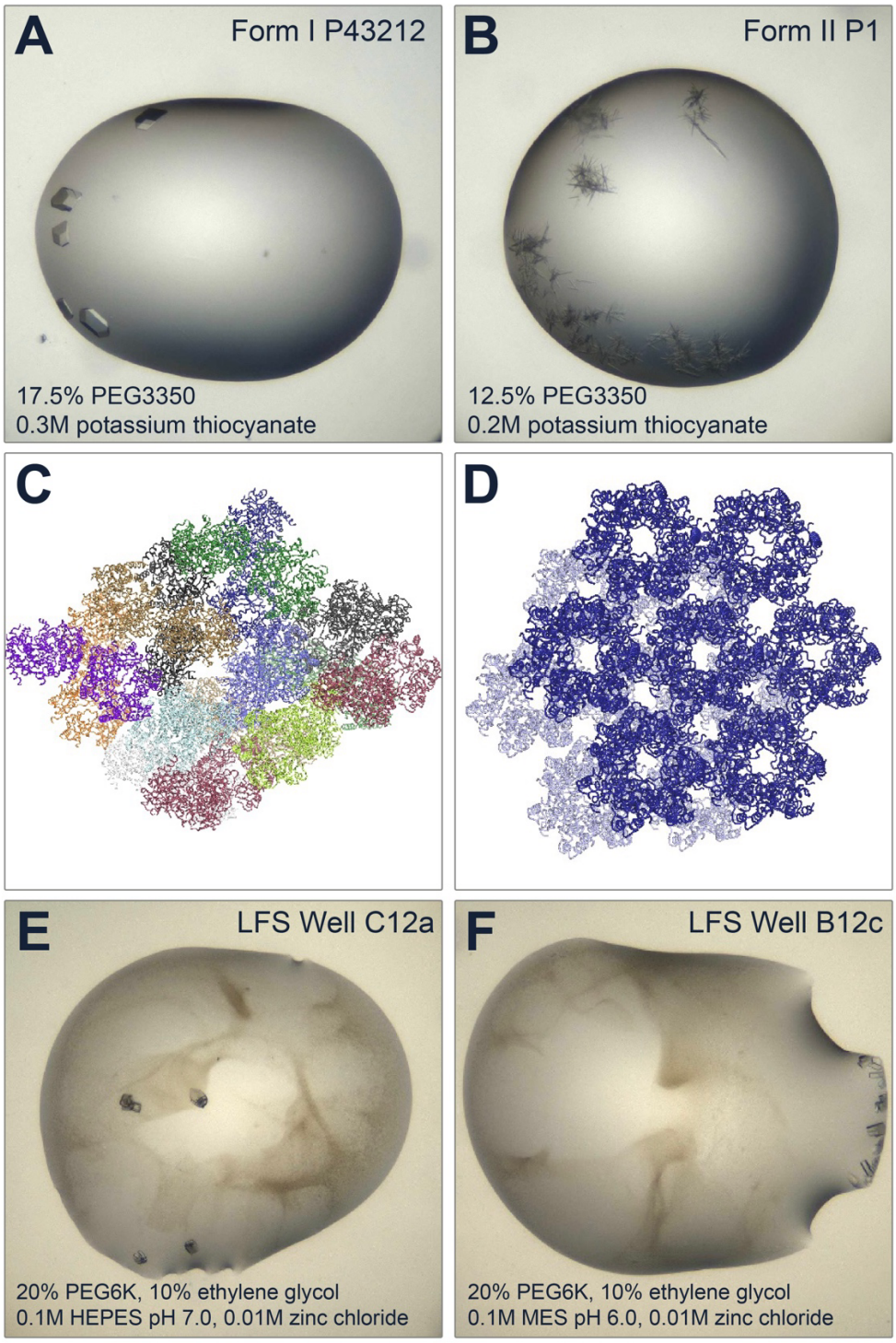


Figure 5.4 Crystal forms of KCTD15 Gly88Asp BTB domain and crystallisation trials of KCTD15 Asp104His. Photographic images of KCTD15 Gly88Asp crystal form I (A) and crystal form II (B) with crystallisation conditions shown in the bottom left corner of the images. Crystal lattice images for KCTD15 Gly88Asp crystal form I (C) and crystal form II (D). Photographic images of KCTD15 Asp104His BTB domain crystallisation trials (E, F). Coarse screen name and wells are presented in the top right corners and well conditions in the bottom left corners of the images.

Table 5.1 KCTD15 G88D crystallographic data collection and refinement statistics.

	Crystal form I PDB: 8PNR	Crystal form II PDB: 8PNM
Data Collection		
Wavelength	0.976254	0.976254
Resolution range	78.0 - 2.25 (2.29-2.25)	91.3 - 1.95 (2.12 - 1.96)
Space group	$P4_32_12$	$P1$
Unit cell dimensions:		
a, b, c (Å)	151.1, 151.1, 156.0	71.3, 72.1, 94.4
α, β, γ (°)	90.0, 90.0, 90.0	89.6, 77.1, 60.5
Total reflections	2341293	276137 (13890)
Unique reflections	85815 (4227)	75791 (3791)
Multiplicity	27.28	3.6
Completeness (%)	100.0 (100.0)	92.5 (61.2)
Mean I/sigma (I)	14.8	14.2
Wilson B-factor	54.44	37.99
R-merge	0.127 (4.460)	0.044 (0.797)
R-meas	0.130	0.052
R-pim	0.025	0.027
CC1/2	0.9945	0.999
Refinement		
R-work	0.246	0.226
R-free	0.285	0.267
Number of non-hydrogen atoms	18138	9623
Macromolecules	18049	9377
Ligands	0	0
Solvent	89	246
Protein residues	1191	1215
RMS (bonds, Å)	0.009	0.006
RMS (angles, °)	1.246	0.798
Ramachandran favoured (%)	94.83	95.29
Ramachandran allowed (%)	4.73	4.37
Ramachandran outliers (%)	0.44	0.34
Rotamer outliers (%)	1.56	0.00
Clashscore	7.76	2.83
Average B-factor ($Å^2$)	79.16	57.09
Macromolecules	81.12	57.94
Ligands	NA	NA
Solvent	65.59	50.90

Statistics for the highest-resolution shell are shown in parentheses.

Confirming prior observations from homology modelling of KCTD15 Gly88, crystal structures of KCTD15 Gly88Asp revealed the Gly88Asp substitution lies in a solvent-exposed surface of the α2-β3 loop of the BTB domain (Figure 5.5B). As previously noted, the Gly88Asp substitution in KCTD15 occurs at the same position as the Gly62Asp substitution of KCTD1. Without a side chain, glycine residues can adopt disfavoured conformations for neighbouring amino acids. Gly62 of KCTD1 adopts such a conformation (ϕ, ψ ~ 95°, 0°). Resultantly, it is predicted that any substitution in Gly62 of KCTD1 would destabilise the protein structure (9). Such a prediction is supported by the crystal structures of KCTD15 Gly88Asp. In each KCTD15 Gly88Asp crystal structure, one asymmetric unit was comprised of two hexamers. Between the two different crystal forms, a total of 24 BTB domains (four hexamers) were modelled. In five of the BTB domains of each of the four hexamers (20 of the 24 BTB domains), the Gly88Asp substitution site was rotated 180° relative to the modelled wild-type KCTD15 and the solved KCTD1 structure (Figure 5.5C-E). The average Phi, Psi (ϕ, ψ) angles of Gly62 in the three deposited KCTD1 structures (5bxb, 5bxd, and 6s4l) are (ϕ, ψ, 104°, -1°) (Figure 5.5E). Averaging the 20 rotated Asp88 residues of the two crystal structures, the Phi, Psi angles are (ϕ, ψ, -107°,18°) (Figure 5.5E). Such a rotation displaces the α2-β3 loop 9 Å. The α2-β3 loop extends towards the oligomerisation interface, suggesting long range effects in this loop shift contributed to the hexameric mutant assembly (Figure 5.5C,D). In the sixth BTB domain of each hexamer (a total of four of the 24 BTB domains), the Gly88Asp position either adopted the predicted wild-type conformation (Figure 5.5D,E) or was disordered and could not be modelled.

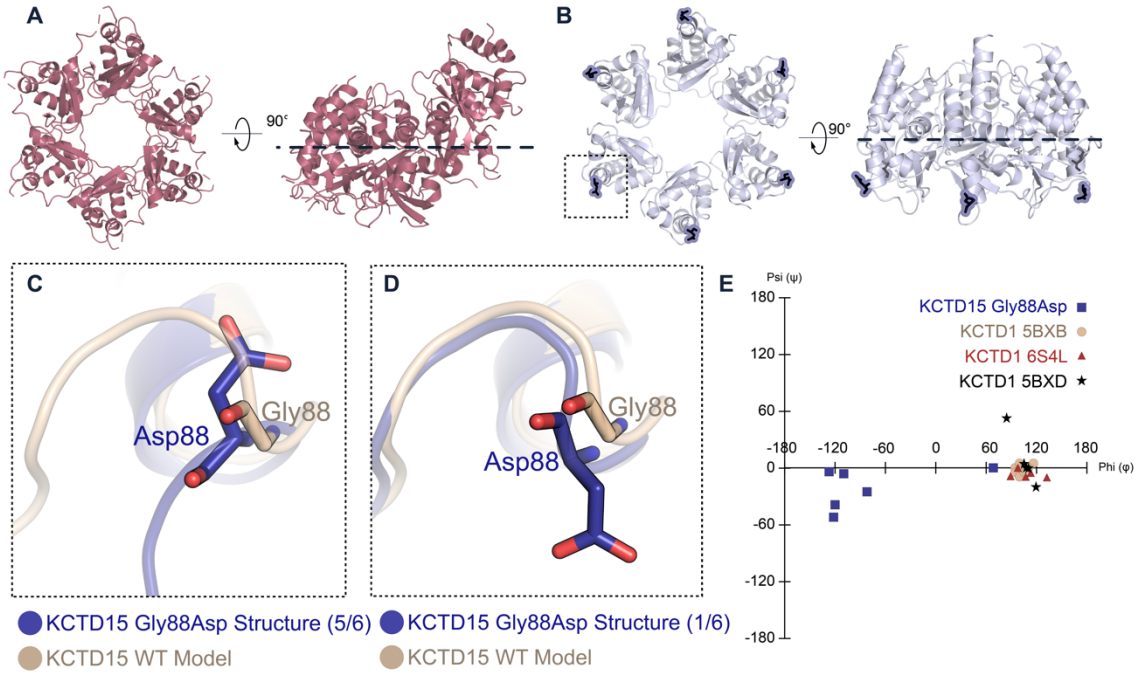


Figure 5.5 Crystal structure of the KCTD15 Gly88Asp variant BTB domain. (A) The previously published crystal structure of the inhibitory hexamer of KCTD16 is shown in two orientations. A dashed line emphasises that the sixth BTB domain subunit is out of plane. (B) Crystal structure of the KCTD15 Gly88Asp variant BTB domain shown in two orientations (crystal form I is shown). A dashed line highlights the in-plane sixth subunit compared to the KCTD16 hexamer. The Asp88 substitution is shown in each subunit in dark blue. (C,D) Stick representations of the wild-type KCTD15 model (light brown) superimposed on the variant crystal structure (blue) at the Gly88Asp substitution site. (E) The Phi, Psi (ϕ, ψ) angles of Gly62 in the three deposited KCTD1 structures (5bxb, 5bxd, and 6s4l) are plotted alongside those of the depicted KCTD15 Gly88Asp hexamer.

Purified protein of sufficient yield for crystal trays was able to be obtained for $KCTD15_{BTB}$ Asp104His. However, the protein precipitated when concentrated beyond 5 mg/mL. Two coarse crystal screens at 20°C (LFS CI083724 and JCSG7 CI083725 screens) were set up and crystals were observed to form in conditions 20% PEG6000, 10% ethylene glycol, 0.01M zinc chloride with a buffer of either 0.1M HEPES pH 7.0 or 0.1M MES pH 6.0 (Figure 5.4E,F). Due to the presence of zinc and the lack of intrinsic fluorescence, it was noted the crystals

were likely zinc crystals and not protein crystals. Nevertheless, crystals from each condition were mounted. None of the mounted crystals diffracted.

For $KCTD15_{BTB}$ WT, sufficient quantities of soluble purified protein were able to be obtained for biophysical studies. However, compared to Gly88Asp and Asp104His $KCTD15_{BTB}$ constructs, wild-type $KCTD15_{BTB}$ expression levels were low and insufficient for crystallisation trials. Similarly, none of the three $KCTD15_{BTB+CTD}$ constructs yielded sufficient protein for crystallisation trials.

5.2.4 Native mass spectrometry analysis of KCTD15 wild type and variants

Unless otherwise stated, all biophysical experiments reported in this chapter were performed using both isolated BTB (residues 52-165; herein $KCTD15_{BTB}$) as well as BTB and C-terminal (residues 52-283; herein $KCTD15_{BTB+CTD}$) domains of wild-type and variant KCTD15. To characterise the structural changes imparted by substitutions Asp104His and Gly88Asp in solution, I performed a series of native mass spectrometry (native MS) experiments.

Consistent with previous reports and modelling, electrospray native MS signatures confirmed the wild-type BTB domains predominantly oligomerised into pentameric species (Figure 5.6A, Table 5.2). The charge distributions of the wild-type pentameric species were symmetric with a full width half maximum (FWHM) value of 2.5, suggesting the species is a closed pentamer. In contrast, native MS signature of the Asp104His variant BTB domain depicted an exclusively monomeric species, supporting observations from homology modelling and the prediction that the substitution ablates the salt bridge critical for BTB domain

oligomerisation (Figure 5.6B, Table 5.2). The Gly88Asp BTB domain native MS signature showed the protein forms predominantly hexameric species, consistent with the obtained structural data (Figure 5.6C, Table 5.2). The lower abundance pentameric species of the Gly88Asp BTB domain variant had an asymmetric charge distribution with a FWHM value of 3.0 charge units. In contrast to the symmetric charge distribution of the wild-type pentamer, this asymmetric charge distribution indicates the Gly88Asp pentamer is an open flexible structure. These native MS signatures highlighted the two human KCTD15 variants can perturb BTB domain oligomerisation.

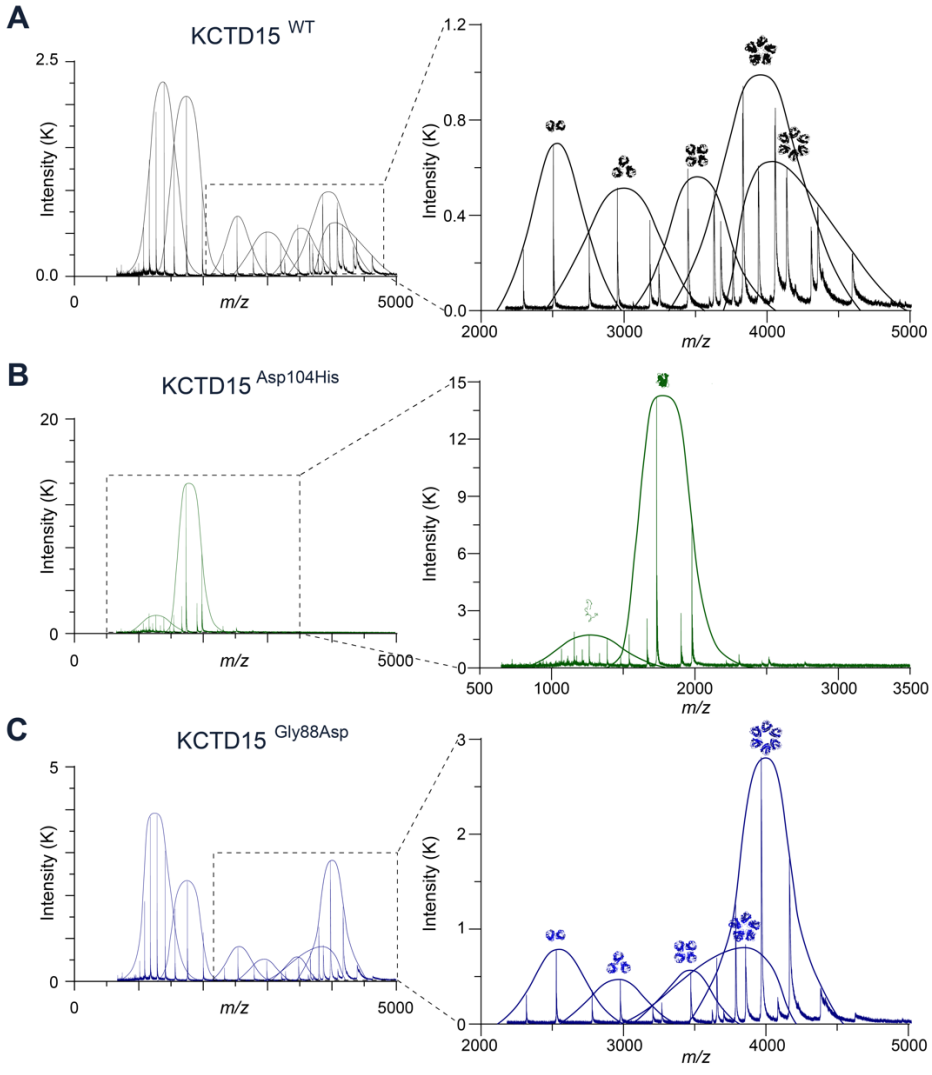


Figure 5.6 Native mass spectrometry of KCTD15 wild-type and variant BTB domains. (A-C) Full native mass spectra of KCTD15 wild-type and variant

BTB domains (left) with inset panels (right) highlighting the major species (note peak intensities decrease exponentially as a function of detector efficiency with increasing m/z; the first two peaks of lowest m/z representing unfolded and folded monomers are therefore disproportionately large compared to their populations). A schematic representation of the oligomer state is shown above each peak. (A) Wild-type KCTD15 BTB domain shows several oligomeric species with pentamers predominating. (B) KCTD15 BTB variant Asp104His fails to oligomerise and adopts an exclusively monomeric state. The smaller of the two peaks represents a partially unfolded monomer. (C) KCTD15 BTB variant Gly88Asp forms a variety of species but with hexameric species predominating.

Native MS experiments were similarly performed with the $KCTD15_{BTB+CTD}$ constructs. As noted in section 5.2.1, the BTB+CTD constructs of each KCTD15 protein had a lower yield and precipitated more readily compared to their isolated BTB domain counterparts. While the two variant and wild-type KCTD15 BTB+CTD constructs were stable enough for biophysical experiments reported later in this chapter, the native MS workflow requires proteins undergo a desalting procedure prior to analysis. Proteins can become unstable in the low salt conditions needed to perform MS. $KCTD15_{BTB+CTD}$ Asp104His precipitated during the desalting procedures required for native MS, preventing an interpretable signature from being acquired (Figure 5.7). $KCTD15_{BTB+CTD}$ WT and $KCTD15_{BTB+CTD}$ Gly88Asp constructs also precipitated upon desalting, but sufficient soluble protein remained to obtain interpretable native MS signatures. $KCTD15_{BTB+CTD}$ WT and $KCTD15_{BTB+CTD}$ Gly88Asp formed predominantly tetrameric species (Figure 5.7A,C, Table 5.2). $KCTD15_{BTB+CTD}$ WT existed as a single tetrameric species with a charge radius of 35.3Å (Figure 5.7A, Table 5.2). In contrast, $KCTD15_{BTB+CTD}$ Gly88Asp formed three different tetrameric species, two isobaric tetramers of differing charge radius (36.4Å and 34.2Å) and one truncated tetramer with a charge radius 35.3Å (Figure 5.7C, Table 5.2). In this context, charge radius refers to the apparent radius of a globular protein and is

derived from the equation $z = R^{1.5}$ where “R” is the charge radius and “z” is the most abundant ESI charge state for the protein of interest (10). The charge radius provides information regarding the amount of solvent accessible surface area, with proteins of larger charge radii having larger solvent accessible surface areas. These results highlight that the oligomeric states of the didomain (BTB plus CTD) constructs differ from those of the isolated BTB domain constructs, suggesting that the CTD has intrinsic oligomerisation potential. Whereas wild-type isolated BTB domain constructs formed pentamers, wild-type didomain constructs formed predominantly tetramers. Similarly, although isolated BTB Gly88Asp variant BTB domains formed hexamers, didomain Gly88Asp variant constructs formed predominantly tetramers.

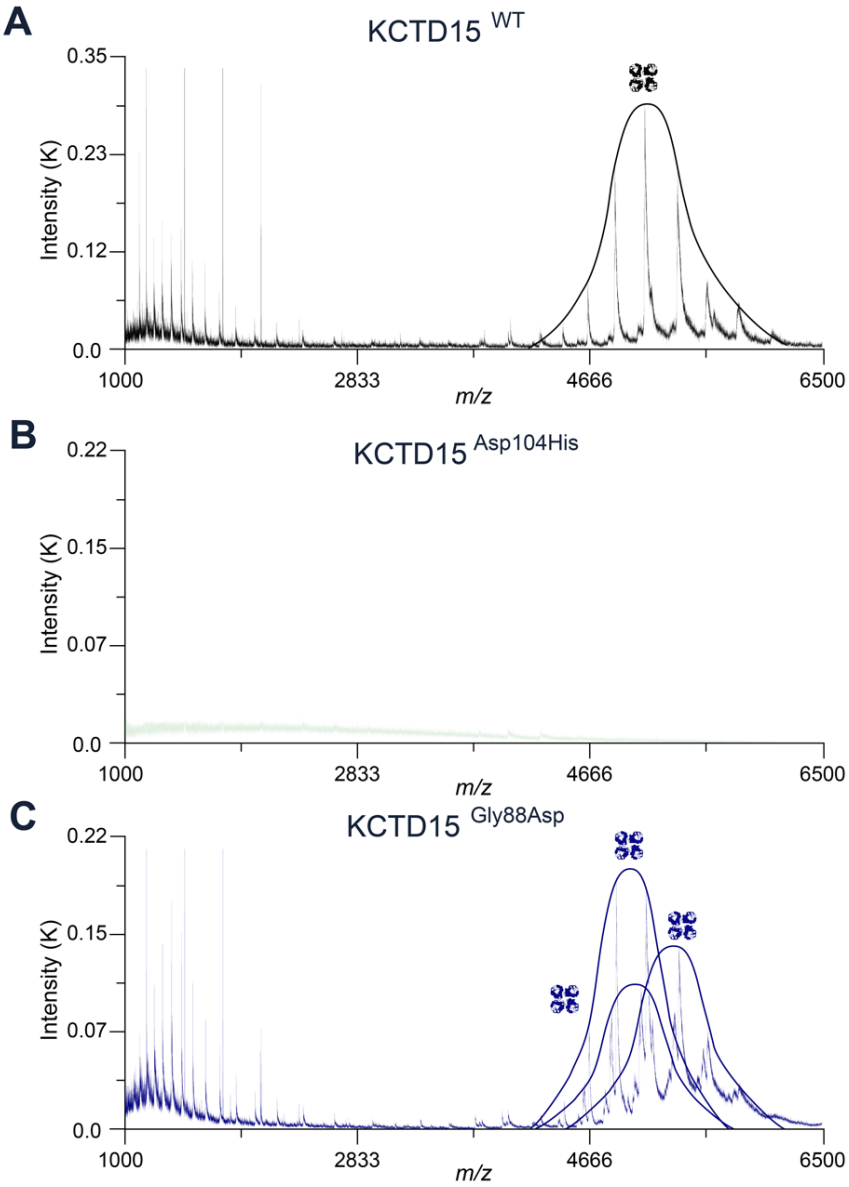


Figure 5.7 Native mass spectrometry of KCTD15 wild-type and variant BTB+CTD domains. (A-C) Full native mass spectra of KCTD15 wild-type and variant BTB plus C-terminal domains highlighting the major species (note peak intensities decrease exponentially as a function of detector efficiency with increasing m/z; the first two peaks of lowest *m/z* representing unfolded and folded monomers are therefore disproportionately large compared to their populations). A schematic representation of the oligomer state is shown above each peak. (A) Wild-type KCTD15 BTB+CTD forms a single tetrameric species with a charge radius of 35.3Å. (B) KCTD15 BTB+CTD variant Asp104His precipitated during the desalting process and an interpretable signal could not be acquired. (C) KCTD15 BTB+CTD variant Gly88Asp forms three different tetrameric species, two isobaric structures with charge radii of 36.4Å and 34.2Å alongside one truncated species with a 35.3Å charge radius.

Table 5.2 Native mass spectrometry results of KCTD15 wild type and two human variants.

	Denatured Mass (Da) Monomer	Native Mass (Da) Monomer	Native Mass (Da) Dimer	Native Mass (Da) Trimer	Native Mass (Da) Tetramer	Native Mass (Da) Pentamer	Native Mass (Da) Hexamer
$KCTD15_{BTB}$ WT	13,837	13,837	27,674	41,512	55,350	69,258	83,068
$KCTD15_{BTB}$ Asp104His	13,859	13,859	N/O	N/O	N/O	N/O	N/O
$KCTD15_{BTB}$ Gly88Asp	13,895	13,895	27,790	41,686	55,582	69,477	83,396
$KCTD15_{BTB+CTD}$ WT	26,904	26,904	N/O	N/O	112,654	N/O	N/O
$KCTD15_{BTB+CTD}$ Asp104His	26,926	N/O	N/O	N/O	N/O	N/O	N/O
$KCTD15_{BTB+CTD}$ Gly88Asp	26,960	26,960	N/O	N/O	106,859 / 107,935 / 107,975	N/O	N/O

N/O = not observed

5.2.5 Additional biophysical analyses confirm human mutations in KCTD15 perturb protein oligomerisation

To further characterise the structural changes imparted by substitutions Asp104His and Gly88Asp, I performed size-exclusion chromatography coupled with multi-angle light scattering (SEC-MALS) and analytical ultracentrifugation (AUC) experiments.

Both SEC-MALS and AUC experiments using $KCTD15_{BTB}$ constructs confirmed the Asp104His variant formed smaller species and the Gly88Asp variant formed larger species than wild type (Figure 5.8A,B, Table 5.3). Similar, but less pronounced, trends were observed using $KCTD15_{BTB+CTD}$ constructs, suggesting intrinsic carboxy-terminal domain oligomerisation contributed to a less pronounced variation in size between mutant and wild-type KCTD15 when both BTB and CTD regions are present (Figure 5.8A,B, Table 5.3). The gradient in MALS data and broadened peaks in the SEC and AUC data suggested Gly88Asp variants and wild-type proteins adopted heterogeneous oligomeric

states and exhibited dynamic behaviours in solution – reminiscent of the range of oligomeric species observed in native MS signatures.

Table 5.3 SEC-MALS and AUC results of KCTD15 wild type and two human variants.

	Denatured Mass (Da)	MALS Mass [range] (kDa)	SEC retention volume (mL)	AUC Predicted Mass (kDa)	Predominant Stoichiometry
KCTD15$_{BTB}$ WT	13,837	44.4 [39.2-45.4]	15.7	48.8	Tetramer
KCTD15$_{BTB}$ Asp104His	13,859	13.2 [12.5-14.7]	17.5	18.4	Monomer
KCTD15$_{BTB}$ Gly88Asp	13,895	44.1 [34.5-47.5]	15.4	53.0	Tetramer
KCTD15$_{BTB+CTD}$ WT	26,904	106.3 [100.1-120.0]	13.9	96.6	Tetramer
KCTD15$_{BTB+CTD}$ Asp104His	26,926	155.0 [101.8-180.3]	14.1	72.9	Trimer or Hexamer
KCTD15$_{BTB+CTD}$ Gly88Asp	26,960	105.0 [97.8-119.4]	13.7	94.2	Tetramer

Note: The broadened AUC peaks of the full-length constructs were consistent with the heterogeneous oligomeric states suggested by the associated MALS data.

5.2.6 Human variant KCTD15 Asp104His displays altered thermal stability compared to wild-type KCTD15

To characterise how KCTD15 substitutions impacted thermal stability, I performed thermal shift assays using differential scanning fluorimetry to determine the apparent melting temperatures (T_m) of KCTD15 wild type and variants. Proteins were mixed with SYPRO Orange fluorescent dye and thermally denatured in an RT-PCR thermocycler. The wild-type KCTD15$_{BTB+CTD}$ construct was 5°C more stable than its KCTD15$_{BTB}$ counterpart (Figure 5.8C, Table 5.4), suggesting the carboxy-terminal domain of the wild-type protein not only contributes to protein oligomerisation (as observed in AUC and SEC-MALS experiments), but also thermal stability. The KCTD15$_{BTB+CTD}$ Asp104His variant's apparent T_m was 35°C, suggesting the protein is partially unfolded at physiological temperatures (Figure 5.8C, Table 5.4). In contrast to wild type, the

Asp104His KCTD15$_{BTB+CTD}$ construct was less thermally stable than its isolated BTB domain counterpart (apparent T_m = 49°C) (Figure 5.8C, Table 5.4). This suggests the loss of oligomerisation in the BTB domain affects the stability of the carboxy-terminal domain, a finding similarly observed in native MS experiments where the KCTD15$_{BTB+CTD}$ construct failed to survive the desalting step of sample preparation (Figure 5.7B). Finally, both Gly88Asp KCTD15$_{BTB+CTD}$ and Gly88Asp KCTD15$_{BTB}$ were destabilised 1°C compared to matched wild-type constructs (Figure 5.8C, Table 5.4).

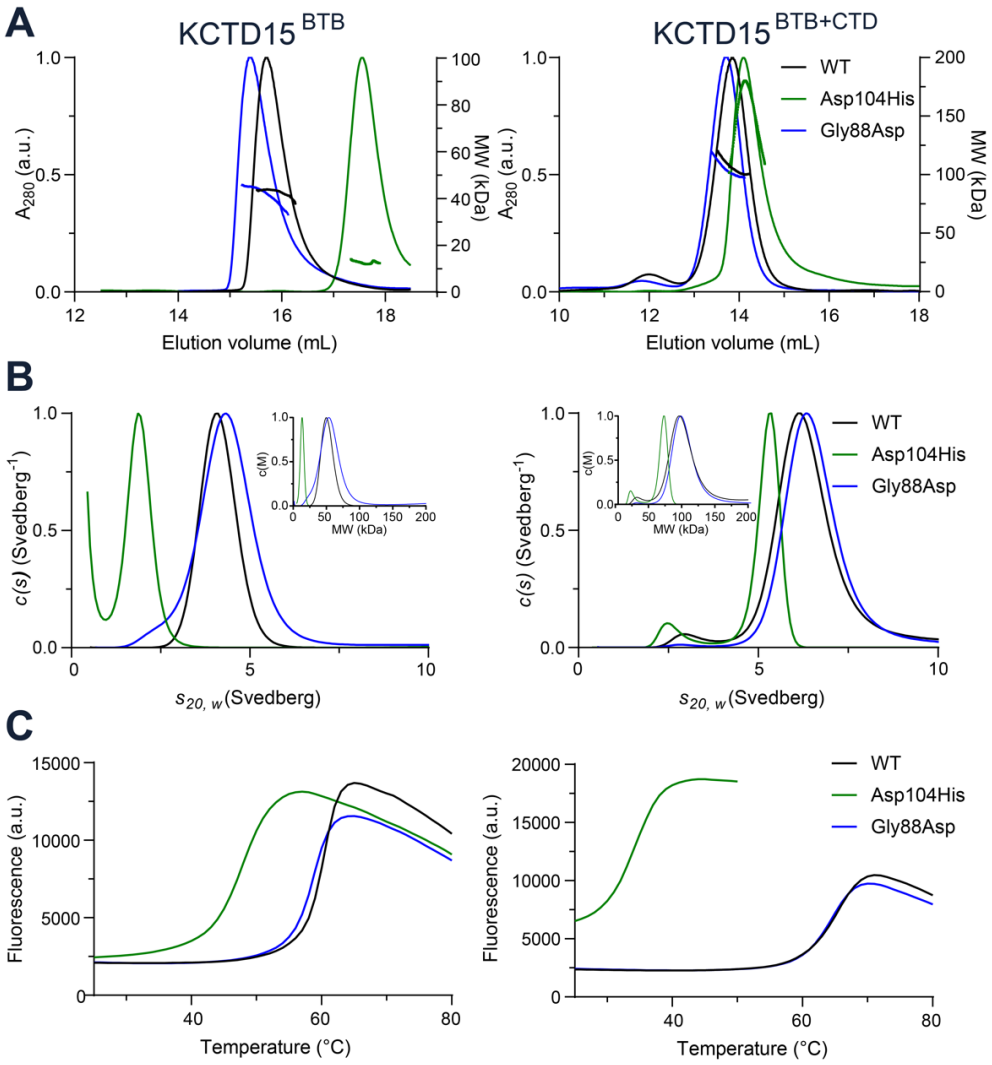


Figure 5.8 AUC, SEC-MALS, and DSF analyses of KCTD15 wild type and variants. (A-C) Biophysical analyses of KCTD15 BTB domain (KCTD15 BTB left panel) and BTB+CTD constructs (KCTD15 BTB+CTD right panel). KCTD15 wild

type and variants are coloured black (wild type), green (Asp104His) or blue (Gly88Asp). (A) SEC-MALS analyses showing the SEC elution absorbance (280 nm, left y-axis) and MALS-estimated masses (right y-axis). A monomer was observed for the Asp104His KCTD15 BTB construct, whereas the Gly88Asp variant BTB was larger than wild type. The KCTD15 BTB+CTD constructs exhibited the same trend, but the differences were less pronounced. A gradient in the MALS data suggested that the Gly88Asp variants, and to a lesser extent wild-type proteins, adopted heterogeneous dynamic oligomeric states in solution. (B) Sedimentation velocity AUC data for KCTD15 wild type and variants. Differential sedimentation coefficient distributions [*c(s)*] are plotted versus apparent sedimentation coefficients (*s20, w*) (main graphs) as well as differential molecular weight distributions [*c(M)*] versus molecular weights (MW) (insets). The Asp104His KCTD15 BTB variant was monomeric, whereas the Gly88Asp variant was again larger than wild type. Broadening of the AUC peak for the Gly88Asp KCTD15 BTB construct was consistent with the heterogeneous oligomeric states suggested by the MALS data. (C) Thermal denaturation of KCTD15 wild type and variants detected using the SYPRO Orange fluorescent dye which binds to exposed hydrophobic surfaces upon protein unfolding. Fluorescence (y-axis) is plotted against temperature (x-axis). Experiments were performed in triplicate.

Table 5.4 Differential scanning fluorimetry apparent *Tm* values of KCTD15 wild type and two human variants.

	Apparent *Tm* (°C)
$KCTD15_{BTB}$ WT	61
$KCTD15_{BTB}$ Asp104His	49
$KCTD15_{BTB}$ Gly88Asp	60
$KCTD15_{BTB+CTD}$ WT	66
$KCTD15_{BTB+CTD}$ Asp104His	35
$KCTD15_{BTB+CTD}$ Gly88Asp	65

5.2.7 Biolayer interferometry indicates KCTD15 substitutions may perturb KCTD15 binding to TFAP2

KCTD1 and KCTD15 have been reported to repress transcription factor activator protein-2 (TFAP2) activity (6, 11). To begin characterising how KCTD15 mutations and the resulting altered protein oligomerisation affected biological function, I sought to determine the binding affinity between KCTD15 proteins and

TFAP2. I first used biolayer interferometry (BLI) to profile the interaction between wild-type KCTD15 proteins encompassing the BTB and carboxy-terminal domains with and without an additional 14 amino acid amino-terminal extension (residues encompassing 38-283 versus 52-283). Whereas the di-domain BTB and CTD constructs used for most biophysical experiments encompassed amino acids 52 through 283, the amino-terminal extended constructs encompassed amino acids 38-283. These extended constructs were produced for TFAP2 binding experiments due to prior observations that the amino-terminus of KCTD1 is critical for its interactions with TFAP2 (personal communications with Alex Bullock). Biotinylated TFAP2 was captured on a streptavidin-functionalized sensor and binding was quantified using serial dilutions of $KCTD15_{38-283}$ and $KCTD15_{52-283}$. KCTD15 binding to TFAP2 was compared to that of a KCTD1 construct that similarly encompassed the BTB and CTD regions of KCTD1 (amino acids 1-257). KCTD1 portrayed a strong interaction with TFAP2 (Figure 5.9A). In contrast, both KCTD15 wild-type constructs showed a weaker binding affinity with TFAP2 (Figure 5.9A), with the amino-terminal extended KCTD15 construct exhibiting a greater affinity for the peptide compared to the truncated KCTD15 construct (Figure 5.9A). These preliminary results suggested KCTD15 exhibits a weaker affinity with TFAP2 compared to KCTD1 and the amino terminus of KCTD15 may be critical for its interactions with TFAP2.

Subsequent BLI experiments sought to determine if KCTD15 variants Asp104His and Gly88Asp altered the binding affinity between KCTD15 and the TFAP2 peptide. Both the Asp104His and Gly88Asp KCTD15 variants exhibited a weaker binding affinity for the TFAP2 peptide compared to KCTD15 wild type (Figure

5.9B). The Asp104His KCTD15 variant exhibited a marginally greater affinity for the TFAP2 peptide compared to Gly88Asp KCTD15 (Figure 5.9B) suggesting the Gly88Asp substitution may lie in a critical position for KCTD15's interaction with TFAP2.

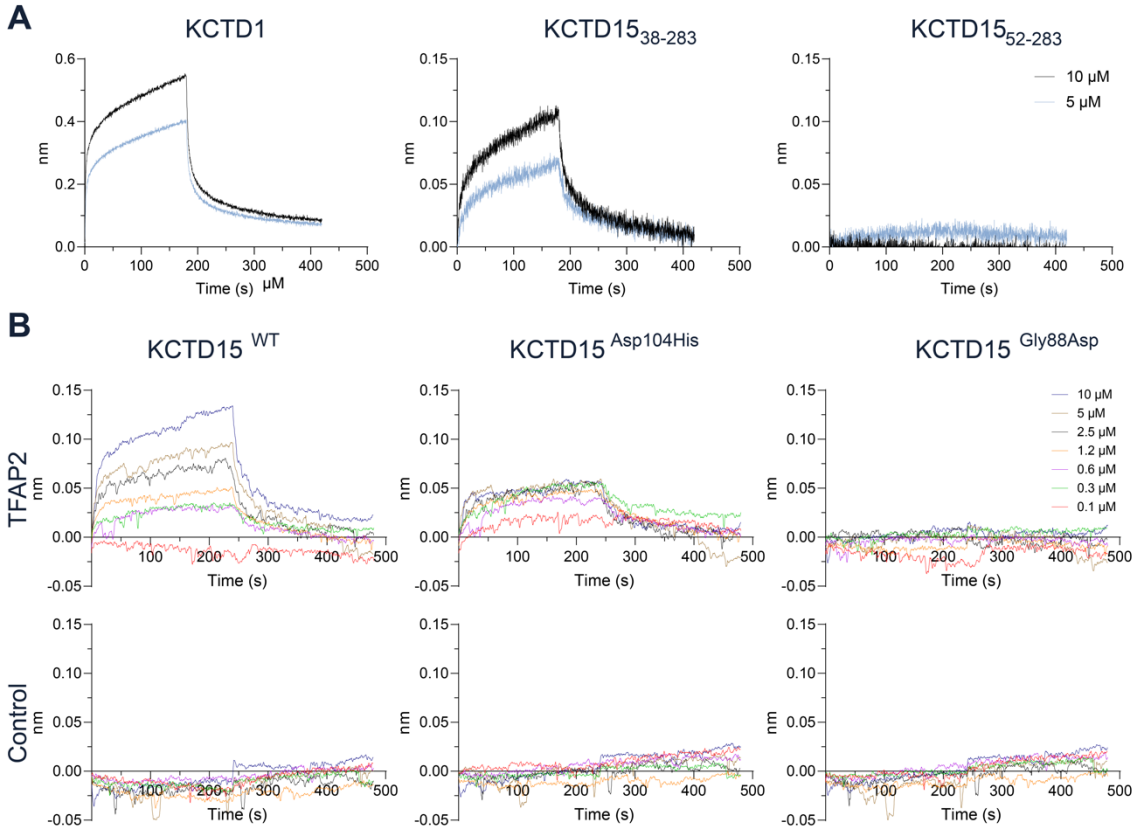


Figure 5.9 Biolayer interferometry of KCTD1, KCTD15 wild type, and KCTD15 variants. TFAP2 peptides (residues 50-63) were immobilised on streptavidin-coated sensor tips. Tips were incubated in serial dilutions of (A) full length wild-type KCTD1 as well as KCTD15 constructs with or without a 14-residue amino-terminal extension (residues 38-283 versus 52-283) and (B) the indicated KCTD15 wild type and variants (residues 38-283). No binding was observed to streptavidin-coated sensor tips lacking TFAP2 peptide. (A) KCTD1 bound the TFAP2 peptide with higher affinity than KCTD15. The amino-terminal extended KCTD15 construct bound TFAP2 with higher affinity than the truncated construct, suggesting the amino terminus of KCTD15 is critical for TFAP2 binding. (B) KCTD15 variants disrupted TFAP2 binding compared to wild type (the wild-type and variant constructs all encompassed residues 38-283 of KCTD15). KCTD15 variant Gly88Asp exhibited the weakest binding with TFAP2, suggesting the Gly88Asp substitution may lie in a critical interface for TFAP2 binding.

5.3 DISCUSSION

Several studies have sought to characterise the genetic architectures of the human face and identify key genes associated with normal and pathogenic facial variation (12, 13). Among such investigations, White et al. found KCTD15 to be associated with shape of the nasal tip (13) and others have suggested the KCTD proteins are capable of influencing formation of the facial skeleton through their interactions with transcription factor TFAP2 (8, 14). As mentioned previously, KCTD1 has been extensively linked to Scalp-Ear-Nipple syndrome which presents with distinct craniofacial anomalies (9, 15). This study is the first to link KCTD15 to human mendelian disease, depicting human missense variants Gly88Asp and Asp104His as the cause of a unique syndrome characterised by a midline frontonasal mass and other craniofacial anomalies. Both *de novo* missense mutations p.(Gly88Asp) and p.(Asp104His) affected codons of *KCTD15* that exhibit no non-synonymous variation in approximately 1 million alleles. The only documented report of a phenotype similar to that described herein is a case report from 2007 in which the clinical presentation was described as a “midline frontal cyst” with cutis aplasia of the scalp and congenital heart disease (16). The clinical geneticists involved in this study were unable to contact the associated family to test for the presence of a *KCTD15* variant. Although the unique clinical features combined with the structural and biophysical evidence of perturbed KCTD15 variant oligomerisation as well as TFAP2 binding provide a strong causal link between the reported KCTD15 variants and the clinical phenotype, additional individuals with similar KCTD15-associated craniofacial anomalies will be required for a more comprehensive characterisation of this disorder.

To characterise mechanisms of pathogenesis, I designed, cloned, and produced recombinant proteins of KCTD15 wild type and variants. I combined crystallography and several biophysical methods to compare the BTB and BTB+CTD domains of variant and wild-type KCTD15. Of note, data suggested KCTD15 normally associates into a multimeric complex, with a closed pentamer being the most common assembly. Initial protein expressions and purifications provided preliminary insights into how the two human substitutions may differentially influence KCTD15 oligomerisation and stability. The Asp104His variant consistently produced the lowest yield of soluble recombinant protein and precipitated upon concentrating, suggesting the Asp104His substitution altered inter-unit interactions in a manner that was detrimental to the assembly of stable higher order species. In contrast, of all constructs designed in this study, the Gly88Asp BTB only domain constructs exhibited the highest yield and stability, suggesting the Gly88Asp substitution may be enhancing inter-subunit interactions and allowing formation of a stable multimeric KCTD15 complex. Based on previously published KCTD1 structures and KCTD15 modelling, the Asp104 residue is shown to participate in key interactions with adjacent subunits of the KCTD15 pentamer while the Gly88 residue appears to lie in a solvent exposed loop (Figure 5.3). While such modelling did not hint at the mechanism of enhanced stability observed in Gly88Asp recombinant proteins, substituting Asp104 with a histidine residue is expected to ablate the inter-subunit interactions mediated by the aspartate (Figure 5.3C,D), supporting our observations of low yield and stability of Asp104His recombinant proteins.

Results from biophysical and crystallography experiments provided additional information pertaining to the differential biophysical natures of wild-type and variant KCTD15. Using crystallography, MS, SEC-MALS, and AUC, I found that both amino acid substitutions abrogated the normal pentameric assembly of KCTD15 albeit through different mechanisms, likely related to the different positions of the amino acids within the KCTD15 monomer. Crystallography showed that substituting the constrained Gly88 with an aspartate promoted a flipped main chain orientation and allowed the packing of a sixth KCTD15 monomer into the typically pentameric complex (Figure 5.5). Of note, this is the first reported crystal structure of a human mutant KCTD protein causative of disease. Such a higher order assembly of KCTD15 Gly88Asp was confirmed by native MS, SEC-MALS, and AUC workflows. In contrast and as predicted through homology modelling, the Asp104His substitution ablates the inter-domain interactions required for KCTD15 oligomerisation with only lower order species observed in native MS, SEC-MALS, and AUC results. Through different mechanisms, both substitutions appear to exert dominant negative effects on the pentameric assembly of KCTD15 (17). A similar mechanism was proposed to explain the pathogenesis of KCTD1 variants implicated in SEN syndrome (9, 15).

How could the proposed altered KCTD15 assemblies lead to the observed phenotypic features? Expressed in the neural crest, KCTD15 has been reported to serve a regulatory role in neural crest development through inhibiting the canonical Wnt pathway as well as negatively regulating the function of the key neural crest transcription factor, TFAP2 (5, 6). Knockout of the paralogues *kctd15a* and *kctd15b* in zebrafish embryos resulted in an expanded neural crest

and manifested as a maxillary deficiency alongside other cranial abnormalities in adults (18). It is possible the human KCTD15-associated phenotype of a midline frontonasal mass arose from diminished neural crest repression secondary to abnormal KCTD15-mediated inhibition. With the neural crest contributing to cardiovascular development (19), such a hypothesis could also explain the congenital heart disease observed in Family 1. This hypothesis is supported by the altered affinity of variant KCTD15 to TFAP2 peptide observed in BLI experiments. Interestingly, while both Asp104His and Gly88Asp variants exhibited diminished TFAP2 binding compared to wild type, the effect of Asp104His was less severe than that of Gly88Asp. Such an observation may be explained by Gly88Asp lying in a solvent exposed interface that may be critical for TFAP2 binding. As noted previously, many of the KCTD15-associated phenotypic abnormalities are shared with those of SEN syndrome caused by pathogenic KCTD1 variants (9, 15). This similarity in presentation may be due to either shared physiological activity and/or the potential existence of dominant negative cross-talk between KCTD1 and KCTD15 as the proteins have been shown to interact to form heterodimers (19, 21). While results of this chapter helped shed light on the mechanism of pathogenesis of these two human variants, several questions remain. The biophysical analyses reported herein occurred *ex vivo*, is KCTD15 oligomerisation similarly altered *in vivo?* Are the mutant KCTD15 oligomers degraded by quality control machinery thus preventing any potential functional activity (22)? The recombinant proteins used in this study were truncated versions of KCTD15. It was clear from native MS, AUC, and SEC-MALS that the CTD of KCTD15 has intrinsic oligomerisation potential. Interestingly, results suggested didomain (BTB plus CTD) constructs of

wild-type and Gly88Asp variant KCTD15 predominantly formed tetramers instead of the pentameric and hexameric species formed by their isolated BTB domain counterparts, respectively. Full-length KCTD15 is the functional physiologic form of the protein. *In vivo*, there may exist a regulatory signalling mechanism that guides KCTD15 to form different types of oligomers to exert different downstream effects. While near full-length constructs of the KCTD15 variants were used for BLI workflows (residues 38-283), it is unclear if the abrogated TFAP2 binding is secondary to altered KCTD15 oligomerisation or due to local changes in KCTD15 subunit folding – the more severe effects seen in the Gly88Asp variant suggest potentially the latter. The development of appropriate animal models together with detailed cellular and biochemical analyses will be required to more clearly address the pathological mechanism of KCTD15-associated human disease.

5.4 REFERENCES

1. Smaldone G, Beneduce G, Incoronato M, Pane K, Franzese M, Coppola L, Cordella A, Parasole R, Ripaldi M, Nassa G, Soricelli A, Vitagliano L, Mirabelli P, Salvatore M. KCTD15 is overexpressed in human childhood B-cell acute lymphoid leukemia. Sci Rep. 2019 Dec 27;9(1):20108. doi: 10.1038/s41598-019-56701-7. PMID: 31882877; PMCID: PMC6934626.
2. Angrisani A, Di Fiore A, De Smaele E, Moretti M. The emerging role of the KCTD proteins in cancer. Cell Commun Signal. 2021 May 17;19(1):56. doi: 10.1186/s12964-021-00737-8. PMID: 34001146; PMCID: PMC8127222.
3. Thorleifsson G, Walters GB, Gudbjartsson DF, Steinthorsdottir V, Sulem P, Helgadottir A, Styrkarsdottir U, Gretarsdottir S, Thorlacius S, Jonsdottir I, Jonsdottir T, Olafsdottir EJ, Olafsdottir GH, Jonsson T, Jonsson F, Borch-Johnsen K, Hansen T, Andersen G, Jorgensen T, Lauritzen T, Aben KK, Verbeek AL, Roeleveld N, Kampman E, Yanek LR, Becker LC, Tryggvadottir L, Rafnar T, Becker DM, Gulcher J, Kiemeney LA, Pedersen O, Kong A, Thorsteinsdottir U, Stefansson K. Genome-wide association yields new sequence variants at seven loci that associate with measures of obesity. Nat Genet. 2009 Jan;41(1):18-24. doi: 10.1038/ng.274. Epub 2008 Dec 14. PMID: 19079260.

4. Willer CJ, Speliotes EK, Loos RJ, Li S, Lindgren CM, Heid IM, Berndt SI, Elliott AL, Jackson AU, Lamina C, Lettre G, Lim N, Lyon HN, McCarroll SA, Papadakis K, Qi L, Randall JC, Roccasecca RM, Sanna S, Scheet P, Weedon MN, Wheeler E, Zhao JH, Jacobs LC, Prokopenko I, Soranzo N, Tanaka T, Timpson NJ, Almgren P, Bennett A, Bergman RN, Bingham SA, Bonnycastle LL, Brown M, Burtt NP, Chines P, Coin L, Collins FS, Connell JM, Cooper C, Smith GD, Dennison EM, Deodhar P, Elliott P, Erdos MR, Estrada K, Evans DM, Gianniny L, Gieger C, Gillson CJ, Guiducci C, Hackett R, Hadley D, Hall AS, Havulinna AS, Hebebrand J, Hofman A, Isomaa B, Jacobs KB, Johnson T, Jousilahti P, Jovanovic Z, Khaw KT, Kraft P, Kuokkanen M, Kuusisto J, Laitinen J, Lakatta EG, Luan J, Luben RN, Mangino M, McArdle WL, Meitinger T, Mulas A, Munroe PB, Narisu N, Ness AR, Northstone K, O'Rahilly S, Purmann C, Rees MG, Ridderstråle M, Ring SM, Rivadeneira F, Ruokonen A, Sandhu MS, Saramies J, Scott LJ, Scuteri A, Silander K, Sims MA, Song K, Stephens J, Stevens S, Stringham HM, Tung YC, Valle TT, Van Duijn CM, Vimaleswaran KS, Vollenweider P, Waeber G, Wallace C, Watanabe RM, Waterworth DM, Watkins N; Wellcome Trust Case Control Consortium; Witteman JC, Zeggini E, Zhai G, Zillikens MC, Altshuler D, Caulfield MJ, Chanock SJ, Farooqi IS, Ferrucci L, Guralnik JM, Hattersley AT, Hu FB, Jarvelin MR, Laakso M, Mooser V, Ong KK, Ouwehand WH, Salomaa V, Samani NJ, Spector TD, Tuomi T, Tuomilehto J, Uda M, Uitterlinden AG, Wareham NJ, Deloukas P, Frayling TM, Groop LC, Hayes RB, Hunter DJ, Mohlke KL, Peltonen L, Schlessinger D, Strachan DP, Wichmann HE, McCarthy MI, Boehnke M, Barroso I, Abecasis GR, Hirschhorn JN; Genetic Investigation of ANthropometric Traits Consortium. Six new loci associated with body mass index highlight a neuronal influence on body weight regulation. Nat Genet. 2009 Jan;41(1):25-34. doi: 10.1038/ng.287. Epub 2008 Dec 14. PMID: 19079261; PMCID: PMC2695662.
5. Dutta S, Dawid IB. Kctd15 inhibits neural crest formation by attenuating Wnt/beta-catenin signaling output. Development. 2010 Sep;137(18):3013-8. doi: 10.1242/dev.047548. Epub 2010 Aug 4. PMID: 20685732; PMCID: PMC2926954.
6. Zarelli VE, Dawid IB. Inhibition of neural crest formation by Kctd15 involves regulation of transcription factor AP-2. Proc Natl Acad Sci U S A. 2013 Feb 19;110(8):2870-5. doi: 10.1073/pnas.1300203110. Epub 2013 Feb 4. PMID: 23382213; PMCID: PMC3581937.
7. Sereikaite V, Fritzius T, Kasaragod VB, Bader N, Maric HM, Schindelin H, Bettler B, Strømgaard K. Targeting the γ-Aminobutyric Acid Type B (GABAB) Receptor Complex: Development of Inhibitors Targeting the K+ Channel Tetramerization Domain (KCTD) Containing Proteins/GABAB Receptor Protein-Protein Interaction. J Med Chem. 2019 Oct 10;62(19):8819-8830. doi: 10.1021/acs.jmedchem.9b01087. Epub 2019 Sep 25. PMID: 31509708.
8. Smaldone G, Pirone L, Pedone E, Marlovits T, Vitagliano L, Ciccarelli L. The BTB domains of the potassium channel tetramerization domain proteins

prevalently assume pentameric states. FEBS Lett. 2016 Jun;590(11):1663-71. doi: 10.1002/1873-3468.12203. Epub 2016 May 24. PMID: 27152988.
9. Smaldone G, Balasco N, Pirone L, Caruso D, Di Gaetano S, Pedone EM, Vitagliano L. Molecular basis of the scalp-ear-nipple syndrome unraveled by the characterization of disease-causing KCTD1 mutants. Sci Rep. 2019 Jul 19;9(1):10519. doi: 10.1038/s41598-019-46911-4. PMID: 31324836; PMCID: PMC6642198.
10. Pinkas DM, Sanvitale CE, Bufton JC, Sorrell FJ, Solcan N, Chalk R, Doutch J, Bullock AN. Structural complexity in the KCTD family of Cullin3-dependent E3 ubiquitin ligases. Biochem J. 2017 Nov 1;474(22):3747-3761. doi: 10.1042/BCJ20170527. PMID: 28963344; PMCID: PMC5664961.
11. Ding X, Luo C, Zhou J, Zhong Y, Hu X, Zhou F, Ren K, Gan L, He A, Zhu J, Gao X, Zhang J. The interaction of KCTD1 with transcription factor AP-2alpha inhibits its transactivation. J Cell Biochem. 2009 Feb 1;106(2):285-95. doi: 10.1002/jcb.22002. PMID: 19115315.
12. Claes P, Roosenboom J, White JD, Swigut T, Sero D, Li J, Lee MK, Zaidi A, Mattern BC, Liebowitz C, Pearson L, González T, Leslie EJ, Carlson JC, Orlova E, Suetens P, Vandermeulen D, Feingold E, Marazita ML, Shaffer JR, Wysocka J, Shriver MD, Weinberg SM. Genome-wide mapping of global-to-local genetic effects on human facial shape. Nat Genet. 2018 Mar;50(3):414-423. doi: 10.1038/s41588-018-0057-4. Epub 2018 Feb 19. PMID: 29459680; PMCID: PMC5937280.
13. White JD, Indencleef K, Naqvi S, Eller RJ, Hoskens H, Roosenboom J, Lee MK, Li J, Mohammed J, Richmond S, Quillen EE, Norton HL, Feingold E, Swigut T, Marazita ML, Peeters H, Hens G, Shaffer JR, Wysocka J, Walsh S, Weinberg SM, Shriver MD, Claes P. Insights into the genetic architecture of the human face. Nat Genet. 2021 Jan;53(1):45-53. doi: 10.1038/s41588-020-00741-7. Epub 2020 Dec 7. PMID: 33288918; PMCID: PMC7796995.
14. Skoblov M, Marakhonov A, Marakasova E, Guskova A, Chandhoke V, Birerdinc A, Baranova A. Protein partners of KCTD proteins provide insights about their functional roles in cell differentiation and vertebrate development. Bioessays. 2013 Jul;35(7):586-96. doi: 10.1002/bies.201300002. Epub 2013 Apr 17. PMID: 23592240.
15. Marneros AG, Beck AE, Turner EH, McMillin MJ, Edwards MJ, Field M, de Macena Sobreira NL, Perez AB, Fortes JA, Lampe AK, Giovannucci Uzielli ML, Gordon CT, Plessis G, Le Merrer M, Amiel J, Reichenberger E, Shively KM, Cerrato F, Labow BI, Tabor HK, Smith JD, Shendure J, Nickerson DA, Bamshad MJ; University of Washington Center for Mendelian Genomics. Mutations in KCTD1 cause scalp-ear-nipple syndrome. Am J Hum Genet. 2013 Apr 4;92(4):621-6. doi: 10.1016/j.ajhg.2013.03.002. Epub 2013 Mar 28. PMID: 23541344; PMCID: PMC3617379.
16. Rodrigues RG. Aplasia cutis congenita, congenital heart lesions, and frontonasal cysts in four successive generations. Clin Genet. 2007 Jun;71(6):558-60. doi: 10.1111/j.1399-0004.2007.00806.x. PMID: 17539905.
17. Zschocke J, Byers PH, Wilkie AOM. Mendelian inheritance revisited: dominance and recessiveness in medical genetics. Nat Rev Genet. 2023

Jul;24(7):442-463. doi: 10.1038/s41576-023-00574-0. Epub 2023 Feb 20. PMID: 36806206.
18. Heffer A, Marquart GD, Aquilina-Beck A, Saleem N, Burgess HA, Dawid IB. Generation and characterization of Kctd15 mutations in zebrafish. PLoS One. 2017 Dec 7;12(12):e0189162. doi: 10.1371/journal.pone.0189162. PMID: 29216270; PMCID: PMC5720732.
19. Creazzo TL, Godt RE, Leatherbury L, Conway SJ, Kirby ML. Role of cardiac neural crest cells in cardiovascular development. Annu Rev Physiol. 1998;60:267-86. doi: 10.1146/annurev.physiol.60.1.267. PMID: 9558464.
20. Rolland T, Taşan M, Charloteaux B, Pevzner SJ, Zhong Q, Sahni N, Yi S, Lemmens I, Fontanillo C, Mosca R, Kamburov A, Ghiassian SD, Yang X, Ghamsari L, Balcha D, Begg BE, Braun P, Brehme M, Broly MP, Carvunis AR, Convery-Zupan D, Corominas R, Coulombe-Huntington J, Dann E, Dreze M, Dricot A, Fan C, Franzosa E, Gebreab F, Gutierrez BJ, Hardy MF, Jin M, Kang S, Kiros R, Lin GN, Luck K, MacWilliams A, Menche J, Murray RR, Palagi A, Poulin MM, Rambout X, Rasla J, Reichert P, Romero V, Ruyssinck E, Sahalie JM, Scholz A, Shah AA, Sharma A, Shen Y, Spirohn K, Tam S, Tejeda AO, Wanamaker SA, Twizere JC, Vega K, Walsh J, Cusick ME, Xia Y, Barabási AL, Iakoucheva LM, Aloy P, De Las Rivas J, Tavernier J, Calderwood MA, Hill DE, Hao T, Roth FP, Vidal M. A proteome-scale map of the human interactome network. Cell. 2014 Nov 20;159(5):1212-1226. doi: 10.1016/j.cell.2014.10.050. PMID: 25416956; PMCID: PMC4266588.
21. Luck K, Kim DK, Lambourne L, Spirohn K, Begg BE, Bian W, Brignall R, Cafarelli T, Campos-Laborie FJ, Charloteaux B, Choi D, Coté AG, Daley M, Deimling S, Desbuleux A, Dricot A, Gebbia M, Hardy MF, Kishore N, Knapp JJ, Kovács IA, Lemmens I, Mee MW, Mellor JC, Pollis C, Pons C, Richardson AD, Schlabach S, Teeking B, Yadav A, Babor M, Balcha D, Basha O, Bowman-Colin C, Chin SF, Choi SG, Colabella C, Coppin G, D'Amata C, De Ridder D, De Rouck S, Duran-Frigola M, Ennajdaoui H, Goebels F, Goehring L, Gopal A, Haddad G, Hatchi E, Helmy M, Jacob Y, Kassa Y, Landini S, Li R, van Lieshout N, MacWilliams A, Markey D, Paulson JN, Rangarajan S, Rasla J, Rayhan A, Rolland T, San-Miguel A, Shen Y, Sheykhkarimli D, Sheynkman GM, Simonovsky E, Taşan M, Tejeda A, Tropepe V, Twizere JC, Wang Y, Weatheritt RJ, Weile J, Xia Y, Yang X, Yeger-Lotem E, Zhong Q, Aloy P, Bader GD, De Las Rivas J, Gaudet S, Hao T, Rak J, Tavernier J, Hill DE, Vidal M, Roth FP, Calderwood MA. A reference map of the human binary protein interactome. Nature. 2020 Apr;580(7803):402-408. doi: 10.1038/s41586-020-2188-x. Epub 2020 Apr 8. PMID: 32296183; PMCID: PMC7169983.
22. Mena EL, Kjolby RAS, Saxton RA, Werner A, Lew BG, Boyle JM, Harland R, Rape M. Dimerization quality control ensures neuronal development and survival. Science. 2018 Oct 12;362(6411):eaap8236. doi: 10.1126/science.aap8236. Epub 2018 Sep 6. PMID: 30190310.

CHAPTER SIX

Conclusions and future directions

The BTB family of proteins are critical regulators of human growth, development, and homeostasis. When these proteins fail to perform their biological functions (e.g., secondary to mutation, altered expression, aberrant oligomerisation, etc.) human pathology results (1-4). Canonical BTB domains assemble into functional homodimers. This thesis characterises the intramolecular and intermolecular protein interactions of atypical BTB proteins – proteins with more than one BTB domain or those with pentameric assembly – and how such interactions may determine function and disease, particularly of the craniofacial complex. Three approaches were used to achieve this aim: 1) characterising the morphogenic role of tandem BTB protein BTBD7 in 3D cell culture, 2) investigating the molecular mechanisms and biophysical properties of the tandem BTB protein class, and 3) characterising the structural, biophysical, and mechanistic alterations caused by mutations in the pentameric BTB protein KCTD15 (Figure 1.6). Novel 3D cell culture techniques were developed and employed to characterise the biological functions of the tandem BTB protein BTBD7. Multiple techniques were employed to show the tandem BTB domain can assume different oligomeric states and may be stabilised through protein-protein interactions. Turning to human disease, I solved the crystal structure of a pathologic human KCTD15 variant and used several methods to characterise the aberrant oligomerisation and abrogated function imparted by human

substitutions in the BTB domain. Summarised in the subsequent paragraphs, this thesis has contributed to our understanding of the mechanisms through which the BTB domain regulates vital cellular processes and has provided key insights that will enable further targeted investigations of these crucial proteins.

6.1 APPROACH 1 – THE MORPHOGENIC ROLE OF BTBD7 IN 3D CULTURE MODELS

Early work of this dissertation (chapter 3) utilised novel 3D cell culture and several imaging assays to expand our understanding of BTBD7's roles guiding tissue growth. *In vivo* data suggested BTBD7, or at least its two BTB domains, did not appear to play a critical role in branching morphogenesis of the glandular organs (5). Nevertheless, results supported my initial hypothesis that BTBD7 drives tissue morphogenesis. However, such a role may not occur through BTBD7-associated changes in cell-ECM and cell-cell interactions, as proposed by others (6, 7). I observed no differences in cell expression nor localisation of the major cell-cell adhesion protein E-cadherin and BTBD7 did not co-localise with adherens junctions (Figure 3.5). Of importance are the unique 3D culture models developed and employed in this chapter. When grown into spheroids then embedded in a collagen matrix, SIMS cells formed intricate tubular networks to provide a novel model of tubulogenesis that can be analysed with various imaging and proteomic methods (Figures 3.3, 3.5, 3.6). In this 3D model system, BTBD7 knockout SIMS cells formed less organised and more numerous protrusions than their wild-type counterparts. The molecular mechanisms driving this differential growth remain to be elucidated. While preliminary 3D culture inhibitor assays suggested the ubiquitin signalling pathway may be involved in

BTBD7's biological mechanism of action (Figure 3.6), BTBD7 did not appear to serve as a substrate adaptor for CUL3 (Figures 4.4, 4.5) – one of the most prevalent roles of BTB domain-containing proteins (8).

While the BTB domains of BTBD7 did not appear to play key roles in developmental processes, numerous reports implicate BTBD7 in cancer progression (6, 7, 9-11) and results from this report similarly suggested BTBD7 may regulate cell proliferation and dynamics *in vitro*. At present, the interaction partners of BTBD7 are poorly characterised. Which of the known roles of BTB domain-containing proteins does BTBD7 serve? It does not appear to serve as an E3 ubiquitin ligase. Does it regulate gene transcription? Is it involved in a cell signalling process central to tumorigenesis? What are the roles of BTBD7s large intrinsically disordered amino- and carboxy-termini? Approximately 30% of the eukaryotic proteome contains regions of disorder and intrinsically disordered proteins (IDPs) are more prevalent in cell signalling processes commonly perturbed in disease (including cancer) (12, 13). The biological roles of IDPs are only beginning to be understood. The intrinsically disordered regions of IDPs tend to allow interaction with a variety of different types of proteins (hence their roles in signalling). Recent insights suggest IDPs are tightly regulated and that dosage-sensitive genes tend to encode proteins with disordered segments (14, 15). Many IDPs can gain structure upon interaction with a binding partner in a process called "coupled folding and binding" (16).

Of note, the BTBD7 constructs used in this thesis removed the intrinsically disordered region for biophysical assays. As noted above, the intrinsically

disordered region of IDPs tend to be the regions that bind protein partners. Removing the intrinsically disordered regions of BTBD7 may have restricted my ability to determine its interacting partners and mechanisms of function. This intrinsically disordered region may be critical to BTBD7's function, particularly with over 40% of the protein (485 of the 1132 residues) predicted to be disordered. Thus, future studies should work to characterise the full length of BTBD7 (including the creation of a complete BTBD7 knockout mouse model), identify binding partners of BTBD7 with mass spectrometry-based proteomics, determine if full-length BTBD7 can become stabilised in the presence of binding partners (using circular dichroism and isothermal titration calorimetry), and unravel the processes leading from a free to a bound and folded state.

6.2 APPROACH 2 – MOLECULAR MECHANISMS OF THE TANDEM BTB DOMAIN

Expanding beyond BTBD7, chapter 4 aimed to more comprehensively investigate the biophysical properties and molecular mechanisms of the tandem BTB domain. 75 constructs of seven tandem BTB domain proteins were successfully cloned in the attempt to produce protein that could be recovered in the soluble cell lysate of *E. coli* (herein "soluble protein"). Of these, only four constructs produced sufficient stable soluble protein for structural and biophysical assays. Of note, the boundaries of these constructs were designed prior to the publication of the AlphaFold database. Moving forward, additional constructs of the tandem BTB proteins can be designed with boundaries that better reflect the predicted secondary and tertiary structures of the proteins – potentially increasing the likelihood of producing stable soluble protein.

Biophysical analyses of BTBD7, RHOBTB1, and LZTR1 suggested that tandem BTB proteins exhibit differing oligomeric states, with BTBD7 and RHOBTB1 existing as monomers and LZTR1 forming dimers. Few studies have explored the oligomeric potential of the tandem BTB domain. A literature search suggests this is the first report characterising the oligomeric state of BTBD7. In contrast, a handful of studies have investigated LZTR1's and RHOBTB1's oligomeric states. Previous publications support findings reported herein showing LZTR1 forms functional dimers (17, 18). In contrast, the one other report investigating RHOBTB1's oligomeric potential reported RHOBTB1 forms dimers (19) in contrast to the monomers reported herein. However, as discussed in chapter 4, the dimeric RHOBTB1 construct reported by Haga et al. encompassed residues 1-210 of RHOBTB1 (the GTPase domain) instead of RHOBTB1's tandem BTB domain.

Data reported herein could not confirm or refute the ability for the tandem BTB domain to form intramolecular dimers, as originally proposed by Stogios et al. (20). Solving the crystal structure of the tandem BTB domain could help shed light on this potential for intramolecular BTB domain dimerisation. While a crystal structure of the tandem BTB domain was not solved in this thesis, the generated LZTR1 construct showed promise for obtaining such a crystal structure. Due to the most promising LZTR1 crystals being discarded by a member of the department before the crystals could be sent for data collections, the conditions reported herein could be repeated to obtain similar crystals. Future work can also attempt co-crystallisation experiments of LZTR1 with full-length CUL3 and

cryogenic electron microscopy experiments of LZTR1 with the full-length CUL3-RBX1 complex. The RHOBTB1 and BTBD7 constructs generated in this thesis were too unstable for crystallisation. The truncated nature of these constructs may have exposed hydrophobic residues, thus preventing stable crystals from forming. SEC-MALS and DSF experiments reported herein highlighted the tandem BTB domain of RHOBTB1 becomes stabilised in the presence of CUL3 (this enhanced stability is common to most protein-protein interactions). Future work can attempt to co-crystallise CUL3 with the RHOBTB1 construct that encompasses the 3-box of the BACK domain ($RHOBTB1_{252-624}$), as the 3-box motif has been reported to stabilise the BTB-CUL3 interaction (21, 22) and may in turn stabilise the RHOBTB1-CUL3 protein complex to a sufficient degree for crystallisation.

Consistent with single BTB domain proteins in which only a subset bind CUL3, not all tandem BTB proteins interact with CUL3 to form E3 ligase complexes. While RHOBTB1 and LZTR1 constructs bound CUL3, the BTBD7 constructs used in this study failed to bind CUL3. Solving the crystal structure of BTBD7 could show how ordered domains relate to disordered domains and could provide preliminary insights into the intermolecular and intramolecular binding mechanisms of atypical BTB domains. To obtain a crystal structure of BTBD7, it could be helpful to identify BTBD7's interacting partners and attempt co-crystallisation trials of BTBD7 with such proteins. New BTBD7 constructs with different domain boundaries can be generated, particularly constructs encompassing portions of the intrinsically disordered domain as such disordered regions have been shown to mediate protein-protein interactions (13, 14, 23, 24).

Remaining questions relating to the tandem BTB domain include: are the domains redundant or does each domain have a distinct function? For the tandem BTBs that bind CUL3, how does the tandem BTB domain assemble with the CRL complex – does one domain bind CUL3 and the other serve a scaffolding role? While answers to these questions may be protein specific, I hypothesise that for the tandem BTB proteins which bind CUL3, only one of the two BTB domains serves as the main functional domain mediating the interaction with CUL3 while the other BTB domain may play a scaffolding/supporting role. This hypothesis is supported by published reports and *in silico* modelling of the tandem BTB domain with CUL3. For example, human disease causing LZTR1 variants predominantly map to the protein's KELCH repeat and second BTB domains, with minimal variants present in the first BTB domain (25). Such observations suggest the second BTB domain (likely binding CUL3) and the KELCH repeat domain (likely binding substrate proteins) could be the main functional domains of LZTR1. Manual structural modelling of RHOBTB1 with CUL3 using the solved KLHL11-CUL3 complex crystal structure as a template suggested there is a similar functional discrepancy between the first and second BTB domains of RHOBTB1. In this model, RHOBTB1 interacts with CUL3 via its second BTB domain (Figure 4.8C). To test these hypotheses and confirm which BTB domains are critical for CUL3 binding, targeted residues in each of the two BTB domains of LZTR1 and RHOBTB1 can be mutated, documenting which mutations abolish the BTB-CUL3 interaction.

As mentioned throughout this text, tandem BTB domains are rare – with only eight tandem BTB proteins documented among the 200+ human proteins with a BTB domain. Why has evolution produced these duplicate domains? Are they truly “tandem BTB domains” or is the scaffolding BTB domain only “BTB-like?” Future works could try expressing tandem BTB proteins in insect or mammalian cells for biophysical and structural studies. Such systems may allow for more examples and larger portions of the tandem BTB proteins to be characterised.

6.3 APPROACH 3 – PATHOGENIC MECHANISMS OF KCTD15 MUTATIONS IN CRANIOFACIAL DISEASE

The final results chapter of this thesis used insights from biochemical and structural assays to characterise the mechanism of pathogenesis imparted by human mutations in the BTB domain. A collaborator identified two *de novo* mutations in KCTD15 causing a distinct craniofacial syndrome (KCTD15 Asp104His and Gly88Asp). Protein constructs containing these human disease-causing KCTD15 variants were produced and compared to wild-type KCTD15 constructs using experiments described in chapter 5 of this thesis.

Both human substitutions in the BTB domain of KCTD15 abrogated the ability for the BTB domain of KCTD15 to oligomerise into a functional pentamer. While data reported herein clearly depicted the variation in oligomeric status of isolated BTB domains (with $KCTD15_{BTB}$ wild type forming pentamers, $KCTD15_{BTB}$ Asp104His forming monomers, and $KCTD15_{BTB}$ Gly88Asp forming hexamers), it is less clear how the CTD of KCTD15 influences protein oligomerisation. In contrast to the isolated BTB domain constructs, didomain constructs were

relatively unstable, with $KCTD15_{BTB+CTD}$ wild type and Gly88Asp forming tetramers and $KCTD15_{BTB}$ Asp104His forming trimers (Figures 5.7, 5.8) (Tables 5.2, 5.3). Prior reports have shown several KCTD protein family members require the presence of protein partners to form stable pentamers (26). The didomain $KCTD15_{BTB+CTD}$ constructs used in this report may similarly require interacting partners to form stable physiologic oligomers. While experiments in this report characterised the ability for the various KCTD15 constructs to bind TFAP2, they did not characterise the oligomeric status of KCTD15 in the presence of TFAP2. Future studies could address this by performing SEC-MALS, AUC, and Native MS experiments of KCTD15 with and without bound TFAP2.

The BLI experiments reported herein showed that the amino acid substitutions in human KCTD15 disrupted its ability to bind to TFAP2. However, the binding between recombinant KCTD15 wild-type proteins and TFAP2 peptides was relatively weak when compared to KCTD1-TFAP2 binding. That being said, the full amino terminus of KCTD15 could not be expressed and may contribute to TFAP2 binding KCTD15 as observed for KCTD1 (Personal communication with Alex Bullock)**.** *In vivo*, KCTD15 may interact with TFAP2 as a functional complex of several additional protein partners. In future studies, cellular functional assays capable of reproducing the physiologic KCTD15-TFAP2 complex can shed further light on the altered TFAP2 interactions caused by human substitutions in KCTD15. Furthermore, future assays can work to identify additional interacting partners of KCTD15. While KCTD15's main biological function is hypothesised to involve regulating TFAP2 (27, 28), different protein partners may determine KCTD15's functional roles in different tissues (e.g., KCTD15 binding

oncosuppressor KCASH2 in medulloblastoma cells [29]). Finally, future work can explore the overlap in function between KCTD15 and KCTD1. There is a high similarity in sequence identity between the BTB domains of KCTD15 and KCTD1 (Figure 1.3D) and high-throughput mass spectrometry proteomics have shown KCTD15 can interact with KCTD1 (30, 31). Such data leads to the hypothesis that KCTD15 and KCTD1 may hetero-oligomerise *in vivo*. Future work can seek to confirm or refute this hypothesis and determine functional relevance for such hetero-oligomerisation.

This dissertation used three distinct yet complementary approaches to strengthen our understanding of the critical biological roles of the highly conserved BTB protein domain. I created a novel 3D culture model to characterise the morphemic role of BTB proteins in oral tissues. Accordingly, this study was the first to characterise the morphogenic roles of the BTB protein BTBD7 in 3D cell culture. This work was among the first to characterise the biophysical properties and molecular mechanisms of the poorly-studied tandem BTB domain and the first to compare CUL3 binding between several tandem BTB domain-containing proteins. Results showed different tandem BTB proteins exhibit differing affinities for CUL3 and different ratios of BTB protein:CUL3 in the BTB-CUL3 complex. Furthermore, this study was the first to report successful crystallisation of the tandem BTB domain. With further optimisation, these crystallisation trials may yield crystals capable of producing diffraction data to solve the first crystal structure of the tandem BTB domain. Finally, this work characterised the mechanism of pathogenesis of novel human substitutions in KCTD15 causing a distinct craniofacial syndrome and was the first to solve the

crystal structure of a human mutant KCTD protein. Altogether, these results make a significant contribution to our understanding of the BTB domain and provide a foundation for future studies of the BTB domain and its critical roles in human biology and disease.

6.4 REFERENCES

1. Smaldone G, Beneduce G, Incoronato M, Pane K, Franzese M, Coppola L, Cordella A, Parasole R, Ripaldi M, Nassa G, Soricelli A, Vitagliano L, Mirabelli P, Salvatore M. KCTD15 is overexpressed in human childhood B-cell acute lymphoid leukemia. Sci Rep. 2019 Dec 27;9(1):20108. doi: 10.1038/s41598-019-56701-7. PMID: 31882877; PMCID: PMC6934626.
2. Marneros AG, Beck AE, Turner EH, McMillin MJ, Edwards MJ, Field M, de Macena Sobreira NL, Perez AB, Fortes JA, Lampe AK, Giovannucci Uzielli ML, Gordon CT, Plessis G, Le Merrer M, Amiel J, Reichenberger E, Shively KM, Cerrato F, Labow BI, Tabor HK, Smith JD, Shendure J, Nickerson DA, Bamshad MJ; University of Washington Center for Mendelian Genomics. Mutations in KCTD1 cause scalp-ear-nipple syndrome. Am J Hum Genet. 2013 Apr 4;92(4):621-6. doi: 10.1016/j.ajhg.2013.03.002. Epub 2013 Mar 28. PMID: 23541344; PMCID: PMC3617379.
3. Angrisani A, Di Fiore A, De Smaele E, Moretti M. The emerging role of the KCTD proteins in cancer. Cell Commun Signal. 2021 May 17;19(1):56. doi: 10.1186/s12964-021-00737-8. PMID: 34001146; PMCID: PMC8127222.
4. Chaharbakhshi E, Jemc JC. Broad-complex, tramtrack, and bric-à-brac (BTB) proteins: Critical regulators of development. Genesis. 2016 Oct;54(10):505-518. doi: 10.1002/dvg.22964. Epub 2016 Aug 22. PMID: 27521773.
5. Daley WP, Matsumoto K, Doyle AD, Wang S, DuChez BJ, Holmbeck K, Yamada KM. Retraction: Btbd7 is essential for region-specific epithelial cell dynamics and branching morphogenesis in vivo. Development. 2020 Aug 12;147(15):dev195560. doi: 10.1242/dev.195560. PMID: 32792339.
6. Shu J, Wang L, Han F, Chen Y, Wang S, Luo F. BTBD7 Downregulates E-Cadherin and Promotes Epithelial-Mesenchymal Transition in Lung Cancer. Biomed Res Int. 2019 Nov 27;2019:5937635. doi: 10.1155/2019/5937635. PMID: 31886230; PMCID: PMC6900955.
7. Fan C, Miao Y, Zhang X, Liu D, Jiang G, Lin X, Han Q, Luan L, Xu Z, Wang E. Btbd7 contributes to reduced E-cadherin expression and predicts poor prognosis in non-small cell lung cancer. BMC Cancer. 2014 Sep 24;14:704. doi: 10.1186/1471-2407-14-704. PMID: 25253020; PMCID: PMC4189533.
8. Pintard L, Willems A, Peter M. Cullin-based ubiquitin ligases: Cul3-BTB complexes join the family. EMBO J. 2004 Apr 21;23(8):1681-7. doi: 10.1038/sj.emboj.7600186. Epub 2004 Apr 8. Erratum in: EMBO J. 2005 Mar 9;24(5):1092. PMID: 15071497; PMCID: PMC394240.

9. Luo FY, Liu ZH, Hu QH, Lin GQ, Tang CE, Zhang WX, Zhuang W. Association of BTBD7 with Metastasis and Poor Prognosis in Non-Small-Cell Lung Cancer Patients. J Cancer. 2015 Mar 26;6(5):477-81. doi: 10.7150/jca.11715. PMID: 25874012; PMCID: PMC4392057.
10. Chen J, Lai YH, Ooi S, Song Y, Li L, Liu TY. BTB domain-containing 7 predicts low recurrence and suppresses tumor progression by deactivating Notch1 signaling in breast cancer. Breast Cancer Res Treat. 2020 Nov;184(2):287-300. doi: 10.1007/s10549-020-05857-2. Epub 2020 Aug 8. PMID: 32772271.
11. Li ZX, Huang ZN, Luo H, Yang XB, Wang YL, Chen JX, Ma XK, Xu F, Wang TT, Lin L. High BTBD7 expression positive is correlated with SLUG-predicted poor prognosis in hormone receptor-negative breast cancer. Ann Transl Med. 2021 Aug;9(15):1252. doi: 10.21037/atm-21-3409. PMID: 34532389; PMCID: PMC8421947.
12. Nguyen Ba AN, Yeh BJ, van Dyk D, Davidson AR, Andrews BJ, Weiss EL, Moses AM. Proteome-wide discovery of evolutionary conserved sequences in disordered regions. Sci Signal. 2012 Mar 13;5(215):rs1. doi: 10.1126/scisignal.2002515. PMID: 22416277; PMCID: PMC4876815.
13. Babu MM. The contribution of intrinsically disordered regions to protein function, cellular complexity, and human disease. Biochem Soc Trans. 2016 Oct 15;44(5):1185-1200. doi: 10.1042/BST20160172. PMID: 27911701; PMCID: PMC5095923.
14. Babu MM, van der Lee R, de Groot NS, Gsponer J. Intrinsically disordered proteins: regulation and disease. Curr Opin Struct Biol. 2011 Jun;21(3):432-40. doi: 10.1016/j.sbi.2011.03.011. Epub 2011 Apr 20. PMID: 21514144.
15. Rice AM, McLysaght A. Dosage-sensitive genes in evolution and disease. BMC Biol. 2017 Sep 1;15(1):78. doi: 10.1186/s12915-017-0418-y. PMID: 28863777; PMCID: PMC5580218.
16. Sugase K, Dyson HJ, Wright PE. Mechanism of coupled folding and binding of an intrinsically disordered protein. Nature. 2007 Jun 21;447(7147):1021-5. doi: 10.1038/nature05858. Epub 2007 May 23. PMID: 17522630.
17. Abe T, Umeki I, Kanno SI, Inoue SI, Niihori T, Aoki Y. LZTR1 facilitates polyubiquitination and degradation of RAS-GTPases. Cell Death Differ. 2020 Mar;27(3):1023-1035. doi: 10.1038/s41418-019-0395-5. Epub 2019 Jul 23. PMID: 31337872; PMCID: PMC7206011.
18. Steklov M, Pandolfi S, Baietti MF, Batiuk A, Carai P, Najm P, Zhang M, Jang H, Renzi F, Cai Y, Abbasi Asbagh L, Pastor T, De Troyer M, Simicek M, Radaelli E, Brems H, Legius E, Tavernier J, Gevaert K, Impens F, Messiaen L, Nussinov R, Heymans S, Eyckerman S, Sablina AA. Mutations in LZTR1 drive human disease by dysregulating RAS ubiquitination. Science. 2018 Dec 7;362(6419):1177-1182. doi: 10.1126/science.aap7607. Epub 2018 Nov 15. PMID: 30442762; PMCID: PMC8058620.
19. Haga RB, Garg R, Collu F, Borda D'Agua B, Menéndez ST, Colomba A, Fraternali F, Ridley AJ. RhoBTB1 interacts with ROCKs and inhibits invasion. Biochem J. 2019 Sep 13;476(17):2499-2514. doi: 10.1042/BCJ20190203. PMID: 31431478; PMCID: PMC6744581.

20. Stogios PJ, Downs GS, Jauhal JJ, Nandra SK, Privé GG. Sequence and structural analysis of BTB domain proteins. Genome Biol. 2005;6(10):R82. doi: 10.1186/gb-2005-6-10-r82. Epub 2005 Sep 15. PMID: 16207353; PMCID: PMC1257465.
21. Adamson RJ, Payne NC, Bartual SG, Mazitschek R, Bullock AN. Structural and biochemical characterization establishes a detailed understanding of KEAP1-CUL3 complex assembly. Free Radic Biol Med. 2023 Aug 1;204:215-225. doi: 10.1016/j.freeradbiomed.2023.04.021. Epub 2023 May 6. PMID: 37156295; PMCID: PMC10564622.
22. Canning P, Cooper CDO, Krojer T, Murray JW, Pike ACW, Chaikuad A, Keates T, Thangaratnarajah C, Hojzan V, Marsden BD, Gileadi O, Knapp S, von Delft F, Bullock AN. Structural basis for Cul3 protein assembly with the BTB-Kelch family of E3 ubiquitin ligases. J Biol Chem. 2013 Mar 15;288(11):7803-7814. doi: 10.1074/jbc.M112.437996. Epub 2013 Jan 24. Erratum in: J Biol Chem. 2013 Sep 27;388(39):28304. Ayinampudi, Vikram [added]. PMID: 23349464; PMCID: PMC3597819.
23. Uversky VN. Intrinsic Disorder, Protein-Protein Interactions, and Disease. Adv Protein Chem Struct Biol. 2018;110:85-121. doi: 10.1016/bs.apcsb.2017.06.005. Epub 2017 Jul 24. PMID: 29413001.
24. Gao XJ, Chong LS, Kim MS, Elowitz MB. Programmable protein circuits in living cells. Science. 2018 Sep 21;361(6408):1252-1258. doi: 10.1126/science.aat5062. PMID: 30237357; PMCID: PMC7176481.
25. Umeki I, Niihori T, Abe T, Kanno SI, Okamoto N, Mizuno S, Kurosawa K, Nagasaki K, Yoshida M, Ohashi H, Inoue SI, Matsubara Y, Fujiwara I, Kure S, Aoki Y. Delineation of LZTR1 mutation-positive patients with Noonan syndrome and identification of LZTR1 binding to RAF1-PPP1CB complexes. Hum Genet. 2019 Jan;138(1):21-35. doi: 10.1007/s00439-018-1951-7. Epub 2018 Oct 27. PMID: 30368668.
26. Pinkas DM, Sanvitale CE, Bufton JC, Sorrell FJ, Solcan N, Chalk R, Doutch J, Bullock AN. Structural complexity in the KCTD family of Cullin3-dependent E3 ubiquitin ligases. Biochem J. 2017 Nov 1;474(22):3747-3761. doi: 10.1042/BCJ20170527. PMID: 28963344; PMCID: PMC5664961.
27. Chambers BE, Clark EG, Gatz AE, Wingert RA. Kctd15 regulates nephron segment development by repressing Tfap2a activity. Development. 2020 Dec 14;147(23):dev191973. doi: 10.1242/dev.191973. PMID: 33028614; PMCID: PMC7758634.
28. Lamontagne JO, Zhang H, Zeid AM, Strittmatter K, Rocha AD, Williams T, Zhang S, Marneros AG. Transcription factors AP-2α and AP-2β regulate distinct segments of the distal nephron in the mammalian kidney. Nat Commun. 2022 Apr 25;13(1):2226. doi: 10.1038/s41467-022-29644-3. PMID: 35468900; PMCID: PMC9038906.
29. Spiombi E, Angrisani A, Fonte S, De Feudis G, Fabretti F, Cucchi D, Izzo M, Infante P, Miele E, Po A, Di Magno L, Magliozzi R, Guardavaccaro D, Maroder M, Canettieri G, Giannini G, Ferretti E, Gulino A, Di Marcotullio L, Moretti M, De Smaele E. KCTD15 inhibits the Hedgehog pathway in Medulloblastoma cells by increasing protein levels of the oncosuppressor

KCASH2. Oncogenesis. 2019 Nov 4;8(11):64. doi: 10.1038/s41389-019-0175-6. PMID: 31685809; PMCID: PMC6828672.
30. Rolland T, Taşan M, Charloteaux B, Pevzner SJ, Zhong Q, Sahni N, Yi S, Lemmens I, Fontanillo C, Mosca R, Kamburov A, Ghiassian SD, Yang X, Ghamsari L, Balcha D, Begg BE, Braun P, Brehme M, Broly MP, Carvunis AR, Convery-Zupan D, Corominas R, Coulombe-Huntington J, Dann E, Dreze M, Dricot A, Fan C, Franzosa E, Gebreab F, Gutierrez BJ, Hardy MF, Jin M, Kang S, Kiros R, Lin GN, Luck K, MacWilliams A, Menche J, Murray RR, Palagi A, Poulin MM, Rambout X, Rasla J, Reichert P, Romero V, Ruyssinck E, Sahalie JM, Scholz A, Shah AA, Sharma A, Shen Y, Spirohn K, Tam S, Tejeda AO, Wanamaker SA, Twizere JC, Vega K, Walsh J, Cusick ME, Xia Y, Barabási AL, Iakoucheva LM, Aloy P, De Las Rivas J, Tavernier J, Calderwood MA, Hill DE, Hao T, Roth FP, Vidal M. A proteome-scale map of the human interactome network. Cell. 2014 Nov 20;159(5):1212-1226. doi: 10.1016/j.cell.2014.10.050. PMID: 25416956; PMCID: PMC4266588.
31. Luck K, Kim DK, Lambourne L, Spirohn K, Begg BE, Bian W, Brignall R, Cafarelli T, Campos-Laborie FJ, Charloteaux B, Choi D, Coté AG, Daley M, Deimling S, Desbuleux A, Dricot A, Gebbia M, Hardy MF, Kishore N, Knapp JJ, Kovács IA, Lemmens I, Mee MW, Mellor JC, Pollis C, Pons C, Richardson AD, Schlabach S, Teeking B, Yadav A, Babor M, Balcha D, Basha O, Bowman-Colin C, Chin SF, Choi SG, Colabella C, Coppin G, D'Amata C, De Ridder D, De Rouck S, Duran-Frigola M, Ennajdaoui H, Goebels F, Goehring L, Gopal A, Haddad G, Hatchi E, Helmy M, Jacob Y, Kassa Y, Landini S, Li R, van Lieshout N, MacWilliams A, Markey D, Paulson JN, Rangarajan S, Rasla J, Rayhan A, Rolland T, San-Miguel A, Shen Y, Sheykhkarimli D, Sheynkman GM, Simonovsky E, Taşan M, Tejeda A, Tropepe V, Twizere JC, Wang Y, Weatheritt RJ, Weile J, Xia Y, Yang X, Yeger-Lotem E, Zhong Q, Aloy P, Bader GD, De Las Rivas J, Gaudet S, Hao T, Rak J, Tavernier J, Hill DE, Vidal M, Roth FP, Calderwood MA. A reference map of the human binary protein interactome. Nature. 2020 Apr;580(7803):402-408. doi: 10.1038/s41586-020-2188-x. Epub 2020 Apr 8. PMID: 32296183; PMCID: PMC7169983.

APPENDICES

Table A.I Key resources.

Reagent or Resource	Source	Identifier
Antibodies:		
Mouse anti-human BTBD7 monoclonal antibody	This report	N/A
Rabbit anti-human BTBD7 polyclonal antibody	This report	N/A
Rat anti-E-cadherin monoclonal antibody, 1 µg/mL IF	ThermoFisher	Cat#13-1900
Mouse α-Tubulin monoclonal antibody, 1:1000 WB	Sigma	Cat#T6199
Rabbit anti-PDI polyclonal antibody, 1:50 IF	Cell Signaling Technology	Cat#2446S
Mouse anti-EEA1 monoclonal antibody, 1:50 IF	Cell Signaling Technology	Cat#48453S
Rabbit anti-20S proteasome polyclonal antibody, 1:50 IF	Invitrogen	Cat#PA1-978
Mouse anti-vimentin monoclonal antibody, 1:200 IF	Sigma	Cat#V5255
Rabbit anti-c-myc monoclonal antibody, 1:1000 WB	Cell Signaling Technology	Cat#5605
Rhodamine Red-X donkey anti-rat antibody, 1:200 IF	Jackson ImmunoResearch	Cat#712-296-153
Rhodamine Red-X donkey anti-rabbit antibody, 1:200 IF	Jackson ImmunoResearch	Cat#711-296-152
Rhodamine Red-X donkey anti-mouse antibody, 1:200 IF	Jackson ImmunoResearch	Cat#715-295-150
Alexa Fluor 488 donkey anti-mouse antibody, 1:200 IF	Jackson ImmunoResearch	Cat#715-545-150
Alexa Fluor 488 donkey anti-rabbit antibody, 1:200 IF	Jackson ImmunoResearch	Cat#711-545-152
Anti-Mouse HRP-linked whole antibody (from donkey), 1:5,000 WB	GE Healthcare	Cat#NA931V
Anti-Rabbit HRP-linked whole antibody (from donkey), 1:5,000 WB	GE Healthcare	Cat#NA934
Goat Anti-Mouse IgG1 antibody, 1:5,000 WB	Abcam	Cat#ab97240
Goat Anti-Mouse IgG2a heavy chain antibody, 1:5,000 WB	Abcam	Cat#ab97245
Goat Anti-Mouse IgG2b heavy chain antibody, 1:5,000 WB	Abcam	Cat#ab97250
Rabbit Anti-Cow IgG H&L antibody, 1:10,000 WB	Abcam	Cat#ab102149
Alexa Fluor 488 phalloidin	Invitrogen	Cat#A12379

Bacterial and Virus Strains:		
NEB stable competent cells	New England Biolabs	Cat#C3040
XL1-Blue competent cells	Agilent Tech	Cat#200249
Rosetta (DE3) competent cells	Sigma-Aldrich	Cat#70954
Lenti-DCW101-BTBD7	This report	N/A
Lenti-DCW102-BTBD7-IRES-BFP	This report	N/A
Chemicals, Peptides, and Commercial Recombinant Proteins:		
Biotin-AP2-(KCTD15-binding-peptide); Biotin-NADFQPPYFPPPYQ	LifeTein	N/A
Biotin-AP2-(KCTD15-binding-peptide)-neg; Biotin-NADFQPPYFAPPYQ	LifeTein	N/A
MLN4924	Sigma	Cat#951950-33-7
CSN5i-3	FisherScientific	Cat#50-196-9032
FGF10	ThermoFisher	Cat#PHG0204
HGF	ThermoFisher	Cat#PHG0254
Experimental Models: Cell Lines		
Immortalized mouse submandibular salivary gland cell line (SIMS WT)	Gift from Kenneth Yamada Lab, NIDCR	N/A
Human embryonic kidney 293T cell line (HEK293T)	ATCC	CRL-11268
SIMS BTBD7 null cell line (SIMS BTBD7 KO)	Gift from Shaohe Wang, NIDCR	N/A
SIMS BTBD7 C-terminal tagged cell line (SIMS BTBD7^{mNeonGreen})	Gift from Shaohe Wang, NIDCR	N/A
Adenocarcinomic human alveolar basal epithelial cell line (A549)	ATCC	CCL-185
Human submandibular salivary gland cell line (SMG-HU1)	Gift from Simon Tran Lab, McGill University	N/A
Adenocarcinomic human breast epithelial cell line (MDA-MB-231)	ATCC	HTB-26
W4/129S6 embryonic stem cells	Taconic	Cat#129SVE
Hybridoma cell lines expressing anti-BTBD7 antibodies	This report	N/A
SIMS tet-BTBD7	This report	N/A
SIMS tet-BTBD7-BFP	This report	N/A
Experimental Models: Organisms/Strains		
Mouse: C57BL/6J	Jackson Laboratory	Cat#000664
Mouse: C57BL/6J BTBD7 homozygous and hemizygous knockout mutants	From the work of Shaohe Wang, NIDCR	N/A
Select Software and Algorithms:		

A Plasmid Editor (APE)	Davis, 2003	https://jorgensen.biology.utah.edu/wayned/ape/
Fiji	Schindelin et al., 2012	https://imagej.net/Fiji
Nikon NIS-Elements	Nikon Instruments	https://www.microscope.healthcare.nikon.com/
Imaris 9.5.0	Bitplane	https://bitplane.com
ImageJ	Schneider et al., 2012	https://imagej.nih.gov/ij/
Proteome Discoverer 2.4	ThermoFisher	https://www.thermofisher.com
SnapGene software	Insightful Science	https://snapgene.com
ICM-Browser	Molsoft molecules in silico	http://www.molsoft.com/icm_browser.html
Pymol	Schrödinger et al.	http://www.pymol.org/pymol. 2020
PHENIX	Liebschner et al., 2019	https://phenix-online.org/
COOT	Emsley et al., 2004	https://www2.mrc-lmb.cam.ac.uk/personal/pemsley/coot/
MolProbity	Chen et al., 2010	http://molprobity.biochem.duke.edu/

Table A.2 Recombinant protein constructs.

Target	Vector	Forward primer name	Reverse primer name	N-terminal residue	C-terminal residue
BTBD7	pNIC28-Bsa4	BTBD7A-f001	BTBD7A-r006	Arg59	Glu258
BTBD7	pNIC28-Bsa4	BTBD7A-f001	BTBD7A-r005	Arg59	Asp400
BTBD7	pNIC28-Bsa4	BTBD7A-f001	BTBD7A-r004	Arg59	Val438
BTBD7	pNIC28-Bsa4	BTBD7A-f001	BTBD7A-r003	Arg59	Glu483
BTBD7	pNIC28-Bsa4	BTBD7A-f001	BTBD7A-r002	Arg59	Ile542
BTBD7	pNIC28-Bsa4	BTBD7A-f001	BTBD7A-r001	Arg59	Leu724
BTBD7	pNIC28-Bsa4	BTBD7A-f002	BTBD7A-r006	Asn77	Glu258
BTBD7	pNIC28-Bsa4	BTBD7A-f002	BTBD7A-r005	Asn77	Asp400
BTBD7	pNIC28-Bsa4	BTBD7A-f002	BTBD7A-r004	Asn77	Val438
BTBD7	pNIC28-Bsa4	BTBD7A-f002	BTBD7A-r003	Asn77	Glu483
BTBD7	pNIC28-Bsa4	BTBD7A-f002	BTBD7A-r002	Asn77	Ile542
BTBD7	pNIC28-Bsa4	BTBD7A-f002	BTBD7A-r001	Asn77	Leu724
BTBD7	pNIC28-Bsa4	BTBD7A-f003	BTBD7A-r006	Ala118	Glu258
BTBD7	pNIC28-Bsa4	BTBD7A-f003	BTBD7A-r005	Ala118	Asp400
BTBD7	pNIC28-Bsa4	BTBD7A-f003	BTBD7A-r004	Ala118	Val438
BTBD7	pNIC28-Bsa4	BTBD7A-f003	BTBD7A-r003	Ala118	Glu483
BTBD7	pNIC28-Bsa4	BTBD7A-f003	BTBD7A-r002	Ala118	Ile542
BTBD7	pNIC28-Bsa4	BTBD7A-f003	BTBD7A-r001	Ala118	Leu724
RHOBTB1	pNIC28-Bsa4	RHOBTB1A-f003	RHOBTB1A-r006	Met1	Val591
RHOBTB1	pNIC28-Bsa4	RHOBTB1A-f003	RHOBTB1A-r005	Met1	Tyr624
RHOBTB1	pNIC28-Bsa4	RHOBTB1A-f003	RHOBTB1A-r004	Met1	Ala696
RHOBTB1	pNIC28-Bsa4	RHOBTB1A-f004	RHOBTB1A-r006	Pro10	Val591
RHOBTB1	pNIC28-Bsa4	RHOBTB1A-f004	RHOBTB1A-r005	Pro10	Tyr624
RHOBTB1	pNIC28-Bsa4	RHOBTB1A-f004	RHOBTB1A-r004	Pro10	Ala696
RHOBTB1	pNIC28-Bsa4	RHOBTB1A-f005	RHOBTB1A-r006	Ser250	Val591
RHOBTB1	pNIC28-Bsa4	RHOBTB1A-f005	RHOBTB1A-r005	Ser250	Tyr624
RHOBTB1	pNIC28-Bsa4	RHOBTB1A-f005	RHOBTB1A-r004	Ser250	Ala696
RHOBTB1	pNIC28-Bsa4	RHOBTB1A-f006	RHOBTB1A-r006	Met385	Val591
RHOBTB1	pNIC28-Bsa4	RHOBTB1A-f006	RHOBTB1A-r005	Met385	Tyr624
RHOBTB1	pNIC28-Bsa4	RHOBTB1A-f006	RHOBTB1A-r004	Met385	Ala696
LZTR1	pNIC28-Bsa4	LZTR1A-f009	LZTR1A-r012	Tyr424	Met766
LZTR1	pNIC28-Bsa4	LZTR1A-f009	LZTR1A-r011	Tyr424	Val803
LZTR1	pNIC28-Bsa4	LZTR1A-f009	LZTR1A-r010	Tyr424	Ile840
LZTR1	pNIC28-Bsa4	LZTR1A-f010	LZTR1A-r012	Leu436	Met766
LZTR1	pNIC28-Bsa4	LZTR1A-f010	LZTR1A-r011	Leu436	Val803
LZTR1	pNIC28-Bsa4	LZTR1A-f010	LZTR1A-r010	Leu436	Ile840
RHOBTB3	pNIC28-Bsa4	RHOBTB3A-f004	RHOBTB3A-r005	Met1	Leu591
RHOBTB3	pNIC28-Bsa4	RHOBTB3A-f004	RHOBTB3A-r004	Met1	Met611
RHOBTB3	pNIC28-Bsa4	RHOBTB3A-f005	RHOBTB3A-r005	Leu244	Leu591
RHOBTB3	pNIC28-Bsa4	RHOBTB3A-f005	RHOBTB3A-r004	Leu244	Met611

BTBD8	pNIC28-Bsa4	BTBD8A-f001	BTBD8A-r003	Met1	Asp303
BTBD8	pNIC28-Bsa4	BTBD8A-f001	BTBD8A-r002	Met1	Ser354
BTBD8	pNIC28-Bsa4	BTBD8A-f001	BTBD8A-r001	Met1	Thr378
BTBD8	pNIC28-Bsa4	BTBD8A-f002	BTBD8A-r003	Gly29	Asp303
BTBD8	pNIC28-Bsa4	BTBD8A-f002	BTBD8A-r002	Gly29	Ser354
BTBD8	pNIC28-Bsa4	BTBD8A-f002	BTBD8A-r001	Gly29	Thr378
BTBD8	pNIC28-Bsa4	BTBD8A-f003	BTBD8A-r003	Glu42	Asp303
BTBD8	pNIC28-Bsa4	BTBD8A-f003	BTBD8A-r002	Glu42	Ser354
BTBD8	pNIC28-Bsa4	BTBD8A-f003	BTBD8A-r001	Glu42	Thr378
ABTB1	pNIC28-Bsa4	ABTB1A-f006	ABTB1A-r007	Met1	Glu378
ABTB1	pNIC28-Bsa4	ABTB1A-f006	ABTB1A-r006	Met1	Cys478
ABTB1	pNIC28-Bsa4	ABTB1A-f007	ABTB1A-r007	Leu73	Glu378
ABTB1	pNIC28-Bsa4	ABTB1A-f007	ABTB1A-r006	Leu73	Cys478
ABTB1	pNIC28-Bsa4	ABTB1A-f008	ABTB1A-r007	Arg98	Glu378
ABTB1	pNIC28-Bsa4	ABTB1A-f008	ABTB1A-r006	Arg98	Cys478
IBTKA	pNIC28-Bsa4	IBTKA-f001	IBTKA-r007	Met1	Glu504
IBTKA	pNIC28-Bsa4	IBTKA-f001	IBTKA-r006	Met1	Ser542
IBTKA	pNIC28-Bsa4	IBTKA-f001	IBTKA-r005	Met1	Ala877
IBTKA	pNIC28-Bsa4	IBTKA-f001	IBTKA-r004	Met1	Leu901
IBTKA	pNIC28-Bsa4	IBTKA-f001	IBTKA-r003	Met1	Ala933
IBTKA	pNIC28-Bsa4	IBTKA-f001	IBTKA-r002	Met1	Ala982
IBTKA	pNIC28-Bsa4	IBTKA-f002	IBTKA-r007	Glu118	Glu504
IBTKA	pNIC28-Bsa4	IBTKA-f002	IBTKA-r006	Glu118	Ser542
IBTKA	pNIC28-Bsa4	IBTKA-f002	IBTKA-r005	Glu118	Ala877
IBTKA	pNIC28-Bsa4	IBTKA-f002	IBTKA-r004	Glu118	Leu901
IBTKA	pNIC28-Bsa4	IBTKA-f002	IBTKA-r003	Glu118	Ala933
IBTKA	pNIC28-Bsa4	IBTKA-f002	IBTKA-r002	Glu118	Ala982
IBTKA	pNIC28-Bsa4	IBTKA-f003	IBTKA-r007	Met127	Glu504
IBTKA	pNIC28-Bsa4	IBTKA-f003	IBTKA-r006	Met127	Ser542
IBTKA	pNIC28-Bsa4	IBTKA-f003	IBTKA-r005	Met127	Ala877
IBTKA	pNIC28-Bsa4	IBTKA-f003	IBTKA-r004	Met127	Leu901
IBTKA	pNIC28-Bsa4	IBTKA-f003	IBTKA-r003	Met127	Ala933
IBTKA	pNIC28-Bsa4	IBTKA-f003	IBTKA-r002	Met127	Ala982
IBTKA	pNIC28-Bsa4	IBTKA-f003	IBTKA-r001	Met127	Cys1353
IBTKA	pNIC28-Bsa4	IBTKA-f004	IBTKA-r007	Asn138	Glu504
IBTKA	pNIC28-Bsa4	IBTKA-f004	IBTKA-r006	Asn138	Ser542
IBTKA	pNIC28-Bsa4	IBTKA-f004	IBTKA-r005	Asn138	Ala877
IBTKA	pNIC28-Bsa4	IBTKA-f004	IBTKA-r004	Asn138	Leu901
IBTKA	pNIC28-Bsa4	IBTKA-f004	IBTKA-r003	Asn138	Ala933
IBTKA	pNIC28-Bsa4	IBTKA-f004	IBTKA-r002	Asn138	Ala982
IBTKA	pNIC28-Bsa4	IBTKA-f004	IBTKA-r001	Asn138	Cys1353
IBTKA	pNIC28-Bsa4	IBTKA-f005	IBTKA-r005	Leu554	Ala877
IBTKA	pNIC28-Bsa4	IBTKA-f005	IBTKA-r004	Leu554	Leu901
IBTKA	pNIC28-Bsa4	IBTKA-f005	IBTKA-r003	Leu554	Ala933
IBTKA	pNIC28-Bsa4	IBTKA-f005	IBTKA-r002	Leu554	Ala982
IBTKA	pNIC28-Bsa4	IBTKA-f005	IBTKA-r001	Leu554	Cys1353
KCTD15 WT	pCDF-LIC, pGTVL2	KCTD15B-f001	KCTD15B-r001	Ser38	Asp283
KCTD15 WT	pCDF-LIC, pGTVL2	KCTD15B-f001	KCTD15B-r002	Ser38	Arg267
KCTD15 WT	pCDF-LIC, pGTVL2	KCTD15B-f001	KCTD15B-r003	Ser38	Ala165
KCTD15 WT	pCDF-LIC, pGTVL2	KCTD15B-f002	KCTD15B-r001	Thr52	Asp283
KCTD15 WT	pCDF-LIC, pGTVL2	KCTD15B-f002	KCTD15B-r002	Thr52	Arg267

KCTD15 WT	pCDF-LIC, pGTVL2	KCTD15B-f002	KCTD15B-r003	Thr52	Ala165
KCTD15 G88D	pCDF-LIC, pGTVL2	KCTD15B-f001	KCTD15B-r001	Ser38	Asp283
KCTD15 G88D	pCDF-LIC, pGTVL2	KCTD15B-f001	KCTD15B-r002	Ser38	Arg267
KCTD15 G88D	pCDF-LIC, pGTVL2	KCTD15B-f001	KCTD15B-r003	Ser38	Ala165
KCTD15 G88D	pCDF-LIC, pGTVL2	KCTD15B-f002	KCTD15B-r001	Thr52	Asp283
KCTD15 G88D	pCDF-LIC, pGTVL2	KCTD15B-f002	KCTD15B-r002	Thr52	Arg267
KCTD15 G88D	pCDF-LIC, pGTVL2	KCTD15B-f002	KCTD15B-r003	Thr52	Ala165
KCTD15 D104H	pCDF-LIC, pGTVL2	KCTD15B-f001	KCTD15B-r001	Ser38	Asp283
KCTD15 D104H	pCDF-LIC, pGTVL2	KCTD15B-f001	KCTD15B-r002	Ser38	Arg267
KCTD15 D104H	pCDF-LIC, pGTVL2	KCTD15B-f001	KCTD15B-r003	Ser38	Ala165
KCTD15 D104H	pCDF-LIC, pGTVL2	KCTD15B-f002	KCTD15B-r001	Thr52	Asp283
KCTD15 D104H	pCDF-LIC, pGTVL2	KCTD15B-f002	KCTD15B-r002	Thr52	Arg267
KCTD15 D104H	pCDF-LIC, pGTVL2	KCTD15B-f002	KCTD15B-r003	Thr52	Ala165
KCTD1	pNIC-NHT-cTStII	KCTD1A-f004	KCTD1A-r005	Met1	Asp257
KCTD1	pNIC-NHT-cTStII	KCTD1A-f004	KCTD1A-r006	Met1	Arg241
KCTD1	pNIC-NHT-cTStII	KCTD1A-f004	KCTD1A-r007	Met1	Glu132
KCTD1	pNIC-NHT-cTStII	KCTD1A-f005	KCTD1A-r005	Ser12	Asp257
KCTD1	pNIC-NHT-cTStII	KCTD1A-f005	KCTD1A-r006	Ser12	Arg241
KCTD1	pNIC-NHT-cTStII	KCTD1A-f005	KCTD1A-r007	Ser12	Glu132

Table A.3 Recombinant protein cloning primers.

Primer name	Primer sequence
ABTB1A-f006	TACTTCCAATCCATGGACACCAGCGACCTGTTC
ABTB1A-f007	TACTTCCAATCCATGCTCTATGGGGCACTGAGT
ABTB1A-f008	TACTTCCAATCCATGCGGGATTACTATGACGACTTCTTGC
BTBD1A-f003	TACTTCCAATCCATGCTCCCCCTGCAGCGGGAA
BTBD1A-f004	TACTTCCAATCCATGCAGGCGACCAAGGCGTCG
BTBD1A-f005	TACTTCCAATCCATGCTCTTCAACTCGGAGCTGC
BTBD1A-f006	TACTTCCAATCCATGATTGACCGACCAAGATGCTGT
BTBD2A-f001	TACTTCCAATCCATGGCTGCTTTGCAGCGCGAA
BTBD2A-f002	TACTTCCAATCCATGCAGGCTAGCAAGCCCACC
BTBD2A-f003	TACTTCCAATCCATGCTCTTCAACAACGAGGTGC
BTBD2A-f004	TACTTCCAATCCATGATTGACCGGCCCCGATGC
BTBD7A-f001	TACTTCCAATCCATGAGAACCTCTGGTCTTGCCA
BTBD7A-f002	TACTTCCAATCCATGAATAGGTCTGCCGATCATGCC
BTBD7A-f003	TACTTCCAATCCATGGCCAGTTTGGCTAGACCA
BTBD8A-f001	TACTTCCAATCCATGGCTCGCTGTGGGGAAGGC
BTBD8A-f002	TACTTCCAATCCATGGGGCCGTGTGAGCGGCGC
BTBD8A-f003	TACTTCCAATCCATGGAGCAGCTCAGCCAGGAT
IBTKA-f001	TACTTCCAATCCATGAGTTCACCCATGCCTGACT
IBTKA-f002	TACTTCCAATCCATGGAAGGCTTGTCAGCTTTGG

IBTKA-f003	TACTTCCAATCCATGAAGGATAGACCAACTCATGTAGTATTCAAGAATACTG
IBTKA-f004	TACTTCCAATCCATGAATACTGATCCTACAGATGTTTATACTTGGGGC
IBTKA-f005	TACTTCCAATCCATGTTGAGGGAAGCAGATGAAATGGA
LZTR1A-f009	TACTTCCAATCCATGTACCCTAAATGCACGCTGC
LZTR1A-f010	TACTTCCAATCCATGCTGTGGGAGAGCCGCCAG
RHOBTB1A-f003	TACTTCCAATCCATGGACGCTGACATGGACTACG
RHOBTB1A-f004	TACTTCCAATCCATGCCCAACGTTGAAACTATCAAATGTGT
RHOBTB1A-f005	TACTTCCAATCCATGGGGACAAATGAAGCTGCC
RHOBTB1A-f006	TACTTCCAATCCATGCAAGTCAACCCCATTTCAAAGC
RHOBTB3A-f004	TACTTCCAATCCATGTCCATCCACATCGTGGCG
RHOBTB3A-f005	TACTTCCAATCCATGTTAAATAACTTGCTGTTCTGCTGCCA
ABTB1A-r006	TATCCACCTTTACTGTCAACAGTCCAGACCGATGGA
ABTB1A-r007	TATCCACCTTTACTGTCACTCGTCTAGCATCTGAGCC
BTBD1A-r006	TATCCACCTTTACTGTCATGTATAAAATATGATTTCTGGAATTTGTCCATCTTCTATTGAAGT
BTBD2A-r001	TATCCACCTTTACTGTCAGGTGTAGAAGATGACCTCGG
BTBD7A-r001	TATCCACCTTTACTGTCAGAGTGGACTTTCATCCCC
BTBD7A-r002	TATCCACCTTTACTGTCAAATCAAGCCTCTTTTCATTGCATCA
BTBD7A-r003	TATCCACCTTTACTGTCACTCTCTATCTGCTATTCTTTTCATCAACTGA
BTBD7A-r004	TATCCACCTTTACTGTCAAACATCCGAAGTCATGACCTG
BTBD7A-r005	TATCCACCTTTACTGTCAATCTAATGAGATGCTCTCAGCAATGA
BTBD7A-r006	TATCCACCTTTACTGTCATTCAGAGTCTGAAGAAAAACTAAGGACG
BTBD8A-r001	TATCCACCTTTACTGTCAGGTTATATTTACTAAGGACTGAATCAACATATTAAGACAACT
BTBD8A-r002	TATCCACCTTTACTGTCAGCTTCTCTCAGACCAAAACC
BTBD8A-r003	TATCCACCTTTACTGTCAATCTCTTCTTAAAATATAGATTGCTACTTCTTTTAATCCTTCTAGTCC
IBTKA-r001	TATCCACCTTTACTGTCAGCATCCATGCTTATTCCACA
IBTKA-r002	TATCCACCTTTACTGTCAAGCTTTTGTTTTTGCTTTCTTGAACATAGT
IBTKA-r003	TATCCACCTTTACTGTCATGCTGGAATCATTTTCCGGT
IBTKA-r004	TATCCACCTTTACTGTCACAATCCTATAAACTGTAAACAAGACAGTTTCAACT
IBTKA-r005	TATCCACCTTTACTGTCAAGCAGCATTCTTCAGGGT
IBTKA-r006	TATCCACCTTTACTGTCAGGACACAGCTGGAATTTCA
IBTKA-r007	TATCCACCTTTACTGTCACTCAAGTCGAATTCTTTCATACACACT
LZTR1A-r010	TATCCACCTTTACTGTCAGATGTCGGCGCCCAGCTC
LZTR1A-r011	TATCCACCTTTACTGTCAGACCTTGGTGAACTGGTG
LZTR1A-r012	TATCCACCTTTACTGTCACATCTCCAGGTTCTGCTT
RHOBTB1A-r004	TATCCACCTTTACTGTCAGGCCACTGCTGGAGATGA
RHOBTB1A-r005	TATCCACCTTTACTGTCAGTAGTTGGTGCAGATGTGG
RHOBTB1A-r006	TATCCACCTTTACTGTCACACGCCACTCGTGGCGGC
RHOBTB3A-r004	TATCCACCTTTACTGTCACATTACTAAGCAACGACATTTCCGG
RHOBTB3A-r005	TATCCACCTTTACTGTCACAAGTACATATTCGACGGCCA
KCTD15B-f001	TACTTCCAATCCATGTCTCCCCTGGCTGCCCA
KCTD15B-f002	TACTTCCAATCCATGACCAAGTCCAATGCACCTG
KCTD15B-r001	TATCCACCTTTACTGTCAGTCCAGGGGTTCCTGC
KCTD15B-r002	TATCCACCTTTACTGTCACCGCCGCTCCTCCCG
KCTD15B-r003	TATCCACCTTTACTGTCAGGCCCGGCTGCGGCG

KCTD1A-f004	TACTTCCAATCCATGTCAAGACCTCTGATCACTAGATCCC
KCTD1A-f005	TACTTCCAATCCATGTCTCCACTGAACAACCAAGGC
KCTD1A-r005	ACCACCACCACTACTGCCGTCCAGAGGCTCTTGC
KCTD1A-r006	ACCACCACCACTACTGCCCCGCCTCAGTTCCCG
KCTD1A-r007	ACCACCACCACTACTGCCTTCTCTGTCCTGCTTCCA
KCTD15Z-f006	TCAATGACACTGAACCCATC *Mutagenesis primer
KCTD15Z-r006	TTCAGTGTCATTGAAGAGGC *Mutagenesis primer